The University Of Sheffield.

Acoustical properties of polymeric fibres and their characterisation

By:

Alistair Hurrell

A thesis submitted in partial fulfilment of the requirements for the degree of

Doctor of Philosophy

The University of Sheffield

Faculty of Engineering

Department of Mechanical Engineering

16/09/2019

Abstract

This thesis is concerned with manufacturing and acoustical characterisation of polymeric fibres. The fibres studied in this work were made from a range of polymers and their material properties varied considerably. This work enabled us to develop a better understanding of the applicability of various empirical and theoretical models for the prediction of acoustical and non-acoustical properties of polymeric fibres. It was shown that these materials can be tailored for various noise control solutions in vehicles whilst meeting a range of design criteria.

In an attempt to improve the acoustical performance of traditional acoustic absorbers thin fibrous membranes were electrospun, characterised and modelled. These membranes presented fibre diameters ranging from 70nm to 2µm and were 10-250µm thick. Acoustic testing revealed that when used in conjunction with relatively thin porous substrates they are able to boost the value of the absorption coefficient of the substrate by up to 100% over a broad frequency range. It was found that existing prediction models are not sufficiently accurate to explain the measured acoustical performance of nanofibrous membranes. There are intrinsic problems with the existing standards for acoustic material characterisation which make it difficult to apply them to nanofibrous membranes. Several approaches to improve prediction and measurement methods, and to minimise the observed errors were made and the results were quantified. It is believed that this is the first systematic attempt to produce a controlled range of nanofibrous membranes, measure their acoustical properties carefully and explain them with a range of existing prediction models.

This thesis reports also presents recommendations on the improvements to the existing material measurement and modelling methods, and points to a fundamental knowledge gap that exists in this area of research. Closing this gap is important for areas of noise control, material engineering and polymer chemistry.

Acknowledgements

First and foremost, I wish to sincerely thank my supervisors Professor Kirill Horoshenkov, and Doctor Anton Krynkin for donating their time, thoughts and help during my time as a student at the University of Sheffield. Their guidance and support truly drove this PhD to progress as far as it did and helped ensure I stay motivated and grounded.

There are several other people to whom I owe my thanks, and without whom there would have been far more hurdles to jump and walls to circumnavigate. I am sincerely grateful to Doctor Paolo Bonfiglio, whose knowledge and assistance in all things impedance tube based proved to be exceedingly helpful. I also want to thank Professor Paul Hatton for graciously allowing me access to a range of equipment that I would otherwise not had, which enabled me to synthesise the materials discussed in this work and further the scope of the PhD.

Immense thanks must also go to the technical staff at the University of Sheffield, especially Les Morton for all of his assistance in the first half of my time here, and whose enthusiasm and spirit truly made me look forward to my time in the lab. Mathew Hall also deserves a great deal of thanks for his help in the Jonas Lab in the latter half of my PhD, and whose work was exemplary. Chris Hill also proved to be extremely helpful in sample preparation and training with regards to the use of scanning electron microscopy, proving to push my knowledge in its use.

Lastly, this PhD would not have been possible without the joint funding from the EPSRC, the CDT for Polymers, Soft Matter, and Colloids and my industrial sponsor John Cotton Group Ltd. Special thanks here must go to my industrial supervisor Doctor Michael Pelegrinis for all his assistance, and Stephen Midgely for his insight relating especially to the development of nonwovens for industrial usage.

Publications

Journal Publications

K.V. Horoshenkov, J.-P. Groby, A. Hurrell, *A three-parameter analytical model for the acoustical properties of porous media*, J. Acoust. Soc. Am, 2019, **145**(4), 2512-2517

A. Romanova, K.V. Horoshenkov, A. Hurrell, *An application of a parametric transducer to measure acoustic absorption of a living green wall*, Applied Acoustics, 2019, **145**, 89-97

T. Yang, R. Mishra, K.V. Horoshenkov, A. Hurrell, F. Saati, X. Xiong, *A study of some airflow resistivity models for multi-component polyester fiber assembly*, Applied Acoustics, 2018, **139**, 75-81

A.I. Hurrell, K.V. Horoshenkov, M.T. Pelegrinis, *The accuracy of some models for the airflow resistivity of nonwoven materials*, Applied Acoustics, 2018, **130**, 230-237

C.J. Fackler, A. Hurrell, D. Beaton, N. Xiang, *Statistical analysis of multilayer porous absorbers with Bayesian inference*, JASA, 2016, **139**(4), 2070**,** doi.org/10.1121/1.4950139

Conference Publications

K. Horoshenkov, A. Hurrell, M. Jiao, *Are nano-fibers an emerging noise control solution?,* JASA, 2018, **144**(3), 1755-1755

A. Hurrell, M. Pelegrinis, *Non-wovens Next Top Model?*, Proceedings of the Institute of Acoustics, 2016, **38**(1), 407

Table of Contents

List of Figures

List of Tables

Nomenclature

Greek Symbols

α	Absorption coefficient
α_∞	Geometric tortuosity
α_{∞_m}	Tortuosity in the membrane in the two-layer model with membrane surface density
Δp	Pressure drop encountered during measurements of airflow resistivity
ζ	Airflow velocity
θ	Real positive coefficient whose values depend only on the assumed pore shape
Π_{dp}^{s}	Static viscous permeability
Π^{s}	Permeability of microporous network in double porosity material
Π_{m}^{s}	Permeability of macroporous network in double porosity material
ρ	Air density
ρ_f	Fibre density
ρ_m	Density of a sample/specimen
$\tilde{\rho}_b(\omega)$	Dynamic density of air in a porous material with non-uniform pores
$\tilde{\rho}_x(\epsilon_\rho)$	Approximation of dynamic density in a single pore
σ	Airflow resistivity
σ'	Thermal flow resistivity

σ_s	Standard deviation of the log-normal distribution of the material pore size. For fibrous media with a relatively high porosity $\sigma_s \approx 0$
$\sigma_{\bar{s}}$	Standard deviation of pore size in the two-layer model
$\sigma_{\bar{s}m}$	Standard deviation of pore size in the two-layer model with membrane surface density
σ_{total}	Value of airflow resistivity, taking into consideration an airgap
σ_x	Airflow resistivity of a single pore
$\sigma_x^{'}$	Thermal flow resistivity in a single pore
ϕ	Porosity of a sample/specimen
ϕ_m	Airflow resistivity in the membrane in the two-layer model with membrane surface density
ϕ_{mat}	Total porosity in a material, in Pilon equations (Pilon, 2002)
ϕ_{total}	Total porosity value in a double porosity material
x_1	Distance between the front of the sample and microphone 1 in an impedance tube
γ	Specific heat ratio
ω	Angular frequency

Roman Symbols

A	Constant in Garai and Pompoli 'New Resistivity Model', with a value of 25.989
a	Mean molecular pathway

B	Constant in Garai and Pompoli 'New Resistivity Model', with a value of 1.404
$\tilde{C}_b(\omega)$	Bulk complex compressibility in a porous material with non-uniform pores
$\tilde{C}_x$	Bulk complex compressibility in a single pore
c	Speed of sound in air
d	Fibre diameter in denier, a unit of weight equivalent to the weight in grams of 9000 metres of the fibre
d_f	Fibre diameter
$\tilde{F}_\rho(\epsilon_p)$	Padé approximant for viscosity correction term
f	Frequency of soundwave
f_n	Describes range of frequencies in which impedance was measured in an Impedance tube
H	Denotes a transfer function in sound impedance tube theory
h	Height of a sample/specimen
I_a	The acoustic intensity which propagates through and is absorbed by the material
I_i	The acoustic intensity incident on the surface of the material
I_r	The reflected acoustic intensity
i	An imaginary number, with the value $i = \sqrt{-1}$
iX	Denotes the imaginary part of the surface impedance describing the acoustical reactance
K	Knudsen number
K_1	Dimensionless empirical constant in Bies-Hansen equation

K_2	Dimensionless empirical constant in Bies-Hansen equation
$\widetilde{K}(\omega)$	Dynamic bulk modulus of air in a porous material with non-uniform pores
k	A constant in Boyle's law, that is described by a given mass of confined gas at a given temperature
k_0	Wavenumber in air
k_b	Wavenumber
$k_b(\omega)$	Wavenumber in a porous material with non-uniform pores
M_w	Molecular weight, the sum of the atomic weights of each monomer unit making up the polymeric molecule
m	Mass of a sample/specimen
N_{Pr}	Prandtl number
P	Pressure
P_s	Amplitude of sound pressure
$\lvert R \rvert$	The absolute value of the pressure complex reflection coefficient
R_a	Acoustical resistance, denoting the real part of the surface impedance
R	The reflection coefficient
r	Radius of sound impedance tube
r_m	Radius of material in the sound impedance tube, taking airgap into consideration
S	Describes the material surface
s	Distance between the two microphones in a two-microphone impedance tube

$\bar{s}$	Median pore size in the two-layer model
$\bar{s}_m$	Median pore size of the membrane in the two-layer model with membrane surface density
$\bar{s}_{total}$	Corrected estimate of median pore size, taking into consideration an airgap
t	Size of airgap, in Pilon equations (Pilon, 2002)
V	Volume of a sample
V_a	Describes the difference in air volume between two chambers according to Boyle's law
V_r	Pressure reflection coefficient
v	Acoustical velocity
Z_{in}	Surface impedance at the boundary conditions

Script Symbols

°C	Temperature in degrees Celsius
⌀ID	Inner diameter
%RH	Relative humidity, the ratio of the partial pressures of water vapour to the equilibrium vapour pressure of water for a given temperature
%w/w	Weight per weight. Represents the weight of a reagent used in a solution, e.g. in a 100g solution made up of 20g of NaCl (salt) in 80g of H_2O (water), NaCl would be 20% w/w
$\sqrt{\bar{x}^2}$	Root mean square error

$e^{ik_0\,[\ldots]}$	Time correction in transfer function method of measuring sound absorption in impedance tubes.

Acronyms

BHET	bis-(2-hydroxyethyl)terephthalate, monomer
BuAC	N-butylacetate, reference material for solvent evaporation rate
CO_2	Carbon Dioxide, molecule
DAQ	Data acquisition, a process of measuring electrical or physical phenomenon
DCM	Dichloromethane, solvent
DMC	Dimethylcarbonate, solvent
DMF	Dimethylformamide, solvent
DMSO	Dimethylsulfoxide, solvent
DMT	Dimethyl terephthalate, reagent
EG	Ethylene glycol, reagent
eROP	Enzymatic ring opening polymerisation
ETA	Ethanolamine, catalyst
EU	European Union
Hz	Hertz, SI unit of frequency
ID	Internal diameter
NO_x	Nitrogen oxides, family of molecules
PCL	Poly(ε-caprolactone), polymer
PET	Poly(ethylene terephthalate), polymer
PLLA	Poly(l-lactic acid), polymer
PMMA	Poly(methyl methacrylate), polymer
PS	Polystyrene, polymer

PU	Poly(urethane), polymer
PVC	Poly(vinyl chloride), polymer
PVDF	Poly(vinylidene fluoride), polymer
SEM	Scanning electron microscopy, characterisation method
SiO_2	Silicon dioxide, catalyst
$Sn(Oct)_2$	Stannous(II) ethylhexanoate, catalyst
TFA	2,2,2-trifluoroacetic acid, solvent
THF	Tetrahydrofuran, solvent
TiO_2	Titanium(IV) oxide, catalyst
TPA	Terephthalic acid, reagent
TPU	Thermoplastic poly(urethane), polymer

Chapter 1: Introduction

1.1 Problem

There is a drive to improve the acoustic insulation in automobiles for a variety of reasons. Firstly, there are numerous physical and psychological impacts that can occur when we as humans are subjected to acoustic noise for extended periods of time. The psychological and physical impacts, alongside the impact on health-related quality of life of being exposed to excessive noise are well documented (Singer, *et al,* 1973; Dockrell, Shield, 2006; Shepherd, *et al*, 2011 ; Bakker, *et al*, 2012) and will not be covered directly herein. It is important to note that the external noise generated by automobiles has been monitored and controlled in the UK since 1929, so it is apparent that this issue has been a long standing one. In 1978, European-wide noise limits were introduced that limited the external noise produced by automobiles to 82 dB(A). This was progressively decreased to its current value of 74 dB(A), which was enforced in 1996 (Vehicle Certification Agency, 2018). In 2014, Regulation (EU) No 540/2014 (Publications of the European Union, 2014) was introduced, which is designed to phase in both tighter noise limits and stricter testing conditions; the noise limit for new automobiles will be 68 dB(A) by 2026. The same document also noted that traffic noise harms health in numerous ways, citing noise-related stress as being a factor in exhausting physical reserves, limiting the effectiveness of organ function, and being a potential risk factor in the development of medical conditions such as high blood pressure or heart attacks (Publications of the European Union, 2014). Additionally, noise produced by vehicle tyres has been tightly controlled and reduced in a similar vein to the external noise limits, through Regulation (EC) No 661/2009 (Eur-Lex, 2009), further highlighting the significance of noise control in automobiles.

Alongside the numerous regulations and directives from both national and EU bodies, there are other factors that have to be considered in the design and implementation of acoustic solutions to automobiles. Manufacturers are keen to improve efficiencies – backed partially by legislations relating to CO_2 emissions, and more recently NO_x emissions. Of course, the

greatest improvements in these areas will be controlled by gains in engine and propulsion technologies, but there are still fairly significant challenges in decreasing vehicle weight. Common automotive acoustic solutions tend to be poly(urethane) (PU) foam based and as such can be quite high in both density and thickness. A switch to nonwoven polymer-based materials would have the potential to decrease both the weight and thickness of the materials whilst maintaining or improving upon the level of acoustic performance.

1.2 Aims and objectives

The main aim of this PhD project was to explore the use of polymer fibres for acoustic absorption and insulation, specifically for use within the automotive industry. Initially this called for an understanding of the materials that are currently used for acoustic purposes within the industry, and what the key points of interest are for industrial manufacturers to facilitate change. Experiments were performed on a range of real-world acoustic solutions taken from several manufacturer brands and models to understand the current level of acoustic performance, as well as to gauge the optimal material parameters such as density, fibre diameter, and thickness. These experiments suggested that there should be two avenues of approach to the problem of acoustic solutions in automobiles.

The first avenue was to investigate maximising the acoustic performance of the types of solutions currently in place, through an understanding of how the material parameters impact the acoustics and hence how those parameters can be optimised to attain the greater performance. The second approach was to produce a different type of acoustic solution, one with the potential to decrease weight and thickness of current solutions whilst maintaining or improving the performance.

Several additional aims were set as a result of these two approaches. The optimisation of current solutions entailed understanding better how the material parameters affect the acoustic performance, in addition to looking into how changing some of those key parameters - specifically airflow resistance and fibre diameter, could result in improved performance without requiring any changes in production industrially. Regarding the generation of

'different' approaches to acoustic solutions, work completed on understanding the material parameters lead to the use of a membrane on the surface of another material, referred to as a substrate. It was shown that this thin membrane (typically <50μm) would provide a substantial increase in the absorption of a porous substrate and so allow the substrate to become significantly thinner and lighter. The development of nanofibrous membranes led to a need to gain an understanding of why the membranes behave the way they do and why it is difficult to predict their acoustical properties using existing theoretical and/or empirical models.

There are two key novel aspects in this PhD. The first novel aspect is to produce a range of nanofibrous membranes for acoustic absorption application and to understand better their effect on the acoustical properties of a porous substrate. The second novel aspect is to gain an increased understanding of the problems associated with the process of measurement and predictions of the acoustical properties of nanofibrous membranes, and to quantify the errors associated with these processes.

1.3 Thesis Outline

The second chapter of this thesis starts by introducing the basics of polymers with a focus on the polymers used within the PhD project. The basics behind both the acoustics and process of the preparation of polymeric fibres are covered, along with the synthesis of both the monomer and polymer units of each material. Within the same chapter key material parameters are explained, along with their impact on the acoustic performance of a material. A discussion of the key sources of noise in automobiles occurs, to give context to the range of frequencies that need to be minimised to improve performance.

Chapter three covers the chemical side of this PhD project, detailing the material preparation methods and observations of both the nonwoven materials, and the nanofibrous and nanoporous membranes. The range of solvents, processing parameters, and polymers used to produce the membranes is documented, along with any problems associated with it. This chapter discusses how these problems can be managed, as well as providing some

information on what was found to be the most stable or reliable approaches for the production of nanofibrous membranes.

Chapter four discusses the characterisation and modelling of the acoustical properties of nonwoven media. It explains the parameter inversion process and explores the performance of some common prediction models. Two in-depth studies are presented on how to choose the best model and how to get the most accurate parameter inversion for this kind of materials. This chapter concludes with a discussion of the downsides of the existing models and explains why it is important to develop a better model for this type of materials.

Chapter five opens with a discussion of how the synthesised membranes were characterised, before presenting the fully characterised membranes. Following this, work on attempting to model these membranes in presented. The observed results from this modelling are then discussed, with the aim of evaluating why the results from these models is generally poor and highlighting the difficulties in applying current models to these materials. The latter part of this chapter studies the acoustic performance of these membranes and attempts to relate changes made during the synthesis procedure, such as voltage or solution properties, to the attained acoustic performance. The aim of this work was to develop the understanding of how the acoustic performance can be customised and tailored throughout the synthesis of nanofibrous membranes.

Chapter six concludes the thesis by reviewing the findings from each previous chapter and the key points identified within. It also discusses the areas in which future work would be undertaken and how perhaps this could be best achieved.

Chapter 2: Literature Review

2.1 Introduction to polymers

A polymer is defined as a macromolecule that is made up of many repeated units. The repeated unit is referred to as a monomer, and its properties dictate the chemical and physical properties of the resulting polymer. A wide range of material properties can be attained by modifying this monomer unit, including physical properties like conductance, stability, tensile strength, as well as thermal properties like degradation profiles, transition temperatures and melting points. Acoustically, different monomers can also indirectly impact absorption. From an industrial point of view, these will all impact the processing of the fibre, and so its general suitability for a given application. Polymers with relatively low degradation properties will be less suited to applications where they are exposed to heat and moisture cycles, whilst polymers that are harder to solvate will be less favourable due to the cost of more effective solvents.

A range of polymers were studied in this thesis. All initial work was done using poly(ethylene terephthalate), as this is the most readily available of the polyesters and was a material of key interest for our industrial partner, John Cotton Group Ltd. Later work moved on to polycaprolactone and poly(methylmethacrylate) in a bid to reduce the cost of production, as these polymers are far easier to solvate and so require cheaper, more environmentally friendly solvents.

2.2 History and syntheses of polyesters

The term ‘polyester’ describes a family of polymers made up from an ester-derived backbone. Of this family, the most commonly encountered polymer and the one most commonly utilised within this PhD is poly(ethylene terephthalate) (PET). Other variants include poly(ε-caprolactone) (PCL), and polylactic acid (PLLA). PET is a synthetic polymer that is used widely

in the form of fibres, films, and molded parts such as bottles. Approximately 60% of all PET produced ends up in usage as a fibre, and PET accounts for 30% of the global fibre market (Li-na, 2013). Its commonality and widespread usage were the main factor in why PET was chosen as the main focus of this work. PET was first patented by Winfield and Dickson in 1941 and was found to have favourable properties because of its high melting point (265°C), hydrolytic stability, and strength which rivalled nylon (Paul, 1985).

The synthesis of PET involves a two-step reaction, in which the PET monomer is formed and then undergoes a polycondensation reaction to form the polymer. There are different methods to form the PET monomer, with most modern methods beginning with the acid (terephthalic acid (TPA), or dimethyl terephthalate (DMT)) as it is available commercially in large quantities.

The first of these methods is the direct esterification reaction (Reaction 2.1), in which the acid reacts directly with the alcohol, usually ethylene glycol (EG), to generate the monomer.

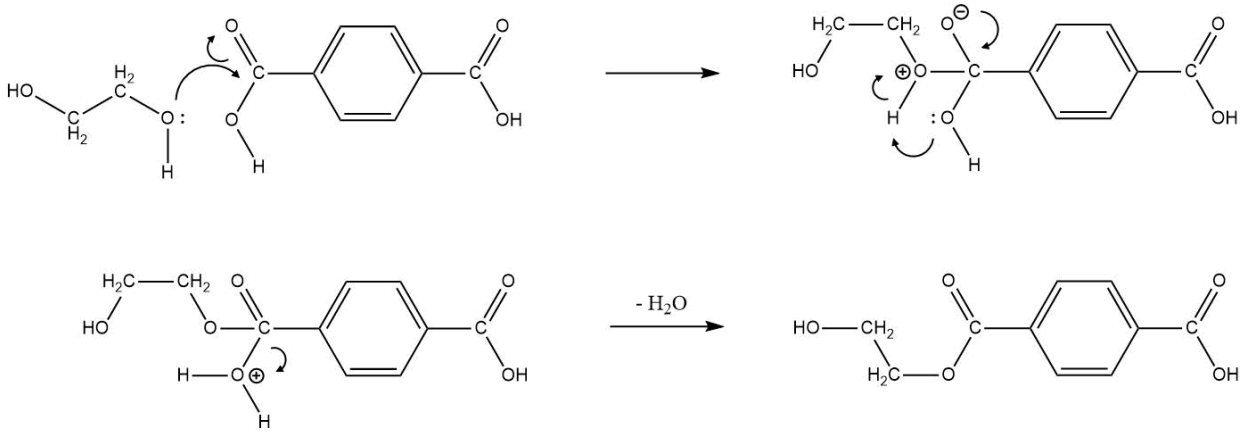

Reaction 2.1

The second method starts from a dimethyl ester instead of the acid (Reaction 2.2) and is an example of an ester interchange reaction. This is a two-step reaction, first generating the acid and then the monomer.

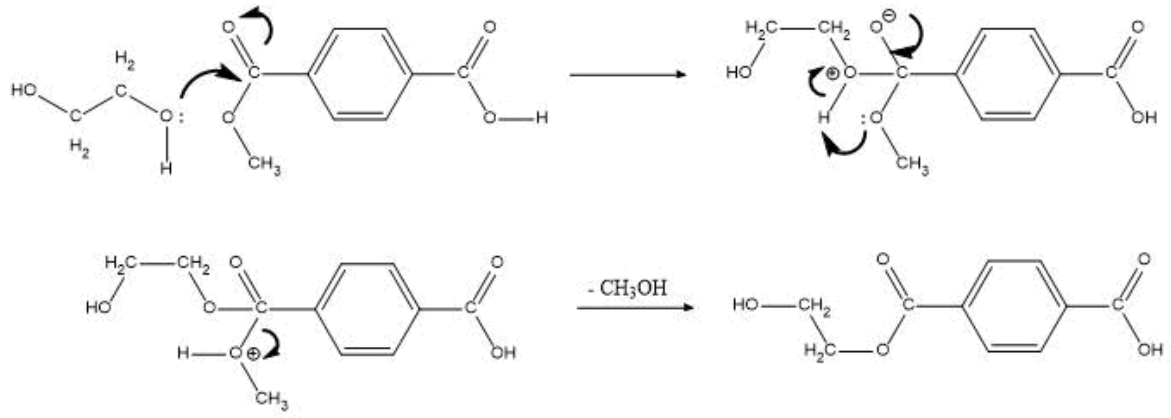

Reaction 2.2

The second step of the PET synthesis is a polycondensation step to generate the polymer. In this step, ethane-1,2-diol ($C_2H_4(OH)_2$) is eliminated in a condensation reaction to generate the PET polymer (Reaction 2.3). This leaves us with a polymer pre-cursor, which in the case of fibrous PET is then fed directly into a variety of processes to generate the fibre. These processes include melt-spinning and electrospinning.

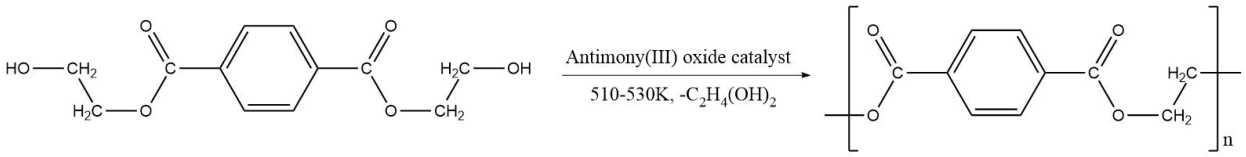

Reaction 2.3

In terms of synthesis conditions, the direct esterification route (Reaction 2.1) would involve mixing the two monomers (TPA and EG) into a slurry at a molar ratio of 1:1.5-3. One study found that low monomer feed ratios and high temperatures or 240-260^{o}C can enhance the solubility of the TPA monomer (Kang, *et al*, 1996). Catalysts are not required for this step of the reaction. The collection and analysis of water formed during the reaction can be used to estimate the conversion percentage of the reaction. It is noted that the addition of PET monomer, also known as bis-(2-hydroxyethyl)terephthalate (BHET), can be used to speed up

the rate of the reaction, but this is primarily employed in commercial application, due to having large amounts of the required feedstock.

The ester interchange pathway (Reaction 2.2), utilises the monomers DMT and EG, which are mixed at molar ratios of 1:2.1-2.3 and the relevant catalysts added. The reaction proceeds under a slow stream of nitrogen and a temperature of between 177-210^{o}C. The by-product methanol can be collected and analysed to allow for the estimation of reaction conversion. Completion of the reaction can be determined once methanol stops distilling, leaving the desired end product BHET.

A further study investigated the effects of adding TPA to the polycondensation stage of Reaction 2.1 and found that its use as an additive resulted in the reaction proceeding at a rate two to three times faster than normal. They proposed that the carboxylic acid group present on TPA was able to form an ion pair, via autoprotolysis, and the proton ion was then able to catalyze the reaction (Chegolya, *et al*, 1979).

With regards to the use of catalysts in the generation of the PET monomer, relatively few have been applied in a commercial setting (Ravindranath, Mashelkar, 1986). This is because it is challenging to find a catalyst that accelerates both steps within the reaction without also promoting side reactions. Naturally, this is undesirable as it will result in decreased yield of the final product.

As a result catalysts are generally only used in the direct esterification and polycondensation stages; typically two catalysts are generally selected for use within the reaction. The catalysts with good commercial acceptance for the direct esterification stage are generally acetates of zinc, magnesium, sodium and calcium due to their solubility and high catalytic effect on transesterification. Of these, an early study found that sodium acetates had the highest catalytic efficiency (Yoda, 1971).

Esterification catalysts within PET synthesis typically react with the EG monomer, leading to the formation of a metal alcoholate and acetic acid. Acetic acid is removed in the reaction,

which drives the reaction equilibrium right. Equation 2.1 presents the equilibrium reaction for this step of the reaction, where M represents the metal catalyst and R represents an abbreviation of any chemical groups attached to the active site in the reaction.

$$M(CH_3CO_2)_2 + 2ROH \rightleftharpoons M(OR)_2 + 2CH_3COOH$$

Equation 2.1

Catalysts for the polycondensation step are generally antimony(III) oxides or antimony triacetate derivatives in industrial applications. There have been a number of earlier studies confirming the method of catalysis (Rafler, *et al*, 1974; Tomita, 1976a,b; Kamatani, Konagaya, 1978; Kamatani, *et al,* 1980). The catalysts allow for the co-ordination of the metal ion to the ester-carbonyl bond, increasing its polarity and its desirability to nucleophilic attack by the hydroxyl end groups. It is worth noting that the activity of these catalysts improves as the reaction proceeds.

One of the main issues surrounding antimony catalysis, despite their widespread usage, is health concerns related to antimony compounds making their way into the final product. As a result, Acordis introduced a supposedly environmentally-friendly and harmless catalyst named 'C-94' I the mid-1990s. This catalyst is primarily only suitable for PETs that will be used within the textiles industry as it does lower the tenacity of the fibre by 10%. 'C-94' is composed of TiO_2 and SiO_2 in a ratio of 9:1, and has been shown to be 6-8 times as active as antimony-based catalysts (Thier-Grebe, Rabe, 2000). The mechanism of catalysis for the 'C-94' catalyst is still poorly understood, and so is not mentioned here. It is also worth noting that 'C-94' is still not considered to be a widely used catalyst in the synthesis of PETs, but was worth mentioning due to environmental considerations which is a minor theme repeated throughout this work.

Other studies have shown that titanium-based catalysts are the most active metal ion based catalyst, but are also seen to impart yellow colour to the polymer (Shah, *et al*, 1984). Titanium-based catalysts are also prone to hydrolysis forming oxoalkoxides, which have reduced

activity and introduce haziness to the polymer (MacDonald, 2002). This colouration and haziness are undesirable in industrial applications. Optimum concentrations for titanium- and antimony-based catalysts are $1.5x10^{-4}$ and $2.4x10^{-4}$ mol/mol BHET respectively (Shah, *et al*, 1984). A paper by MacDonald also found that germanium oxide could be used for the catalysis, but despite superior activity it has high costs which rule it out from industrial consideration (MacDonald, 2002).

As a result and despite the mentioned health concerns, the two most commonly used catalysts for the synthesis of PET are sodium acetates for the direct esterification stage, and antimony(III) oxides for the polycondensation stage.

2.3 History and syntheses of PCL

Poly(ε-caprolcatone) (PCL) was one of several polymers synthesised by the Carruthers group towards the early stages of the 1930s (Van Natta, *et al*, 1934). It is a hydrophobic and semi-crystalline polymer with a low melting point (59-64°C) and good solubility that became commercially viable due to its biodegradability.

PCLs primary use was as a biopolymer in the biomedical field (Chandra, Rustgi, 1998; Okada, 2002; Nair, Laurencin, 2008; Hutmacher, Woodruff, 2010) typically within drug delivery applications due to a resorbable nature and the ability to have tailorable degradation kinetics and mechanical properties. More recently, PCL has excelled in the tissue-engineering field, which stemmed from the realisation that PCL has some of the best rheological and viscoelastic properties of any biodegradable polymer, making it excellent at synthesising a wide range of scaffolds (Zein, *et al*, 2002; Lee, *et al*, 2003; Huang, *et al*, 2007; Luciani, *et al*, 2008). Further advantages of PCL are its inexpensive synthesis routes, being significantly cheaper to synthesise than other members of its polyester family. This is partially due to its relative ease to solvate.

One thing to consider with the application of PCL to fields other than biomedical is the biodegradability mention earlier. Within the human body PCL can degrade in a period of

months depending on the molecular weight, degree of crystallinity and the degradation conditions. The best case scenario for degradation is a matter of years (Kesel, *et al*, 1997; Gross, Kalra, 2002; Sinha, *et al*, 2004; Sun, *et al*, 2006; Pena, *et al*, 2006; Lam, *et al*, 2007). The rate of degradation within automobiles would have to be assessed and would need to take into consideration heat cycling and whatever environmental exposures the material is subjected to, for example any heat cycling, exposure to UV, oils, solvents, or water. Degradation of PCL occurs in several stages. Firstly, the amorphous phase is degraded resulting in an increase in crystallinity but no change in the molecular weight. Secondly, cleavage of ester bonds occurs, which causes mass loss and a decrease in molecular weight. This cleavage is essentially self-catalysed by the carboxylic acid groups that are lost during the hydrolysis step of the cleavage (Sinha, *et al*, 2004), but it can be further catalysed through the use of enzymes in nature or the body (Lam, *et al*, 2007).

Synthesis of the ε-caprolactone monomer is produced industrially from oxidising cyclohexanone in peracetic acid (Rocca, *et al*, 2003). This synthesis reaction can be seen in Reaction 2.4 and utilises a catalyst composed of antimony trifluoride and silica in a ratio and method currently still protected by patent law.

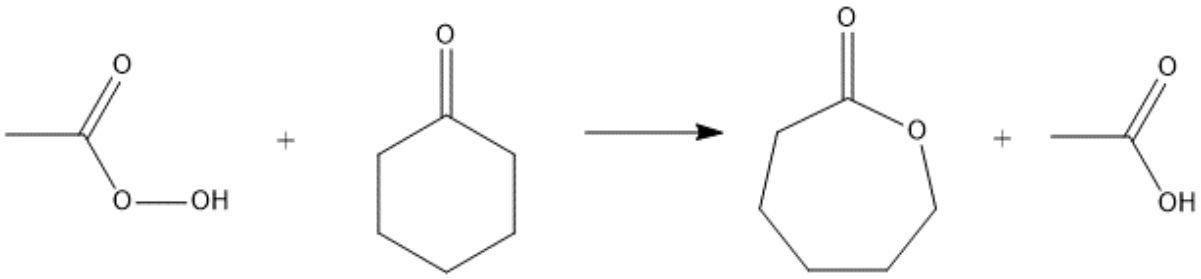

Reaction 2.4

The preferred synthesis of PCL proceeds through a ring-opening polymerisation of the monomer ε-caprolactone. The ring-opening polymerisation is the preferred route as it able to yield PCL with a greater molecular weight and lower polydispersity. There are four main routes through which ring-opening polymerisation can occur: anionic; cationic; monomer activated; and co-ordination inserted. The route which is seen is dependent on what catalyst

is used. A basic representation of the co-ordination inserted pathway can be seen in Reaction 2.5, as this is the most common form of ring opening. An alternative synthesis route is through the polycondensation of 6-hydroxycaproic acid, but this yields polymers with lower molecular weight and a lower polydispersity value (Labet, Thielemans, 2009).

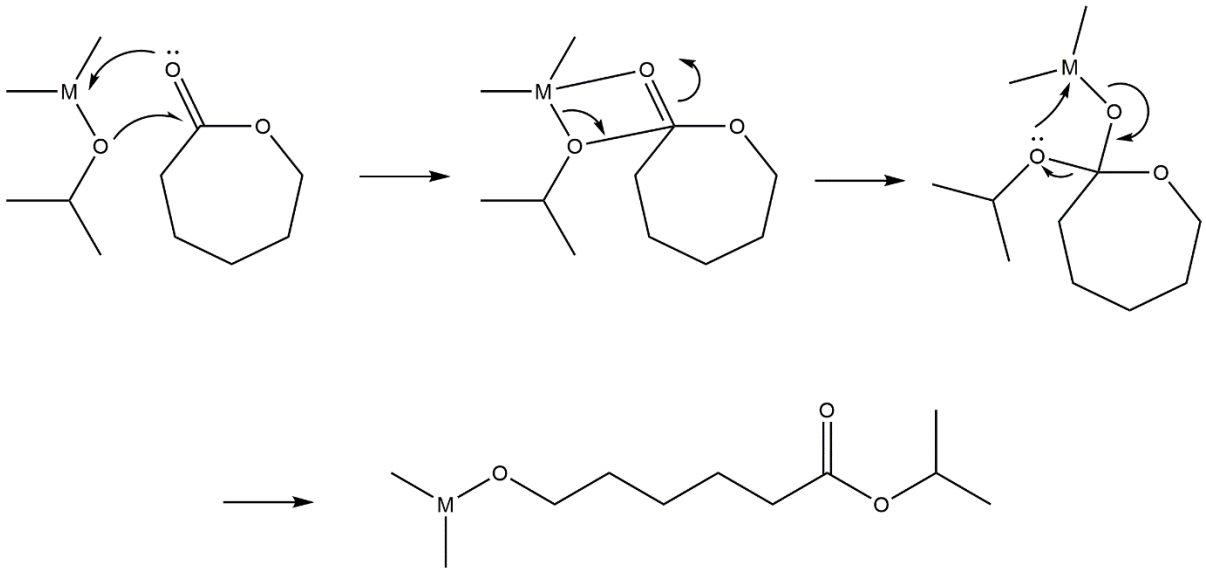

Reaction 2.5

There are three different catalytic systems involved in the synthesis of PCL: metal based, enzymatic, and organic. For the metal-based catalysts the main types are alkali- and alkaline-based catalysts. Of these two, alkaline-based catalysts are typically more attractive. There are further metal-based catalysts in the form of poor-metal, rare-earth metal, and transition-metal options. Alkali-based catalysts are typically ionic compounds, which results in transesterification in the polymerisation leading to poor control over the reaction. Alkaline-based catalysts on the other hand are attractive due to high activity and low toxicity (Platel, *et al*, 2009). The most common alkaline-based catalysts are magnesium and calcium, both of which are extremely abundant and widely used through nature, making them both a cheap and biologically benign catalyst (Browning, 1969). The mechanism for catalysis by alkyl-magnesium compounds is believed to be initiated by alkyl transfer to the ε-caprolactone monomer. Bulkier alkyl-magnesium based catalysts are able to produce greater reaction

speeds, which is attributed to a minimisation in side-reactions caused by the bulkier ligands acting as a steric barrier (Ko, Lin, 2001). In the case of alkyl-calcium catalysts, catalysis routes depend on the type of calcium-based system that is used.

A third alternative system is based on poor metal-based catalysts, including aluminium- or tin-based catalysts. These type of catalysts are widely used, despite their relatively low activity for the ring-opening polymerisation of lactones. Their usage is predominately down to good control over the reaction – especially aluminium-based options (Platel, *et al*, 2009). The most commonly used catalyst for the ring-opening polymerisation of ε-caprolactone is the tin-based stannous(II) ethylhexanoate ($Sn(Oct)_2$); its commonality largely due to its ease to handle, readily soluble, and commercially viable. In order to use $Sn(Oct)_2$ for the ring-opening polymerisation it must be used in conjunction with a nucleophilic compound in order to initiate and control the reaction. The nucleophilic compound used is typically an alcohol such as ethanolamine (ETA) and a general reaction scheme for the catalysis and ring-opening using $Sn(Oct)_2$ and ETA can be seen in Reaction 2.6. Other alcohols which can be used for the reaction include butanol which in a study was found to lead to the greatest increase in the number of active sites, which yields a faster polymerisation rate. There are also transition metal-based catalysts and rare-earth metal catalysts, but due to the relative scarcity of these types of catalyst due to their cost, they will not be mentioned in further detail.

In terms of enzymatic ring-opening polymerisation (eROP) this is relatively new method that typically utilises lipases. The lipases then react with the monomer to form a complex, which then goes on to react with an alcohol. In eROP methods polymerisation, degradation, and the deactivation of the enzyme have been shown to happen simultaneously (Sivalingam, Madras, 2004). The proposed method for these enzymes will not be shown, despite being proposed several years ago there is still some ambiguity as to how the reaction occurs. However, the proposed route is believed to proceed via ring-opening of the ε-caprolactone very early in the polymerisation, followed by linear condensation to form the polymer (Dong, *et al,* 1999). One possible explanation for the lack of industrial uptake of eROP methods could be the large variety of reaction conditions and reagents that have to be monitored and selected.

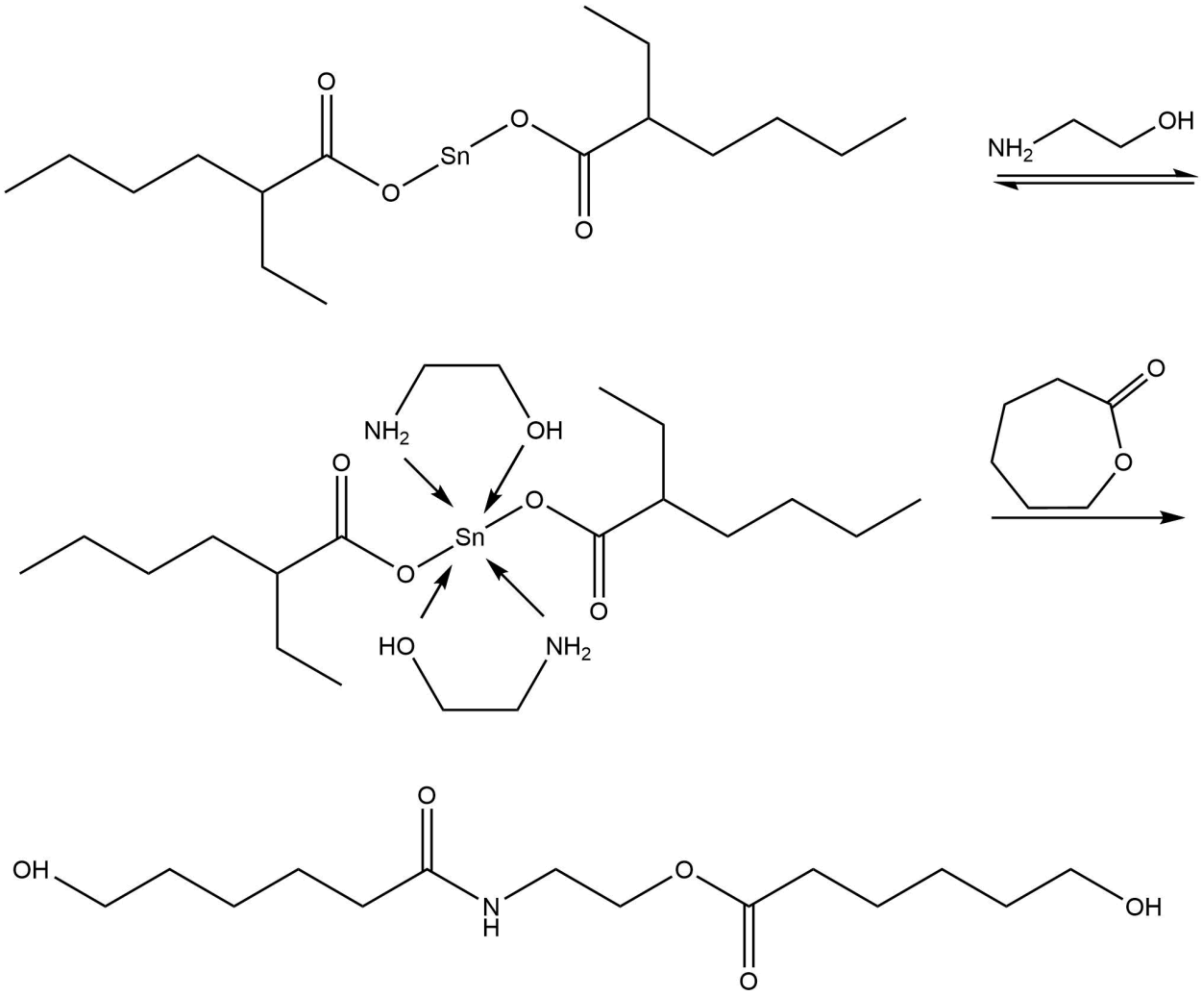

Reaction 2.6

As an example of this, when considering the lipase enzyme, its catalytic activity is dependent on its origin and the type of lipase (Kobayashi, 2000). Furthermore the choice of solvent, particularly with regards to hydrophobicity has also been shown to have a significant impact on the efficiency of polymerisation (Kobayashi, *et al*, 1998). Hydrophilic solvents result in a much lower conversion of monomer to polymer and the resulting polymer also suffers from a lower molecular weight. Additionally, water levels must be managed carefully too as water is proposed to be the initiator of the eROP.

The last type of catalysis used within ring-opening polymerisation of ε-caprolactone is organic compound and inorganic acid catalysts. There is not much work completed on this type of catalysis and it is not particularly prominent in industry, due to the various cost and environmental concerns associated with organic and inorganic acids. Their major advantage, however, is that they are able to catalyse both the alcohol and the monomer which increases the reaction rate.

2.4 History and Synthesis of thermoplastic polyurethane

Thermoplastic polyurethane (TPU) is classed as a linear segmented block copolymer. A copolymer is a polymer made up from two or more different monomer units, and the term block copolymer defines a copolymer that is made up from blocks of each monomer unit – also known as block macromolecules. The term linear segmented here means that the blocks are separated linearly, that is to say the chain is in a straight line with no branching and essentially appears to have an A-B-A-B arrangement (where A and B are different monomer units).

TPU is fully thermoplastic which means that it is both elastic and melt-processable. All TPUs will be composed of 'hard' block and 'soft' block macromolecules, but there are two main compositions for the 'hard' block: aromatic and aliphatic. Aromatic blocks will be composed from isocyanates with a ring of resonance bonds, such as a benzene ring. Aliphatic blocks will also typically be composed from isocyanates but will lack the ring of resonance bonds which make aromatics inherently stable.

With regards to the 'soft' block macromolecule, it is either based on a polyether or a polyester, and the composition will vary depending on the end application. The molecular weight and the ratio of the two block macromolecules can also be varied, leading to a high degree of customisability in the end products characteristics. The molecular weight of a 'hard' block macromolecule will be fairly low (60-400 M_w), relative to the 'soft' block, which will have

a much higher molecular weight (600-4000 M_w) (Ye, *et al*, 2008). The high molecular weight sections provide high flexibility while the lower molecular weight sections affect hardness and the moduli (Coa, *et al*, 2006).

There are a variety of synthesis methods for TPU depending on the type of block macromolecules used. Most commonly, TPUs will be synthesised through solution polymerisation. Solution polymerisation is a synthesis method in which all the reaction reagents (monomer, catalyst, initiator etc) are dissolved in a solvent or solvent system in the reaction vessel. Once started the reaction will proceed and the synthesised polymer will remain contained and solvated in the same reaction vessel. The resulting polymer will have increase the viscosity of the solution, and as such the volume of solvent must be monitored and increased throughout the reaction. The reaction rate can be controlled by altering the amount of catalyst or initiator, which is of key importance towards the end of the reaction. As a result of this the choice of solvent, initiator, and catalyst are of considerable importance. The effect of viscosity will have a noticeable effect on the mechanical properties, especially tensile strength, but will also have a significant impact on additional properties like elongation at break and hardness. As an example, whilst dimethylformamide (DMF) is readily available and relatively cheap as a solvent for TPUs its high boiling point of 135°C makes it difficult to remove fully from the polymer during the drying stages. This has a detrimental effect on the mechanical properties, showing as much as a 400% decrease in tensile strength and a 25% decrease elongation – which will make the material much more brittle (Ye, *et al*, 2008).

There are no chemical reactions shown for TPU as the exact process of monomer synthesis and polymerisation I not known for the TPU materials sourced in this PhD.

Altering the properties and components of the polymers was not a focal point of this work, however, so this was not explored in greater detail and will not be covered further here.

2.5 How are fibrous materials produced?

Fibrous media is generally made through one of two processes: melt-spinning or electrospinning. There are advantages to using either methods, for example melt-spinning is a more cost-effective and faster process, but electrospinning allows for higher specific surface area and smaller fibre sizes, as well as improved mechanical properties. The specific surface area of an electrospun polymer on the nanofibre scale can be as much as 10^3 times greater than that of a conventionally processed polymer on the microscale (Huang, *et al*, 2003). Interestingly, processing via electrospinning may also allow the polymer to retain its electrostatic charges which can then be affected by external fields and polarity – changing the electrical properties of the polymer (Frenot, Chronakis, 2003).

Changes to the polymer structure, for example introducing star confirmations or branching, could result in difficulties when utilising electrospinning methods, and so melt-spinning may be more appropriate for these polymer variations. Due to the author's interest in nanofibrous media, this section will focus primarily on electrospinning which was used throughout this work.

2.5.1 Melt-spun fibre processing

Melt spinning is a cost-effective method, with the potential to attain high production speeds at low cost with very little need for post-processing in terms of washing, solvent extraction, or any other methods. In the melt-spinning process, granulated polymers are melted and extruded through a spin head, generating filaments. Air is then blown over the filaments, cooling them, before a lubricant is applied to allow the filaments to be spun into a fibre. One significant advantage of melt-spinning over other approaches is that it does not require solvation of the polymer granules, and therefore does not have associated issues with solvent suitability, drying time, or waste disposal.

The speed at which the spin head rotates has an impact on the alignment of the filaments within the fibre – which is a key factor in the tensile strength of the fibre. Control of fibre

diameter can be managed by altering the size of the heads, but despite this melt-spinning is unable to obtain fibres as small as those processed via electrospinning, or centrifugal jet spinning.

2.5.2 Electrospun fibre processing

Electrospinning, shortened from 'electrostatic spinning', is a process in which a polymer melt solution - also called a 'dope' - is extruded through an electrically charged needle at a fixed rate. A fixed rate is employed to ensure the size of the dope drop at the end of the needle remains constant. The electric field imparts a charge on the surface of the polymer dope, and as the intensity of the electrical charge is increased it causes the polymer dope drop to form a conical shape (a Taylor cone, Figure 2.1) at the end of the needle's capillary. At a certain intensity, a critical value will be reached at which the repulsive force of the electrostatic charge overcomes the surface tension of the polymer dope and a charged 'jet' of the polymer dope is discharged from the tip of the Taylor cone. The jet then undergoes a 'whipping process', during which the solvent component of the dope evaporates, yielding a charged polymer fibre which then lays itself on a grounded metal screen (Frenot, Chronakis, 2003).

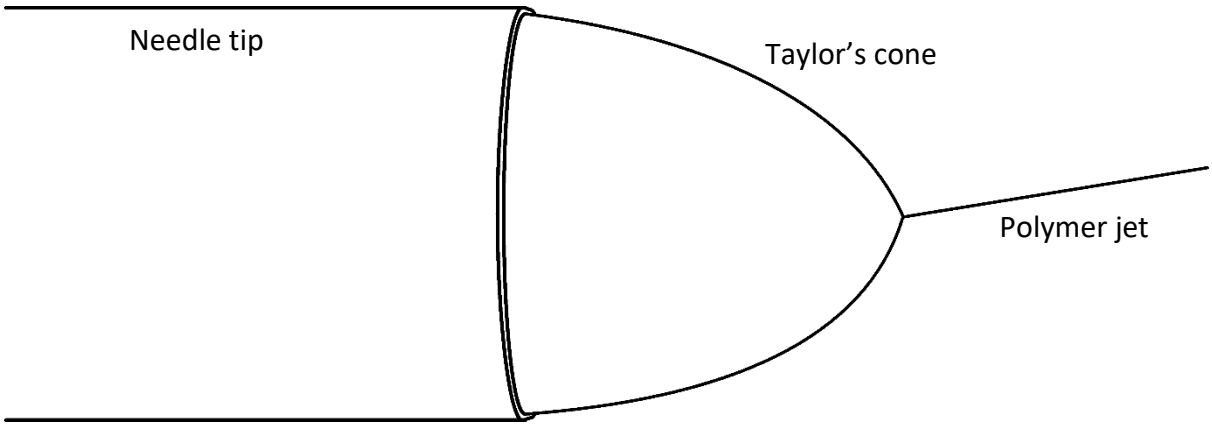

Figure 2.1: Image highlighting the needle tip, with the resulting Taylors cone and the fibre jet whipping from the cone.

The basic components required in order to electrospin are a syringe driver/pump, a high voltage power supply and some form of collector. A simplistic schematic for electrospinning can be seen in Figure 2.2. The syringe driver is used to provide a constant and regular flow of the polymer solution to the needle tip, while the power supply is responsible for the supply of a stable and variable voltage to the needle tip – resulting in the electrostatic repulsion required for spinning. The collector can be static or rotating and is required to provide a surface that attracts the whipping polymer jet, so gathering the fibres.

There are a number of ways in which one can control the resulting fibre within the electrospinning process. These can broadly be split into two terms: processing parameters and chemical parameters. The former relates to the physical setup of the electrospinning rig, such as voltage or collector distance; the latter relates to the dope solution, such as concentration or viscosity. The following paragraphs explore in greater detail a few methods that can be used for the control of electrospinning.

With regards to chemical parameters, two of the most important within this area are the concentration and solvent. The effects of changing these two parameters on spun PET fibres has been well studied (Lopes-da-Silva, *et al*, 2008; Peace, *et al*, 1999). The most common solvents for PET tend to be either chlorinated phenols or strong organic acids. 2,2,2-trifluoroacetic acid (TFA) is one such example, used either on its own or mixed with dichloromethane (DCM). The mixed system is preferable, as it only requires a small amount of acid to solvate PE. This avoids any significant degradation of the polymer chain as a result of esterification occurring between the hydroxyl end groups of PET and TFA (Peace, *et al*, 1999).

In the study by Lopes-da-Silva *et al*, they found that PET pellets were easily dissolved at room temperature within a period of 4 hours in solvent mixtures up to 70% DCM. Above this value 30% (w/v) PET concentrations could not be dissolved. It was also reported that for PET solutions with <10% (w/v) a polymer jet could not be formed during the electrospinning

process. Notably, at lower PET concentrations there was still a high number of droplets being formed in conjunction with a small amount of fibrous media (Lopes-da-Silva, *et al*, 2008).

Increasing amounts of TFA in the solvent mixture was also found to increase the thinning of the polymer jet during the electrospinning process, which results in greater splaying and splitting. Increasing the volume of DCM increases the rate of solvent evaporation and so reduces jet instabilities. Reportedly, electrospinning with solvent mixtures of 40:60 or 30:70 TFA:DCM resulted in narrower but less stable jets – causing multiple breakdowns and decreased yield (Lopes-da-Silva, *et al*, 2008). These variations in the polymer jet yielded differences in material properties that were visible on a macroscopic level. Higher TFA:DCM ratios generated fibres that were softer and lustrous, whilst lower TFA:DCM ratios generated more brittle fibres with rougher surfaces.

Several morphological impacts were also reported. For example, at higher volumes of TFA branching of the fibres was seen to occur, but this appeared alongside an increase in the irregularity of the fibres with increasing amounts of flat and beaded morphologies being seen. This is proposed to be caused by the higher boiling point of TFA, which results in slow evaporation of the solvent from the jet.

More generally, there have been several papers identifying a trend that as the polymer concentration increases so does the average fibre diameter and the number of fibre defects, such as beading, or ribbons, decreases (Deitzel, *et* al, 2001; Zhong, *et al*, 2002; Shenoy, *et al*, 2005; Tan, *et al*, 2005; Gupta, *et al*, 2005). At lower concentrations, the solutions have low viscosities and so the surface tension of the solution is the dominant factor of the morphology of the fibre. A low viscosity and high surface tension system is more likely to yield droplets as opposed to fibres, due to the polymer jet collapsing. Alternatively, at high concentrations polymer solutions are dominated by the surface viscosity, which can yield problems due to the inability to maintain the flow of the polymer solution to the needle tip.

It was also found that at lower viable concentrations (i.e. concentrations at which fibres are dominant) the fibres had an irregular and undulating morphology and variation in diameter

along its length (Deitzel, *et al*, 2001). Increasing the concentration was shown to form more regular and uniform fibres with larger overall diameters. This effect can be seen in Figure 2.3 and 2.4.

Another factor that will impact both the formation and the type of fibre yielded through electrospinning is related to the combination of two solvents. It is not uncommon to mix solvents, either to reduce the volume of toxic solvent used or to change the viscosity or chemical properties of the polymer solution to make it easier to spin. It has also been found that nanoporosity can be introduced on the fibres using a combination of two different solvents, by a mechanism known as spinodal decomposition. Spinodal decomposition refers to the mechanism describing the rapid un-mixing of two or more liquids or solids from one phase into two co-existing phases. In a single solvent system, the polymer jet is only subject to one constant change in solvent composition.

When a second solvent is introduced - especially one with a significantly different evaporation rate - then the composition of the system is subject to heterogenous changes. As the more volatile solvent evaporates faster, the ratio of solvents will be progressively decreasing whilst the concentration of the polymer will be increasing. It is also typically noted that the solvent evaporation occurs from the surface of the jet as opposed to the core of the jet. When this is combined with the diffusion of the polymer being lower than this evaporation rate an alteration in the jet characteristics can be observed both locally and generally, giving rise to variations in morphologies and the introduction of surface features such as pores (Katsogiannis, *et al*, 2015).

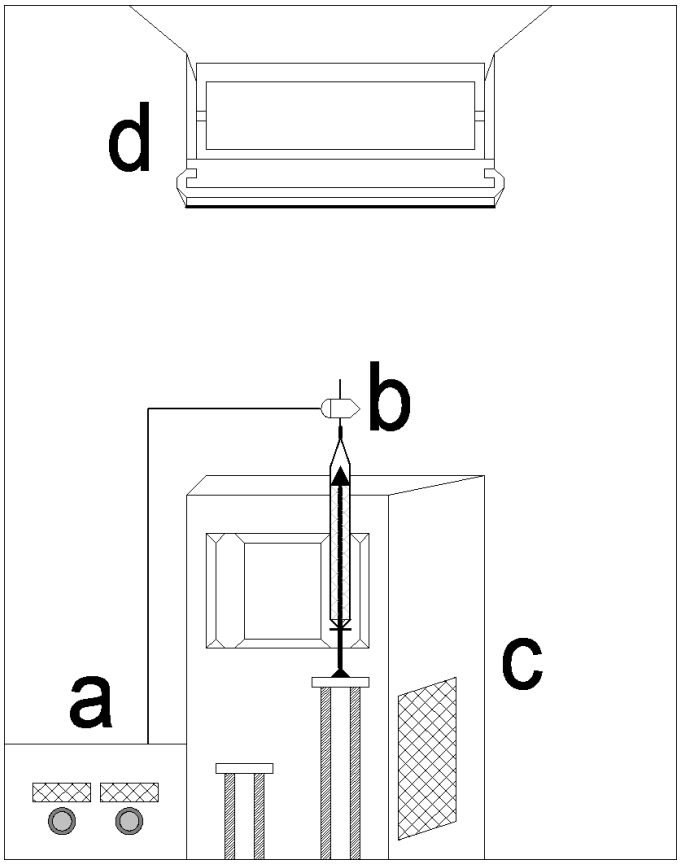

Figure 2.2: Schematic of a typical electrospinning rig set-up used in this PhD. (a) is the high voltage power supply, connected to (b) the syringe and needle tip. (c) is the syringe pump, and (d) is the collector which can either be a static plate or a rotating drum (both pictured).

There have been several publications looking at the introduction of nanoporosity to polymer fibres via this approach. The first example successfully generated highly porous polystyrene (PS) fibres by altering the vapour pressure of a tetrahydrofuran (THF):dimethylformamide (DMF) solvent blend alongside the PS concentration in the

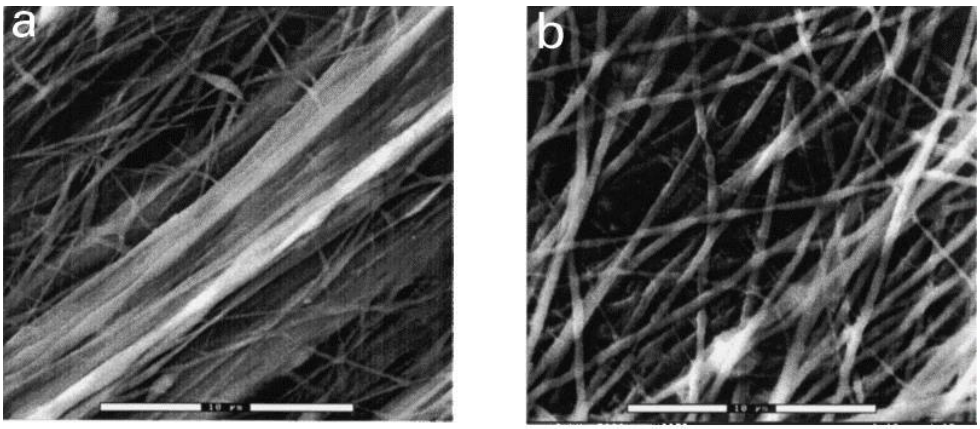

Figure 2.3: Two SEM images of nanofibres spun from (a) 4% wt and (b) 10%wt solutions of PEO in water. Image sourced from Deitzel, et al, 2001.

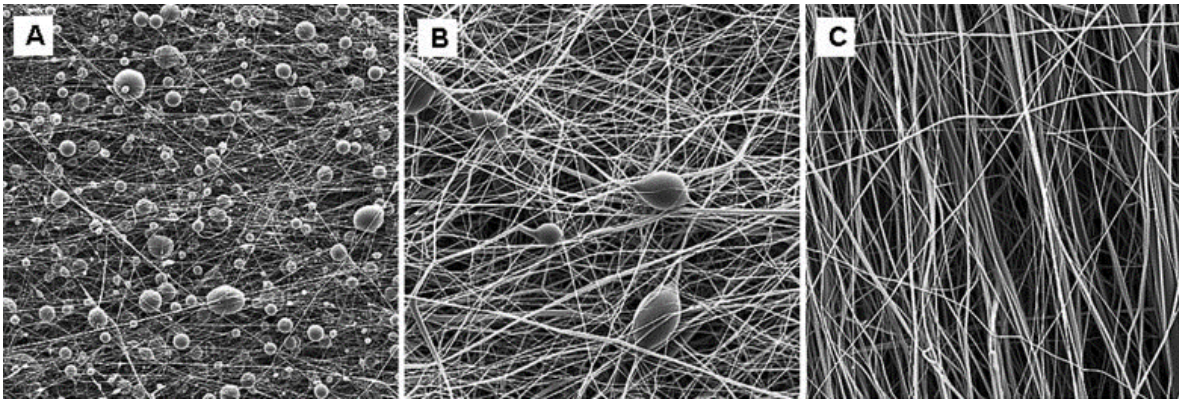

Figure 2.4: SEM images of nanofibres spun from (a) 10%, (b) 20%, (c) 30% PET concentrations. Image sourced from Lopes-da-Silva, et al, 2008. No scale bar was provided within the images. Note that with increasing concentration the presence of beads and ribbons decreases markedly.

polymer solution (Hsieh, *et al*, 2010). The vapour pressure can be altered by varying the ratios of each solvent within the blend. In their paper, it was reported that a polymer solution of 5 %w/w PS in a 1:3 ratio of THF to DMF resulted in the greatest specific surface area and pore volume. The effects of changing the ratio of THF:DMF is shown in Figures 2.5 and 2.6, where the ratio is varied and the exterior and interior of the fibres can be seen. These figures clearly highlight the impact that combining and varying two solvents can have on fibre formation, and so this must be tightly controlled.

Within this example THF has a faster evaporation rate than DMF, so increasing the ratio of DMF results in a decrease in the vapour pressure. As vapour pressure decreases, the solidification rate of the polymer jet is slowed due to a decreased solvent evaporation. It was observed that both pore formation and pore size are heavily dependent on the relative rate of solvent evaporation (and so jet solidification) to spinodal decomposition.. In this case it applies to the PS and THF:DMF mixture, and its separation as one vapourises and the other forms the PS fibre. It is noted that faster solidification rates (through high vapour pressure) can preserve the polymer-rich phase, generating nanopores. Conversely, a decrease in vapour pressure allows for better phase-separation (spinodal decomposition), which generates pore structures on a larger scale and with smooth surfaces. The nanoporosity formed in this way can also go beyond surface pores, it can also be introduced as open porous networks running throughout the fibre. This can be seen in Figure 2.5 and 2.6.

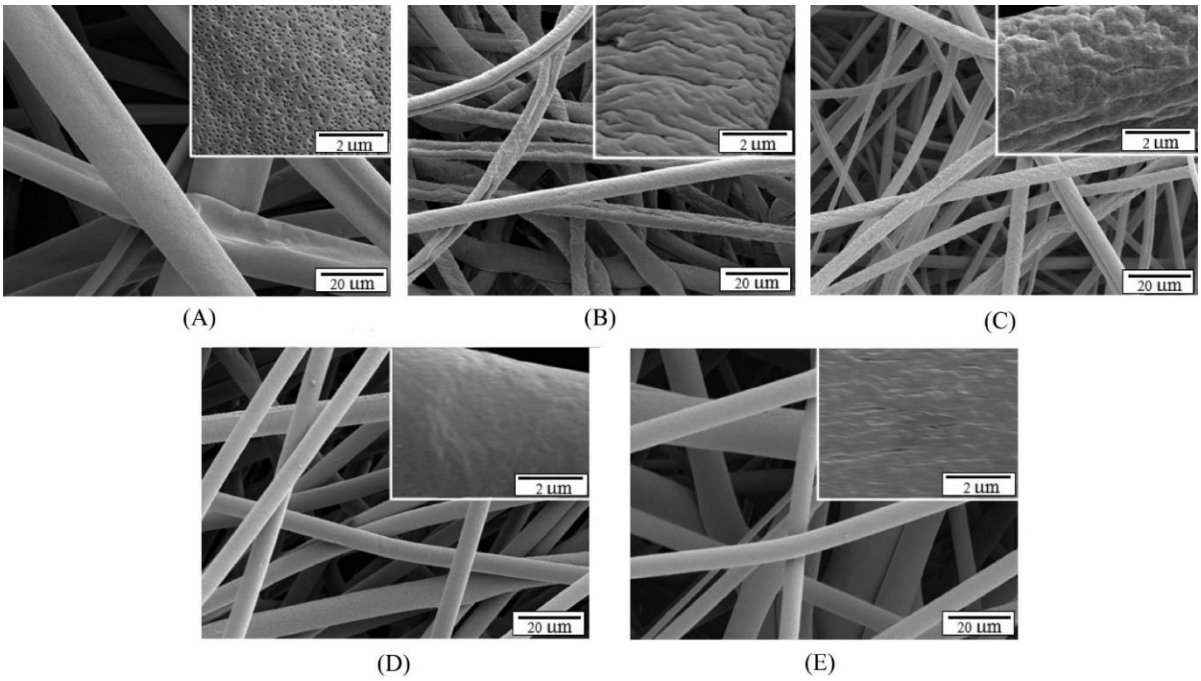

Figure 2.5: SEM images of the exterior of PS fibres spun with varying weight ratios of THF/DMF. (A) = 4/0, (B) = 3/1, (C) = 2/2, (D) = 1/3, (E) = 0/4. Image taken from Hsieh, et al, 2010.

When forming nanopores an important consideration to make when altering the polymer concentrations is that lower polymer concentrations will make it easier for the solvents to evaporate. If the polymer concentration reaches sufficiently low volumes, then it is possible to observe the solvent evaporating faster than the rate at which air and vapour can enter the fibre – leading to the collapse of the fibre structure into a more ribbon like shape. Alongside the ribbon morphology sufficiently low polymer concentrations can also lead to the formation of 'beads-on-string' morphologies, which are likely caused by instability of the fluid jets because of the low polymer concentration combined with solvents featuring high dielectric constants and conductivity. As such is it crucial to manage the concentration of the polymer jet well to avoid unwanted morphologies.

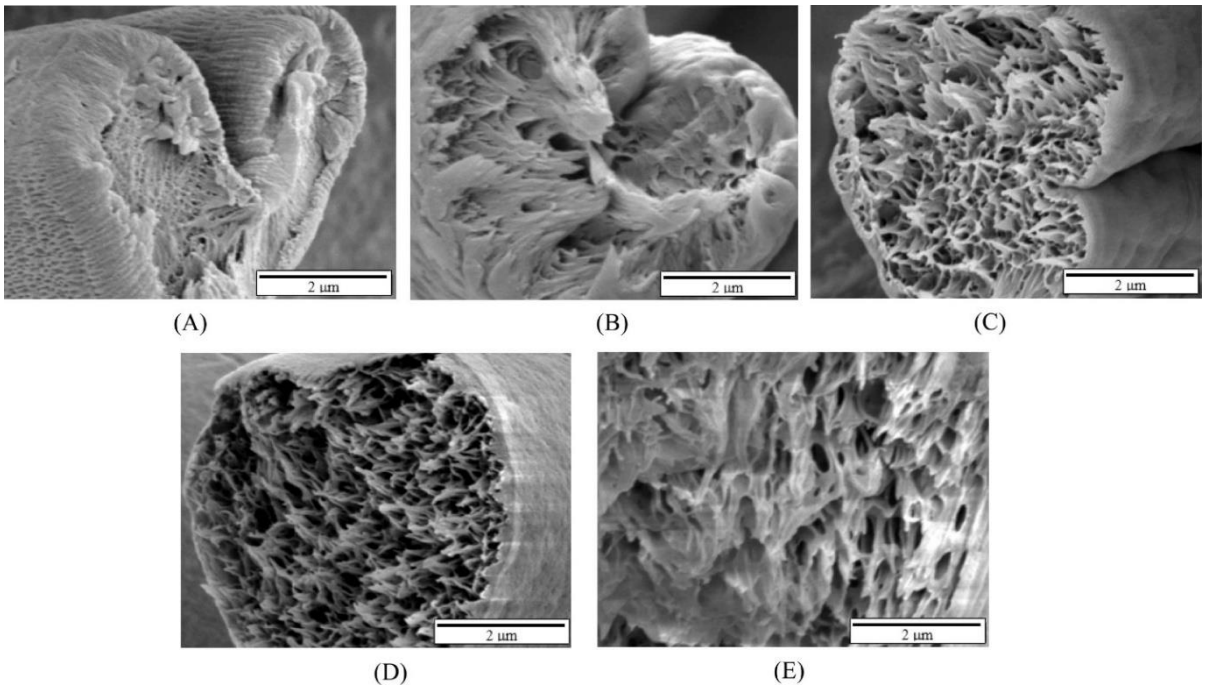

Figure 2.6: SEM images of the cross-section of PS fibres spun with varying weight ratios of THF/DMF. (A) = 4/0, (B) = 3/1, (C) = 2/2, (D) = 1/3, (E) = 0/4. Image taken from Hsieh, et al, 2010.

It should be noted that the nanopores demonstrated by Figure 2.6 would not be considered to be 'open' pores acoustically as they are not accessible to acoustical flow and therefore would not have an impact on the acoustic performance. This figure simply demonstrates the degree of pores sizes and structures available when using spinodal decomposition.

Moving on to the processing parameters and considering firstly the voltage parameter, increasing the current will increase the mass flow rate from which the polymer jet moves from the tip to the grounded collector plate, with some papers linking this increased rate to increase fibre deformation in the form of bead structures (Deitzel, *et al*, 2001). This increase in mass flow rate is largely governed by the decrease in time taken to overcome the surface tension of the dope solution. The change in voltage is also able to change the shape of the Taylor cone and where the jet originates from within it. It was found that at lower

voltages the fibre jet originated from the base of the Taylor cone, which had a shape in agreement with Taylor's theoretical predictions (Taylor, 1964). The nanofibers which were produced at this low voltage were found to have a cylindrical morphology with very few bead defects. By increasing the voltage the total volume of the droplet decreases, and the jet is seen to originate from the liquid surface within the needle. At the highest voltages the jet was observed to originate from the tip with no visible droplet being formed (Deitzel, *et al*, 2001). As this voltage increased the number of defects was seen to increase, though the cylindrical morphology of the fibre was still dominant.

Controlling the flow rate does not have any significant impact on the fibre diameter or the fibre shape. It was found that increasing the flow rate only results in more polymer solution than needed being present, forming an excess at the needle tip. It was noticed from the authors own experimentation that the formation of such an excess had a detrimental impact on both the stability and the yield of the spinning process. As the excess forms the solvent begins to evaporate from it and the excess dries; ultimately leading to a blockage and bringing the spinning to a halt.

Collector distance refers to the distance between the tip of the electrospinning needle and the collector. Generally, this value ranges from 10-20cm as this allows the polymer jet sufficient time to evaporate its solvent and form a stable fibre strand. Of course, the range can be both shorter or longer as needed depending on the choice of solvent – less volatile solvents may need a greater distance to allow them to properly dry. Increasing the collector distance has been shown to result in a decrease in fibre diameter (Mazoochi, *et al*, 2012) as long as the distance stays within the 'optimal range' defined by the strength of the electrostatic field (Ding, *et al*, 2010; Bosworth, *et al*, 2012).

If the collector distance is too short, the solvent will not have enough time to properly evaporate and this could lead to the formation of fused fibres. The same can occur when the collector distance is too large, producing fused fibres and a much larger fibre diameter (Ghelich, *et al*, 2015). This increase in fibre diameter is proposed to be caused by a reduction in the electrostatic field strength. As the electrostatic field strength decreases there is a

corresponding decrease in the stretching of the polymer jet, leading to larger fibres. A decrease in stretching cause an increase in the size of the fibre strand which in turn increases the volume of solvent trapped within the strand. Once the strand has been deposited on the collector the solvent continues to evaporate, causing the fusing with other deposited strands.

2.6 Sources of noise in automobiles

One major source of noise in automobiles is the vehicles drivetrain. The internal combustion engine is the primary source of all noise (Helmer, 2002), due to the combustion process which resonates through the engine components such as the cylinder block, heads, valve cover as well as other major components such as the gearbox housing. It has also been found that the fuel pump and injector systems contribute to engine noise substantially. The addition of forced induction to the drivetrain further increases engine noise but is of a higher frequency; this is generated due to the rotation of the turbine vanes in either turbochargers or superchargers, which rotate at extremely high revolutions per minute (rpm). Exhaust noise, caused by the opening and closing of the exhaust covers during each cycle of the engine, is also a major source of noise in automobiles (Baxa, 1982).

Suspension systems also contribute to noise in an automobile. These systems typically have a frequency lower than 500 Hz and often under the frequency of 250 Hz – this type of noise is normally referred to as 'booming noise' within the passenger cavity (Oh, *et al*, 2002) and is again structural borne. Noise here is caused by compression and rebound of both shocks and dampers, as well as the springs.

Another source of noise in automobiles can be described as road noise and is caused by the interaction of automobiles tyres and the road surface. The tread pattern of the tyre allows air to become trapped in the tyre tread before being squeezed out as the tyre rotates. This occurrence produces a high frequency noise that increases as the speed increase (and so as the frequency of the air being sucked into and thrown out of the tread increases). The

vibration of the tyre sidewall when the automobile is in motion also adds to the noise (Mohanty, Fatima, 2006). Road noise is predominantly airborne and so does not tend to resonate through structures.

When in motion, an automobile is having to 'cut' through the air, which can be forced through any panel gaps present in the automobile, such as door and frame gaps, and any seals, such as windows and the windscreen. This can be referred to as wind noise which is predominately airborne and broad in frequency. It is also proportional to the speed of the vehicle, with noise increasing as the speed of the vehicle increases (Mohanty, Fatima, 2006).

The passenger cavity of any vehicle will have a specific acoustic mode at a given sound pressure (Harrison, 2004), even very small levels of structural borne noise – when applied across large panel areas, such as a roof or dashboard – can cause significant increases in the sound pressure of the interior causing excitation of resonant modes of acoustic vibration (Freymann, 2000). This can induce or enhance more low frequency noise which can be a major cause of discomfort for passengers (Cameron, *et al*, 2010). Low enough frequencies of noise may induce nausea and/or sickness.

Due to the combination of structural and airborne noise, the frequencies encountered in an automobile can vary across a range of a few Hz up to several thousand Hz. It is therefore important to limit the noise within a passenger compartment for the sake of passenger comfort as noise can have numerous negative side-affects, including, most seriously, loss of hearing, but also having negative impacts on psychological moods and increasing stress (Gross, *et al*, 2011).

2.7 Application of fibrous media to acoustic problems

Acoustic noise in automobiles is typically reduced via four potential methods: dampers, isolators, acoustic absorbers and acoustic barriers. Acoustic barriers and absorbers

are typically used to decrease airborne noise problems, whilst dampers and isolators are used to decrease structural-borne noise (Saha, 2002).

An acoustic barrier is a material that prevents the propagation of sound through any medium, for example the bulkhead between the passenger cabin and the engine compartment of an automobile. Barriers are typically non-porous materials with a high density and a comparably large size. Sound waves are prevented from propagating through the barrier due to the bulk resistance of the material, which then prevents the excitation of air on the other side of the material.

An acoustic absorber can be defined as a product that absorbs energy in the incident sound wave and reduces the strength of reflections. By doing so it reduces sound-build up and reverberation within an enclosed area, such as a passenger car. Absorbers are typically porous in nature. Foams and fibrous media are used extensively for this purpose. These materials allow acoustic waves to enter them to be rapidly attenuated as these waves propagate. When a porous material (such as a nonwoven) is exposed to a sound wave, the air molecules within the pores are forced to vibrate. The viscous friction, inertia, and thermal exchange effects in the material pores results in the loss of acoustic energy. There is further energy loss caused by the sound wave scattering on individual fibres of the material, causing further frictional based losses (Zwikker, Kosten, 1949).

A damper is a material that is specifically used to dissipate the vibrational energy present in the vehicle structure. By reducing the vibrational energy, it also reduces sound radiation, generally through a process transferring vibrational energy into heat losses (Rao, 2003). Damping can be attained using visco-elastic material layers, but the methods, location and effectiveness of these materials varies and requires a large amount of experimentation (Subramanian, *et al*, 2004). The performance of a damping material can be affected by factors such as molecular structure, visco-elastic properties and volume. Given that visco-elasticity is subject to temperature, damping materials are also sensitive to temperature changes and their acoustic performance can be altered as such (Saha, 2011).

The most traditional and more common approach to control airborne noise is with acoustic barriers. Acoustic barriers are typically characterised by transmission loss – which is the ratio of the incident sound energy to the transmitted sound energy after it has passed through the material. A greater transmission loss means more sound energy has been prevented from propagating. This type of approach is most useful for areas where noise can be transmitted into the cabin – for example at the bulkhead between the engine and cabin compartments or on large panel areas such as the roof. Transmission loss can be improved by utilising multi-wall construction, combining two or more barriers with a slight gap (either filled with air or a decoupling material). It is worth noting that the transmission loss of a multi-wall acoustic barrier is dependent on several factors: the surface density and stiffness, the size of the gap or of the decoupler material, and the stiffness/construction of the decoupling material (Wentzel, Saha, 1995).

The most common approach to reducing airborne noise in a space with a noise source is through the application of acoustic absorbers. Porous materials are a common class of acoustic absorber and are typically more efficient at controlling higher frequency airborne sound (Sagartzazu, *et al*, 2008). Acoustic absorbers are typically applied to or built into areas such as the headliner, floor lining, carpeting, door cavities, seats and other interior trim components. The acoustic absorber approach is becoming more common within the automotive industry and is an alternative to a relatively heavy sound barriers (Buskirk, Middleton, 1999). This is important as the move towards more lightweight components and automobiles is gradually occurring, driven by efficiency requirements and regulations. Sound barriers tend to follow the mass-density law, whereby increasing transmission loss is most easily obtained through an increase in thickness and mass of the material layer. Sound absorbers on the other hand tend to be light-weight highly porous materials, such as foams or fibrous media, which are orders of magnitude light than sound barrier media.

2.8 Intrinsic material parameters affecting acoustic performance

The acoustic performance of a fibrous material is governed by its intrinsic properties. There are a wide range of material properties, which will have varying degrees of impact upon the acoustics, and it is important to understand how each parameter affects the performance so that research can be focused on the parameters that will have the most significant impact and make the greatest contribution to increased acoustic performance and decreased weight.

2.8.1 Fibre Diameter

Different fibrous media can be made up from a variety of different fibre diameters, or even a range of fibre diameters, described by two standard units: denier or micrometre. Denier is a unit of weight equivalent to the weight in grams of 9000 metres of the fibre. Micrometre simply describes the diameter of the fibre in terms of micrometres. The two terms are interchangeable, and the fibre diameter in microns can be determined from:

$$d_{\mathrm{f}} = 11.89 \times \sqrt{\frac{d}{\rho_f}}$$

Equation 2.2

where d_f is the fibre diameter in micrometres, d is the fibre diameter in denier, and ρ_f is the fibre density in kg/m^3. Denier is a unit of weight describing the weight in grams of 9000m of fibre.

Both Delany and Bazley and Bies and Hansen noticed a positive correlation between the sound absorption coefficient, α, and decreasing fibre diameter (Delany, Bazely, 1970; Bies, Hansen, 1980).

2.8.2 Airflow Resistivity

Airflow resistivity, σ, is arguably one of the most important parameters influencing sound absorption in fibrous media. Higher values of airflow resistivity result in the higher rate of decrease in the amplitude of the sound wave in these media via viscous friction and inertia effects (Conrad, 1983). Ingard reported that in the case of fibrous media the flow resistance per unit thickness of that material is inversely proportional to the square of the fibre diameter (Ingard, 1994). However, a material with higher flow resistivity also makes it more difficult for the incident sound to penetrate it to be rapidly absorbed. The airflow resistivity is typically measured in an experiment whereby a material sample is placed within a tube and a constant airflow is passed through the sample (ISO9053, 1991). Within this experiment, the airflow velocity, ζ, the pressure drop through the sample, Δp, and the sample thickness, h, are measured. The airflow resistivity, σ, can then be defined as:

$$\sigma = \frac{\Delta p}{\zeta \cdot h}$$

Equation 2.3

2.8.3 Porosity

Porosity, ϕ, is defined as the ratio of the volume of air within a material's pores to the total volume of the material (Allard, *et al*, 1989). In the case of acoustics, there is much greater importance given to pores which are inter-connected and 'open' to the incident soundwave than there is to pores which are 'closed' and inaccessible to the soundwave.

For an impeding sound wave to be dissipated via friction, the wave has to be able to enter the pores of the material. This means that there must be sufficiently high open porosity to allow the wave to enter and pass through the material pores. The number of pores per unit volume, their size, and connectivity within a porous material are therefore important considerations when designing a material for acoustic absorption. Open and closed pores will have different effects on the level of absorption in a material. Open pores, meaning those which pass

through the material with no terminus, offer greater thermal and viscous losses to the energy in the passing sound wave. Closed pores, meaning pores which have a terminus and do not pass through the material, will tend to act more like resonators contributing to the material stiffness mainly and only reducing the amplitude of specific frequencies of sound.

2.8.4 Density

The material density is an important factor in dictating the sound absorption properties of fibrous media. It also controls the flow resistivity and material cost. This study highlighted that increasing density correlated to an increase in absorption for medium and high frequencies (Koizumi, *et al*, 2002). An increase in density will inherently increase the number of fibres per a given volume, which will in turn increase the flow resistivity and the number of wave-fibre interactions, so increasing the amount of acoustic absorption via higher frictional losses as the impeding sound wave propagates through the material.

It is important to note that in fibrous nonwoven media, density is dependent on porosity according to the equation:

$$\phi = 1 - \left(\frac{\rho_m}{\rho_f}\right)$$

Equation 2.4

Despite this relation, it is possible to vary density without changing the value of porosity or vice versa. An example of this would be in the case of hollow fibres, which – if classed as open pores – will increase the porosity of the material but not necessarily have an impact on density.

2.8.5 Tortuosity

The tortuosity, α_∞, is defined by Zwikker and Kosten as *"a measure of the elongation of a passage through the pores of the material, relative to the thickness of the sample"*

(Zwikker, Kosten, 1949). The tortuosity can also be described as the influence of the interior structures upon the acoustical properties (Knapen, *et al*, 2003).

The tortuosity predominantly affects the location of the quarter-wavelength peak in the acoustic absorption spectrum of a hard-backed layer of a porous material. This differs from both porosity and airflow resistivity, which tend to control the height and width of this peak (Allard, *et al*, 1989). It can also result in an increase in acoustic performance; increasing tortuosity will slow down the sound wave and increase the number of interactions between the soundwave and the pore structure per unit length.

2.9 Extrinsic Properties Affecting Sound Absorption

In addition to the range of intrinsic properties presented in Section 2.8 of Chapter 2, there are several extrinsic properties of materials which can impact the sound absorption properties.

2.9.1 Compression

Compression is of considerable importance when considering applications of the acoustic treatment. In the case of non-woven materials such as cotton or natural fibres in the automotive industry they will typically be applied in headliners, carpeting, seating and other interior trim pieces, all of which will be subjected to compression as they are used. This compression will result in a change in the physical properties, including density. Unfortunately, the impacts of compression on the acoustical properties of a material have not been very well reviewed.

It has been observed that the absorption properties of a material may decrease when it is compressed (Castagnède, *et al*, 2000; Horoshenkov, *et al*, 2001). During compression, the fibres within the material are brought into closer proximity but are not physically deformed, resulting in a slightly decreased porosity but more significantly increased airflow resistivity and tortuosity. From this, it would be expected that absorption may increase, though this is not always the case. It is proposed that the primary cause for the decrease in the absorption

is the reduction in the materials thickness. The work by Castagnède conducted computational modelling and numerical predictions to estimate the effect of compression and found that this effect can be predicted with an analytical model, e.g. with the Johnson-Allard "equivalent fluid" model (Allard, 1993).

2.9.2 Air Gap

It has been found that the introduction of an air gap behind a porous layer results in an increase in the absorption coefficient, e.g. Ingard, 1994. There is an optimum value for the width of the air gap after which no further increase has a significant impact. The same experiment reported that an air gap has also been found to have more substantial impact on mid- and high frequencies (Ingard, 1994).

2.9.3 Thickness

Generally, increasing the thickness of a material will increase its acoustic performance up to a limit. More specifically, thickness has been shown to impact the low frequencies acoustic performance of a material more significantly than higher frequencies (Ibrahim, Melik, 1978). In the case of automobiles there is a greater source of lower frequency noise - from a combination of drivetrain noise, wind noise and tyre noise (Baxa, 1982; Helmer, 2002; Oh, *et al,* 2002; Mohanty, Fatima, 2006) than there is higher frequency noise, making this parameter rather important for acoustic treatments in automobiles. A separate study found that optimal sound absorption can be attained when the thickness of a material is roughly equivalent to one-tenth of the wavelength of the impeding sound wave (Coates, Kierzkowski, 2002) with the optimal airflow resistivity of $\sigma \approx 2\rho c$ (see page 3-6 in Ingard, 1994). Here ρ is the air density and c is the sound speed in air.

2.10 Modelling Fibrous Media

The first mathematical explanations of the physical nature of sound absorption in porous media occurred in the 19th century and were largely based on recent developments in analytical fluid mechanics. Rayleigh's '*Theory of Sound*' (Rayleigh, 1877) and Kirchoff's '*Vorlesungen uber Mathematische Physik*' (Kirchoff, 1876) were amongst the first and most prolific of such works. Zwikker and Kosten then wrote the first dedicated textbook on the theory and application of sound absorbing materials (Zwikker, Kosten, 1949). These works became the basis for a range of theoretical acoustical models for porous media, several of which will be presented later in this thesis. Most theoretical models based on these earlier texts assume that rigid frame porous media can be modelled as a stack of capillary tubes, in which the fluid trapped in them is a homogenous fluid with a frequency dependent complex characteristic impedance, z_b, and a complex wavenumber, k_b – which is relative to the speed of sound, c, in the porous space and the rate of its attenuation. The ability of sound waves to enter the porous space in the stack of capillary tubes is determined by the value of characteristic impedance and boundary conditions.

Modelling the frequency dependent behaviour of the characteristic impedance can be approached in two ways: (i) theoretical and (ii) empirical. Theoretical models treat the viscous and thermal effects in the capillaries separately by introducing complex expressions for the dynamic density, $\tilde{\rho}_b(\omega)$, and compressibility, $\tilde{C}_b(\omega)$ of the fluid. ω is the angular frequency, equal to $2\pi f$ where f is the frequency in Hertz [Hz]. The influence of these characteristics on sound speed, attenuation and impedance have been known for a long time and are described in the three early works (Kirchoff, 1866; Rayleigh, 1867; Zwikker, Kosten, 1949) and numerous analytical forms have been developed to predict their frequency dependent behaviour (Zwikker, Kosten, 1949; Biot, 1956; Attenborough, 1985; Johnson, *et al*, 1987).

In reality, any realistic porous material is significantly more complex than a simple stack of parallel capillary tubes. To account for this, semi-empirical factors were considered alongside measured macro-structural data. This ultimately led to a physically-founded model being

suggested (Allard, 1993) which proved to be excellent, but required the knowledge of viscous and thermal characteristic lengths – two parameters which are difficult and time-consuming to measure. From this, several simple empirical models were developed which made use of a phenomenological approach to solving the viscous and thermal characteristic lengths (e.g. Delany, Bazley, 1970; Miki, 1990; Allard, 1992; Voronina, Horoshenkov, 2003; Garai, Pompoli, 2005). In addition to these comparatively simple models, there are also a range of increasingly complex empirical models based around both macro- and micro-structural material parameters (e.g. Biot, 1956; Allard, 1993; Horoshenkov, *et al*, 1998) which are able to accurately describe the acoustical processes in porous media, provided those parameters have been well characterised.

Both the history and development of simple through to complex theoretical and empirical models are already well covered in literature (e.g. Attenborough, 1982; Horoshenkov, 2006; Egab, *et al,* 2014; Horoshenkov, 2017), and so will not be covered in further detail within this thesis.

2.11 Conclusion

There are a wide variety of polymers that can be processed into fibres for use as nonwoven media. The type of polymer used is typically dictated by two factors, cost and desired properties in the finished product. PET for example is a cheap option with good processability and the ability to be processed from recycled media, whilst PCL has good biodegradability, so can be used in applications which have short product-lifetimes before disposal. In addition to the variety of polymers that can be used there is also a variety of different processing methods that can be used to obtain the fibre. The most commonly used methods are melt-spinning to obtain fibres on the microscale, and electrospinning to obtain nanoscale fibres for specialist applications. The industrial sponsor of the PhD was able to provide PET and recycled microscale fibres for the investigations into nonwoven fibrous media, whilst the work done looking into more specialist applications such as the membranes

was done via electrospinning here at the University of Sheffield. Electrospinning itself is a highly controllable and customisable process, which can be used to dictate not only the material properties (such as fibre diameter, fibre density, and thickness) but also additional properties like fibre morphology – which can be useful in certain specialist applications like filtering. This chapter has covered in detail the methods and approaches that can be used during electrospinning to tailor the resulting fibrous product to a certain design. In the case of this PhD the main focus was to reduce fibre size and increase fibre density, with the aim of increasing airflow resistivity and hence the thermal and viscous losses within the material. It was also found that it is possible to change the morphology of the fibre, by introducing nano-porosity to the surface of the fibre, and this is of significant interest for acoustical applications.

We have also covered the typical sources of noise in an automobile, and differentiated between the two types, airborne and structural. The work in this PhD focused on reducing the airborne noise, such as that generated by the engine and drivetrain, wind resistance, and the deformation of tyres and the air trapped within their treads. Overall, these sources produce noise across a wide frequency range, typically from 250 Hz up to 5000 Hz. As such, any noise solution has to be effective across such a frequency range, as opposed to being effective at a single frequency. It was also found that the most common solution to airborne noise in automobiles is currently through acoustic absorbers, which are typically lightweight, porous, fibrous media. This then dictated the direction this PhD took, looking at ways to improve the performance of such media without significantly increasing their thickness or weight, both of which are at a premium in the automotive industry.

This chapter has also presented the key material parameters which affect the acoustic performance of a material, which gave a better understanding on how to first approach the task of improving the performance of nonwoven materials currently used as acoustic absorbers in industry, and how to potentially go about designing a ‘novel’ product for acoustic insulation in automobiles. Those parameters are the fibre diameter, the airflow resistivity, and the density – all of which increase the acoustic performance by enhancing the thermal and viscous interactions and increasing the attenuation within the material pores. In addition to these parameters which have the largest effect on the acoustic performance, there are

some further parameters that must be considered given the application of these material. In an automotive environment, it is quite plausible that any acoustic materials will be compressed either during installation or use, and so understanding how that can impact the acoustic is important. Knowing that the acoustic performance will be affected reinforces the need to develop materials with an even greater acoustic performance when uncompressed, to counter the effects of compression in the end application.

Chapter 3: Materials synthesis and characterisation overview

This chapter covers the synthesis of the materials that were investigated throughout the course of this work. Initially this study was focused on nonwoven fibrous media typically used within the automotive industry as acoustic absorbers. The relationship between the various material properties, such as fibre diameter, layer thickness and material density, and the resultant acoustic performance were studied. Subsequently, it was discovered that the addition of a thin, high resistive layer to the surface of a traditional nonwoven material results in a substantial increase in the acoustic absorption coefficient. As a result, this study was extended into the synthesis of nanofibrous membranes and their noise control applications. Electrospinning was chosen as the fibre processing technique as a result of its high degree of experimental control.

The acoustical properties of these materials were carefully characterised. This chapter also covers the range of material characterisation methods which were used to understand what controls the acoustic performance of both traditional and nanofibrous nonwoven materials.

3.1 Nonwoven fibrous materials

John Cotton Group Ltd supplied a wide range of nonwoven samples with varying material properties. These materials are either being developed for automotive applications or are already used in the automotive industry to control airborne noise in the cabin. They are and are applied to areas beneath the carpets, in the boot and behind the dashboard. The acoustical properties of these materials were measured and correlated with intrinsic material properties such as fibre diameter and density. This allowed for the optimisation of samples to fit a certain automotive application. Modelling was used to understand better the observed acoustical behaviour. Figure 3.1 shows some photographs of these materials to give an understanding of the type of materials typically used for this purpose.

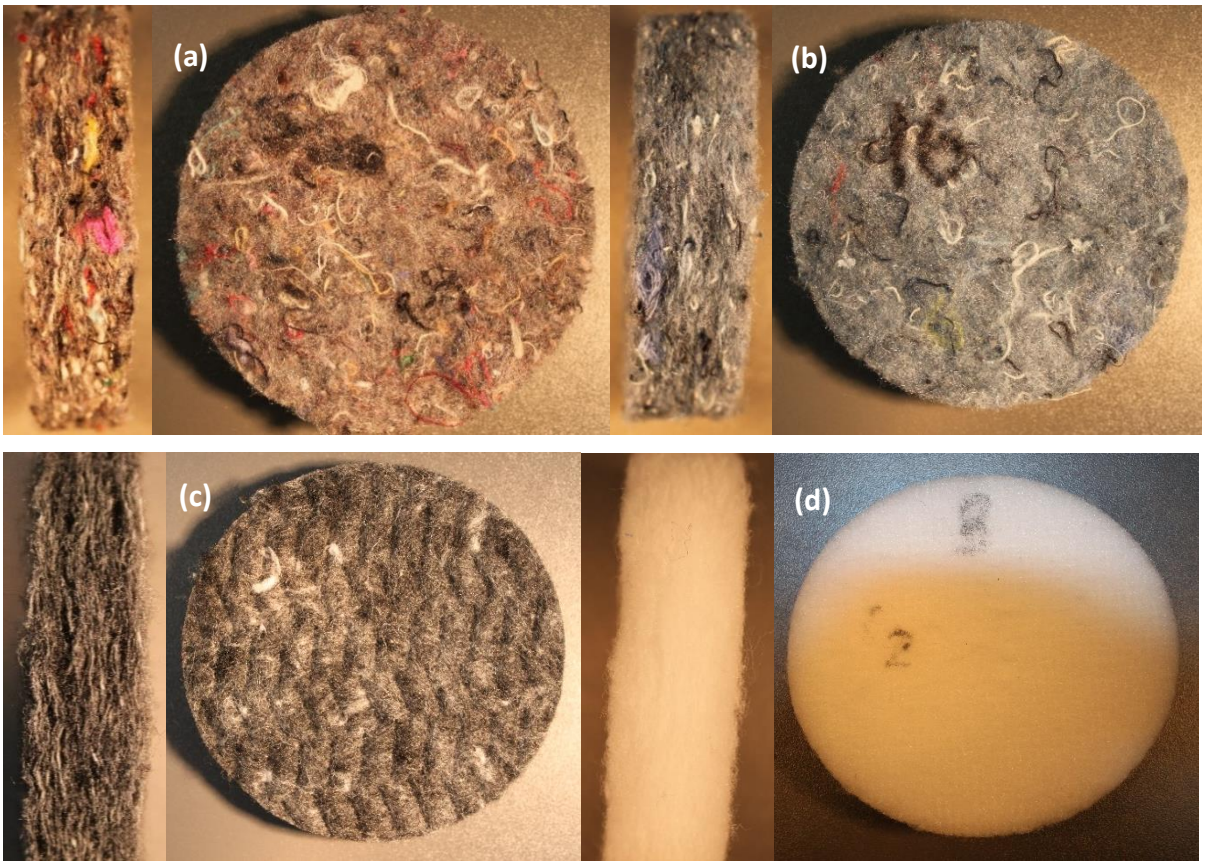

Figure 3.1: Photographs of current solutions for the reduction of airborne noise in the automotive industry, (a) is a high density fibrous nonwoven made from recycled textiles, (b) is a medium density fibrous nonwoven made from recycled denims, Both (a) and (b) are designed to be used behind interior plastics such as the dashboard and centre console (c) is a high density nonwoven product, applied in areas such as the boot, (d) is a lightweight nonwoven designed to be applied beneath carpets.

3.1.1 Improving nonwovens

A range of traditional nonwoven materials made of polymeric fibres with fibre diameters much greater than 1 µm were supplied by John Cotton Group Ltd. They had a wide variety of material properties such as fibre diameter, thickness, density, and porosity. The properties of these materials can be seen in Table 3.1. The fibre diameter for 'Rebound Felt' and 'RPC Denim' is absent as a reliable estimate of the diameter could not be obtained from

the recycled materials. It can be seen that some materials have identical porosities and fibre densities but different values of bulk density. This is somewhat unexpected as porosity and density are typically dependent upon each other, but in this case it is potentially caused by a number of factors such as compression or the type of fibres (e.g. hollow fibres) present in the material. For example, some materials in this table will have been heat pressed, increasing the measured value of density but decreasing the thickness.

Material sample	Fibre diameter d_f [μm]	Thickness h [mm]	Bulk density ρ_m [kg/m^3]	Fibre density ρ_f [kg/m^3]	Porosity ϕ [-]
Autobloc	23.65	15.07	49.00	1381	0.96
Memory Fibre 8	18.83	21.43	17.57	1379	0.99
Rebound Felt	N/A	21.21	121.50	1378	0.91
RPC Denim	N/A	20.96	43.82	1383	0.97
PE Sample 3	24.71	22.87	27.94	1383	0.98
PE Sample 8	14.36	21.15	21.71	1379	0.98
PE Sample 10	14.36	21.18	24.68	1379	0.98
WT3950b	23.74	26.81	38.47	1383	0.97

Table 3.1 Material properties of a range of nonwoven materials supplied by John Cotton Group Ltd.

Subsequently, John Cotton Group Ltd processed and manufactured four additional materials to our specification that were used to study the hypothesis that decreasing the fibre diameter can have significant gains on the acoustics, and that altering the blend of current solutions according to this hypothesis can have further benefits. These samples were referred to as

"NW Blend". Table 3.2 shows the material composition in terms of fibres for each of the four blends, whilst Table 3.3 shows the corresponding material properties.

	Sample composition
NW Blend 1	55% 24.79 μm fibre, 20% 20.24 μm fibre, 25% binder fibre
NW Blend 2	55% 24.79 μm fibre, 20% 12.40 μm fibre, 25% binder fibre
NW Blend 3	55% 20.24 μm fibre, 20% 24.79 μm fibre, 25% binder fibre
NW Blend 4	55% 12.40 μm fibre, 20% 24.79 μm fibre, 25% binder fibre

Table 3.2 The sample composition of the blends made up by John Cotton Group Ltd to test hypothesis of smaller fibres improving acoustics in current solutions. These particular blend ratios relate to the composition of some successful acoustic material solutions currently sold in the automotive industry.

Sample	h [mm]	ρ_m [kg/m^3]	d_f [kg/m^3]	ϕ [-]
NW Blend 1	16	11.789	1380	0.99
NW Blend 2	19	7.992	1380	0.99
NW Blend 3	18	14.846	1380	0.99
NW Blend 4	22	8.574	1380	0.99

Table 3.3 Material properties of the blends made up by John Cotton Group Ltd.

In addition to the above solutions, an investigation into the impact of fibre angle and processing method on airflow resistivity was conducted in collaboration with the University of Liberec, Czech Republic. Three samples (WM, ST T1, and ST T2) were produced by different

processing methods. Specimens with the 'WM' prefix were made using rotating perpendicular processing. The 'ST T1' prefixes and 'ST T2' prefixes refer to specimens produced by vibrating perpendicular technology. Each of the three samples was then treated using heat-pressing in order to yield a range of specimens with varying thickness and densities. The material properties of these specimens are presented in Table 3.4. Each specimen had the same fibre content - 30% hollow PET, 45% monofilament PET, and 25% iii-bicomponent PET.

The quoted porosity values do not take into account the voids in the hollow fibres, as they are classed as closed pores and are inaccessible to airflow so have little to no effect on airflow resistivity or sound absorption. The quoted values of airflow resistivity in Table 3.4 are taken as the average value plus or minus the standard deviation, which were taken from the results for ten tests per specimen.

The third area of work for improving the performance of nonwovens was the addition of a skin. 'Skin' is the term used to describe a thin, resistive layer that is placed on top of another material, typically referred to throughout this work as the 'substrate'. Generally, this layer is also made up of nonwoven fibrous media of a high flow resistance, and can then be further processed, through perforation for example.

In the case of the nonwoven fibrous materials utilised in the early stages of this work, most experimentation was based on materials with lightweight perforated skins composed of polyesters, which were lightly bonded to the underlying nonwoven substrate with adhesive. The skins were provided by John Cotton Group Ltd, and had a fibre density of 1380 kg/m^3, and a thickness of around 300 μm.

Specimen	Porosity ϕ [-]	Bulk density ρ_m [kg/m^3]	Thickness h [mm]	Airflow resistivity σ [Pa·s/m^2]
WM	0.976	21.07	24.09	5757 ± 589
WM	0.972	24.45	20.76	7319 ± 243
WM	0.970	36.71	19.00	8630 ± 408
WM	0.969	27.54	18.43	10329 ± 376
WM	0.959	35.56	14.27	14990 ± 285
WM	0.959	35.87	14.15	15410 ± 167
WM	0948	45.56	11.14	22230 ± 433
ST T1	0.981	16.87	28.36	4011 ± 316
ST T1	0.973	23.54	20.32	7498 ± 332
ST T1	0.972	24.54	19.49	7412 ± 328
ST T1	0.965	30.94	15.46	13400 ± 277
ST T1	0.958	36.88	12.97	16750 ± 442
ST T2	0.981	16.93	27.48	4108 ± 199
ST T2	0.978	19.49	23.87	5337 ± 217
ST T2	0.974	22.48	20.69	7029 ± 356
ST T2	0.969	27.61	16.85	10180 ± 259
ST T2	0.960	34.95	13.31	13370 ± 199
ST T2	0.949	44.60	10.43	20470 ± 687

Table 3.4: Material properties of the specimens used in the experiments assessing the accuracy of flow resistivity prediction in bi-component fibrous materials.

3.2 Nanofibrous materials

The development of nanofibrous materials in this PhD was inspired by the effects of the skin on the acoustic absorption by nonwovens. There was an interest in understanding the reasons for this phenomenon through modelling and experimentation. It was also of interest to understand the effect of the diameter of nanofibres on the airflow resistivity of the skin and effect on the overall absorption of the porous layer system. One of the easiest ways of doing this was to decrease the pore size of the skin by reducing the fibre diameter below 1 μm and increasing the fibre density. This section of the chapter will cover the synthesis of the range of membranes used in this part of the work.

3.2.1 Electrospun fibres

There currently exists a wide range of methods within electrospinning that can be utilised for the synthesis of nanofibrous or nanoporous membranes. The basis for all of these methods is the generation of a polymer solution, consisting of the chosen polymer dissolved in the chosen solvent system, and the physical spinning of it according to chosen parameters. Section 2.5.2 in Chapter 2 reviewed in detail the existing methods of fibre electrospinning. This section will outline the specific methods that were used in this PhD which were predominately chosen for their relative ease of synthesis and stability.

All initial work on electrospinning took place at the School of Clinical Dentistry, University of Sheffield. This work was completed using an in-house manufactured electrospinning rig consisting of a needle flow pump, a high voltage power supply and a collector. These are the key components required for an electrospinning rig, but they can be expanded according to the desired fibre properties. For example, the addition of a focusing ring, connected to a secondary power supply and a rotating collector plate can be very beneficial in producing aligned fibres. A schematic of the electrospinning set-up used for the completed work can be seen in Figure 2.2 in Chapter 2.

Further electrospinning work took place within the department of Chemistry at the University of Sheffield. Experiments were again conducted on an in-house built rig, comprising of the same components as that at the School of Clinical Dentistry, but with a variety of needle options varying from single needle set-ups to multiple needle set-ups. Multiple needles allow for more solution to be spun in a given timeframe, increasing the speed of the experiment as well as having the potential to change the density of the resulting fibres.

In addition to this, some membrane samples were produced in collaboration with the University of Surrey and were synthesised at the Advanced Technology Institute within the Nano-Electronics Centre.

3.2.2 Solution preparation

The preparation of the polymer solution is a key step in the electrospinning process as it will determine many of the chemical parameters which will impact the resulting acoustical properties of the nanofibrous membranes. Ensuring that the concentration of the solution and so its viscosity and electrical properties are accurate is crucial. During this work the polymer solutions were prepared according to the following two methods. Both methods were equally effective in terms of the resulting polymer solutions but had varying levels of simplicity and some advantages during preparation.

The first method, (a), used to prepare the solutions was to weigh out all materials into the same glass vial. Typically, the first step involved weighing and zeroing the mass of the glass vial that the polymer solution would be stored in, followed by weighing out the correct mass of polymer granules, before re-zeroing the scales. The second step involved weighing out the mass required for each solvent, transferring them from solvent flask to the glass vial through the use of disposable glass pipettes. The final step of the process would be the addition of a magnetic stirrer flea to the glass vial and placing it on a magnetic stirrer plate to dissolve.

The second method, (b), required the use of two glass vials, one for the weighing of the polymer granules and one for the weighing of the solvent system. The order of the steps

remained the same, with the polymer granules being weighed out first and into a zeroed glass vial. At this point, however, the glass vial was removed from the balance and put to one side. A second vial was then placed on the balance and zeroed, and the solvent(s) were weighed out into this vial. The magnetic stirrer 'flea' is then added to the second glass vial, and lastly the contents of the vial containing the polymer granules is added. This vial was then placed on the magnetic stirrer plate and left to dissolve.

With regards to the choice of polymers, PET was the initial polymer of choice for this work due to its low cost, recyclability and stability - all meeting the many requirements necessary of a material suitable for industrial use. Despite these advantages, PET has several downsides when considering its application as fibrous acoustic media; the largest of which is related to its processability. Namely, that it is difficult to dissolve in most solvents. Trifluoroacetic acid (TFA) is one of the few solvents that are capable of dissolving PET (Mahalingam, *et al*, 2015), but it has its own drawbacks in that it is highly corrosive and acutely toxic to both humans and any wildlife that may come into contact with it via waste streams. A combination of two solvents can be used in order to try and reduce the volume of TFA required for the dissolution, but TFA cannot be removed entirely. Typically, TFA is combined with dichloromethane (DCM), a milder and significantly less toxic solvent. The combination of two different solvents is not without its problems, however, as the two different solvents will have two different evaporation rates. The evaporation rate describes the time taken for a solvent to change from a liquid phase into a gaseous phase. This introduces a new factor which must be considered and accounted for, along with spinodal decomposition (discussed in Section 2.5.2 in Chapter 2). This means that there is a great expense associated with the use of PET, aggregated from the initial cost of the two solvents and the high costs of safe disposal. This high cost of processing the material counter-acts the relative affordability of the polymer feedstock, making PET an expensive material to use overall.

PET was purchased from Sigma-Aldrich in granular form, with 30% glass particles as a stabiliser. During scanning electron microscopy (SEM) analysis, the glass stabilisers were not observed to visibly impact the formation of fibres in electrospinning and exist only to stabilise

the polymer in its granular form. The glass stabilisers are not chemically bound to the polymer (Hahladakis, *et al*, 2018). The PET granules were dissolved into trifluoroacetic acid (TFA), 99% reagent grade, sourced from Alfa Aesar. The solvent was not further purified before use and no other materials were used throughout the syntheses. Dissolution occurred over 4 hours, using a magnetic stirrer bar and plate. A 1 mL solution was then extracted and spun onto a static collector plate covered in aluminium foil. After spinning, the membranes were left to evaporate for 8 hours before being placed in a desiccator for a further 24 hours, prior to characterisation. All electrospinning for the initial PET experiments were performed at 19°C ±1°C, and a humidity of 37% ±2%, using a needle with 0.81mm internal diameter (ID).

3.2.3 Poly(ethylene terephthalate) membrane generation

The first work done with PET was the generation of five solutions with varying concentrations, tabulated in Table 3.4 where the headings describe the main electrospinning parameters that were altered within this first experiment. The concentration refers to the mass concentration of PET, 'PET mass' and 'TFA mass' are the masses of TFA used to achieve this concentration, whilst 'Collector distance', 'Voltage' and 'Flow rate' describe the values assigned to each of these parameters in the set-up of the electrospinning rig. These parameters and their impacts are explained in Section 2.5.2 in Chapter 2.

This work aimed to determine the range of concentrations at which it was possible to spin PET in the solvent trifuoroacetic acid (TFA). The approximate upper and lower boundaries for the concentration of PET were taken from a range of literature sources which had electrospun PET. Electrospinning parameters were based roughly as an average of parameters encountered in those same sources (Lopes-da-Silva, Veleirinho, 2009; Strain, *et al,* 2015; Wang, *et al*, 2015; Zander, *et al*, 2016). The humidity was relatively low at 37 ± 2 %RH at a temperature of 19 ± 1 °C.

Concentration [% w/w]	PET mass [g]	TFA mass [g]	Collector distance [cm]	Voltage [kV]	Flow rate [mL/h]
22.5	1.125	3.875	16	18	2.0
25.0	1.250	3.750	16	18	2.0
27.5	1.375	3.625	16	18	2.0
30.0	1.50	3.500	16	18	2.0
32.5	1.625	3.375	16	18	2.0

Table 3.5: Concentrations and electrospinning parameters used in the first experiments with PET.

Whilst all five samples dissolved in TFA, the 32.5% w/w PET sample had a viscosity too high to be electrospun, suggesting that 30.0% was the highest concentration that could be used in further experiments. 22.5% was fully solvated and easily spun, which led to the use of a lower 20.0% concentration being used as the lower limit in further experiments. As can be seen from Table 3.5, 5g of each sample was prepared and electrospun using the conditions given. The main problem encountered with all solutions over 25.0% was that the low humidity in the lab lead to the needle becoming blocked frequently. The higher concentration means a lower volume of solvent and as such the solution dries quicker at the needle tip. In the case of the 30% sample this led to some sputtering during the electrospinning, in which a stable jet was not formed so the solution was 'spat' out by the repulsion.

Figure 3.2 shows an SEM image of the typical fibre diameter, density, and membrane structure obtained using PET in electrospinning. Please refer to Section 3.3 in Chapter 3 for more information on how this image was taken and how data such as fibre diameter, density, and membrane structure was obtained. It is apparent that these samples are relatively thick with a relatively low fibre density, as there is a very visible depth-of-field affect. Fibre size is

also quite varied, with most fibres being around 1 µm but some smaller 500 nm fibres are also visible, along with a stack of three fibres around 3-4 µm.

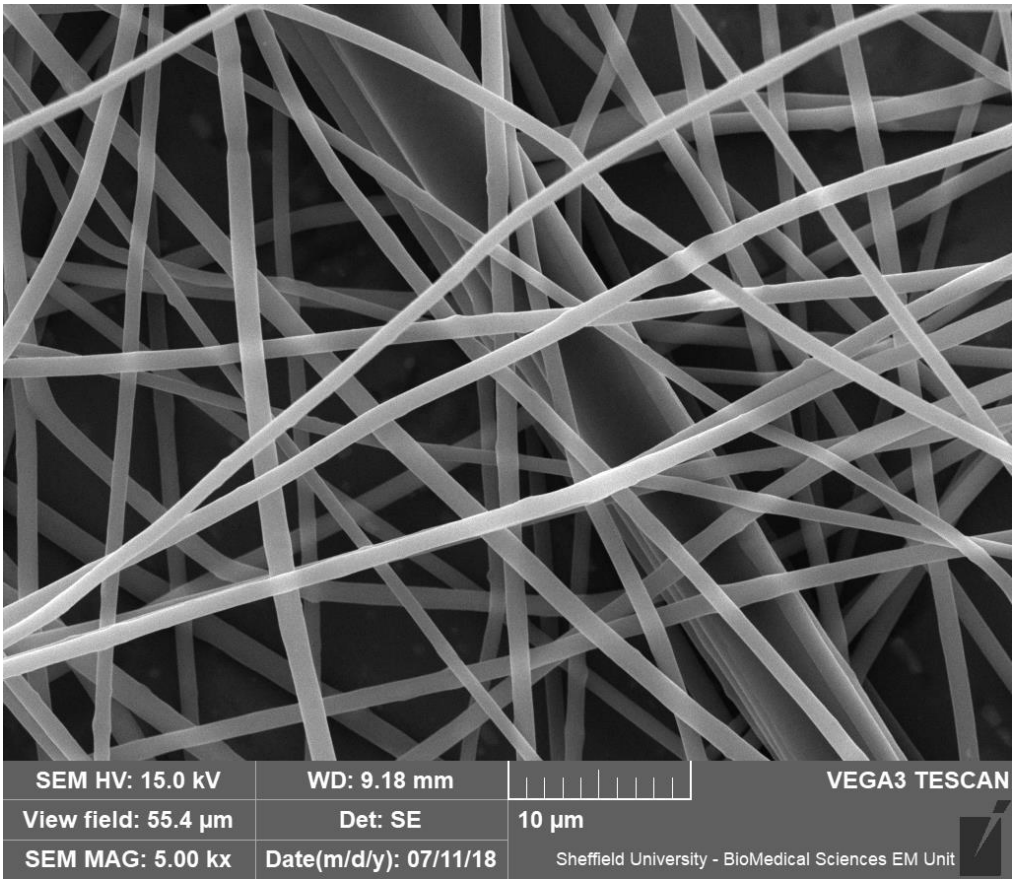

Figure 3.2: An SEM image showing the typical fibre density, diameter and membrane structure obtained by electrospinning PET fibres.

Following the initial experimentation, a separate study was completed to look into the effects of varying the electrospinning parameters on the fibre diameters of PET. The three main parameters that can be altered are: flow rate, collector distance, and voltage. A total of five samples were spun. The full range of concentrations and other electrospinning parameters used to produce these samples is shown in Table 3.6. In this instance 10g of each solution was prepared, and 1mL was spun into fibre.

During the spinning of Sample I it was found that the collector distance was too great, leading to fibres forming off the collector plate. Therefore, in subsequent experiments at the same concentration the distance was reduced to 14cm. For Sample III the flow rate was increased in order to increase the mass flow and to prevent the solution drying at the tip as occurred towards the end of spinning Sample II.

Sample	PET Concentration [%w/w]	Collector Distance [cm]	Voltage [kV]	Flow Rate [mL/h]
I	20	16	20	2.0
II	20	14	25	2.0
III	20	14	18	2.5
IV	25	16	18	2.0
V	27.5	15	18	2.0

Table 3.6 Electrospinning conditions for the five initial PET-derived membranes.

In a further bid to deal with the issue of the solution drying at the needle tip due to the low relative humidity an experiment was conducted to determine if increasing the needle diameter would help to reduce this problem. Due to the set-up of the electrospinning rig, and its location, it was not possible to directly control the humidity. Therefore, for these experiments the concentration of 25.0% w/w was chosen as it had been found the most stable and consistent solution during the electrospinning. A single 4g solution of PET was made up and dissolved overnight. The electrospinning conditions were the same as used for Sample IV: a collector distance of 16cm, voltage of 18kV, and flow rate of 2.0mL/h. An 18 gauge (0.838 mm øID) needle was used to spin 1mL of the solution, before a 21 gauge (0.514 mm øID) needle was used to spin a further 1mL of the same solution. 18 gauge was the largest needle

tip that was compatible with the rest of our set-up and was observed to make no difference to the problem of the Taylors cone drying out and so no further diameters were tested.

3.2.4 Poly(ε-caprolactone) membrane generation

Following on from the work on poly(ethylene terephthalate), alternative polymers from the polyester family were investigated. This began with some studies on poly(ε-caprolactone) (PCL). In this instance PCL was purchased from Sigma-Aldrich, average M_w=14,000, and dissolved in a ratio of 90:10 dimethylcarbonate (DMC) : dimethylformamide (DMF) at a concentration of 10% w/v. 15 mL of polymer solution was synthesised, using 1.5 g of polymer, and set to dissolve on a magnetic stirrer plate for 4 hours prior to electrospinning. The first membrane produced from this solution was electrospun using a 0.838 mm øID needle, at a flow rate of 1.5mL/h, with a collector distance of 19 cm, at a voltage of 17 kV. Temperature throughout the experiment was 22.3°C ±0.3, and the relative humidity was 31.4% ±0.2. A total of 2 mL of polymer solution was spun.

A study was also carried out to look at the impact of changing key electrospinning parameters (i.e. flow rate, voltage, collector distance) upon the resulting fibre diameter. For this work, a 12.5% PCL in 90:10 THF:DMSO solution was used, and parameters were varied as illustrated in Table 3.7. For this assay, a total of 0.1 mL of polymer solution was spun for each of the tests, temperature was 22°C ± 1 °C, and %RH was 40% ± 3%. This is a very small volume of polymer, which may ultimately have impacted the observed properties and acoustical performance of these materials. Unfortunately, the volume that was able to be spun was governed by time constraints on shared and in demand lab equipment. The tests were spun onto a static collector plate, covered in aluminium foil. Figure 3.3 shows SEM images of the typical fibre diameter, density and membrane structure for these PCL-based membranes. It is immediately apparent that the fibre density is much greater than with the PET samples, whilst the fibre diameter is roughly the same, averaging 1 µm or so for each fibre in this image.

Sample	Collector Distance [cm]	Voltage [kV]	Flow Rate [mL/h]
V1	20	16	1.00
V2	20	18	1.00
V3	20	20	1.00
CD1	16	16	1.00
CD2	18	16	1.00
CD3	22	16	1.00
FR3	20	16	1.50
FR2	20	16	1.25

Table 3.7: Electrospinning parameters used to study the impact upon fibre diameter.

The next step in the electrospinning process was to change the solvent system. The aim here was to introduce some sort of surface characteristics to the fibre, either through changing the morphology to introduce beaded or ribboned sections, or pores on the surface of the fibre. As previously stated, spinodal decomposition was the method chosen to try and develop this sort of characteristic. Spinodal decomposition requires the use of a solvent system featuring at least two different solvents with different evaporation rates. The first test of spinodal decomposition utilised two 'good' solvents for PCL, THF, and DMF. Good and poor solvents refer to how well they are able to solvate a solute. If the solute is fully dissolved quickly and without needing heat or stirring it is a good solvent. A poor solvent may require heating, stirring, and a lot of time to fully solvate the solute, if it can dissolve it at all. This combination was chosen since both solvents are good at dissolving PCL whilst offering different evaporation rates. Later work resulted in the introduction of DMSO to the solvent system,

chosen due to its relatively poor solvation of PCL and its different evaporation rate. Table 3.8 shows a comparison of the evaporate rates of the four solvents used in the experiments relating to spinodal decomposition. N-butylacetate (BuAC) is a reference material for evaporation rates and is assigned a relative evaporation rate of 1. The evaporation rates listed are relative to that of BuAC. A higher value equates to the solvent being more volatile and evaporating more rapidly.

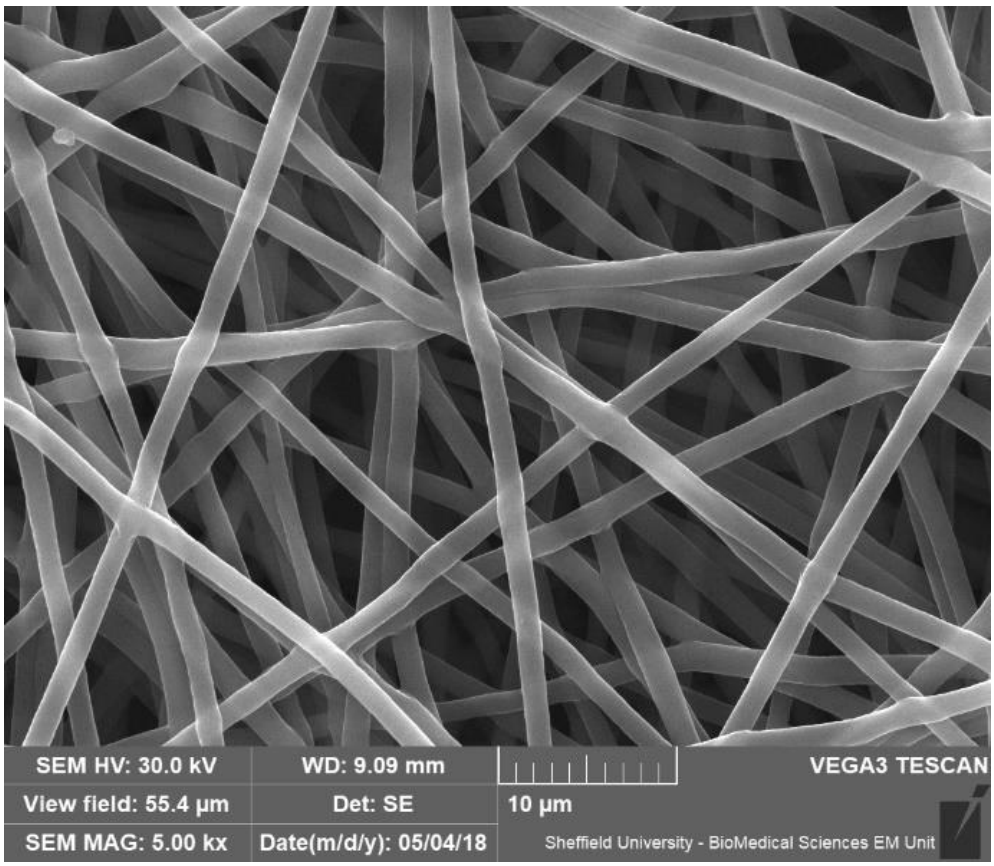

Figure 3.3: SEM image taken at 5000x to highlight fibre diameter, density, and membrane structure typically seen with the PCL based membranes.

Solvent	Evaporation Rate @25°C (Reference: BuAC =1)
CF	11.6
DMF	0.17
DMSO	0.026
THF	6.3

Table 3.8: Evaporation rates of the chosen solvents for PCL. Values of evaporation rates taken from the Handbook of organic solvent properties (Smallwood, London, 1996).

Initially two solutions using the DMF/THF solvent system were prepared. The solution ratios and electrospinning parameters can be seen in Table 3.9. Solutions C and F were spun at a temperature range of 23.5°C ± 0.6°C, with a relative humidity of 27.2% ± 0.7%. The preparation of these solutions was significantly easier than those performed with PET, yielding a much lower viscosity solution that was easier to electrospin. The electrospinning process also ran much more smoothly, with no visible sputtering. The only issue that arose throughout the process was the formation of enlarged Taylors cones, which if left to get suitably large were seen to collapse and disrupt the jet. This was occurring repeatedly in the case of the THF_C solution, highlighting the fact that the process parameters were not fully optimised. The parameters were adjusted to increase the flow rate in a bid to reduce the enlargement of the bubble formation. Ultimately, this did little to mitigate the enlargement of the Taylors cones. This test was labelled as C(ii) and spun for another 0.52mL to generate Sample THF_C(ii). Despite the formation of the enlarged Taylors cone, it did appear to be more stable than that of the ones seen at the lower flow rate used in solution C; at no point

did the cone collapse, despite the size of enlargement ultimately exceeding that seen within solution C.

For solution F the flow rate was reset to 1mL/h, and the applied voltage was increased to 18kV. After the limited success in the reduction of the Taylors cone through increasing the flow rate, it was thought that increasing the voltage might reduce the issue by increasing the rate at which the solution was turned into a polymer jet. This proved to work, with no significant enlargement occurring and the spinning remaining stable, with no stuttering or breaks, for the full 0.68mL spin. At the time it was assumed that by increasing the flow rate there would be a greater concentration of solvent at the needle tip, thereby reducing the problem. It was also assumed that increasing the voltage would increase the rate at which the solution was converted into a polymer jet, so decreasing the amount of time spent at the needle tip. In reality, the greatest contributor to this issue is humidity which I was unable to control throughout the experiments. Increasing the voltage resulted in a more stable spinning set-up but did not solve the problem. Instead it just changed the location of the problem, resulting in the fibres having bead-on-chain morphologies instead as the jet began to break down before reaching the collector.

As opposed to using two good solvents, a switch to a poor solvent in combination with a good solvent was tested. The first system tried in this manner was a combination of THF and DMSO. A further solvent system was also introduced, CF and DMSO. The ratios and electrospinning parameters for tests using this system can be seen in Table 3.10.

Solution	PCL concentration (%w/w)	DMF:THF ratio	Collector distance [cm]	Voltage [kV]	Flow rate [mL/h]
THF_C	12.5	20 : 80	20	17	1.00
THF_C(ii)	12.5	20 : 80	20	17	1.50
THF_F	12.5	50 : 50	20	18	1.00

Table 3.9: Solvent ratios and electrospinning parameters for initial experimentation into spinodal decomposition.

Solution	PCL concentration [%w/w]	Solvent ratio [X : DMSO]*	Collector distance [m]	Voltage [kV]	Flow rate [mL/h]
THF_A	12.5	90:10	20	16	0.75
CF_B	12.5	90:10	20	16	1.00
CF_C	12.5	80:20	20	16	1.00

*Table 3.10: Electrospinning parameters and solvent ratios used in the experiments with DMSO as the 'bad' solvent. *X = THF/CF.*

Figure 3.4 shows some of the alterations to the fibre surface, achieved through spinodal decomposition using the two solvent systems described above. What is not clear from these images is whether the nanopores are open or closed.

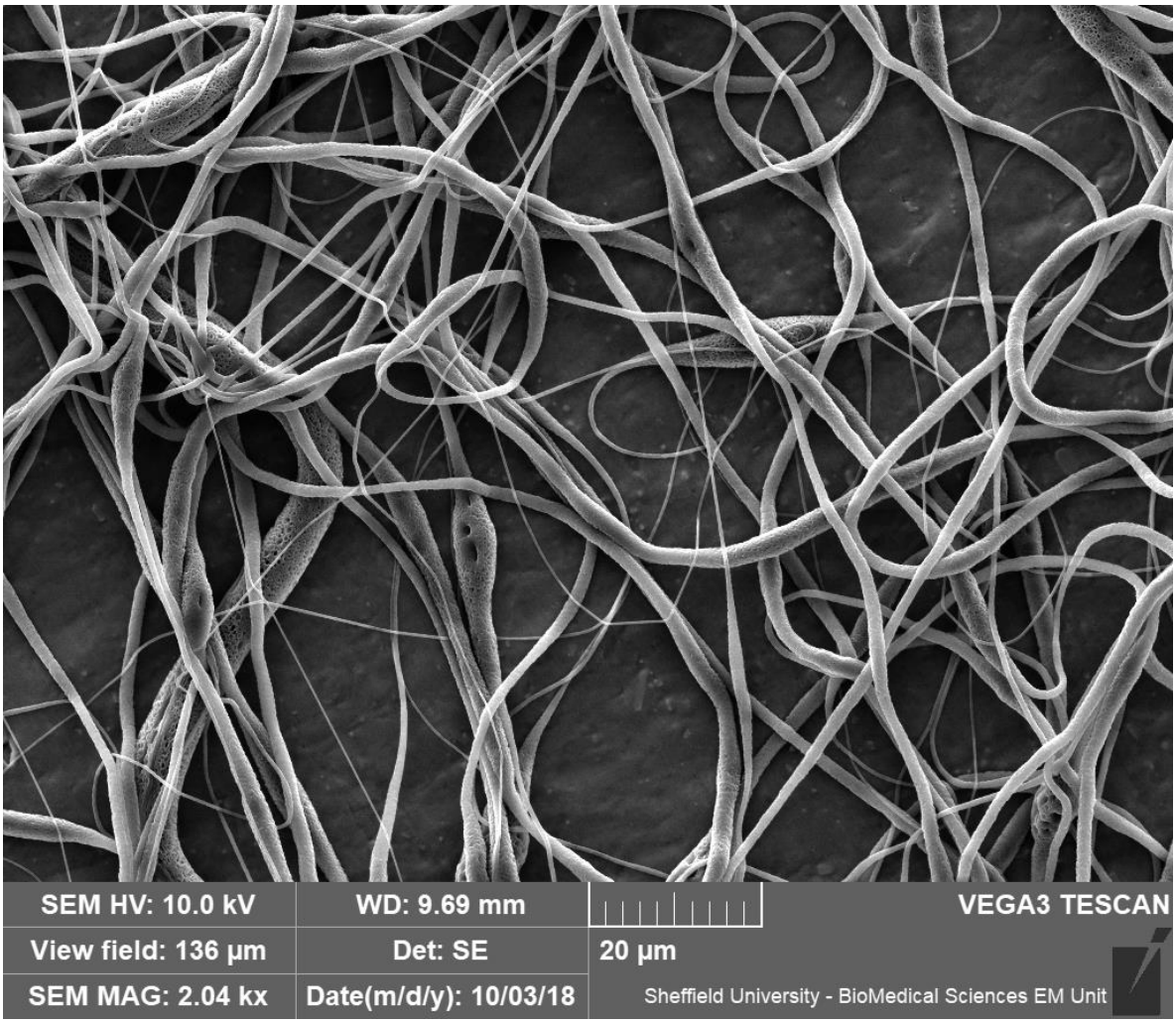

Figure 3.4: Changes to fibre morphology caused by spinodal decomposition using different solvent systems. Nanopores are clearly visible on the surface of the fibre, as is bead-and-chain morphology.

3.2.5 NXTNANO

In order to complement the range of nano-fibres produced through the detailed experiments, three nanofibrous samples were acquired from NXTNANO LLC (Oklahoma, USA). Two of these samples were made from thermoplastic polyurethane (TPU), and the remaining sample was made from poly(vinylidene fluoride) (PVDF). The properties of these materials, as stated by NXTNANO, are summarised in Table 3.11.

Sample	h [µm]	$\bar{s}$ [µm]	d_f [nm]	ρ_m [kg/m^2]
11gsm TPU	20	0.45	271 ± 113	0.011
5gsm TPU	20	0.70	379 ± 155	0.005
8gsm PVDF	20	0.80	330 ± 218	0.008

Table 3.11: Properties of the NXTNANO membranes.

Details on the synthesis of these materials such as concentration, viscosity, solvents, or electrospinning parameters like voltage, distance, etc were not shared as the company was looking to market these materials in the future.

Figure 3.5 shows some SEM images of the membranes, highlighting fibre size and density which is typical for the NXTNANO membranes. It is apparent from comparison with both the PET and PCL membranes that the fibre density is significantly higher, with both smaller fibre diameters and much smaller inter-fibre pore sizes. It also appears as if there is some fusing present, identifiable by the branched and linked appears of fibres, with rounded joins and more circular pore structures.

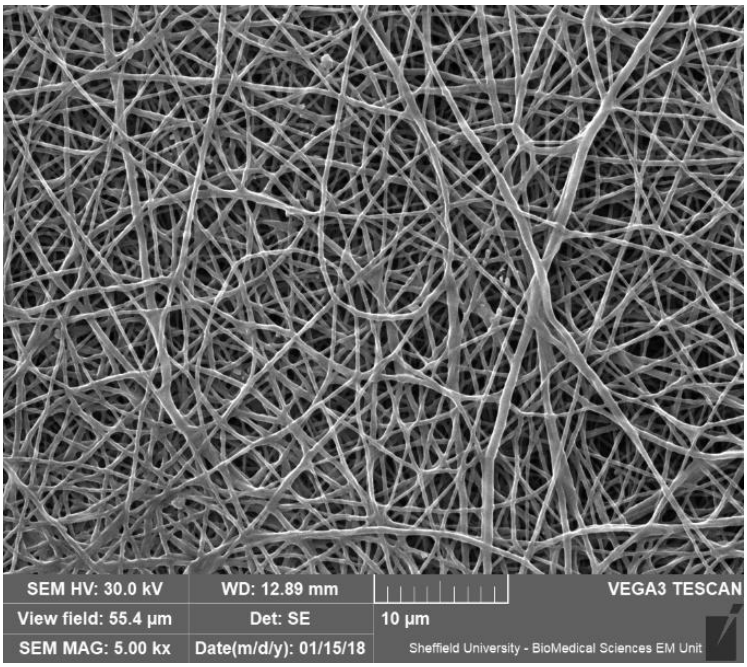

Figure 3.5: SEM image of a NXTNANO membranes taken at 5000x.

3.2.6 Poly(methyl methacrylate) membrane generation

An additional four nanofibrous membranes were obtained through a collaboration with Dr Simon King and Dr Vlad Stolojon at the University of Surrey. These membranes were poly(methyl methacrylate) (PMMA) based, due to its relative ease of solvation and its availability within the University of Surrey. PMMA with M_w= 120,000 was supplied by Sigma (Merck KGaA, Darmstadt, Germany) and made up to a concentration of 20%w/w in combination with a solvent system of Acetic Acid : Formic Acid, varying in ratio from 1:4 to 1:1 depending on the relative humidity (%RH). The volume of acetic acid was increased to lower the solution volatility in lower %RH environments. Due to significant instabilities being encountered during the electrospinning process, the parameters used were varied constantly throughout the experiments in order to maintain ideal flow. The parameters that were kept constant can be seen in Table 3.12. In each case 12 mL of solution was spun, and a rotating

collector drum was used to serve two purposes: to allow for slightly thinner more homogeneous fibres; and to yield a larger sample. Utilising a rotating collector drum allows the fibre to be further stretched and it also allows for slightly more aligned fibres – both of which contribute to increased homogeneity in the resulting membranes. For the stretching of fibres to occur, the rate of rotation must be greater than the rate of deposition, accelerating the deposited fibre away from the jet. The polymer must still be solvated at this point. If the rate of rotation is too fast relative to the rate of deposition then instead of stretching, the deposited fibres will be fragmented (Robb, Lennox, 2011).

The flow rate was varied throughout the experiments to maintain an ideal flow in relation to the chosen voltage and fluctuations in humidity. A higher kV value would increase the rate at which the solution is consumed, requiring greater flow rates. Variations in humidity, even minor percentages, affect drying time at the tip of the needle and so the flow rate had to be altered to avoid an excess or insufficient volume of polymer solution at the tip. Further attempts to minimise this included using a hot water bath in the enclosed electrospinning set-up at the University of Surrey to try to ensure a stable humidity and a relatively constant temperature.

Sample	Concentration [%w/w]	Voltage [kV]	Humidity [% RH]	Temperature [°C]	Collector distance [cm]	Collector speed [rpm]
15kV PMMA	20	15	80	30	20	10
18kV PMMA	20	18	80	30	20	10
21kV PMMA	20	21	80	30	20	10
24kV PMMA	20	24	80	30	20	10

Table 3.12 Parameters for electrospinning of the nanofibrous membranes produced in collaboration with University of Surrey.

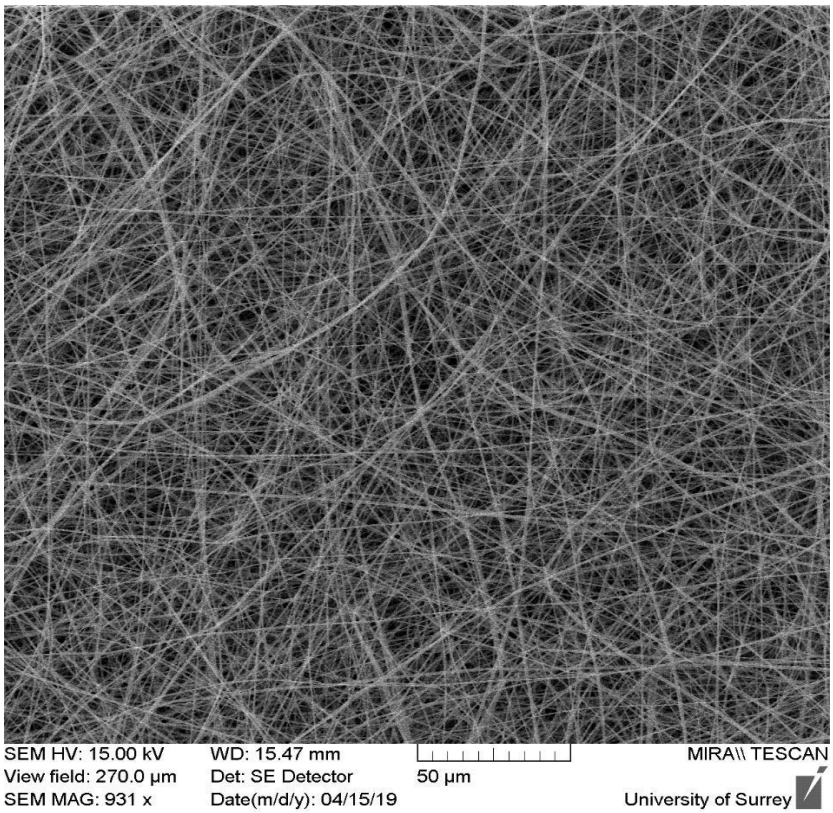

Figure 3.6: SEM image of the PMMA membranes, taken at the University of Surrey.

Figure 3.6 shows an SEM image of the typical fibre diameter, fibre density, and membrane structure seen within these PMMA samples. Fibre density and diameter is similar to that seen with some of the later PET samples. Section 3.3 in Chapter 3 provides information on how fibre diameter, fibre density, and membrane structure are assessed via SEM.

3.3 Material characterisation methods

There are a number of approaches that can be used to characterise the material parameters of nanofibers, but it is not a trivial task. Perhaps the most crucial thing to characterise initially is the fibre diameter. In the scope of this work, fibre diameter was characterise using scanning electron microscopy, which is an imaging method that allows for the visualisation and characterisation of the dimension of individual fibres either through built-in or external image analysis software. Other important parameters to consider are the material density and thickness, which are important for understanding their effects on the measured acoustic performance, and for modelling the acoustical properties of nanofibres. In this PhD the density was measured by weighing the materials with a balance and thickness was measured from scanning electron microscopy images of the membrane edge. These approaches are described in detail in the following sections.

3.3.1 Scanning Electron Microscopy

Scanning electron microscopy (SEM) is a type of microscopy that utilises a focused beam of electrons to reveal a higher level of detail and resolution than that attainable with optical microscopy. The resolution, in microscopy terms, is defined as the ability to distinguish objects in close proximity as separate. Optical microscopes typically have a maximum resolution of 200 nm, which is limited by the wavelength of light waves. In the case of SEM the resolution is close to 10 nm, due to the substantially shorter wavelength of the electron beam. In addition to a greater resolution, SEM can offer greater depth of field than optical microscopes, which allows greater topographical detail to be seen. SEM can also offer

microanalysis of the sample, such as its chemical composition or the crystallographic, magnetic or electrical characteristics. These factors make SEM a very powerful characterisation method. Scanning electron microscopy was performed on a TESCAN Vega3 microscope (TESCAN, Kohoutovice, CZ), using the accompanying TESCAN software package at the Faculty of Science Electron Microscopy Facility, University of Sheffield.

Throughout the scope of the PhD the samples were always gold-sputter coated. The primary purpose for the sputter coating is to reduce the electron-charging that can occur, allowing for higher accelerating voltages to be run without compromising resolution too significantly. Charging was a common occurrence in the type of samples used within this PhD as they are plastic based and therefore non-conductive. This lack of conductivity results in the material acting as an electron trap, accumulating electrons (this is the process named 'charging'), resulting in very bright regions that can mask surface detail or information. By sputter coating the material any electron traps are removed as the electrons can be channelled along the samples. There is a secondary advantage to sputter coating the samples used within this work, and that is to lower the risk of damage to the samples. As the electron beam passes over the sample some of its energy will be lost as heat to the sample. This heat is capable of damaging the structure of biological samples or softer materials such as plastics – especially on smaller scales such as those encountered throughout this work. All sputter coating was done on an Edwards S150B Gold Sputter Coater (Edwards, Sussex, UK). The deposition time is two minutes at a voltage of 1Kv and a current of 20 µA. The thickness of gold deposited under these settings has not been directly measured but has been estimated to be around 20 nm. To allow for comparability between samples, images of fibre diameter were always taken at similar working distances, the same acceleration voltages and the same levels of magnification. Typically, this equated to magnifications of 1000x, 2500x and 5000x. These magnifications were chosen as they were found to provide a good overview of sample structure, and a good estimate of fibre diameters (Figure 3.7). For the determination of

membrane thickness there was no set magnification used, as it depended on the mounting method and thickness of the membrane.

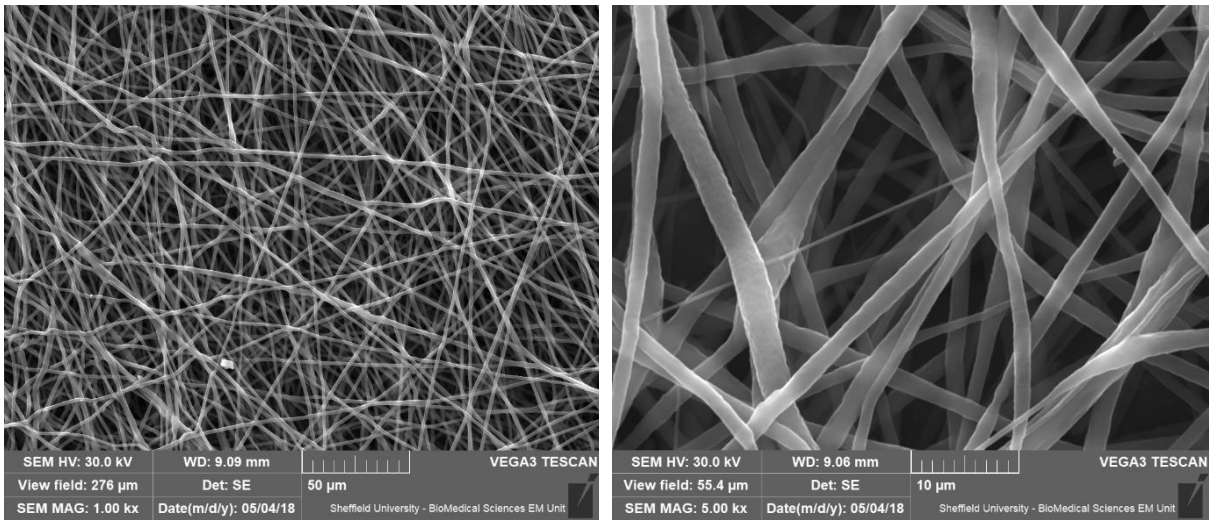

Figure 3.7: SEM example images of 1.0kx and 5.0kx magnifications, chosen to provide good overall illustration of fibre density, structure, and size.

3.3.2 Density

Density is a seemingly relatively easy parameter to measure. For the nonwoven samples, density values were given by the manufacturer (John Cotton Group Ltd), but it was also measured independently using a Kern KB2000-2N (Kern & Sohn GmbH, Germany) digital scale. Once circular nonwoven samples were cut to size for acoustic or airflow resistivity experiments they were accurately measured using a set of digital callipers, weighed, and then the density (ρ_m) was calculated from the volume of the sample (V) and its mass (m) as:

$$V = \pi r^2 \cdot h$$

Equation 3.1

$$\rho_m = \frac{m}{V}$$

Equation 3.2

where, h is the height of the specimen [m], r is the radius of the specimen [m], m the mass [kg], V is volume [m^3], and ρ_m is the density [kg/m^3].

For the electrospun materials this was not a feasible option as their mass was too low to be measured accurately by the Kern KB2000-2N scale. As a result, weight was measured using an Ohaus AX124 analytical balance (OHAUS Europe GmbH, Switzerland). Thickness, or the specimen height, was taken from SEM measurements, though this proved to be a much harder task than expected. Two approaches were initially attempted: (i) tilting the stage of the SEM to try to get an edge in view; and (ii) attempting to 'fold' a part of the membrane up to allow for a clear view of the edge. Both approaches had advantages and disadvantages, as well as commonalities. With regards to the first method, this is a rather simplistic approach that did not involve any specific preparation or special materials. In terms of sample preparation, it only required the sample to be cut and placed on an SEM stub. Once the sample has been prepared and is inserted into the SEM, and the stage is tilted to a chosen reproducible angle, enabling an edge-on view on the sample. The second approach involved the folding of one side of the sample so that it sits at a 90° angle to the rest of the sample. This eliminated problems associated with parallax errors in the microscope and its software, as were seen in the first approach. Both of these approaches were found to suffer from the same problems related to the cutting and mounting of the sample during the preparation stage. It was found that significant tearing, delamination, and rounding of the sample was occurring – making measuring the edge thickness particularly challenging, as illustrated in Figure 3.8.

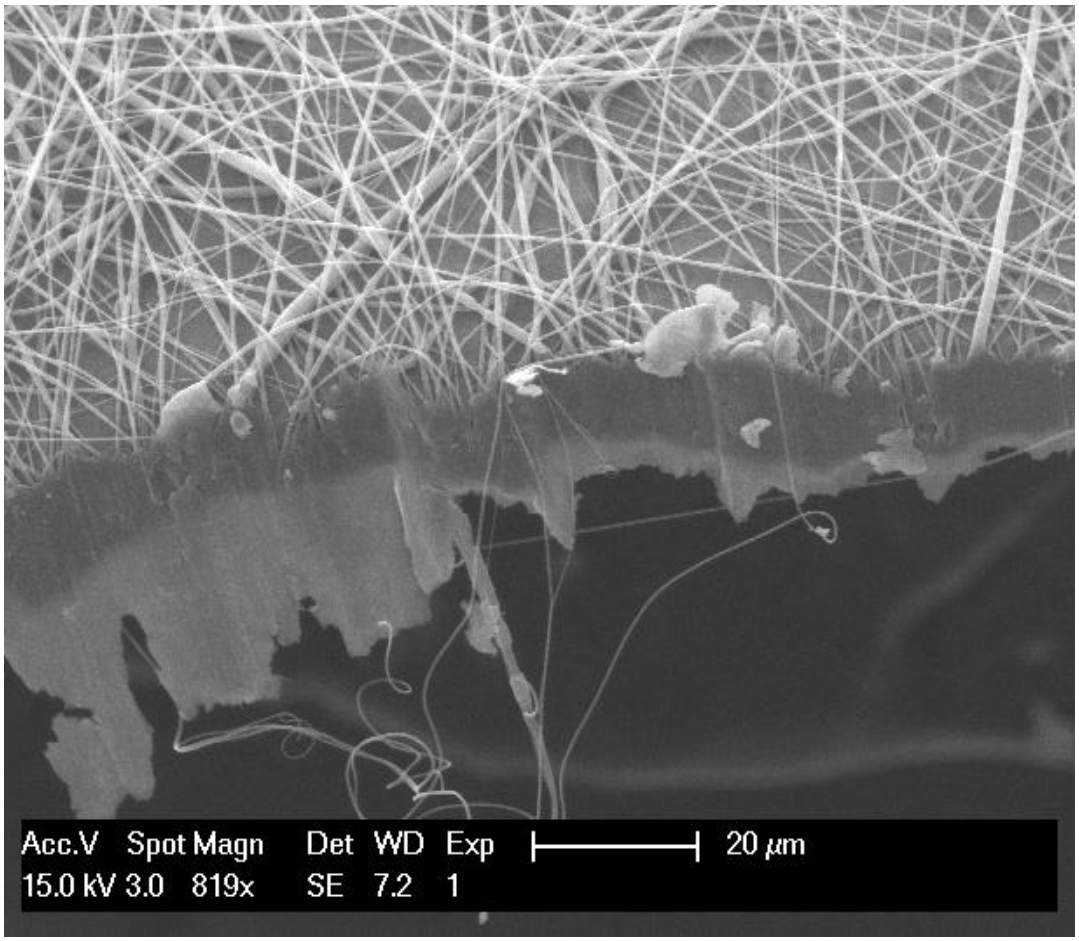

Figure 3.8: SEM image highlighting the damage to and uneven nature the edge of a membrane caused by cutting the sample to size using standard scissors.

In order to minimise this, a cryostat was used to try and ensure a clean cut of the sample to make the thickness measurement more accurate. The cryostat used was a Leica CM1860 UV (Leica Biosystems, Milton Keynes, UK). The membrane sample was placed into Lecia OCT compound/tissue freezing medium and rapidly frozen using liquid nitrogen. The frozen sample, now encased in the solid OCT medium, was mounted onto a stub and placed in the cryostat at a temperature of -20°C. The cryostat was then used to shave 100 µm thick slices off the encased-sample until it could be seen that the sample had been reached. The encased sample was then removed from the stub, turned through 180° and remounted onto the stub. The shaving procedure was repeated until it was apparent that the sample had been reached

and a clean edge had been achieved. Cuts were made at both ends to ensure that two clean edges were present on the sample, making identification of the clean edges easier when mounting and viewing the sample via SEM. The encased sample was removed from the stub and placed in de-ionised water to dissolve the resin, after which the sample was blotted on filter paper and dried prior to processing for SEM.

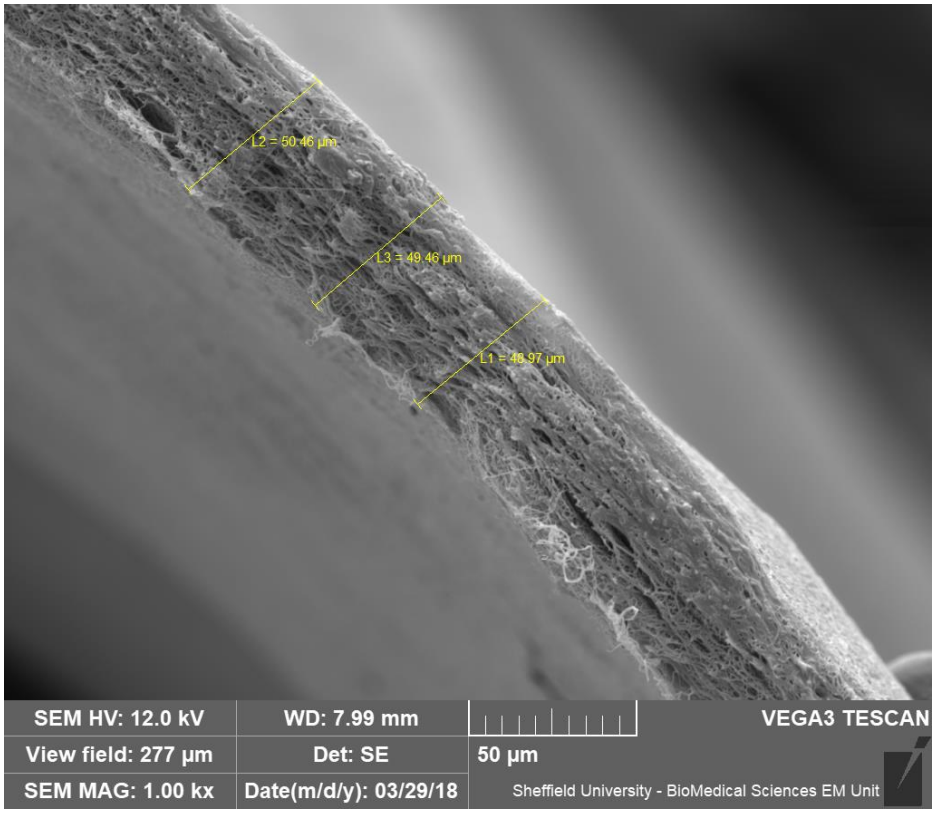

Figure 3.9: SEM image showing the cleanliness of the edge obtained via cutting with the cryostat method.

3.3.3 Porosimetry

The estimation of the porosity for the nonwoven samples was accomplished through an in-house manufactured rig which measured the difference in volumes of air between an experimental chamber and a calibration chamber. Boyle's law was then used to calculate the difference in air volume. Boyle's law, or the Boyle-Mariotte law, is an experimentally derived gas law describing the increase in pressure occurring in a gas as its volume decreases (Boyle, 1662). It can be described mathematically as:

$$PV = k$$

Equation 3.3

In equation 3.3, P is the pressure (Pa), V is the volume (m^3), and k is a constant that applies for a given mass of confined gas and a given temperature.

In the in-house built porosimeter there are two chambers under the same temperature, so the equation 3.4 comes into effect, showing that with an increase in volume pressure will decrease proportionally, and vice versa. Despite the dependence of Boyle's Law on temperature, there is no means by which to control it on this rig. A round robin test revealed an accuracy of 1% as assessed by comparisons of calibration samples analysed through alternative methods at a variety of institutions globally (Horoshenkov, *et al*, 2007). The in-house built porosimeter is shown in Figure 3.10.

$$P_1V_1 = P_2V_2$$

Equation 3.4

As the volume of air in the sample chamber is decreased by the addition of a sample, the pressure in this chamber will increase. By then increasing the volume of air present in the opposite chamber until the pressure between sample and calibration sides are equal it is

possible to determine the difference in air volume. This volume of air can then be used to estimate porosity using Equation 3.5 as follows:

$$\phi = 1 - \frac{V_a}{V}$$

Equation 3.5

V_a is the difference in air volume between the two chambers (or the volume of air displaced by the sample), and V is the volume of the sample.

Porosity was estimated for the nanofibrous membranes using their material density, ρ_m, and fibre density, ρ_f, according to the following equation:

$$\phi = 1 - \frac{\rho_m}{\rho_f}$$

Equation 3.6

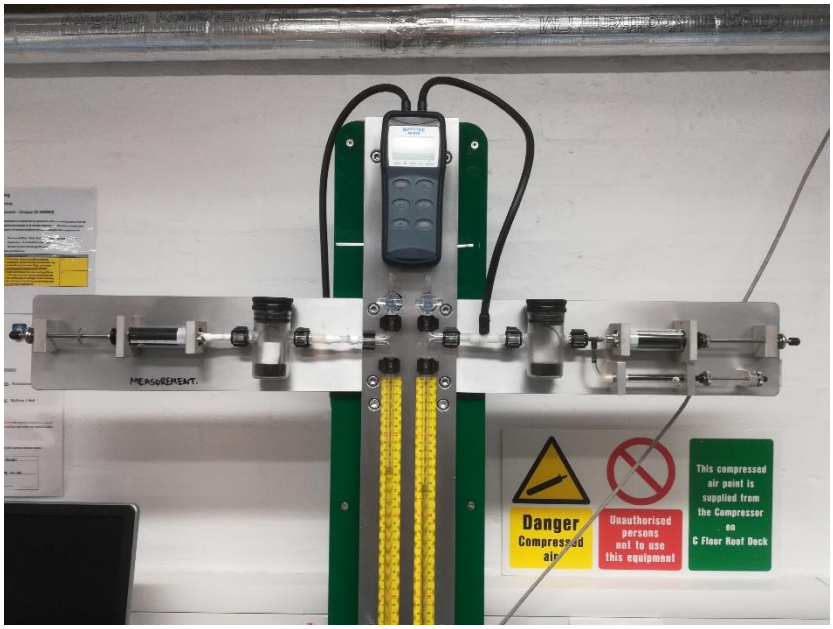

Figure 3.10: In house built porosimeter, highlighting the two chambers affected by Equation 3.4.

3.3.4 Airflow resistivity

Airflow resistivity is one of the key parameters in determining the acoustic performance of a porous material. It was either measured directly or inverted from acoustical data. Direct measurements were conducted through the use of two air flow rigs, initially using an AFD AcoustiFlow 300 device (Akustik Forschung Dresden, Dresden, Germany), paired with AFD 311 software (Akustik Forschung Dresden, 2017). The AFD AcoustiFlow 300 was able to non-destructively measure the airflow resistivity of any open-porous sample in accordance with the standard direct-flow method (ISO9053:1991, 1991). Testing of nonwoven samples in the AFD AcoustiFlow 300 was performed using 100mm diameter samples, cut using an in-house manufactured circle-cutter. In order to ensure a perfect fit of the samples, PTFE tape was applied to the inner edges of the sample holder to minimise any air gap that could have led to an erroneous result. In all cases, measurements of each sample were performed for a minimum of five specimens. Generally ten repeats were used to ensure repeatability and accuracy of the results (Horoshenkov, *et al*, 2017).

In the case of samples of particularly low density or with higher values of airflow resistivity the design of the AFD AcoustiFlow 300 meant that the samples could be blown up the sample tube or deformed under the pressure from the induced airflow. This would yield erroneous results as the actual air pressure at the surface of the sample would be significantly lower than assumed by the device. In the case of the low density samples, this was countered by the addition of a second layer or even third layer of the sample to increase the mass and wall friction without drastically changing the material properties. In order to ensure that this did not have an effect on the reported values of airflow resistivity, a nonwoven sample was tested for ten repeats at both single and double thickness. The sample in question was supplied by John Cotton Group Ltd, and is their Autobloc product, properties of which are summarised in Table 3.13.

Sample	Fibre diameter d_f [µm]	Bulk density ρ_f [kg/m^3]	Fibre density ρ_m [kg/m^3]	Porosity ϕ [-]	Thickness h [mm]
Autobloc	23.66	1381	60.35	0.96±0.001	17±0.2

Table 3.13: Material characteristics of the Autobloc sample, supplied by John Cotton Group Ltd, used to ensure that increasing the thickness within airflow resistivity testing has no impact on measured values.

For Autobloc of a single thickness, the average value of the airflow resistivity retrieved from the ten repeats was 10812 ± 203 Pa·s/m^2. For double thickness, the average value from the ten repeats was 10143 ± 68 Pa·s/m^2. The minimum value for airflow resistivity occurred within the double thickness tests, equalling 9968 Pa·s/m^2; the maximum value for airflow resistivity was seen in the singe thickness tests, equalling 11162 Pa·s/m^2. Table 3.14 shows the averaged results for the ten repeats for each of the thicknesses. The difference between the two average values equates to 1.07%, a value well below the type of percentage error typically taken as experimental error in this field, and as such the thickness does not have an effect on the measured value of airflow resistivity (Hurrell, *et al*, 2018).

Sample	Airflow resistivity σ [Pa·s/m^2]	Sample	Airflow resistivity σ [Pa·s/m^2]
Double Average	10143 ± 68	Single Average	10812 ± 203

Table 3.14: Experimental data from the AFD AcoustiFlow 300, showing averages and standard deviation for single and double thickness samples of Autobloc, supplied by John Cotton Group Ltd.

Modelling the airflow resistivity was carried out using a variety of approaches. For this purpose, one of the empirical models discussed in Section 4.3 of Chapter 4 was adopted. It has previously been shown that these models can be accurate to within 0.5% for polyester based fibrous materials with a bulk material density within the range of $22.9 \leq \rho_m \geq 40.1$ kg/m^3 (Pelegrinis, *et al*, 2016).

The alternative route used for the modelling of airflow resistivity was through the inversion process as outlined in Chapter 4.3. This process was based on the application of the Miki or the Padé approximation models to surface impedance data obtained from an impedance tube experiment (refer to Section 4.3.1 in Chapter 4).

3.4 Conclusion

This chapter has presented the methodologies for both the synthesis and characterisation of the nonwoven fibrous and nanofibrous materials. In the case of nonwoven materials, John Cotton Group Ltd supplied a range of samples to either pre-existing specifications, which meet automotive industry requirements, or to specifications given as a result of optimisation work conducted during the PhD. Nanofibrous materials were synthesized in house via electrospinning and were also supplied through collaboration with NXTNano (OK, USA) and University of Surrey (Surrey, UK). The variation of both electrospinning and solution parameters allowed for a reasonable control of material properties like fibre diameter, thickness, and pore size.

The intrinsic material properties were characterisation alongside their acoustical properties. Material properties were retrieved from measurements of mass and thickness – completed via the use of balances and either callipers or scanning electron microscopy. Other material properties like the airflow resistivity and porosity were generally retrieved from the use of flow resistivity rigs and porosimeters. Where the porosimeters was deemed unsuitable due

to time or accuracy constraints due to there not being sufficient amounts of sample, porosity was attained through inversion modelling applied to the measured acoustic properties or through measurement of the membrane density and thickness. The acoustical properties themselves were measured using a 45mm and a 100mm sound impedance tubes supplied by Materiacustica and set up in a 2-mic configuration. Nonwoven specimens were tested individually, whilst nanofibrous specimens were tested using Melamine as a substrate due to their inherent material properties – namely thickness on the microscale and a low stiffness.

Chapter 4: Acoustical properties of nonwoven materials

In addition to the range of material characterisation methods used and presented in Chapter 3, the materials studied in this work were also characterised acoustically. This was significant for several reasons. Firstly, the end goal of this project was to understand and to improve the absorption properties of these materials. Secondly, through the characterisation of these materials acoustically it was possible to assess the accuracy of a variety of models that are used by academia or in industry. Thirdly, by obtaining values of absorption coefficient and surface impedance it was possible to invert the intrinsic material parameters of these materials acoustically. Assuming a model can accurately reproduce the acoustic performance of a material sample, it can hence be used to invert the intrinsic material properties of that same sample. A reliable acoustical model can allow for a rapid characterisation of a range of fibrous media properties that are otherwise much trickier and more costly to measure non-acoustically. Theoretically this also facilitates the optimisation of a material through modelling rather than through repeated batch production and testing.

This chapter will present the methods used to acoustically characterise the materials. It presents the theory behind those methods, as well as the approach taken for their modelling, and the models used.

4.1 Nonwoven acoustical characterisation

The two most commonly used descriptors of the acoustic performance of porous media are the absorption coefficient and the surface impedance. These can be measured experimentally using a sound impedance tube which allows for rapid and accurate testing of a material sample (ISO10534-2, 1998). Testing can take as little as 30 seconds per sample depending on the frequency range swept. This process can retrieve a range of acoustical parameters including the absorption coefficient, normalized surface impedance, reflection coefficient, and transmission loss.

4.1.1 Absorption coefficient theory

The absorption coefficient is defined as a ratio between the acoustic intensity which propagates through and is absorbed by the material, I_a, and the acoustic intensity incident on the surface of the material, I_i (Ingard, 1994),

$$\alpha \equiv \frac{I_a}{I_i} = \frac{I_i - I_r}{I_i} = 1 - \frac{I_r}{I_i}$$

Equation 4.1

where I_r is the reflected acoustic intensity.

The absorption coefficient can also be defined in terms of the absolute value of the pressure complex reflection coefficient, $|R|$,

$$\alpha = 1 - |R|^2,$$

Equation 4.2

where $|R|$ is the ratio:

$$\frac{I_r}{I_i} = |R|^2.$$

Equation 4.3

Broadly speaking, this means that the absorption coefficient is the ratio of sound intensity that enters the material and never leaves it to the sound intensity that is incident on the material. A larger value of absorption coefficient means that the material is good in terms of damping sound energy. For example, a value of 0.6 would mean that 60% of the sound energy that enters the material is absorbed by it.

4.1.2 Surface impedance theory

The acoustic surface impedance is the ratio of the amplitude of the total sound pressure on the material surface, P_s, in the incoming and reflective sound wave to the acoustical velocity, v, at the material surface S, i.e.

$$Z_s = \left[\frac{P_s}{v}\right]_S = R_a + iX$$

Equation 4.4

where Z_s is the surface impedance, v is the acoustic velocity, and S refers to the surface, and $i = \sqrt{-1}$. The surface impedance is made up of two parts, real and imaginary, in which the real part is the acoustical resistance, R_a, while the imaginary part describes the reactance, X.

4.1.3 Sound Impedance Tube Theory

A sound impedance tube is a standard characterisation method that is fast, non-destructive and easy to use (see ISO 10534-2, 1998). It can be applied to a range of materials from loose fibres to nonwoven materials, to fully bound and formed products. Impedance tubes can also be set up in a variety of configurations to retrieve different characteristics of the tested samples. The most common configuration used throughout the scope of this thesis has been the two-microphone set-up, for which a general schematic can be seen in Figure 4.1.

A two-microphone set-up can retrieve three acoustical parameters from testing: (i) the absorption coefficient, α; (ii) the reflection coefficient, R, (iii) and the surface impedance, Z_s.

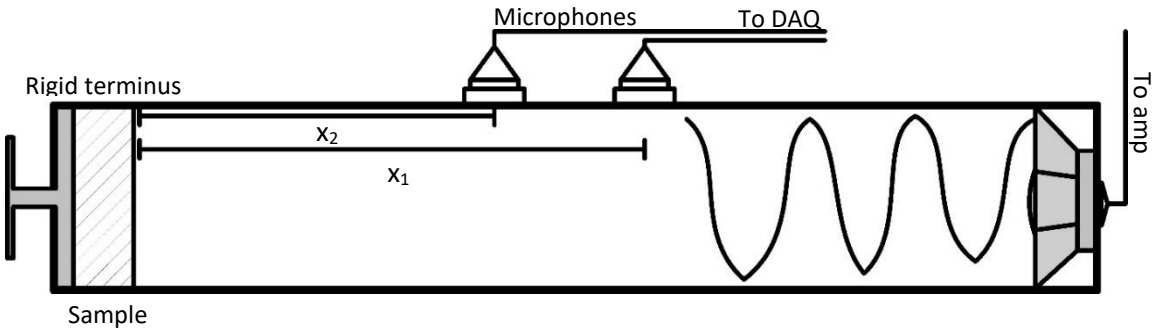

Figure 4.1: Schematic of a two microphone set up.

In a two-microphone set-up, the reflection coefficient, R, is derived as follows,

$$R = \frac{H_{12} - H_I}{H_R - H_{12}} e^{ik_0 2x_1}$$

Equation 4.5

Here k_0 is the wave number in air, and x_1 corresponds to the distance in the impedance tube between the front of the sample and microphone 1.

H correspond to a series of transfer functions, each of which is defined as,

$$H_I = \frac{p_I(x_2)}{p_I(x_1)} = \frac{\hat{p}_I e^{-ik_0 x_2}}{\hat{p}_I e^{-ik_0 x_1}} = e^{ik_0 s}$$

Equation 4.6

$$H_R = \frac{p_R(x_2)}{p_R(x_1)} = \frac{\hat{p}_R e^{ik_0 x_2}}{\hat{p}_R e^{ik_0 x_1}} = e^{-ik_0 s}$$

Equation 4.7

$$H_{12} = \frac{p_2}{p_1} = \frac{\hat{p}_I e^{-ik_0 x_2} + \hat{p}_R e^{ik_0 x_2}}{\hat{p}_I e^{-ik_0 x_1} + \hat{p}_R e^{ik_0 x_1}} = \frac{e^{-i(k_0 x_2 + \varphi)} + R e^{i(k_0 x_2 + \varphi)}}{e^{-i(k_0 x_1 + \varphi)} + R e^{i(k_0 x_1 + \varphi)}}$$

Equation 4.8

In the above equations, $s = x_2 - x_1$, or is the distance between the two microphones.

The surface impedance, Z_s, is given a complex number. Its real part describes the resistance of the material to sound, and the imaginary part describes any changes in the phase of the incident wave during propagation.

$$Z_s = Z \frac{1 + R}{1 - R}$$

Equation 4.9

where $Z = \rho c$, or the characteristic impedance of air.

4.1.2 Sample preparation for acoustical characterisation

For the early work conducted on fibrous nonwoven media, specimens were prepared by cutting with an in-house manufactured circle-cutter (45mm and 100mm in diameter) in combination with a pillar drill. The specimens prepared from each sample were tested in triplicate in all cases for both tubes. No further preparation was conducted on the samples prior to testing, with the exception of the use of PTFE tape if samples were slightly undersized. This was done to reduce any air gaps at the edge of the material which could otherwise give erroneous results. For the nonwoven samples used at the early stages of this PhD there was sufficient material for all testing to be completed using both the 100mm and 45mm tube. For the nanofibrous membranes, specimens were prepared by cutting to size using a form and sharp pair of scissors. It was found that the inherent properties of the membranes meant they were unable to be tested individually, and so testing of membranes was done using melamine

foam as a substrate. Melamine foam was chosen as the substrate as it is a well-known material, which is easy to characterise and for which the properties do not appear to be susceptible to minor fluctuations in temperature or humidity in the local environment. The material properties of the melamine foam substrate can be seen in Table 4.1. These properties were obtained using the standard material characterization methods described within this chapter.

Substrate	h [mm]	ϕ [-]	σ [Pa·s/m^2]	ρ_m [kg/m^3]
Melamine	16	0.97	1.59x10^4	11.00

Table 4.1: Material properties of the melamine substrate used to mount the membranes for acoustic testing.

All melamine foam specimens were cut from the same sample, a 16mm thick sample provided by Foam Techniques Ltd (Foam Techniques Ltd, Wellingborough, United Kingdom). The melamine foam itself is an open-cell material produced by BASF (BASF, Ludwigshafen, Germany) and marketed as Basotect G+. These membranes were either wrapped around or placed upon the melamine substrate. Experiments were carried out to study the effect of mounting the membranes, and the observations from these experiments are presented in Chapter 5.

4.1.3 Sound impedance tube set-up

The actual acoustical testing was performed using two sound impedance tubes with diameters of 45mm and 100mm, which were both supplied by Materiacustica (Materiacustica S.R.L., Ferrara, Italy). The sound impedance tubes were set-up in accordance with ISO10534-2 (ISO10534-2, 1998; Materiacustica S.R.L., 2010). The two tubes have two key differences:

the diameter and the frequency range. The 45mm tube had a frequency range of 50 – 4200Hz, whilst the 100mm tube had a frequency range of 50 – 1600Hz. To ensure comparability between these tubes the same software, microphones, microphone sensitivities, amplifiers and DAQs were used. The two tubes have different frequency ranges as the tube diameters and mic spacings are different. Microphone spacing is largely responsible for low and high frequency limits in impedance tubes, and the diameter also dictates the high frequency limits. This is due to the need to avoid any non-plane waves within the tube (Materiacustica, 2016). ISO10534-2 details expressions for determining the frequency range for a given diameter tube with a given mic spacing (ISO10534, 1998).

4.2 Nonwoven acoustic characterisation results

The acoustic performance of the nonwoven materials is presented in the following section. The results are laid out chronologically, following their preparation methods as outlined in Chapter 3.

The first acoustic testing was performed on a range of samples supplied by John Cotton Group Ltd, with the aim of establishing which material parameters have the greatest impact on acoustic performance for this type of nonwoven material. Figure 4.2 shows a comparison of the acoustic absorption coefficient of these materials as a function of frequency. The key intrinsic material parameters were first presented in Table 3.1 but are repeated in Table 4.2, to allow for easier interpretation of Figure 4.2.

Material sample	Fibre diameter d_f [μm]	Thickness h [mm]	Bulk density ρ_m [kg/m^3]	Fibre density ρ_f [kg/m^3]	Porosity ϕ [-]
Autobloc	23.65	15.07	49.00	1381	0.96
Memory Fibre 8	18.83	21.43	17.57	1379	0.99
RPC Denim	N/A	20.96	43.82	1383	0.97
PE Sample 3	24.71	22.87	27.94	1383	0.98
PE Sample 8	14.36	21.15	21.71	1379	0.98
PE Sample 10	14.36	21.18	24.68	1379	0.98
WT3950b	23.74	26.81	38.47	1383	0.97

Table 4.2: Intrinsic material parameters of the samples presented in Figure 4.2.

From Figure 4.2 it can be seen that the maximal performance is obtained in the case of PE Sample 10, whilst the minimal performance is shown by PE Sample 3. Until approximately 400Hz, the performance of the materials is nearly identical, suggesting their compositions are not effective at low frequency sound absorption, and that there is insufficient variation in the material parameters of each material to create a significant difference in performance. Prior to 400 Hz the spectra for PE Sample 10 and PE Sample 8 have very similar gradients to the other materials. However, at around 400 Hz the gradient of both these PE Samples is seen to increase sharply. As has been discussed in Section 2.8.6 low frequency absorption is primarily dictated by thickness (Ingard, 1994), and except for Autobloc and WT3950b all samples have comparable thicknesses. It is well documented that decreasing fibre diameters increases the value of the absorption coefficient, α, (Delany, Bazely, 1970) and so the observed increases in gradient match what we would expect to see based on literature.

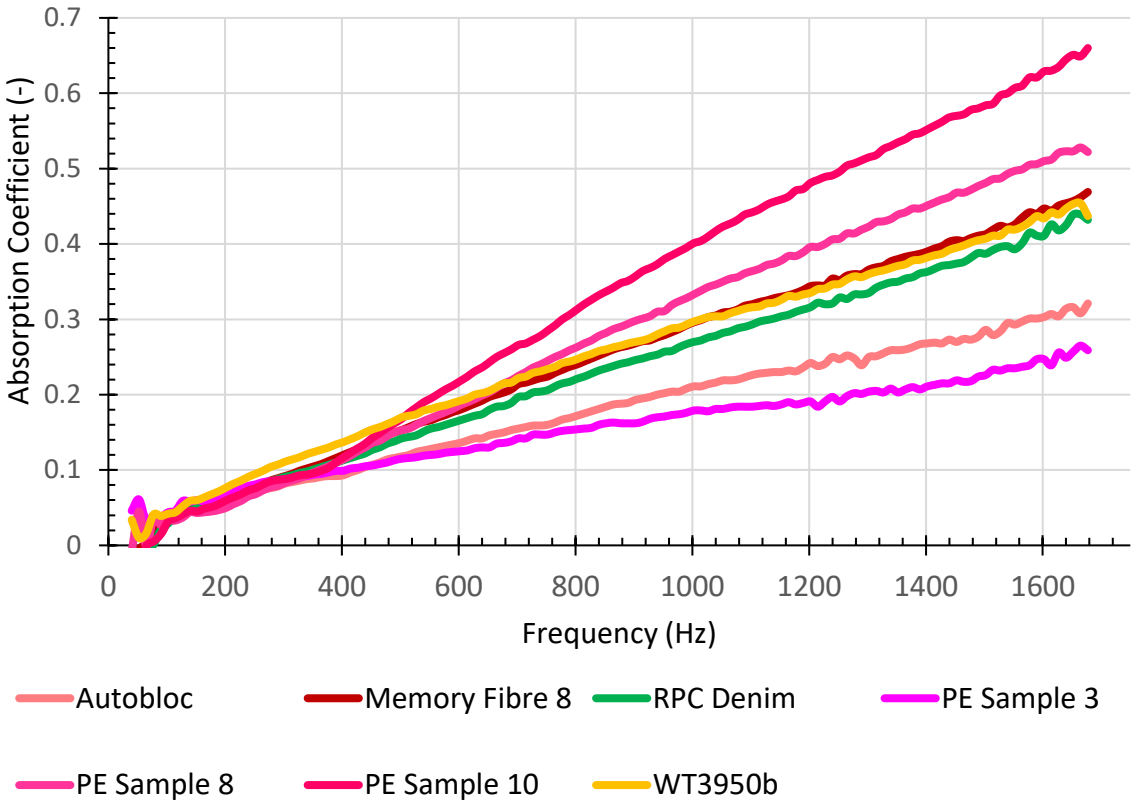

Figure 4.2: Comparison of the absorption coefficient values for the initial John Cotton Group Ltd supplied samples. Absorption coefficient spectra averaged from three repeats using the 100mm impedance tube in a two-microphone set-up.

PE Sample 8 and 10 have the smallest fibre diameter, some 30% smaller than the next sample, and so it follows that they have the greatest absorption. Despite having identical fibre diameters, the two samples do not have identical performance. This indicates that there is at least one more parameter affecting the overall absorption. From comparing their intrinsic material parameters, the one parameter that is noticeably different between them is the bulk density. It is reported in the literature that there is a correlation between increasing density and increased values of α in the medium to high frequencies (Koizumi, *et al*, 2002). PE Sample 10 has the greater bulk density of the two samples, and so its greater performance (see Figure 4.2) is to be expected based on the literature.

Three samples, Memory Fibre 8, RPC Denim, and WT3950b all exhibit very similar performance (Figure 4.2) in spite of having differing material properties. By comparing their material properties in Table 4.2 in Chapter 4 it becomes apparent that there is more than one parameter that impacts the acoustic properties. The three parameters that are noticeably different between these materials are the fibre diameter, the thickness, and the bulk density. By comparing Autobloc and WT3950b, two materials with similar fibre diameters and density but different thickness we can say that thickness does not have as great an impact as the bulk density or the fibre diameter. It was therefore deduced that the bulk density and the fibre size have the greatest impact on the acoustic performance. This is most apparent by looking at PE Sample 8 and PE Sample 10. Both have a fibre diameter of 14.36 µm and a thickness of around 21.2mm, however PE Sample 10 has a significantly better absorption coefficient. The only parameter that is different between PE Sample 8 and PE Sample 10 is the bulk density, which was assumed to account for the increase in the absorption coefficient.

To better understand the relationships between fibre diameter, density and thickness observed above, a simple experiment was conducted via modelling. The acoustical performance of the Memory Fibre 8 sample (Table 4.2) was modelled using the Miki model (covered in detail in Section 4.3.1 in Chapter 4). Each of the above parameters were then taken and modified individually to assess their impact on the absorption. Figures 4.3 – 4.5 show the changes in absorption observed when these parameters are changed.

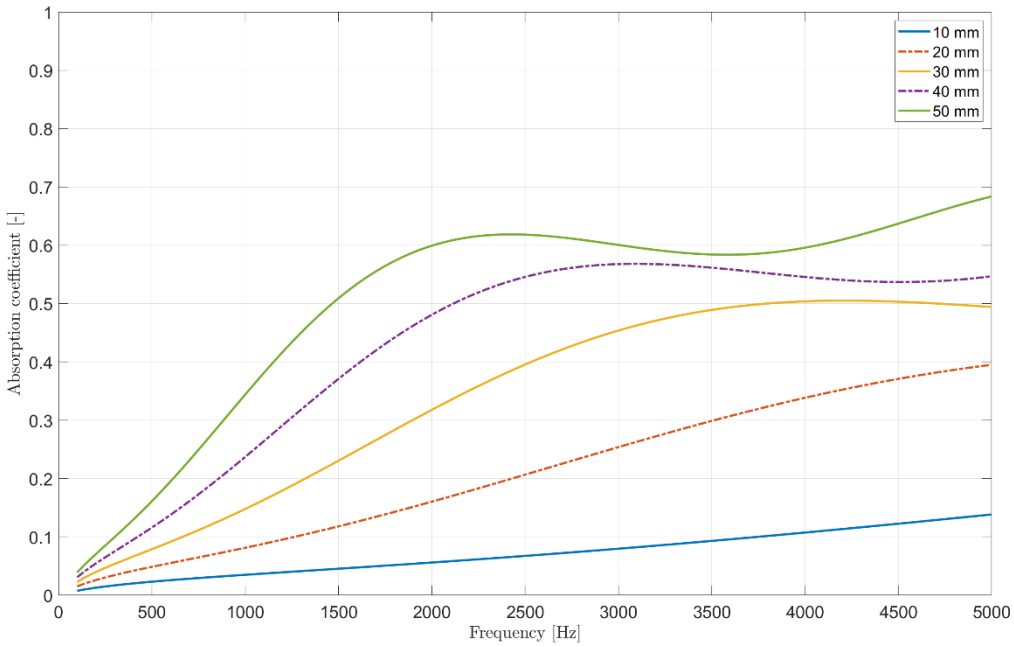

Figure 4.3: Effect of changing the thickness of Memory Fibre 8, as modelled.

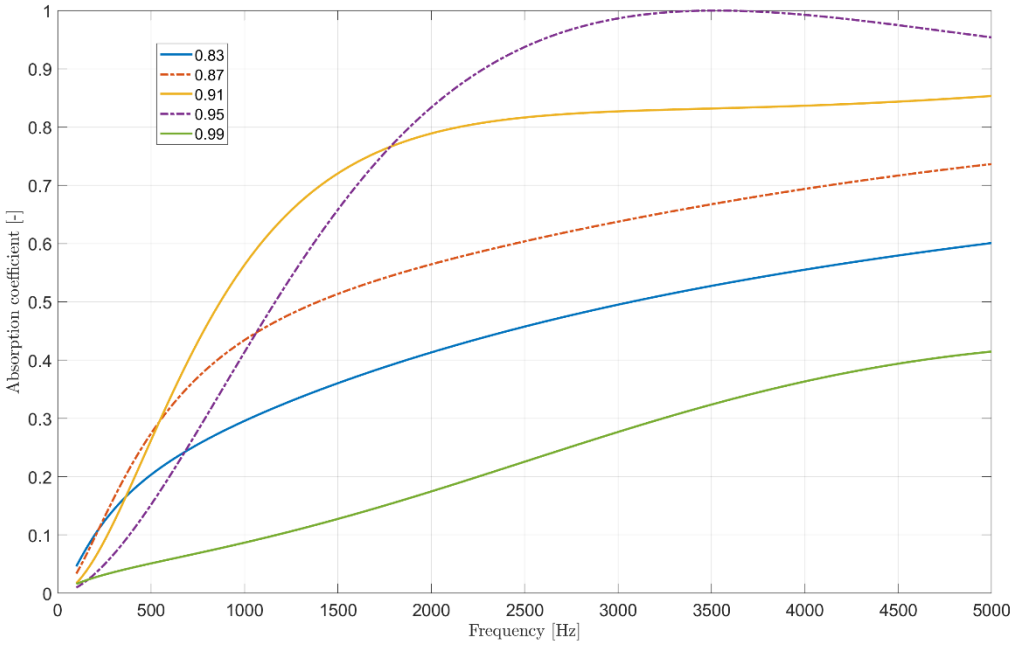

Figure 4.4: Effect of changing porosity of Memory Fibre 8, as modelled.

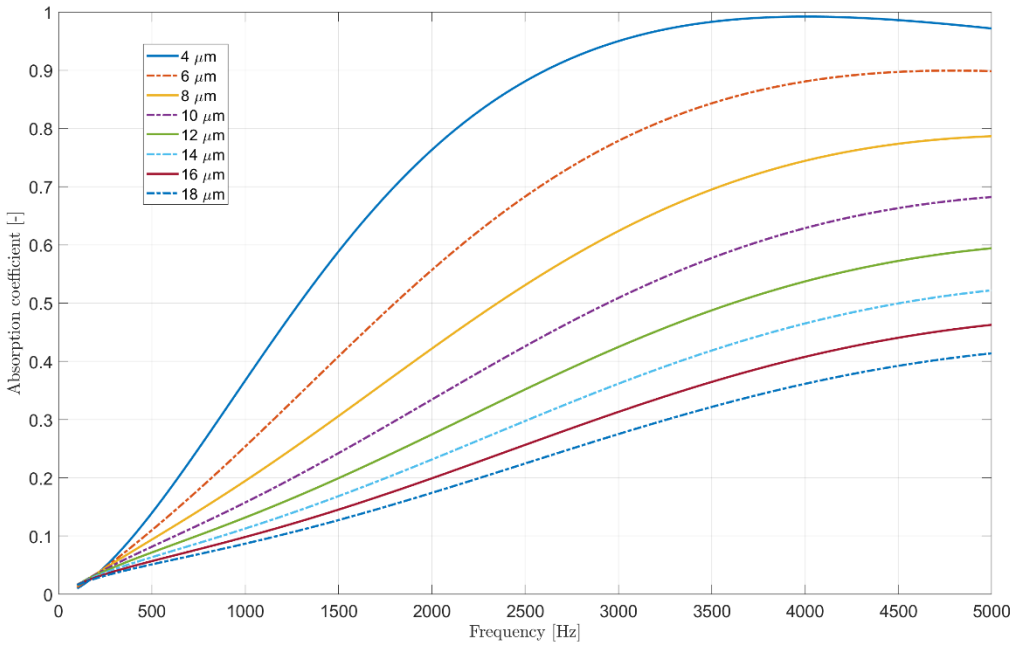

Figure 4.5: Effect of changing the average fibre diameter of Memory Fibre 8 on the absorption, as modelled.

The most noticeable impact of changing the thickness (Figure 4.3) of the material is that the absorption curve shifts to the left at lower frequencies, which agrees with the reports in literature (Ibrahim, Melik, 1978; Ingard, 1994). High frequency absorption does not increase in the same manner, and within the frequency range modelled appears to be subject to a law of diminishing returns. Thickness also requires a substantial increase in order to have a notable increase in acoustic performance. If we address Table 4.2 again, the increases in thickness between two materials with other comparable non-acoustical parameters, is approximately 5mm – and fall within the 20mm and 30mm range spectra in Figure 4.3. Such an increase in thickness could have a large impact on the acoustics, increasing the absorption coefficient by around 50% (0.2-0.3) in the mid-frequencies (2500Hz) and 12.5% (0.4-0.45) in the high-frequencies (5000Hz). This can be seen experimentally by comparing PE Sample 3 and WT3950b.

Considering porosity, which can also be used to infer information on bulk density, it can be seen that porosity does not have a linear relationship with absorption. Porosity values close to unity can actually exhibit lower absorption values than less porous materials. If a material has very high porosity it will have a very low flow resistivity. If the flow resistivity is sufficiently low this will result in very few viscous or thermal losses as the impeding sound wave cannot propagate through the material. Referring again to Table 4.2, Memory Fibre 8 and RPC Denim have similar non-acoustical parameters except for porosity, which changes by a value of 0.2 – this will also be accounting for the slight change in density. The calculated values of the absorption as shown in Figure 4.4 suggests there should be a much greater change in absorption than seen experimentally. Combining this observation with the literature reports on the increase in absorption caused by increasing density (Koizumi, *et al*, 2002), it is clear that whilst this is clearly an important parameter to consider it is not the most influential parameter for fibrous media which are already highly porous.

The last parameter that was identified as having a significant impact on the absorption of this type of material is the fibre diameter. Halving the fibre diameter (from 8µm to 4µm) increases the absorption of Memory Fibre 8 by over 80% (0.42-0.8) at 2500Hz, and approximately 40% (0.7-0.95) at 5000Hz. This change in absorption is even greater when looking at larger fibre diameters (18µm to 10µm for example), which can be seen in Figure 4.5. PE Sample 3 and PE Sample 8 highlight this very well experimentally. This work confirmed that thickness, density, and fibre diameter can all have large effects on absorption values. It was also shown that for these types of materials density has less of an impact than thickness or fibre diameter. From this, the focus switched to the fibre diameters, as in the automotive industry it is more of a challenge to change the material density due to its negative impact on thickness and weight.

In order to confirm the fibre diameter results seen in Figure 4.5 experimentally, the next set of acoustic testing was conducted on raw PET fibres which had not been carded or laid into a nonwoven material. These samples had a density of 480 kg/m^3 and the thickness of the samples was 18 mm ± 2mm. The thickness varied as a result of keeping a constant density despite changing the size and hence density of the fibres. As can be seen in Figure 4.6, the

absorption coefficient is seen to increase with a decrease in fibre diameter. Generally, halving the fibre diameter results in an increase in the acoustic performance by 50% between the frequency range of 1500-4250 Hz. This is a substantial improvement, and that it occurs across such a wide frequency range is very beneficial for applications in the automotive industry, where noise typically covers a wide frequency range due to the variety of sources (Section 2.6 in Chapter 2). The increase in absorption seen with decreasing fibre diameter is attributed to the changes in the material structure that occur as a result of this decrease in diameter. As a result, impeding soundwaves are forced to take a longer narrower and more tortuous path through the material, making a greater number of interactions with the fibres of the material. This increases the amount of frictional and viscous losses, so increasing the amount by which the soundwave is dampened. Figure 4.7 shows that the relationship between fibre diameter and absorption is linear.

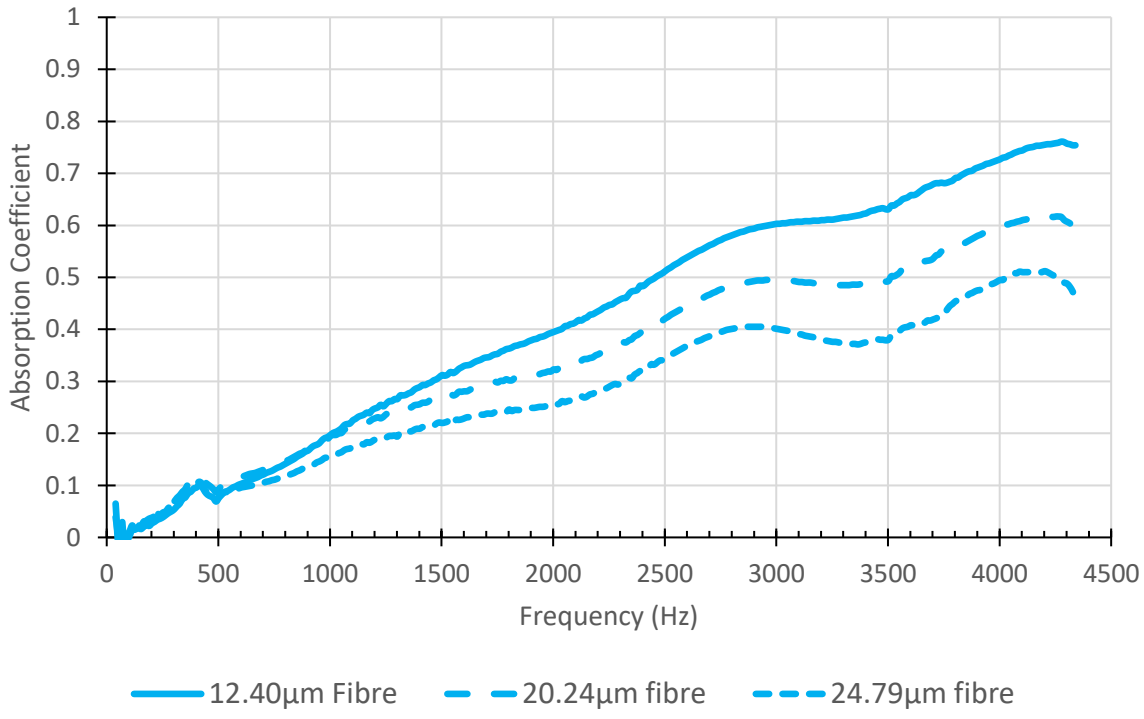

Figure 4.6: Acoustic absorption coefficient for the raw PE fibre samples.

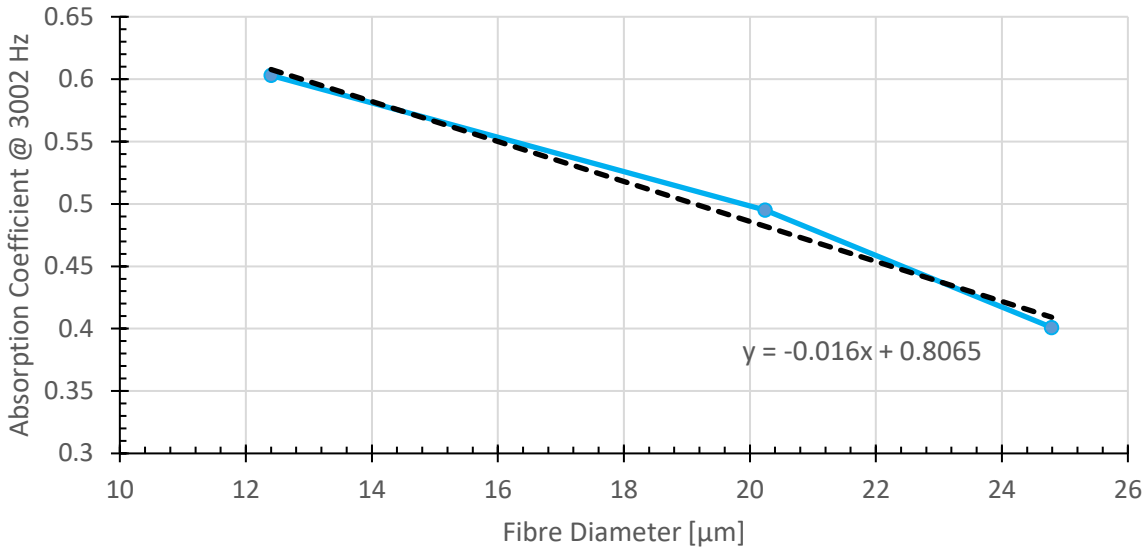

Figure 4.7: Relationship between the fibre diameter and absorption coefficient for the three fibre diameter samples, 12.79 µm, 20.24 µm and 24.79µm, at 3002 Hz.

The next step was to apply this knowledge to a current automotive product and see if that the observed impacts for raw fibres also applied to processed nonwoven materials. In order to achieve this, a current automotive insulation product, Autobloc, was taken and compared to four new blends of varying fibre diameters. A key point to note is that the composition, in terms of percentage of each component and binder fibre, remained consistent with the original Autobloc product. NW blends 1-4 have their compositions and material properties summarised in 3.2 respectively, and the acoustic results for them can be seen in Figure 4.8.

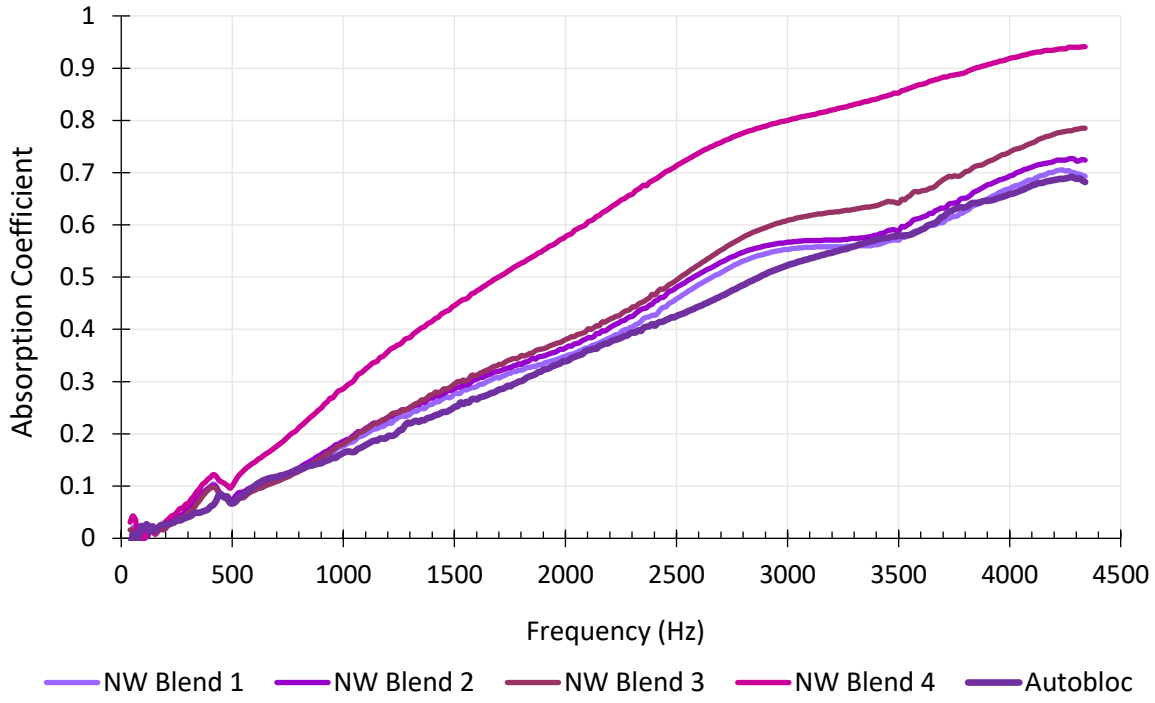

Figure 4.8: Acoustic absorption coefficient for the NW Blend 1-4 samples and standard Autobloc product. Spectra are averaged from three repeats of measurement in a two-microphone impedance tube.

As expected, this acoustic performance of the material is seen to increase with a decrease in fibre diameter (Figure 4.8). The greatest acoustic performance is seen with NW Blend 4, and the greatest increase in absorption performance occurs at a lower frequency range of 2500-3500 Hz, with an average increase of 75% over the standard Autobloc product. Rather interestingly at first glance is that NW Blends 1 and 2 are not significantly different in performance – or much better than the standard Autobloc product. NW Blend 2 has 20% 12.40 µm fibre in place of NW Blend 1's 20% 20.24 µm fibre, and as such from our results in the raw fibre testing we would expect an increase in performance. However, looking at the remainder of the composition we can see that the remaining 80% is composed of 24.79 µm fibre (55% 24.79 µm and 25% binder fibre, which is also 24.79 µm). This means the average

fibre diameter in the two samples is 23.88 µm for NW Blend 1 and 22.31 µm for NW Blend 2. This is a difference of around 6% and so explains the similarities between their performance. NW Blend 4, however, has an average fibre diameter of 17.98 µm which is 24% smaller than the standard Autobloc sample. These materials are all not the same thickness, with the minimal thickness being 16mm and the maximal being 21 mm, so it would be expected that the thicker sample would have increased absorption at lower frequencies. It is observed that the thickest sample, NW Blend 4, has the better low-frequency absorption, but the shape of the absorption curve matches that seen in Figure 4.6, where thicknesses were identical. As such, it appears that the increase in absorption is being dominated by the fibre diameter and not impacted especially by the thickness in the range of thicknesses present.

Whilst it must also be noted that NW Blend 4 has a greater thickness than the standard Autobloc product (22 mm vs 15.07 mm, respectively) this difference is caused by keeping the fibre density consistent between the two samples. Autobloc has a much greater density than NW Blend 4, in addition to a substantially higher mass, but these parameters do not seem to offset the increase in performance offered by the decreased fibre diameter.

From this, it was gathered that the fibre diameter used in a material can be tailored to obtain the desired acoustic performance with some control over material properties like density and thickness – given both can be predicted from the composition of fibre diameters.

The next set of acoustic characterisation was done on two materials which were tested with and without 'skins'. In both cases the skin was a lightweight perforated polyester layer with a thickness of 300 µm and a fibre density of 1380kg/m^3. Figures 4.9 and 4.10 show the impact this skin has on two materials with different material parameters. The two materials presented in Figure 4.9 and 4.10 were made to our specification by John Cotton Group Ltd based on the two most commonly seen thicknesses and densities seen in acoustic absorbers in automobiles. Only 100mm impedance tube data could be recovered for these two materials as the 45mm impedance tube data and other data was lost due to file corruption during a software upgrade in the Jonas Lab at the University of Sheffield.

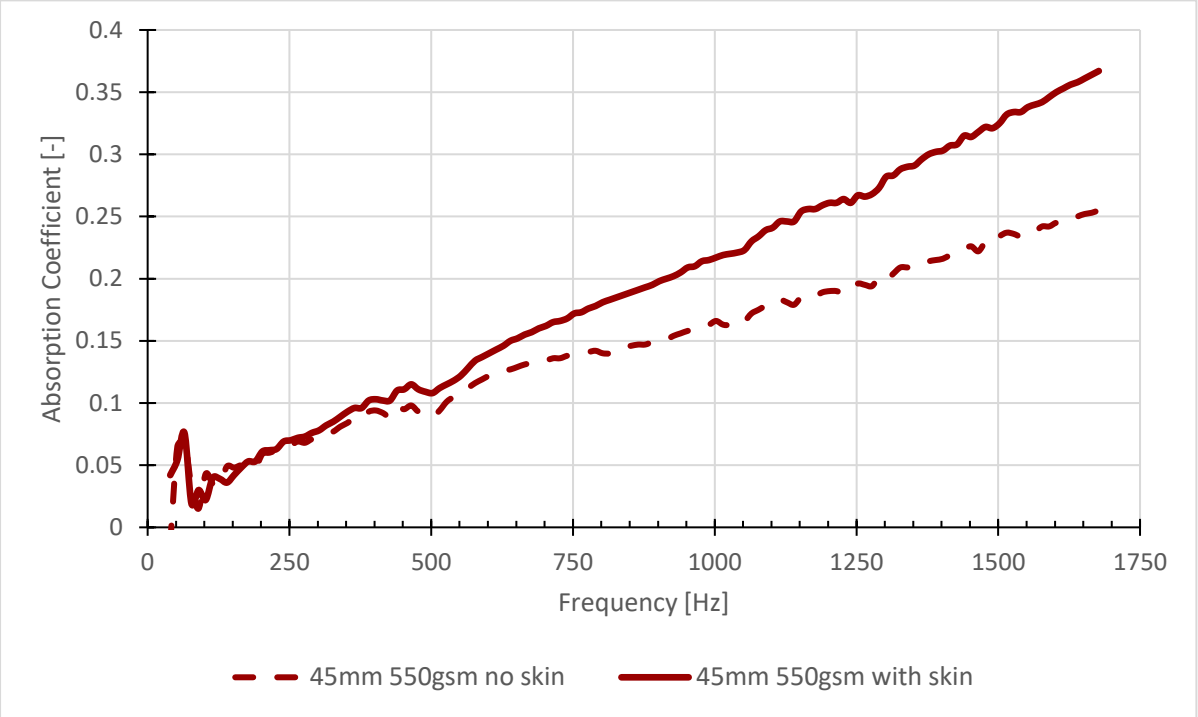

Figure 4.9: Impact on absorption from the addition of a skin to a 45mm thick 550gsm sample.

It can be seen that from as low as 500Hz the skin yields improved absorption properties (20% increase). At 1000Hz there is a 28.4% increase in absorption, rising to a 33.5% increase at 1500Hz. This increase in absorption is believed to be caused by an increase in airflow resistivity by the skin. The skin itself is 300 µm thick and so it is unlikely that this increase in thickness explains the increase in acoustic performance, especially when greater thickness primarily affects low frequency absorption (Ibrahim, Melik, 1978) and the greatest gains seen in Figure 4.9 occur beyond 1000Hz. The skin is also perforated, which means it is not impervious and so the increase in absorption is also not being caused by a mass effect on the surface of the substrate (the 45mm 550gsm sample in this case).

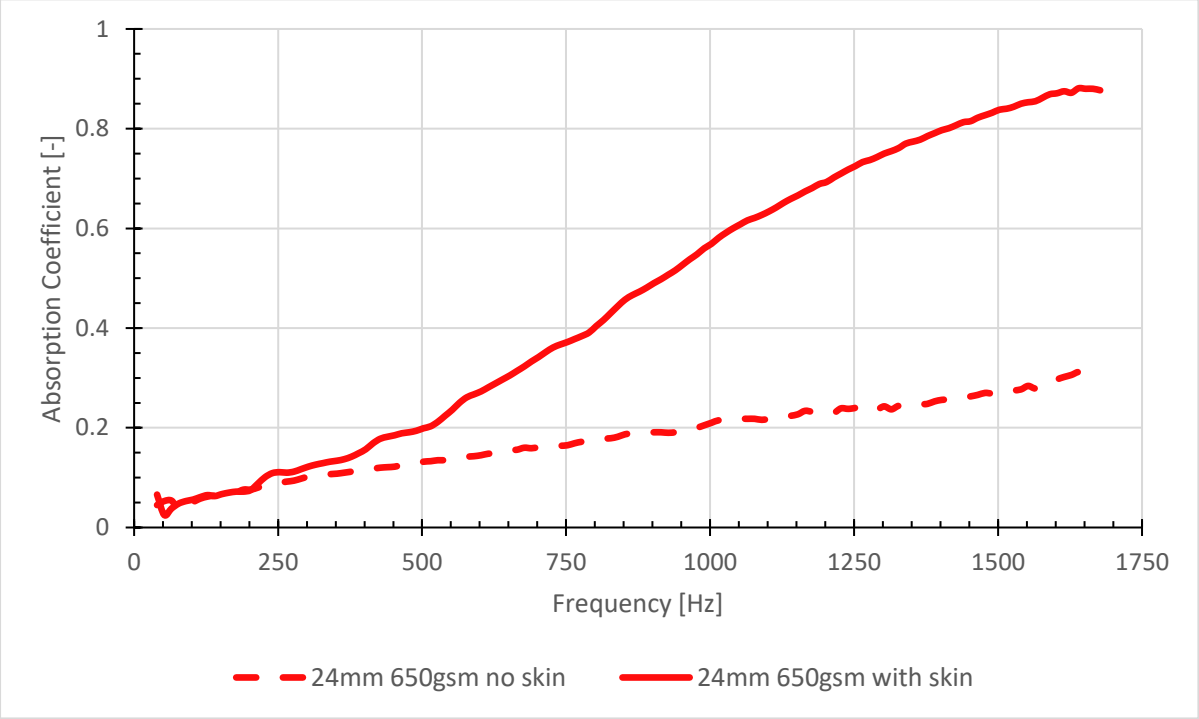

Figure 4.10: Increase in absorption seen through the addition of a skin to a 24mm 650gsm sample.

The performance increase seen through the addition of a skin in Figure 4.10 is even greater than that seen in Figure 4.9. There is a 41.0% increase in absorption at 500Hz, and a 92.2% increase at 1000 - 1650Hz. As with Figure 4.9 the increase in absorption is likely caused by the increased airflow resistivity. A potential reason for the much greater performance seen here is related to impedance matching. This combination of skin and substrate may have better impedance mismatch that the combination in Figure 4.9, leading to greater absorption. It is also possibly related to the thickness; it has been shown that optimal sound absorption occurs when the thickness of a material is roughly equivalent to one-tenth of the wavelength of the impeding sound wave (Coates, Kierzkowski, 2002) with the optimal airflow resistivity of $\sigma \approx 2\rho c$ (Ingard, 1994). The combination of skin and substrate in Figure 4.10 may more closely match this optimal airflow resistivity and thickness value than the combination in Figure 4.9.

4.3 Nonwoven inversion modelling

The next challenge was to accurately model the acoustical properties of these materials to understand better the differences in the absorption performance shown in the previous section (Section 4.2). There are a wide range of models that have been proposed and are used within both academia and industry for application to porous media. The airflow resistivity is directly linked to the acoustic properties of fibrous media so it is a key parameter for consideration when modelling the type of media most commonly used in this work. There have been several studies since the original work by Nichols (Nichols, 1947) which proposed a relationship between airflow resistivity, fibre diameter and density of a material (Yang, *et al*, 2018). Despite this, it is not always obvious how accurately any of the proposed equations or models can represent the true value of flow resistivity within a nonwoven material. There are three typical approaches to modelling within acoustics: (i) theoretical models, (ii) empirical models, and (iii) computational models. Theoretical modelling is based on nature-derived laws, like Newton's law of fluids. These laws are then applied to derive an approximation of the desired parameter. Empirical modelling is based on the relation of experimentally derived data to the desired parameter, for example calculating the value of absorption coefficient from measured airflow resistivity data. Computational modelling normally refers to the inversion of the desired parameter from a measured data set – like the retrieval of non-acoustical parameters like flow resistivity or porosity from acoustical data.

Two studies were carried out during the PhD to look into a variety of both empirical, theoretical and computational models with the aim of assessing which ones would be able to most accurately predict airflow resistivity values of a range of nonwoven fibrous media. The first study looked into the prediction of airflow resistivity for nonwoven media of with a solid core fibres, varying in fibre diameter, densities, and thicknesses. The second study looked into predicting airflow resistivity for nonwoven media composed of different fibre types, just as composite fibres, and hollow fibres.

4.3.1 Model introduction

The first study completed was to look into the accuracy of some models for the prediction of airflow resistivity. It was aimed directly at fibrous nonwoven materials such as those presented earlier in Chapter 3. The type of model used to invert the non-acoustical parameters of materials will typically depend on a variety of factors, such as what parameters are to be recovered, and more intrinsic material parameters such as the fibre diameters, fibre type and homogeneity of the samples. Given that these materials were the focus of the PhD at the time, being able to accurately model them was of great importance. The second study looked into the accuracy of some other models, utilising different approaches to sound propagation theories to again predict the airflow resistivity of nonwoven porous

The models used for the direct estimation of the airflow resistivity in these media were chosen for the experiment reported in the first investigation were: (i) the Bies-Hansen equation; (ii) the Garai-Pompoli equation: and (iii) the Kozeny-Carman equation (Bies, Hansen, 1980; Garai, Pompoli, 2005; Kozeny, 1927; Carman, 1937). The equations for the retrieval of airflow resistivity are presented below.

(i) The Bies-Hansen equation (Bies, Hansen, 1980) is an empirical model relating the airflow resistivity of a material to its fibre diameter and bulk density, i.e.:

$$\sigma d^2 \rho_m^{-K_1} = K_2,$$

Equation 4.10

where σ is the material airflow resistivity [Pa s/m^2], ρ_m is the bulk density of the fibres [kg/m^3], d is the mean fibre diameter in the sample [m], K_1 and K_2 are dimensionless empirical constants – which have values of 1.53 and 3.18x10^{-9} for glassy-fibre materials, respectively (Bies, Hansen, 1980). This equation, presented by Bies and Hansen (Bies, Hansen, 1980), assumes that there is a uniform fibre diameter, which is less than 15 µm, and that there is a negligible binder fibre content within the material.

(ii) The Kozeny-Carman equation is also an empirical model, originating from the 1930s. Originally designed to relate the porosity of granular media to airflow resistivity (Kozeny, 1927; Carman, 1937), it has since been adapted to estimate the airflow resistivity of fibrous textiles, especially polymer fibres (Pelegrinis, *et al*, 2016). This model was adapted by taking into consideration the density of the sample, and correcting for it by relating the fibre density (represented by the particle size, d, in the Kozeny-Carman equation) to the bulk density as seen in Equation 4.12 (Pelegrinis, *et al*, 2016).

$$\sigma = \frac{180\mu(1-\phi)^2}{d^2\phi^3}$$

Equation 4.11

$$d = \left(\rho_m - d_f\right)^2$$

Equation 4.12

where μ is the dynamic viscosity, a constant derived from Poiseuille's equation of laminar flow for a liquid (assigned the value of 1.81x10^{-5} Pa·s for air, used in this work). In this case, d is the particle size, which was assumed to be equivalent to the fibre diameter and ϕ the porosity. The porosity can be calculated from the ratio of bulk material density, ρ_m, to fibre density, ρ_f, as shown in Equation 3.6 in Chapter 3.

From the above two equations (Equations 4.11 and Equation 3.6) it is apparent that the airflow resistivity of a sample is inversely dependent to the square of the fibre diameter.

(iii) The Garai-Pompoli equation (Garai, Pompoli, 2005) is another empirical model which, like the Bies-Hansen equation, relates airflow resistivity to the fibre diameter and fibre density. This equation was born out of experiments by Garai and Pompoli and based on the Bies-Hansen equation to predict the airflow resistivity of polyester-based fibrous materials. It was found that the Bies-Hansen equation can significantly underestimate the airflow resistivity values of some types of fibrous media. Garai and Pompoli later suggested that this

was as a direct result of the polyester fibres they were studying having a larger fibre diameter than the fibreglass samples originally modelled by Bies and Hansen. In the Bies-Hansen equation, fibre diameter was assumed to be homogenous and of a size smaller than 15µm. This is not the case for most commercially used polyester fibres, which means that the constants proposed in the Bies and Hansens work were not sufficiently accurate to predict airflow resistivity of polyesters.

Garai and Pompoli proposed a new model, which they refer to as the "new resistivity model (NRM)" (Garai, Pompoli, 2005).

$$\sigma = A\rho_m^B$$

Equation 4.13

where

$$A = K_2\langle d\rangle^{-2}$$

Equation 4.14

and

$$B = K_1$$

Equation 4.15

Garai and Pompoli proposed new values for the constants relating to fibre diameter, labelled K_1 and K_2 in equation 4.14 and 4.15, respectively. They reported that values of $A = 25.989$ and $B = 1.404$ yielded the best fit for polyester fibres, and as such those values were used throughout the scope of this PhD thesis (Garai, Pompoli, 2005). It was also reported that an analysis of four different types of polyester materials with varying surface treatments and varying binder fibre percentage that no noticeable impact on the precision of their equation was observed.

The airflow resistivity values predicted with these three models were then compared to those deduced via two mathematical models, which are able to invert the airflow resistivity of fibrous media from their acoustical properties. The method for determining the acoustic properties can be seen in Section 4.2 in Chapter 4. The mathematical models were the Miki model (Miki, 1990), and the Padé approximation model (Horoshenkov, *et al*, 2016), and a summary of each follows.

Inversion modelling is essentially the retrieval of unknown material parameters from their relationship with known material parameters. Within acoustics it is common to predict the surface impedance, $z(f)$, of a hard-backed porous material, with a thickness, h, from known values of characteristic impedance, z_b, and wavenumber, k_b, as seen in Equation 4.16:

$$z(f) = z_b \coth(-ik_b h)$$

Equation 4.16

The surface impedance data is normally used instead of the absorption data as surface impedance measurements are more sensitive to calibration effects. It is possible to obtain a good absorption curve with a comparably poor calibration. This is not the case with impedance, and as such using the impedance data ensures that the material has been accurately measured acoustically and the inverted values are as accurate as possible.

The airflow resistivity of the same material can then be inverted by finding the minimum of the function defined by Equation 4.17, where $z^{exp}(f_n)$ is the measured surface impedance spectrum, $z^{th}(f_n, \sigma)$ is the predicted surface impedance spectrum, and f_n is the range of frequencies at which the impedance data were measured.

$$F(x) = \sum_{n=1}^{N} \{z^{exp}(\, f_n) - z^{th}(f_n, \sigma)\} \rightarrow min$$

Equation 4.17

In this thesis, the minimisation problem was solved computationally using a Nelder-Mead optimisation algorithm (Nelder, Mead, 1965). The Nelder-Mead optimisation algorithm is a pre-existing function in Matlab, which facilitated ease of modelling. A recent publication has also justified its use by showing that models run with this optimisation give realistic results that agree with both direct non-acoustic measurements and results from other more common optimisations, such as the Bayesian optimisation (Horoshenkov, *et al*, 2019). Then the inversion was carried out using either the Miki model or the Padé approximation model initially (Miki, 1991; Horoshenkov, *et al*, 2016).

First published in 1989, the Miki model was suggested to be an improvement to the empirical model of Delany and Bazely (Delany, Bazely, 1970). The proposed modifications to the Delany-Bazely model enabled a greater accuracy and better causality across a broader frequency range than those originally attained with the Delany-Bazley model (Miki, 1989). According to the Miki model, the characteristic impedance of porous media can be calculated accurately from:

$$z_b(f) = \mathrm{r}(f) + ix(f)$$

Equation 4.18

where

$$r(f) = 1 + 0.070\left(\frac{f}{\sigma}\right)^{-0.632}$$

Equation 4.19

$$x(f) = 0.107\left(\frac{f}{\sigma}\right)^{-0.632}$$

Equation 4.20

Miki also modified the complex wavenumber for sound propagation in porous media, now represented as:

$$k_b(f) = \alpha(f)i + \beta(f)$$

Equation 4.21

where

$$\alpha(f) = \frac{2\pi f}{c}\left[0.160\left(\frac{f}{\sigma}\right)^{-0.618}\right]$$

Equation 4.22

$$\beta(f) = \frac{2\pi f}{c}\left[1 + 0.109\left(\frac{f}{\sigma}\right)^{-0.618}\right]$$

Equation 4.23

In equations 4.17 – 4.22, f is the frequency of the sound wave [Hz], c is the speed of sound in air [m/s], and $i = \sqrt{-1}$ (Miki, 1989).

Proposed in 2016, the Padé approximation model is a new model that approximates a viscosity correction function that affects both the characteristic impedance and wavenumber in a porous material with non-uniform pores (Horoshenkov, *et al*, 2016). This viscosity correction function corrects for deviations from Pouseille's Law with changes with frequency. Viscosity in porous media is frequency dependent, with two limits: (i) when the size of the boundary layer is greater or comparable to the fibre diameter, and (ii) when it is much less or comparable to the fibre diameter, introducing inertial effects on rigid skeleton. The characteristic impedance and wavenumber are represented by the following equations:

$$z_b(\omega) = \sqrt{\tilde{\rho}_b(\omega)/\tilde{C}_b(\omega)}$$

Equation 4.24

and

$$k_b(\omega) = \omega\sqrt{\tilde{\rho}_b(\omega)\tilde{C}_b(\omega)},$$

Equation 4.25

where $\tilde{C}_b(\omega) = 1/\tilde{K}(\omega)$ describes the bulk complex compressibility, $\tilde{K}(\omega)$ describes the dynamic bulk modulus of air in the pores, $\tilde{\rho}_b(\omega)$ describes the dynamic density of the air in the pores, and $\omega = 2\pi f$ is the circular frequency.

The Padé approximant theory is derived from the expansion of a given function as a ratio of two power series, determining coefficients of the numerator and denominator. A power series is best described as an infinite series of the expression:

$$\sum_{n=0}^{\infty} a_i z^n.$$

Equation 4.26

In the work by Horoshenkov *et al*, Padé approximants are used for expressing the dynamic density (Equation 4.27) and complex compressibility (Equation 4.30).

$$\tilde{\rho}_x(\epsilon_\rho) = 1 + \epsilon_\rho^{-2}\tilde{F}_\rho(\epsilon_p),$$

Equation 4.27

where the viscosity correction term, $\tilde{F}_\rho(\epsilon_p)$, is given by a Padé approximant so that:

$$\tilde{F}_\rho(\epsilon_p) = \frac{1 + \theta_{\rho,3}\epsilon_\rho + \theta_{\rho,1}\epsilon_\rho}{1 + \theta_{\rho,3}\epsilon_\rho}$$

Equation 4.28

where $\epsilon_\rho = \sqrt{-i\omega\rho/\sigma_x}$.

In the above Padé approximation (Equation 4.27) the coefficients $\theta_{\rho,1} = \frac{1}{3}$, $\theta_{\rho,2} = \sqrt{1/2}e^{1/2(\sigma_s \log 2)^2}$, and $\theta_{\rho,3} = \theta_{\rho,1}/\theta_{\rho,2}$ are positive real numbers.

$$\tilde{C}_x(\epsilon_c) = \frac{1}{\gamma P}\left(\gamma - \frac{\gamma - 1}{1 + \epsilon_c^{-2}\tilde{F}_c(\epsilon_c)}\right)$$

Equation 4.29

where

$$\tilde{F}_c(\epsilon_c) = \frac{1 + \theta_{c,3}\epsilon_c + \theta_{c,1}\epsilon_c}{1 + \theta_{c,3}\epsilon_c}$$

Equation 4.30

The coefficients in Equation 4.30 are $\theta_{c,3} = \theta_{c,1}/\theta_{c,2}$, $\theta_{c,2} = \sqrt{1/2}e^{3/2(\sigma_s \log 2)^2}$, $\theta_{c,1} = \frac{1}{3}$ and the frequency dependent parameter is $\epsilon_c = \sqrt{(-i\omega\rho N_{Pr}/\sigma_x')}$.

In Equation 4.30, σ_x is the air flow resistivity of a single pore and σ_x' is the thermal flow resistivity in the pore. The thermal flow resistivity is commonly modelled as thermal permeability, an expression which describes the thermal exchanges between the frame of a material and the impeding and reflected soundwaves, primarily affecting low frequency behaviour (Lafarge, *et al*, 1997). It is the thermal equivalent of Darcy's Law (Darcy, 1856), which describes the relationship between the pressure gradient at either end of porous media with a fluid flowing through it. N_{Pr} is the Prandtl number – defined as the ratio of viscous permeability to thermal permeability and was calculated to have a value of 1.680 for a typical σ_s value of 0.3. γ is the specific heat ratio, and σ_s is the standard deviation of the log-normal distribution of the material pore size. Generally, for fibrous media with a relatively high porosity $\sigma_s \approx 0$ (Horoshenkov, *et al*, 2016), which would mean that the viscous and thermal permeabilities were equal.

The equations presented above are for single pore materials, and as such bulk materials with a plurality of pores will require some parameters to be changed so that the effective flow resistivity is expressed as:

$$\sigma = \frac{\sigma_x \alpha_\infty}{\phi}$$

Equation 4.31

and the effective bulk density expressed as:

$$\tilde{\rho}_b = \frac{\alpha_\infty}{\phi} \tilde{\rho}_x$$

Equation 4.32

with

$$\epsilon_\rho = \sqrt{\frac{-i\omega\alpha_\infty\rho}{\phi\sigma}}$$

Equation 4.33

$\tilde{C}_x$ for a single pore must also be replaced, becoming:

$$\tilde{C}_b = \phi \cdot \tilde{C}_x$$

Equation 4.34

where

$$\epsilon_c = \sqrt{\frac{-i\omega\alpha_\infty\rho}{\phi\sigma'}}$$

Equation 4.35

and

$$\sigma' = \frac{\sigma_x{}' \cdot \alpha_\infty}{\phi}$$

Equation 4.36

The equations for the characteristic impedance and wavenumber can be used to predict the surface impedance of a hard-backed porous specimen of thickness, h using Equation 4.16. In this case, the flow resistivity of the fibrous material specimen can be inverted by finding the minimum Equation 4.17.

There are other theoretical and empirical models that can be used to predict the airflow resistivity of fibrous media. These can be segregated into capillary channel theoretical

models, drag force theoretical models, and empirical models. The capillary channel theoretical models are based on works completed by Hagen-Poiseuille and later Kozeny-Carman (Kozeny, 1927; Carman, 1937). Within this theory, it is assumed that the flow through a porous material behaves in the same was as conduit flow between parallel cylindrical tubes, and so is subjected to side friction as it moves through the material.

In the case of drag force theory, it assumes that the fibres making up the walls of the pores are rigid obstacles to flow. As such, each fibre that is encountered during the flow through the material adds resistance (or a 'drag'), and the sum of these 'drags' is assumed to be the total resistance to flow within the material (Scheidegger, 1963). The empirical models estimate flow resistivity based on the values of other measureable material characteristics, such as density, fibre diameter distribution, and fibre orientation. A summary of each of the models and their equations can be found in the published work (Yang, *et al*, 2018), whilst the equations used to estimate airflow resistivity can be seen in Tables 4.3 to 4.5:

Model	Airflow resistivity calculation
Kozeny-Carman (Kozeny, 1927; Carman, 1937)	$\sigma = \frac{180\mu(1-\phi)^2}{d^2\phi^3}$
Davies (Davies, 1953)	$\sigma = \frac{64\mu(1-\phi)^{1.5}(1+56(1-\phi)^3)}{d^2}$
Lind-Nordgren (Lind-Nordgren, Goransson, 2010)	$\sigma = \frac{128\mu(1-\phi)^2}{d^2\phi}$
Doutres (Doutres *et al,* 2011)	$\sigma = \frac{128\mu(1-\phi)^2}{d^2}$
Pelegrinis (Pelegrinis, *et al*, 2016)	$\sigma = \frac{180\mu(1-\phi)^2}{d^2}$

Table 4.3: Airflow resistivity equations based on the capillary channel flow theory.

Model	Airflow resistivity calculation
Langmuir (Langmuir, 1942)	$\sigma = \frac{16\mu(1-\phi)}{d^2\left[-\ln(1-\phi) - 1.5 + 2(1-\phi) - \frac{(1-\phi)^2}{2}\right]}$
Hasimoto (Hasimoto, 1959)	$\sigma = \frac{32\mu(1-\phi)}{d^2[-\ln(1-\phi) - 1.476]}$
Kuwabara (Kuwabara, 1959)	$\sigma = \frac{32\mu(1-\phi)}{d^2\left[-\ln(1-\phi) - 1.5 + 2(1-\phi) - \frac{(1-\phi)^2}{2}\right]}$
Happel (Happel, 1959)	For flow parallel to fibre direction: $\sigma = \frac{72\mu(1-\phi)}{d^2[-\ln(1-\phi) - 3 + 4(1-\phi) - (1-\phi)^2]}$ For flow perpendicular to fibre direction: $\sigma = \frac{72\mu(1-\phi)}{d^2\left[-\ln(1-\phi) - \frac{1-(1-\phi)^2}{1+(1-\phi)^2}\right]}$

Tarnow (Tarnow, 1996)	For flow parallel to square lattice: $$\sigma = \frac{16\mu(1-\phi)}{d^2[-\ln(1-\phi)+0.5-2\phi]}$$ For flow parallel to random lattice: $$\sigma = \frac{16\mu(1-\phi)}{d^2[-1.280\ln(1-\phi)+0.526-2\phi]}$$ For flow perpendicular to square lattice: $$\sigma = \frac{16\mu(1-\phi)}{d^2\left[\{\ln(1-\phi)^{-\frac{1}{2}}\}-0.5\phi-0.25\phi^2\right]}$$ For flow perpendicular to random lattice: $$\sigma = \frac{16\mu(1-\phi)}{d^2[-0.640\ln(1-\phi)+0.263-\phi]}$$

Table 4.4: Airflow resistivity equations based on the drag force theory.

Model	Airflow resistivity calculation
Bies-Hansen (Bies, Hansen, 1980)	$\sigma = \frac{3.18\text{x}10^{-9}\rho_m^{1.53}}{d^2}$
Garai-Pompoli (Garai, Pompoli, 2005)	$\sigma = \frac{2.83\text{x}10^{-8}\rho_m^{1.404}}{d^2}$

Manning-Panneton (Manning, Panneton, 2013)	For mechanically bonded fibres: $\sigma = \frac{2.03\text{x}10^{-8}\rho_m^{1.485}}{d^2}$ For resin bonded fibres: $\sigma = \frac{3.61\text{x}10^{-9}\rho_m^{1.804}}{d^2}$ For thermally bonded fibres: $\sigma = \frac{1.94\text{x}10^{-8}\rho_m^{1.516}}{d^2}$

Table 4.5: Airflow resistivity equations based on empirical data.

It must be noted that these two studies did not encompass every model currently being used for the purpose of determining flow resistivity in a material. The goal of these studies was instead to try and utilise some of the more commonly used models in the textile industry. There are also some popular models missing from the list, most notably the Johnson-Champoux-Allard (JCA) model (Allard, Atalla, 2009). The JCA model was not used in this work, as the model requires the knowledge of a significant number of material parameters, many of which – such as the thermal permeability, or the viscous and thermal characteristic lengths – are either difficult or time consuming to measure. It has been demonstrated (Horoshenkov, *et al*, 2016) that relating these parameters to more routinely characterised parameters like the pore size distribution can yield comparable or better results.

The porosity, ϕ, of the fibrous samples was measured independently and it was used in the inversion process. It is easy to show that for this type of fibrous media with low density and high porosity the tortuosity, α_∞, is close to unity within 1-3%. In this case the computational models become relatively independent of porosity and therefore, this parameter was set to one to enhance the convergence of computation during this work.

As mentioned, the nonwoven material samples for single-component fibres were provided by John Cotton Group Ltd. Tables 4.6 and 4.7 show the composition of these materials and some of their material parameters. In these tables, the nomenclature “PET” refers to polyester, and “binder” stands for a polyester binder fibre. Images of the samples used can be found in Appendix A. The fibre composition was taken into account to generate an average fibre diameter based on the weighted proportion of each fibre in the blend. The fibre diameter of the samples NW Sample 3 and NW Sample 4 was unknown, as these samples were made from recycled materials, and no denier value was provided by John Cotton Group Ltd. We were also unable to obtain a value for the fibre diameter through the measurement of the samples. These samples are composed of an inconsistent variety of diameters, which were distributed randomly throughout the sample, making it a challenge to get a representative average value of diameter. Despite not being able to get a reliable average, the range of fibre diameters seen was typically between 12 μm and 64 μm.

Measurement of the material characteristics such as bulk density, porosity, and thickness were all completed in the Jonas Lab at the University of Sheffield using the characterisation methods outlined in Chapter 3. In each case the thickness values have been rounded to the nearest millimetre to minimise any inaccuracies caused by partial compression of the samples by the callipers. The porosimeter had an accuracy of 1% (Horoshenkov, *et al*, 2007). Given the accuracy of the porosimeter, any deviations in the value of porosity were likely to be negligible and have minimal effect on the calculated values of airflow resistivity for the majority of models used in these two studies. One important observation to note with the drag force theory models is that they all take the natural log of one minus the porosity, $\ln(1-\phi)$. In this instance, the 1% error associated with our porosimeter could become substantially larger. For example, if the measured value of porosity is 0.98, then $\ln(1-0.98)=-3.91$. A 1% error attached to this value of porosity would then mean the porosity could range from 0.9702 to 0.9898. Taking the upper boundary for our example, $\ln(1-0.9898=-4.59)$ which is a difference of 16%.

As an example of how the porosimeter accuracy affects models not based on drag force theory, consider the Padé approximation model. Changing the porosity value of Sample 1 to 0.98, from 0.96 (a value much greater than the differences encountered during the measurements, see Table 4.8), would then change the value of airflow resistivity as evaluated by the Padé approximation model to 27242 Pa·s/m² from its original value of 27243 Pa·s/m², or 0.004%. The experimental error associated with this work was 10%. This experimental error was chosen as the value of bulk density for a sample can vary by a similar amount due to several uncertainties during measurement due to fibre compression, variation in fibre density, errors associated with the averaging of the weighted fibre diameter in media with multiple fibre diameters present, and any inaccuracies or noise present during the acquisition of the acoustical data which may have given slightly erroneous data.

Sample	Fibre composition
Sample 1	25% 20.24 µm PET, 55% 24.79 µm PET, 20% binder
Sample 2	52% 20.24 µm PET, 20% 13.19 µm PET, 28% 20.24 µm PET binder
Sample 3	10% 20.24 µm PET, 75% rags, 12% 39.20 µm PET, 3% binder
Sample 4	15% 20.24 µm PET, 50% cotton, 17.5% 6d 24.79 µm PET, 17.5% binder
Sample 5	75% 26.20 µm PET, 25% binder
Sample 6	75% 12.40 µm PET, 25% binder
Sample 7	75% 12.40 µm PET, 25% binder
Sample 8	40% 12.39 µm PET, 35% 39.20 µm PET, 25% binder

Table 4.6: The material compositions of the eight samples used in the reported experiments. The percentages show the relative composition of fibres with a particular fibre diameter value. The binder fibre has a fibre diameter of 20.24 µm.

Sample	d_f [µm]	ρ_f [kg/m^3]	ρ_m [kg/m^3]	ϕ [-]	h [mm]
Sample 1	23.66	1381	60.35	0.96±0.0010	34±0.5
Sample 2	18.83	1379	32.68	0.98±0.0007	46±0.4
Sample 3	N/A	1378	43.82	0.97±0.0009	45±0.3
Sample 4	N/A	1383	27.94	0.98±0.0005	50±0.2
Sample 5	24.71	1383	21.71	0.98±0.0010	47±0.3
Sample 6	14.36	1379	24.68	0.98±0.0005	42±0.3
Sample 7	14.36	1379	38.47	0.97±+0.0004	43±0.5
Sample 8	23.74	1383	17.57	0.99±0.0003	54±0.4

Table 4.7: The key material data for the eight samples used in the reported experiments.

The measured values for surface impedance and other non-acoustical parameters for the nonwoven materials described in Table 4.7 were then substituted into Equation 4.17 to solve the minimisation problem, making use of the standard MATLAB minimisation subroutine 'fminsearchbnd ( )' (Matworks, 2016). The subroutine was applied in the frequency range of 200-1500 Hz. The lower boundary of 200 Hz was applied to avoid any inaccuracies caused by phase mismatch or structural vibrations in the acoustic impedance tube, whilst the upper boundary is governed by the limitations of the frequency range that can be swept in the 100mm impedance tube. There are slightly fewer losses in the 100mm impedance tube than are present in the 45mm impedance tube, so wherever there was sufficient material available the 100mm impedance tube was used preferentially. In both cases the root mean square errors were generated from the difference between the predicted and measured absolute values of the surface impedance. Figure 4.11 presents the measured and modelled (through the minimisation algorithm, Equation 4.17) real and imaginary parts of the surface impedance for Sample 1. The root mean square error between the measured

and predicted value of the normalized surface impedance for all material samples was below 9.6%, and had an average of 1.6% for all samples. These models use the minimisation algorithm to fit the non-acoustical parameters and hence modelled value of surface impedance to the experimentally obtained data. As such, a good fit between the measured and modelled results means the values retrieved by the model are robust.

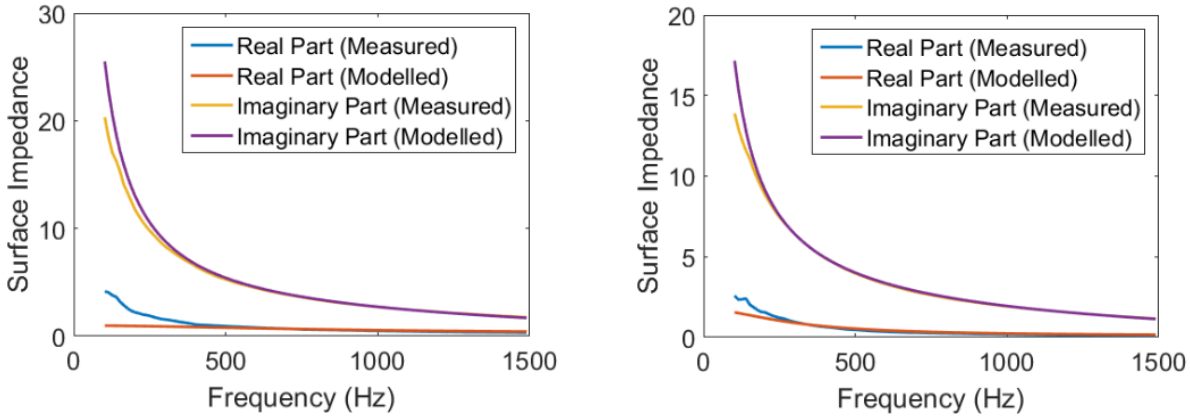

Figure 4.11: Examples of the measured and predicted (via optimisation) values of the normalised surface impedance (-) for the Miki (left) and Padé approximation (right) models for the blended samples found in Table 4.2.

The airflow resistivity was also measured directly using an AFD AcoustiFlow 300, supplied by Akustik Forschung Dresden, and used alongside their AFD 311 software package (Akustik Forschung Dresden, 2017) via a direct-airflow method, as outlined in the ISO9053 (ISO9053, 1991). Five specimens for each sample were tested and the airflow resistivity value was taken as an average of these five specimens.

Figure 4.12 presents a summary of the measured, inverted and predicted flow resistivity data for all fibrous samples studied in the first investigation. Figure 4.13 shows the average

percentage error of each model across all samples. There is generally limited agreement between the flow resistivity predicted by the three equations (Section 4.2.1 to 4.2.3) which make use of fibre diameter and material density data. The maximum difference of 88% is observed in the case of the Bies-Hansen equation applied to Sample 8 material data. The Bies-Hansen equation consistently underestimates the airflow resistivity when compared to the results from the Garai-Pompoli and Kozeny-Carman equations. The Garai-Pompoli equation tends to overpredict the flow resistivity except in the case of Sample 8 material. The Kozeny-Carman equation tends to underpredict the flow resistivity except in the case of Sample 1 material. The maximum difference of -75% is between the flow resistivity predicted by the Kozeny-Carman equation and the measured value for Sample 8 material. The maximum difference of 59% is between the flow resistivity predicted by the Garai-Pompoli equation and the measured value for Sample 2 material.

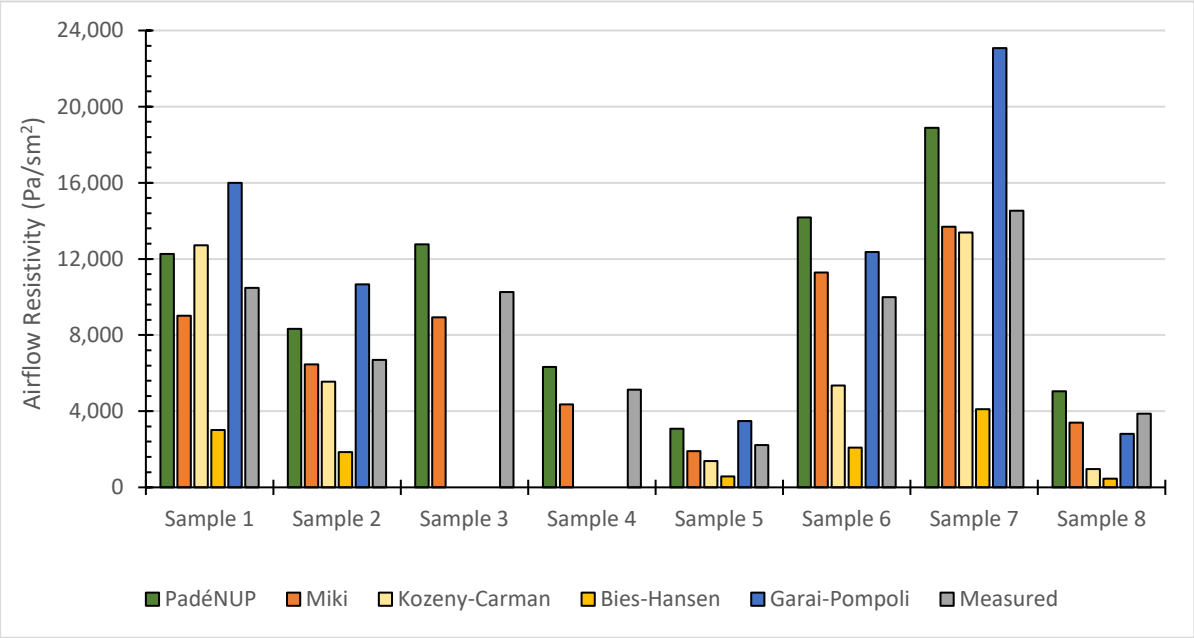

Figure 4.12: A summary of the measured, inverted and predicted flow resistivity values for the material samples. The inverted values are represented by the PadeNUP and Miki models; predicted values the Kozeny-Carman, Bies-Hansen, and Garai-Pompoli equations.

The values of airflow resistivity inverted by the Padé approximation and Miki models more closely fit the measured values than those obtained from the empirical and theoretical equations covered above. The maximum difference of 42% is between the flow resistivity inverted with the Padé approximation (PadéNUP) and that measured for Sample 6. The flow resistivity values inverted with the Miki model is much closer to their measured equivalents. The maximum difference of 15% is for the case of Sample 4 material. For the other materials, the differences between the value of the flow resistivity inverted with the Miki model and its measured value are much less. The maximum mean error produced by the Miki model occurs during the inversions of Sample 3, with a value of 8.8%. The maximum mean error produced by the Padé approximation model occurs during the inversions of Sample 1, with a value of 9.3%.

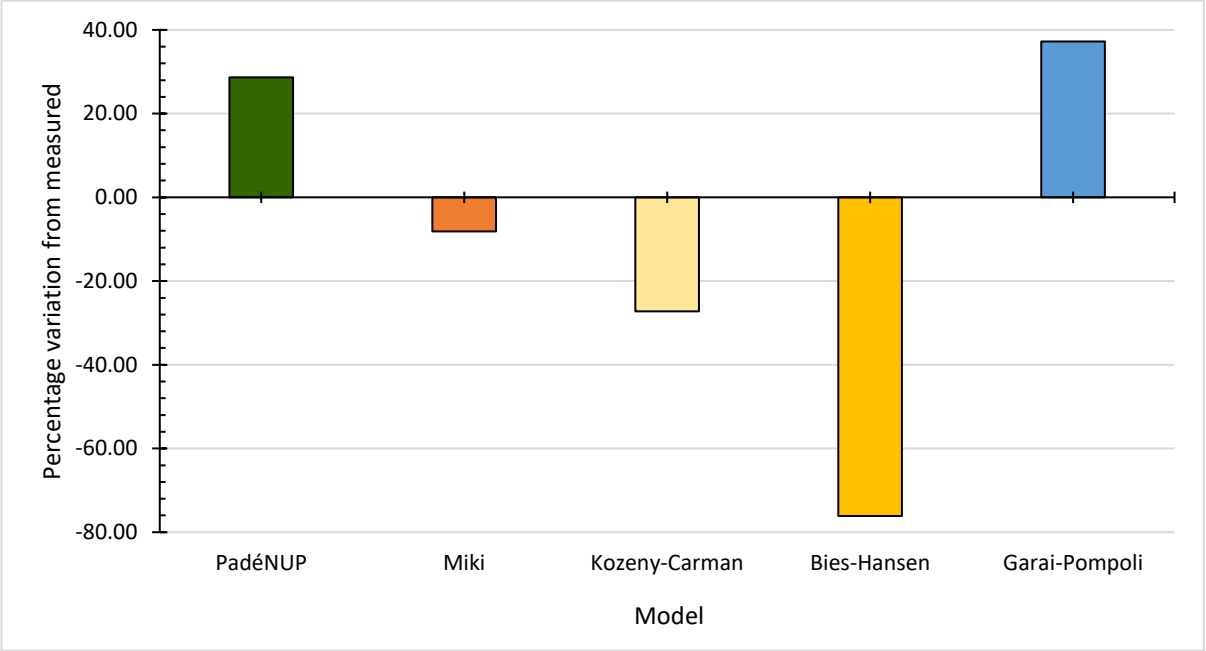

Figure 4.13: A comparison of the inverted (Miki, PadeNUP) and predicted (Kozeny-Carman, Bies-Hansen, Garai-Pompoli) values of airflow resistivity, presented as the average percentage variance from the measured value from all material samples.

From these results, it could be concluded that the Miki model is superior in terms of the flow resistivity inversion when compared to the Padé approximation model, Bies-Hansen, Kozeny-Carman and Garai-Pompoli equations. The greater accuracy of the Miki model is derived from the use fewer parameters, so it is more stable in the parameter inversion process. The pore structure of fibrous media with high porosity is also relatively uniform so that the convergence of the Miki model for this type of media is better than that of the pore distribution model based on the Padé approximation. Among the three equations used to predict flow resistivity, the Kozeny-Carman models appear more accurate than the Bies and Hansen and Garai-Pompoli equations.

A suspected reason for a relatively limited performance of the three equations is that these equations are only valid for media with a uniform fibre diameter. In the case of the Bies-Hansen equation, it is assumed that the fibre diameter is a uniform size smaller than 15µm, and that there is limited binder fibre present in the material (Bies, Hansen, 1980). All of the materials present in this sample make use of multiple fibre diameters and have an average composition of 20% binder fibre. Similarly, only two of the eight materials tested have average fibre diameters lower than 15µm, which means that the coefficients used by this model will be incorrect. This same conclusion was reached by Narang, when investigating polyester based materials with fibre diameters ranging from 12 µm to 26 µm, stating that the airflow resistivity of polyester based materials did not appear to follow the same empirical relationships used in the case of fibreglass materials (Narang, 1995). The Garai-Pompoli model recalculated the value of those coefficients to best fit that of polyester fibres with diameters ranging from 18µm to 45 µm (Garai, Pompoli, 2005). As a result of this, and given this range covers all the fibre diameters present in the test samples, it would be reasonable to assume that this model would be more accurate than the Bies-Hansen model upon which it is based, which was found to be correct, with the Garai-Pompoli model having an error half the size of the Bies-Hansen model. However, it still differs from the measured value by an average of 37%. Whilst this could be due to the presence of multiple fibre diameters, it is perhaps worth noting that the materials used in the original paper by Garai and Pompoli had airflow resistivity values which are significantly lower than the materials used in this study (Garai,

Pompoli, 2005). Furthermore it does not report on the porosity of those materials. As such it is hard to conclude why there is such a disparity between the results reported by Garai and Pompoli and the results seen in this study. The relatively good performance of the Kozeny-Carman equation echoes the results seen in literature (e.g. Pelegrinis, *et al*, 2016), which is likely due to its consideration of material density alongside fibre diameter.

Considering ease of application, all the models and equations have some drawbacks. The Bies-Hansen, Kozeny-Carman, and Garai-Pompoli equations have a few significant drawbacks such as the requirement to know several material parameters in advance of the experiment. Some parameters, e.g. fibre diameter and its distribution, can be difficult to measure or to predict. Conversely, the Miki and Padé approximation models can be run to a good accuracy without the knowledge of any non-acoustical parameter other than the material's thickness. The main parameter used in the inversion process with both Miki and Padé approximation models is the airflow resistivity. As such, it would be reasonable to assume that this value must be known, but these models are able to invert the value of airflow resistivity from the acoustical data, and so it is not required to be known. Of course, this does require that the samples be tested acoustically, which is the biggest drawback of the inversion models as the equipment for this is far from common outside of academia.

4.3.2 Accuracy of some models for multicomponent fibrous nonwovens

After the completion of the first study, a further study was completed in collaboration with Tao Yang, from the Technical University of Liberec. This study looked at the accuracy of models for the retrieval of airflow resistivity from the multicomponent polyester fibre materials shown in Table 3.4 (Yang, *et al*, 2018). This study conducted a detailed analysis of the accuracy of thirteen theoretical and empirical models when compared to measured values of airflow resistivity attained using the standard ISO9053 direct airflow method (ISO9053, 1991). The samples being evaluated were composed of three different types of fibres: monofilament PET, hollow-fibre PET, and bi-component PET. In this study the three types of different fibres mentioned were prepared as a total of 3 samples, with an average of 6 ± 1 specimens tested from each sample. The material parameters and their synthesis

methods were discussed in Section 3.1.1 and their values were listed in Table 3.4 in Chapter 3.

In order to evaluate the accuracy of each of the models, the predicted values of airflow resistivity were compared to the measured values retrieved using the AcoustiFlow 300. Their relative accuracy was assessed by comparing the relative prediction errors. In the case of the capillary channel theoretical models, shown in Figure 4.14, the Doutres and Lind-Nordgren models predicted similar values of airflow resistivity (Doutres *et al,* 2011). The only difference between the two models is that the Lind-Nordgren model features the porosity in the denominator (Lind-Nordgren, Goransson, 2010). When considering fibre diameters in the range of 18µm - which is the average fibre diameter present in the multicomponent materials used in this study, the addition of porosity to the denominator will make very little difference when the porosity is close to a value of 1, as can be seen in Table 3.4 of Chapter 3. This may explain why they have near identical results, and also explains why they start to differ at higher densities; samples at higher density also had a lower value of porosity, decreasing the size of the denominator in the models.

The error associated with the Kozeny-Carman model had a maximum value of 12.3%, whilst the maximum error for the Pelegrinis *et al* model is 8.4%. That the Kozeny-Carman model agreed closely with the adaption proposed by Pelegrinis *et al* which is not surprising; the original paper (Pelegrinis, *et al*, 2016) concluded that it was able to retrieve the airflow resistivity values from absorption data to within 10% of values predicted by the Kozeny-Carman equation. The adaption also proposed changes derived from Poiseuille's equation which account for flow resistivity, fibre diameter, and bulk material density (Pelegrinis, *et al*, 2016). The difference in predictions from the Doutres/Lind-Nordgren models and the Kozeny-Carman/Pelegrinis models is a result of the two sets of models using different regression coefficients in the flow resistivity equations: 180 for the Kozeny-Carman/Pelegrinis models; and 128 for the Doutres/Lind-Nordgren models.

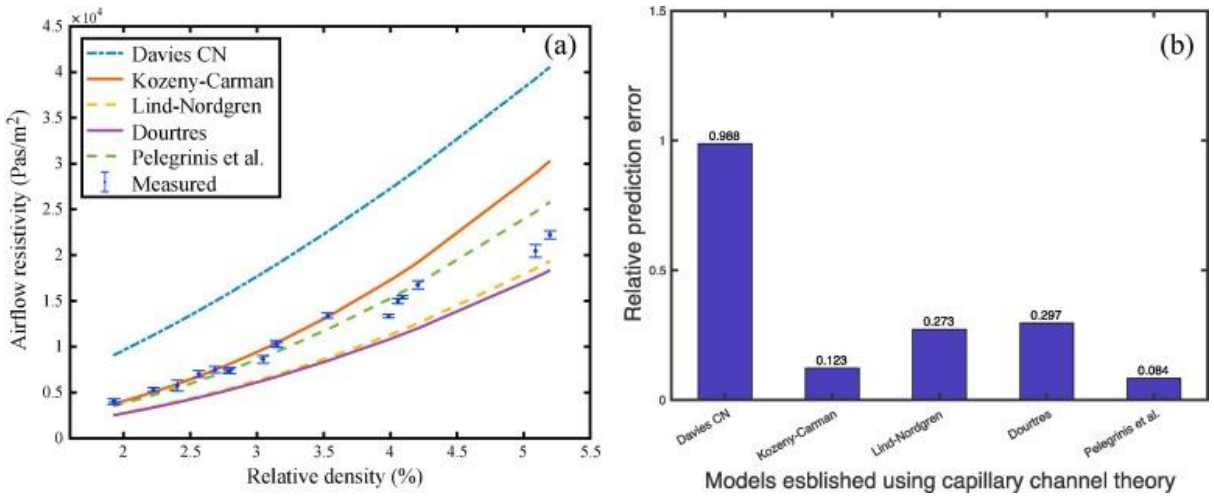

Figure 4.14: (a) Comparison of measured versus predicted values of airflow resistivity against relative density for the models based on capillary channel theory, and (b) the relative prediction error of each model. Figures taken from Yang, et al, 2018.

The Davies model (Davies, 1953) showed the highest value of predicted airflow resistivity and a relatively high error of 98.8%. It is suspected that such a large error is simply down to this model not being applicable to the types of materials tested herein. Whilst it is still a fairly popular model, it was originally written for the application of airbourne filtration by a uniform filter composed of a single fibre diameter. By contrast, the materials studied in this study are not a in a uniform arrangement.

In the case of the drag force theoretical models, shown in Figure 4.15, the results suggested that the model by Happel 'B' for the airflow perpendicular to fibre (Happel, 1959) significantly overestimated the resistivity by over 400%. The predictions by Hasimoto, Kuwabara, Happel 'A' and Tarnow 'C' are very similar and significantly overestimated the airflow resistivity by 180–210% (Hasimoto, 1959; Kuwabara, 1959; Happel, 1959; Tarnow, 1996). The equations in the Langmuir and Kuwabara models are identical, except for the value of the coefficient

multiplied by the dynamic viscosity, μ. The Langmuir model has a coefficient of 16, whilst the Kuwabara model uses a coefficient of 32. The doubling of this coefficient has halved the error associated with the prediction of the airflow resistivity of these materials, suggesting that this coefficient is better optimised for the type of materials tested in this study. It is to be expected that the Happel and Kuwabara models are similar to that of the Langmuir model, as both are based upon it. Similarly, the Happel and Kuwabara models are very similar in both result and formulation as they both use to same approach to solve the problem Langmuir encountered when trying to model flow parallel to the fibre direction. Both Happel and Kuwabara solved this by using two concentric cylinders to represent fluid flow through an assembly of cylinders (Kuwabara, 1959; Happel, 1959). All three of these models were originally created to predict sedimentation and resistance to flow in assemblies of cylinders; whilst the authors stated that these models did show '*good agreement […] for cases where it can be reasonably expected to apply*' (Happel, 1959) it is likely that the tortuous pathways present in the materials used in this study are outside the scope of these models, which may explain their inaccuracy. Despite this, these models are still common choices in the filtration industry, amongst others.

The predictions by Tarnow 'D' model yielded estimates within those of Tarnow 'A' and Tarnow 'C'. The most accurate drag force theory model for the flow resistivity for these multi-component media was the Tarnow 'B' model, which is accurate to within 10% and is more accurate when the materials have relatively low density.

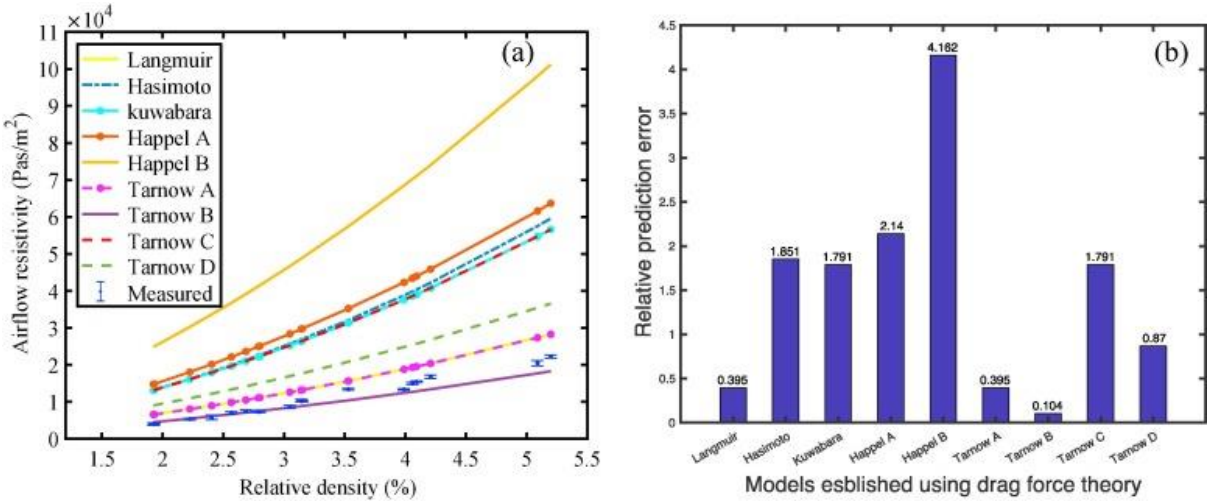

Figure 4.15: (a) Comparison of measured versus predicted values of airflow resistivity against relative density for the models based on drag force theory, and (b) the relative prediction error of each model. Figures taken from Yang, et al, 2018.

As mentioned in Section 4.3.1 of Chapter 4, all the drag force theory models contain $\ln(1-\phi)$. This can lead to a 16% error in just the porosity values, as demonstrated. This may explain why the observed results for the majority of the drag force theory models tested were more inaccurate than the capillary flow theory models. The drag force theory models are also the only models tested which consider the direction of flow relative to the fibre direction. The samples used in these studies were prepared from rotating perpendicular or vibrational perpendicular methods, which means that in all cases the angle of the fibre in the material could not be truly perpendicular to the direction of flow whilst taking the airflow resistivity measurements. Fibre orientation angles measured from the dominant fibre axis to the surface of the material specimen varied from 21.88° to 87.26° with a median value of 42.90°, with 61% of the samples have a fibre orientation angle less than 45°. From this, it could be deduced that the perpendicular models would perform better than the parallel models, as the majority of samples have fibre orientation angles which are closer to lying flat than standing vertical (and so are more perpendicular). This is not the case however, and the two most accurate models from this category are based on the assumption of parallel flow. It can therefore be

concluded that fibre orientation angle is of key importance when modelling materials using models applying drag force theory. In Table 3.4 in Chapter 3, there is a correlation between the relative density of the material and the fibre orientation angle – this makes sense, as a denser sample will have more perpendicular fibres. As such, you would expect that the parallel flow models would be more accurate at higher densities and the perpendicular models would be more accurate at lower densities. Figure 4.13 shows the opposite however, and I cannot account for this repeated observation.

In the case of the empirical models, shown in Figure 4.16, the Bies-Hansen and Manning Resin Bonded (RB) models significantly underestimated airflow resistivity of this multi-component media (Bies, Hansen, 1980; Manning, Panneton, 2013). The Garai-Pompoli, and Manning Mechanically Bonded (MB) and Thermally Bonded (TB) models (Garai, Pompoli, 2005; Manning, Panneton, 2013) were seen to produce a relatively close agreement with the measured airflow resistivity values, with errors that ranged from 11.1% to 15.7%. This result largely agrees with the results seen in the first study, where the Garai-Pompoli model was found to be more accurate than the Bies-Hansen equation upon which it is based (Hurrell, *et al*, 2018). The comparably poor performance of the Manning RB model is relatively simple to explain, in that these materials have not been resin bonded, and as such the coefficients are incorrect. The Manning TB model and MB model are significantly more accurate than the RB model, and give somewhat similar results as the regression coefficients present are similar. That the TB model is the most accurate of the Manning models is to be expected, as the Manning TB model does not take into consideration fibre diameter and assumes that the fibres are thermally bonded – which is accurate for the materials used in this study.

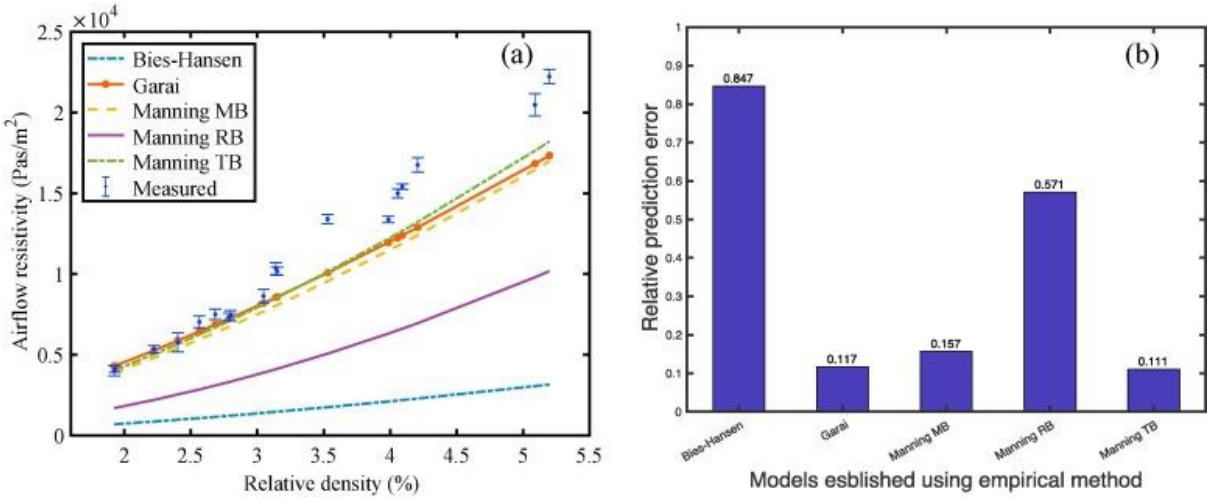

Figure 4.16: (a) Comparison of measured versus predicted values of airflow resistivity against relative density for the models based on empirical theories, and (b) the relative prediction error of each model. Figures taken from Yang, et al, 2018. Figures taken from Yang, et al, 2018.

4.4 Conclusion

This chapter has covered the acoustic testing and modelling of the nonwoven fibrous samples that made up the first half of the work completed during this PhD. The first step was to investigate a range of nonwoven samples with varying parameters to identify which of those material parameters has the greatest impact on the acoustic performance. From that testing it was established that fibre diameter was arguably the biggest parameter, as noted in Figure 4.2, where PE Sample 10 with a smaller average fibre diameter was able to out-perform much thicker or denser samples. This then developed into a small assay to confirm the observations noted in the earliest testing. Three fibre diameters were tested as raw samples and it was conclusively shown that the smaller fibre diameters were vastly superior. This hypothesis was further confirmed when four samples were made up with progressively smaller fibre diameters in the same composition as for a current automotive insulation product. Once more it was conclusively shown that the sample with the smaller fibre diameter

offered the greatest acoustic performance. This increase in performance is attributed to the increase in tortuosity and fibre density caused by decreasing the fibre diameter whilst maintaining the thickness and or bulk density. Using smaller fibres means that more fibres can be packed into the same volume. An increase in the tortuosity has been shown experimentally and theoretically to decreases the sound speed (Johnson, *et al*, 1982; Basu, 1992), increasing the number of interactions the wave has with the fibre, and increasing the amount of drag exerted on the wave – both of which significantly contributing to an large increase in viscous and thermal losses, which absorbs the sound energy better. The impedance mismatch between air and the sample will also increase with a decrease in porosity, which is often caused by an increase in the material density, which will also result in a greater reduction of sound propagation.

It was also demonstrated in Figure 4.9 and 4.10 that the addition of a thin highly resistive layer, or 'skin', to a material can result in significant (up to 92%) increases in absorption.

The second part of this chapter looked at the modelling of these fibrous nonwoven media. There exists a large number of models for porous media, which whilst generally fitting into three categories are sufficiently different in their calculation that they yield vastly different results for different types of media. It is often a challenge to know which model(s) will yield the most accurate results for the retrieval of either acoustical or non-acoustical parameters. Furthermore, some models require the knowledge of a great deal of parameters before they can accurately estimate the results, whilst others are much simpler. Two studies were conducted to explore the accuracy of some of the more commonly used and latest models. The first study was looking directly at the materials used in the acoustic characterisation stage, whilst the second study was expanded to include materials with varying types of polyesters – such as hollow fibres, which are becoming more common in industrial applications.

The conclusion of the first study was that for the eight nonwoven fibrous material samples tested, the value of the flow resistivity inverted with either Padé approximation or Miki model is more accurate than that predicted using Bies-Hansen, Garai-Pompoli or Kozeny-Carman

equations. In particular, the Miki model enables the inversion of flow resistivity of this type of fibrous media from measured surface impedance data with an accuracy of better than 15%. The Padé approximation model enables the inversion of flow resistivity with the accuracy of better than 42%. The latter error is likely related to the fact that the Miki model requires fewer parameters so that it can be more stable in the parameter inversion process. The pore structure of fibrous media with high porosity is relatively uniform so that the convergence of the Miki model for this type of media is better than that of the pore distribution model based on the Padé approximation. The proposed parameter inversion is a straightforward process which can be used to understand better the relationship between the material density and fibre diameter distribution and the resultant value of the flow resistivity of a porous medium. The flow resistivity inversion based on the Miki or Padé approximation model is attractive as it can be run without the prior knowledge of any intrinsic material property other than the material's thickness. The second study was conducted on multicomponent fibrous nonwovens, and concluded that the results indicated that the adaption of the Kozeny-Carman model as proposed by Pelegrinis *et al* was the most suitable for the retrieval of the airflow resistivity value in multicomponent polyester media, with a prediction error of 8.43%. The Tarnow 'B' model, making use of drag force theory also exhibited relatively high accuracy, with a prediction error of 10.41%. It was also made clear that the choice of model is crucial to attaining reliable estimates of material parameters – especially the airflow resistivity of multi-component nonwoven materials.

However, both studies suggest that new equations are required to relate the flow resistivity of blended fibrous media to the material density and fibre diameter distribution. It would further beneficial if these equations or models are able to accurately retrieve results without requiring the knowledge of a wide range of parameters. In a lot of cases the characterisation methods used to obtain material parameters like pore size or porosity are either destructive or very slow, requiring expensive equipment. In this sense, inversion models applied to acoustical data would be preferable due to the short testing times and non-destructive nature.

Chapter 5: Nanofibrous membrane acoustic and modelling characterisation

The key findings from the work completed on nonwovens detailed in Chapter 4 were that: (i) the presence of a 'skin' on the material can significantly increase the acoustic performance, (ii) there are a range of material parameters that can be changed and optimised to yield significantly improved absorption performance, and (iii) inversion modelling using acoustical data and models for the acoustical properties of porous media can accurately predict the properties of nonwovens. This chapter will characterise the nanofibrous membranes synthesised in Chapter 3, determine their acoustic performance and then attempt to outline the relationship between the material parameters of the membranes and how they perform acoustically.

As with the nonwovens, the first step was to acoustically characterise the nanofibrous membranes, followed by the application of the same models as described in Chapter 4 to invert the material properties. It was found that the models used for the inversion and prediction of porous material properties are not accurate when applied to the nanofibrous membranes. In addition to the acoustical parameters and modelled non-acoustical parameters, these membranes were also characterised using the methods described in Chapter 3, such as the use of SEM to estimate fibre diameter and thickness. The focus of this section is on nanofibrous membranes, which were occasionally difficult to fabricate in sufficient quantity to test them in both the 100 mm and 45 mm impedance tubes. As a result, testing for the membranes was exclusively done using the 45 mm impedance tube. In some instances, the yield of the electrospinning experiments was insufficient even for the 45 mm tube so these membranes were unable to be acoustically characterised at all. For membrane measurements it was frequently found that the membranes were unable to be tested by themselves, and so they were tested by placing them upon a well-characterised substrate of a reasonable thickness and stiffness. The reason for the membranes being unable to be tested without a substrate is related to their inherent material properties. The membranes synthesised in this PhD were very thin, less than 300 µm, and with a very low stiffness. This

means they were unable to support themselves structurally. Their thinness also makes them very hard to characterise. Because these membranes were so thin their acoustic absorption was almost identical to that of the empty tube as illustrated in Figure 5.1.

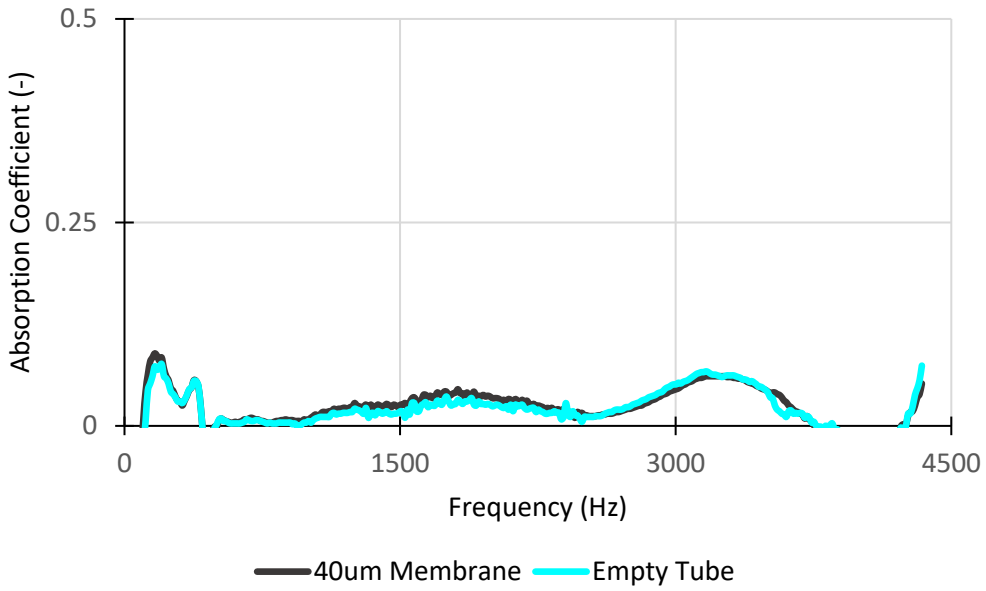

Figure 5.1 Comparison of the absorption coefficient for a 40 µm thick nanofibrous membrane versus empty tube response.

For Figure 5.1, the response of the 40µm thick membrane was retrieved by placing the membrane on the rigid terminus of the impedance tube. It is acknowledged that a more robust method of testing these membranes would be to have an airgap behind the membrane sample, and this was attempted in later work with a 100mm airgap (though this still proved unsuccessful for the thinner membranes, and was omitted as a result). This was done to illustrate the issues with testing the membranes in a manner consistent with other porous fibrous media.

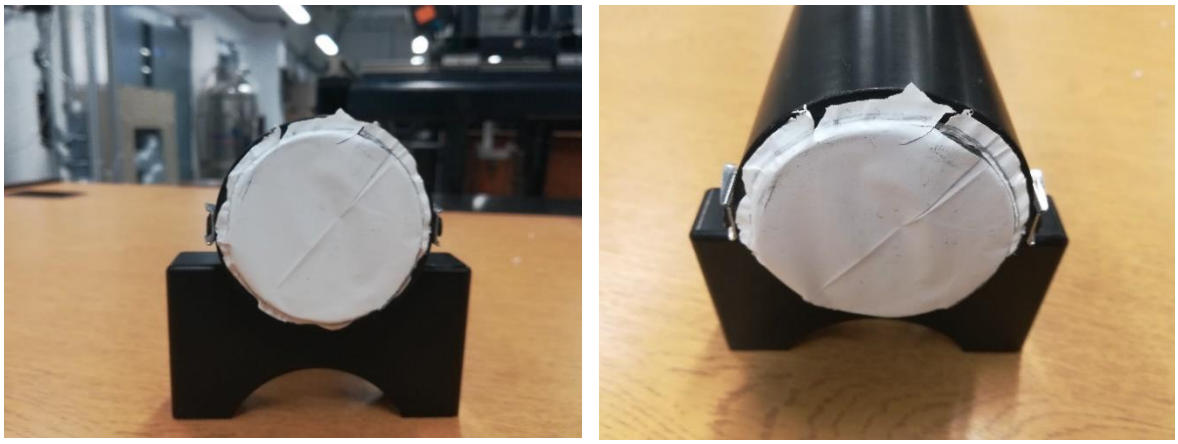

Figure 5.2: Images highlighting the first method used to mount the membrane. As can be seen, the membrane is cut oversized, and placed over the substrate in the tube. When inserted the mating face of the impedance tube ensures a tight seal.

Initially, dressmakers pins were used in an attempt to keep the membrane attached securely to the surface of the substrate to reduce any vibrations or the presence of air gaps between the membrane and substrate. It was found, however, that this was yielding erroneous data, as the real part of the normalized surface impedance was not increasing in the way it had been expected. The pins resulted in holes which reduced the effective flow resistivity of the membrane dramatically, as the size of the holes was larger than the average pore size present in the membrane. In a bid to fix this issue and simultaneously reduce the possibility and/or impact of membrane vibration or circumferential air gaps, two additional mounting methods were trialed. The first of such was to prepare oversized membrane samples and to place them directly in front of the melamine substrate in the impedance tubes. The mating faces of the impedance tube and sample holder were then used to hold the membrane sample taut in place, as illustrated in Figure 5.2.

The second method also involved preparing oversized membrane samples, but these were then wrapped around the substrate using the pressure from the substrate against the interior of the sample holder to keep the membrane in place, as illustrated in Figure 5.3. The presence of airgaps can significantly impact the measured surface impedance of the tested

substrate/membrane combination, especially when the size of the circumferential airgap is larger than the pore sizes present in the membrane (Pilon, 2002). Therefore, there were initial concerns about the folds of the membranes generating some gaps along the edge. This effect proved very hard to control and to characterise. It is clearly dependent on the thinness of the membranes and its ability to deform to fit between the substrate and the tube wall. Unfortunately, not all electrospun samples generated sufficient material to cover the substrate completely. In addition to this, problems with the removal of the membranes from their backing materials, and their inherent static properties also made it difficult to ensure complete coverage of the substrate.

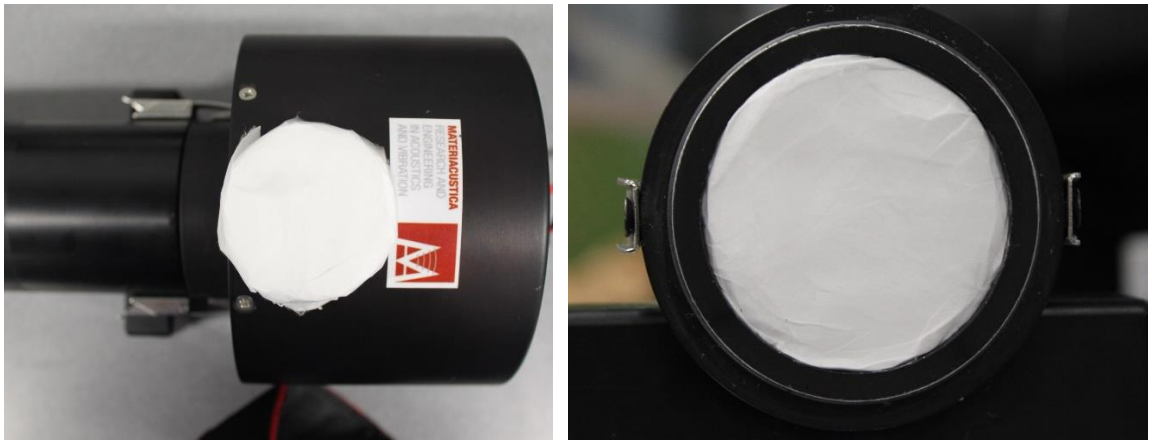

Figure 5.3: Image highlighting the second method used in lieu of pinning the membrane. The membrane can be seen wrapped around a 45 mm diameter melamine sample. The folds of the membrane can also be seen as straight sections relative to the curve present in other areas.

Once the membrane's material properties had been described as well as possible given the various difficulties encountered during their characterisation, the absorption spectra were presented and attempts were made to relate the observed acoustic response to the material properties.

5.1 Modelling of nanofibrous membranes

The next step in characterising the nanofibrous membranes was to model the non-acoustical properties of these membranes from their acoustical parameters, as it was found that the non-acoustical parameters were difficult or time consuming to measure directly. In order to measure the acoustical parameters these membranes have to be placed on a substrate. This complicated the modelling process, as it was not possible to input the acoustical data for membrane only into one of the computational models presented in Section 4.3.1 in Chapter 4. Instead, a different approach had to be taken to use a melamine substrate for which the non-acoustical properties were accurately characterised. This approach led to the development of a two-layer model, in which there were two steps: (i) modelling the non-acoustical parameters of the melamine substrate; (ii) to use these data to inverting the non-acoustical parameters of the the membrane from the parameters retrieved in (i) and the acoustical data from the membrane + substrate system. In both of these steps, the normalised surface impedance was used in the parameter retrieval process. In addition to two models developed which make use of this two-step process, the Kozeny-Carman equation was also used to determine if that was a valid prediction method for these materials. The two-layer models and their application will be explained in depth in Section 5.1.1 of Chapter 5.

The four PMMA samples obtained in collaboration with the University of Surrey were chosen as the materials to be investigated in the modelling initially, as it was felt that these were the best characterised samples of those available. The material parameters of these samples are summarised in Table 5.1, and Figure 5.4 shows the SEM images for each PMMA sample.

Sample	Thickness h [µm]	Fibre diameter d_f [nm]	Bulk density ρ_m [kg/m^3]	Porosity ϕ [-]
15kV PMMA	22.17	440 ± 140	360.18	0.68
18kV PMMA	27.58	310 ± 80	193.78	0.83
21kV PMMA	32.38	390 ± 110	157.68	0.86
24kV PMMA	26.33	520 ± 140	211.34	0.81

Table 5.1: Material properties of the four PMMA samples.

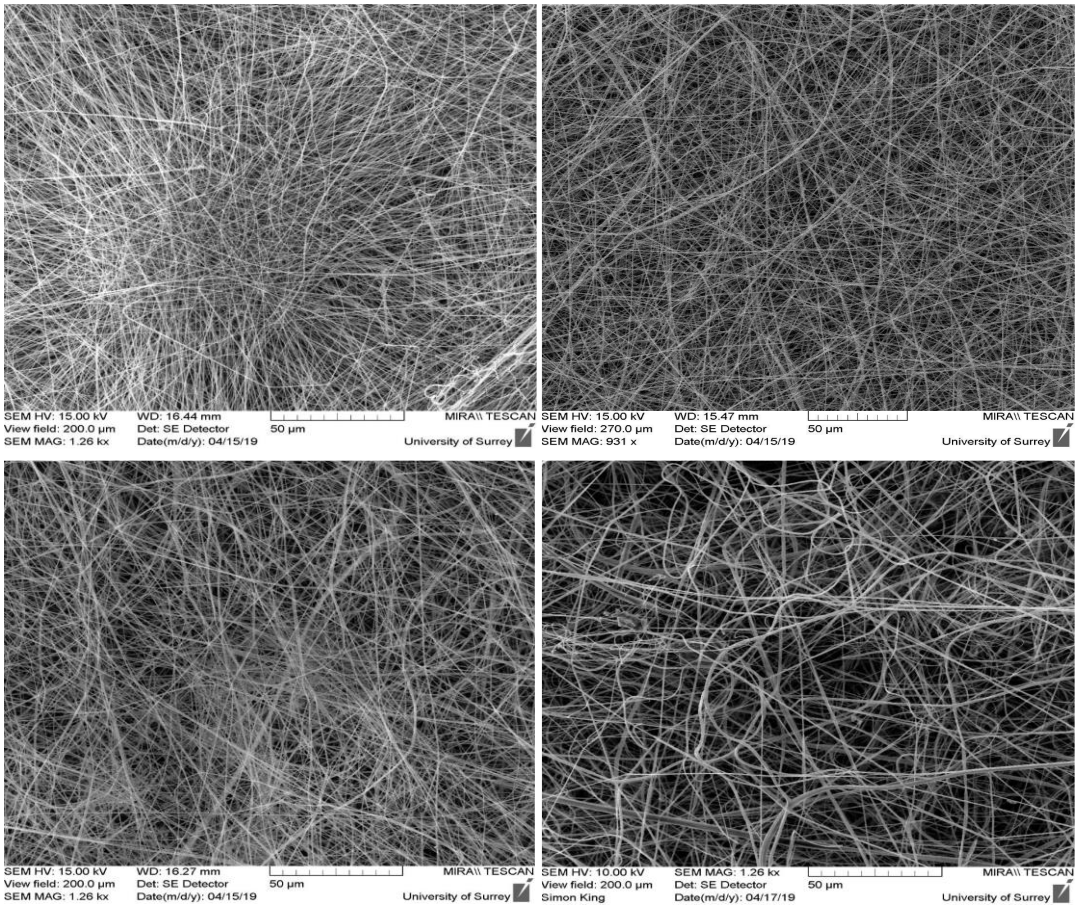

Figure 5.4: SEM images of the PMMA samples (Top left: 15kV, top right: 18kV, bottom left: 21kV, bottom right: 24kV).

5.1.1 Material modelling

This section will explain the three modelling approaches used for the prediction of the non-acoustical parameters of the nanofibrous membranes.

Kozeny-Carman Equation:

The Kozeny-Carman equation was covered in Section 4.3.1 (Equation 4.13) in Chapter 4. This equation was used to predict the airflow resisitvity values for each of the four PMMA samples, using the average fibre diameter as the particle size, d, and values of porosity, ϕ, as estimated using Equation 3.6 in Chapter 3.

Double Layer Model:

The first attempt at developing a two-layer model as outlined at the beginning of Section 5.1 was named the 'Double Layer model'. This model will be referred to as the '2L' model in the following text. Both of the two-layer models used in this section operate on the basis that the membrane + substrate system is a three layer medium in which the first and third layer are semi-infinite, and the incident and reflective soundwaves obey Snell's Law.

On the assumption that the second layer, in this case melamine, has a thickness equal to d, then the pressure reflection coefficient, V_r, can be described as

$$V_r = (Z_{in} - Z_3)/(Z_{in} + Z3)$$

Equation 5.1

where Z_{in} is the surface impedance of the stack at the boundary, and $Z_3 = \rho_3 c_3 / cos\theta_3$.

The sound pressure in the second layer (melamine - 2) is the combination of the wave propagated in this layer from third layer (membrane - 3) and the wave reflected from the interface between the melamine (2) and the first layer (rigid backing of impedance tube - 1) i.e.

$$p_2(x,z) = Ae^{ik_2(z\cos\theta_2 + x\sin\theta_2)} + Be^{-ik_2(z\cos\theta_2 - x\sin\theta_2)}$$

Equation 5.2

As mentioned above this system will obey Snell's Law, so it is required that

$$k_1 \sin\theta_1 = k_2 \sin\theta_2 = k_3 \sin\theta_3$$

Equation 5.3

to ensure that the projections of the wavenumber vectors on each of the two interfaces in this system are equal and the acoustical vectors remain continuous.

The ratio of the coefficients A and B can be found from the boundary conditions and the equation of the pressure reflection coefficient at the interface between the melamine (2) and the rigid backing (1):

$$\frac{B}{A} = \frac{Z_1 - Z_2}{Z_1 + Z_2}$$

Equation 5.4

where $Z2 = \rho 2c2/\cos\theta 2$ is the impedance of melamine (2).

At the interface between the membrane (3) and the melamine (2) there must be a continuity of the pressures and velocities, such that $p_3(x,d^+) = p_2(x,d^-)$ and $v_z^{(3)}(x,d^+) = v_z^{(2)}(x,d^-)$, where $+$ and $-$ indicate the side of the interface, and $z = d$ where the pressure velocity is assigned. The sound pressure at $z = d^-$ is calculated by Equation 5.5.

$$p_2(x,d^-) = Ae^{ik_2(d\cos\theta_2 + x\sin\theta_2)} + Be^{-ik_2(d\cos\theta_2 - x\sin\theta_2)}$$

Equation 5.5

The z-component of the acoustic velocity is hence:

$$v_z = -\frac{1}{i\omega\rho_2}\frac{\partial p_2}{\partial z} = -\frac{cos\ \theta_2}{\rho_2 c_2}\left(Ae^{ik_2(d\ cos\ \theta_2 + x\ sin\ \theta_2)} - Be^{-ik_2(d\ cos\ \theta_2 - x\ sin\ \theta_2)}\right)$$

Equation 5.6

The input surface impedance can then be expressed as:

$$Z_{in} = \frac{p_2(x, d^-)}{v_z^{(2)}(x, d^-)} = Z_2\frac{Z_1 + Z_2\ tanh(-ik_2 d\ cos\theta_2)}{Z_2 + Z_1\ tanh(-ik_2 d\ cos\theta_2)}$$

Equation 5.7

where $Z_1 = \frac{\rho_1 c_1}{cos\theta_1}$ is the characteristic acoustic impedance of the rigid backing (1).

There are two important limits for Equation 5.7. In the case when $d \to 0$, Equation 5.7 reduces to $Z_{in} = Z_1$, i.e. the input (surface) impedance at the interface becomes equal to the characteristic impedance of medium (1). Because the first layer (1) in this example is a rigid backing with $Z_1 \to \infty$, Equation 5.7 reduces to

$$Z_{in} = Z_2\ coth(-ik_2 d\ cos\ \theta_2)$$

Equation 5.8

The acoustic characteristic impedance, Z_2, and wavenumber, k_2, are complex and frequency dependent. The acoustic characteristic impedance of porous media and the wavenumber in porous media can be expressed through the frequency-dependent complex dynamic density ($\rho(\omega)$), and the bulk modulus ($K(\omega)$) of the equivalent fluid which saturates the porous material frame, such that:

$$Z_2(\omega) = \sqrt{\rho(\omega)K(\omega)} \quad \text{and} \quad k_2(\omega) = \omega\sqrt{\rho(\omega)/K(\omega)}$$

Equation 5.9

There are a number of models which can predict the behaviour of the dynamic density and bulk modulus from the material microstructural data. A summary of these models can be found in Section 2.10 in Chapter 2. In this instance, the values of dynamic density and bulk modulus are inverted from acoustical data using the Padé approximation model (Horoshenkov, *et al*, 2016).

When there is a stack composed of N individual layers, the input impedance of the n-th layer from the bottom of this stack can be predicted using a standard transfer matrix approach which is based on Equation 5.10:

$$Z_{in}^{n} = Z_n \frac{Z_{in}^{(n-1)} + Z_n \tanh(-ik_n d_n \cos\theta_n)}{Z_n + Z_{in}^{(n-1)} \tanh(-ik_n d_n \cos\theta_n)}$$

Equation 5.10

where Z_n, k_n and d_n are the acoustic characteristic impedance, wavenumber and the thickness of the n-th layer in the stack.

Equation 5.10 can be applied recursively starting with the bottom layer in this three layer stack - in this case a rigid backing (1). In this instance, the impedance at the interface between the bottom of the melamine (2) and the top of the rigid backing is given by $Z_{in}^{1} = Z_1 \coth(-ik_1 d_1 \cos\theta_1)$.

The pressure reflection coefficient, V_r, and energy absorption coefficients of the stack of N-layers can then be calculated from

$$V_r = \frac{Z_{in}^{N} \cos\theta_N - \rho_N c_N}{Z_{in}^{N} \cos\theta_N + \rho_N c_N}$$

Equation 5.11

and

$$\alpha = 1 - |V_r|^2$$

Equation 5.12

respectively. Here θ_N , ρ_N and c_N are the refraction angle, density and sound speed in the fluid in layer (N) from which the wave is incident on the stack.

Using the above theory, the 2L model first deduces the non-acoustical parameters of the substrate that the nanofibrous membrane is mounted on, and then uses these parameters to model the non-acoustical parameters of the nanofibrous membrane from the acoustical properties of the membrane and substrate system. The inversion used to retrieve the non-acoustical parameters for both parts was based on the Padé approximation model which is covered in detail in Section 4.3.1 (Equations 4.26 – 4.36) in Chapter 4. The Padé appoximation was chosen because it is a valid theoretical model with rigorous asymptotic limits which can accurately predict the acoustical properties of a range of porous media including fibrous membranes (Horoshenkov, *et al,* 2016).

As mentioned above, the first step in the 2L model is to invert the non-acoustical parameters of the substrate from the normalised surface imedpance data using the Padé approximation model. In the case of the membrane substrate systems covered so far in Chapter 5, this required the melamine layer to be tested without the membrane in the sound impedance tube. The non-acoustical parameters of melamine were then retrieved using the Padé approximation model (Equations 4.26-4.36, Chapter 4) and the Nelder-Mead optimisation (Equation 4.17, Chapter 4), using the same method as covered in Section 4.3.1 in Chapter 4.

The non-acoustical parameters retrieved from the Padé approximation model are the mean pore size of melamine, $\overline{s}$, the porosity of the substrate, ϕ, the tortuosity, α_∞, and the standard deviation of the pore size, $\sigma_{\bar{s}}$. In addition to retrieving these non-acoustical parameters, this model also plots the measured values of real and imaginary impedance against the predicted values, allowing for a visual comparison of the fit. This fit can further be

evaluated using the root mean square method comparing the difference between measured and theoretical values of both real and imaginary parts of the surface impedance, presented as a percentage.

The seed parameters used to invert the non-acoustical parameters for melamine, and the values of the parameters inverted from this step can be can be seen in Table 5.2 and 5.3 respectively.

Output			
Mean pore size $\bar{s}$ [m]	Porosity ϕ [-]	St.Dev. pore size $\sigma_{\bar{s}}$ [-]	Tortuosity α_∞ [m]
1.09 x10^{-4}	0.8192	0.2428	1.0583

Input			
Thickness h [m]	Mean pore size $\bar{s}$ [m]	Porosity ϕ [-]	St. Dev. pore size $\sigma_{\bar{s}}$ [-]
0.016	1.00 x10^{4}	0.995	0.2

Table 5.2 and 5.3: Input and output parameters for melamine in the first step of the 2L model.

The value for porosity in Table 5.2 is significantly lower than that in Table 5.1, because the values of porosity, pore size, and tortuosity seen here are obtained from fitting the acoustical parameters of the modelled material to the measured results.

After retrieving the non-acoustical parameters of the substrate, the next step is to repeat this for the membrane layer. The parameters $\bar{s}$, ϕ, $\sigma_{\bar{s}}$, and h for the melamine substrate as

retrieved in the first step are used as some of the input seed values. In addition to these seed values, the model also requires the thickness of the membrane, h_m. From this the model retrieves the mean pore size of the membrane, $\bar{s}_m$, the porosity of the membrane, ϕ_m , the tortuosity of the membrane, α_{∞_m}, and the standard deviation of the pore size in the membrane, $\sigma_{\bar{s}_m}$. As with the first step of the model, the fit between measured and theoretical values for the surface impedance of the membrane are compared.

It was noticed that there was generally a poor fit between predicted and measured values when using the 2L model, especially with regard to the imaginary part of the impedance. The average error – as assessed by the root mean square error – between measured and predicted values, equated to 12.08%. Whilst this value is not extremely high, it does not accurately highlight the issues observed with the fit. Figure 5.5 shows the typical fit of the 2L model. From this figure it is apparent that the model significantly underpredicts the imaginary part of the impedance, whilst also underpredicting the real part of the impedance for frequencies below 2000Hz. It was thought that this could have been caused by the membrane vibrating slightly on the surface of the substrate, introducing very small airgaps - which on a relative scale could be similar in size to the pore size or length. This vibration could potentially explain the larger than expected increase in the imaginary part of the impedance that was observed. The imaginary part of the impedance should increase as a result of the membrane having an increased finite mass, which will impact the reactance at the surface of the membrane + substrate system.

A second variant of the 2L model was then prepared which took into consideration the surface density of the membrane. This was an attempt to correct for the increase in the imaginary part of the impedance caused by the membrane vibrating on the surface of the substrate. This model will be referred to as ‘2LDensity’ model in the text.

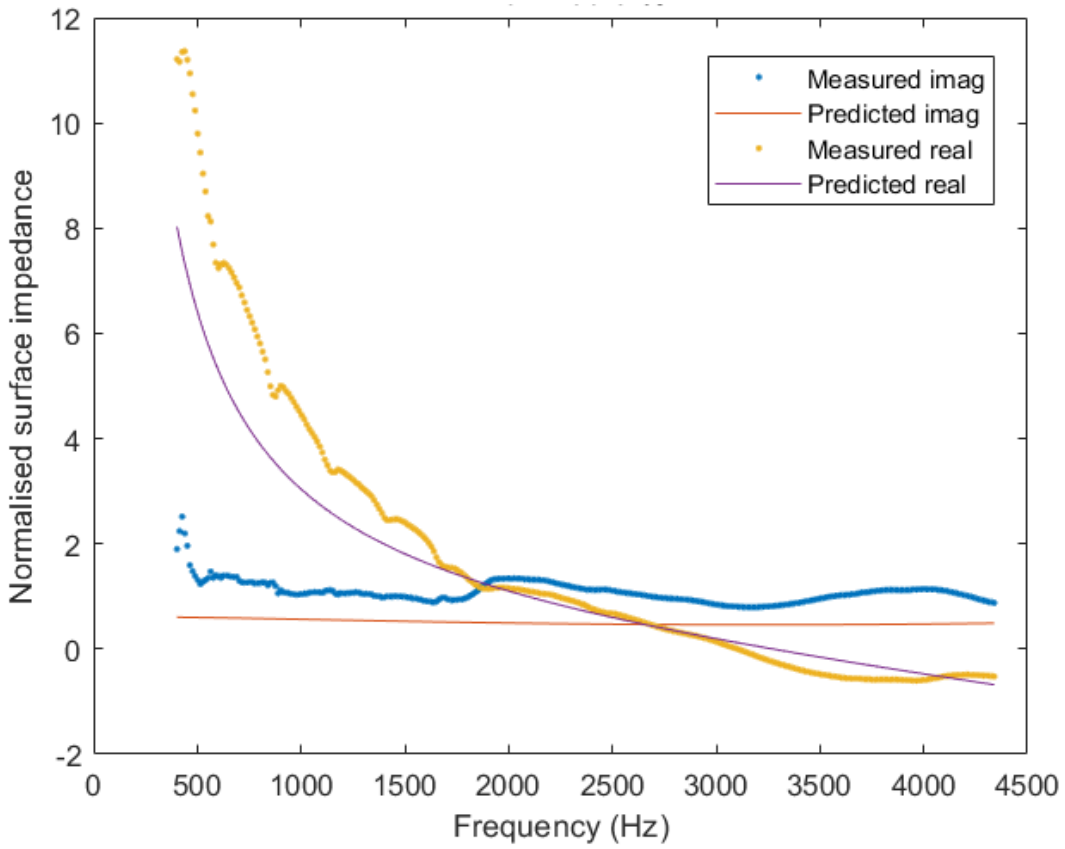

Figure 5.5: A comparison of measured and predicted values of impedance using the '2L' model.

Double Layer with Density Correction Model:

The first step of this '2LDensity' model is the same as was seen in the 2L model described in Section 5.1.1 just above. Melamine foam was tested individually, and then the non-acoustical parameters were retrieved using the Padé approximation model. As in the 2L model some seed values are required, namely the thickness of the melamine, and estimations of its mean pore size, $\overline{s}$, porosity, ϕ, and the standard deviation of pore sizes in the melamine sample, $\sigma_{\bar{s}}$. The method of estimation for these parameters is outlined in Horoshenkov, *et al*, 2016. The parameters retrieved from the first step are the mean pore size of melamine, $\overline{s}$, the porosity of the substrate, ϕ, the tortuosity, α_∞, and the standard deviation of the pore size, $\sigma_{\bar{s}}$.

After retrieving the non-acoustical parameters of the substrate, the inversion is repeated for the membrane layer. The values of melamine retrieved in the first step are used in combination with the thickness of the membrane layer, h_m, and estimates of the seed for mean pore size, $\bar{s}_m$, and the membrane surface density, ρ_{s_m} .

Output			
Mean pore size of membrane $\bar{s}_m$ [m]	Porosity of membrane ϕ_m [-]	Standard deviation of pore size $\sigma_{\bar{s}_m}$ [m]	Tortuosity $\alpha_{\infty_{\mathrm{m}}}$ [m]
1.00x10^{-4}	0.7905	0.01	1.0001

Input			
Thickness h [m]	Mean pore size of substrate $\bar{s}$ [m]	Porosity of substrate ϕ [-]	Standard deviation of pore size in substrate $\sigma_{\bar{s}}$ [m]
0.016	1.00x10^{-4}	0.995	0.2

Table 5.4: Input and output parameters used in the 2LDensity model for the melamine substrate. As with Table 5.3, the value of porosity here is much lower than in Table 5.1. This again is because this value is obtained from fitting the acoustical parameters.

5.1.2 Model review

In the case of both '2L' and '2LDensity' models, it is also possible to predict the airflow resistivity value, σ, from the mean pore size, $\bar{s}_m$ (Horoshenkov, *et al*, 2019.). This can be done using equation 5.13, which shows the relationship between airflow resistivity, mean pore size, and dynamic viscosity, μ:

$$\sigma = \frac{8\mu\alpha_\infty}{\phi\ \bar{s}_m{}^2} e^{6\sigma_{\bar{s}} \cdot \log 2^2}$$

Equation 5.13

where q is the mean pore length, $\sigma_{\bar{s}}$ is the standard deviation of the pore size, and ϕ is the porosity of the material. This equation can be simplified to Equation 5.14, as the modelled values of ϕ are sufficiently close to 1, and the standard deviation can be taken as 0.

$$\sigma = \frac{8\mu\alpha_\infty}{\bar{s}_m{}^2}$$

Equation 5.14

The derivation of these equations can be seen in Horoshenkov, *et al*, 2019. In equation 5.14, we assume that porosity is equal to 1. It is not possible to conclude whether or not this is the correct assumption, as porosity was a parameter that could not be properly measured for these membranes, and the results obtained varied greatly (0.79 – 0.97). In this assumption, we used the measured values of porosity presented in Table 5.1.

The retrieved values of airflow resistivity from each of the three modelling approaches can be seen in Table 5.5. Given that three specimens of each membrane sample were tested, there are three separate results for each of the two-layer based models. The Kozeny-Carman value remains the same, as the porosity and thickness of the membrane samples is consistent throughout specimens.

It must also be noted that it was not possible to obtain measurement data of airflow resistivity for the nanofibrous membranes, as when attempts were made to do so in accordance with ISO9053, the membrane samples either ruptured or were inflated and stretched due to their apparent very low permeability. The method used in this instance was to cut the samples oversize and use the sample holder to maintain tension and stop the very lightweight samples from being blown out of the flow resistivity rig. An additional attempt to overcome this by sandwiching the membrane in between two layers of melamine foam was also unsuccessful

as the membrane was still inflated. Had this been successful the airflow resistivity of the membrane could be retrieved by measuring the airflow resistivity of the substrate individually, and then the sandwiched system. The value of airflow resisitvity for the membrane could then caluclated from transfer functions.

Sample	Kozeny-Carman ($Pa \cdot s/m^2$)	2L ($Pa \cdot s/m^2$)	2LDensity ($Pa \cdot s/m^2$)
15kV PMMA	4.91×10^7	117.57	5.23×10^6
2		53.36	6.11×10^6
3		209.76	5.74×10^6
18kV PMMA	9.89×10^7	48.79	6.32×10^6
2		51.98	6.55×10^6
3		9.68×10^6	6.50×10^6
21kV PMMA	6.25×10^7	269.85	9.34×10^6
2		1.16×10^7	9.41×10^7
3		41.08	4.53×10^7
24kV PMMA	3.51×10^7	1.46×10^4	6.20×10^6
2		95.53	6.18×10^6
3		93.21	6.20×10^6

Table 5.5: Predicted and inverted values of airflow resistivity for the PMMA samples. In the case of the 2L model, the majority of the inverted values for airflow resistivity are very low. The 2LDensity model attempts to account for this by considering the surface density of the membrane.

As can be seen, in the case of the Kozeny-Carman equation the predicted airflow resistivity values (see Table 5.5) are generally consistent with the increase in fibre diameter. These values vary quite significantly between membrane samples. The flow resistivity data for these PMMA samples, recovered acoustically, do not correlate well with the predicted values. The airflow resistivity for the 18kV PMMA membrane sample is 50% higher than that for the 21kV PMMA membrane sample, or three times larger than the 24kV PMMA membrane sample. Figure 5.6 shows the that 18kV and 24kV PMMA samples have very similar

absorption spectra, despite the fact that their fibre diameters are noticeably different (310 vs 520 nm). The similar performance of these membranes may potentially be explained by the difference in fibre diameter being offset by the difference in density.

Overall, it seems that the results obtained from the Kozeny-Carman equation are questionable, and that the model may not be well suited for predicting the airflow resistivity of nanofibrous media. It was also well documented in the paper by Hurrell, *et al*, 2018 that the Kozeny-Carman equation can incorrectly estimate the flow resistivity of a material when there is a range of fibre diameters present. Furthermore, the diameter of these fibres is several orders of magnitude smaller than those originally described by the Kozeny-Carman equation, which may lead to further erroneous predictions.

For the '2L' model, the values of the inverted airflow resistivity values are significantly different, even between specimens of the same sample. A good example of this is the 21kV PMMA sample, where one specimen has a retrieved value of 1.16×10^7 Pa·s/m^2 which seems fairly appropriate for this type of materal, whilst the other two specimens are 270 and 41 Pa·s/m^2, which are nonsensical results. Overall, the retrieved values from this model make little sense, but this is likely related to the issues with fitting both the real part (beneath 2000Hz) and the imaginary part, as illustrated in Figure 5.5. This issue is likely to be brought about by the circumferential air gap which will be discussed in Section 5.2.3.

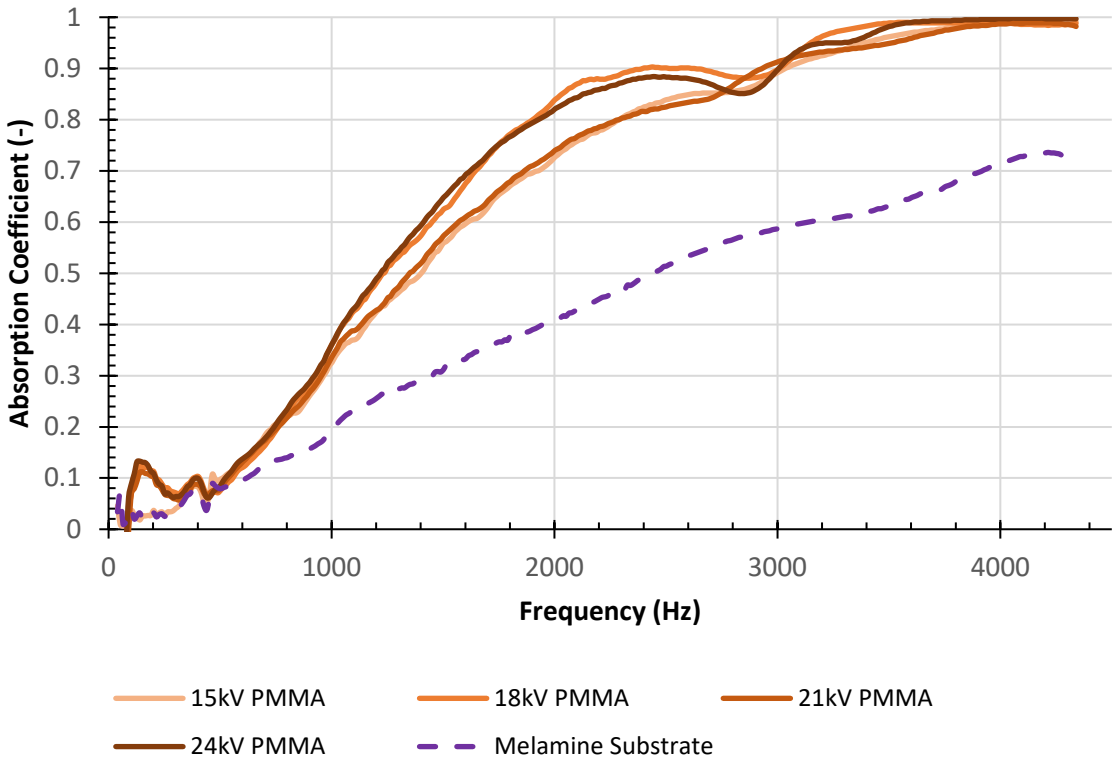

Figure 5.6: Acoustic results from the samples obtained in collaboration with the University of Surrey.

The '2LDensity' model, which includes an estimate of the membrane surface density in an attempt to account for the effect of the membrane vibrating on the surface of the melamine substrate, appears to be much more stable in its prediction. The values retrieved from this model are more consistent and, importantly, considerably more plausible than those retrieved from the '2L' model. As a result of this, the '2LDensity' model was chosen as the model to use for the inversion of airflow resistivity values in the acoustical characterisation process.

In addition to values of σ, the '2L' and '2LDensity' models are also able to retrieve additional parameters, like the median pore size (and its standard deviation), as well as the membrane surface density, alongside mean pore length and porosity. The values of $\overline{s_m}$, ϕ_m, α_{∞_m}, and

$\sigma_{\overline{s_m}}$ for the membrane samples as retrieved by the '2L' model can be seen in Table 5.6. Table 5.7 shows the inverted values of $\overline{s_m}$ and m as retrieved by the '2LDensity' model. The values shown in the tables are averaged for each of the three specimens from each membrane sample.

Specimen	Median pore size $\bar{s}_m$ [m]	Porosity ϕ_m [-]	Mean pore length α_{∞_m} [m]	St. Dev. pore size $\sigma_{\bar{s}_m}$ [-]	Root mean square error [%]
15kV PMMA	1.18×10^{-3}	1.00	9.62	1.55	2.1
18kV PMMA	1.16×10^{-3}	1.00	7.99	1.07	12.0
21kV PMMA	8.79×10^{-4}	1.00	6.87	1.03	18.1
24kV PMMA	8.60×10^{-4}	0.74	7.53	1.36	16.1

Table 5.6: Retrieved parameters for the four PMMA samples using the '2L' model.

Specimen	Median pore size $\bar{s}_m$ [m]	Membrane surface density m [kg/m^2]	Root mean square error [%]
15kV PMMA	4.08×10^{-6}	1.04×10^{-5}	3.8
18kV PMMA	3.84×10^{-6}	1.56×10^{-5}	4.4
21kV PMMA	4.05×10^{-6}	1.88×10^{-5}	6.2
24kV PMMA	1.71×10^{-5}	8.03×10^{-6}	5.0

Table 5.7: Retrieved parameters for the four PMMA samples using the '2LDensity' model.

The results for mean pore size as retrieved by the '2LDensity' are more realistic than those seen with the '2L' model. The mean pore size retrieved for 15-21 kV PMMA membrane samples are approximately 4 µm, which is believable based on the SEM images as seen in Figure 5.4, where the scale bar is 50 µm.

5.2 Nanofibrous membrane characterisation results

A total of 34 membranes were produced during the PhD at the University of Sheffield. All of them were tested acoustically, however only 26 were able to be fully characterised. The eight membranes which were not fully characterised were the first five PET-based membranes that were synthesised. These were not fully characterised as after the acoustic testing the samples were unable to be recovered from the melamine substrate, as a result of their static charges and apparent affinity for the foam. Despite this, their acoustic results are used in some discussion.

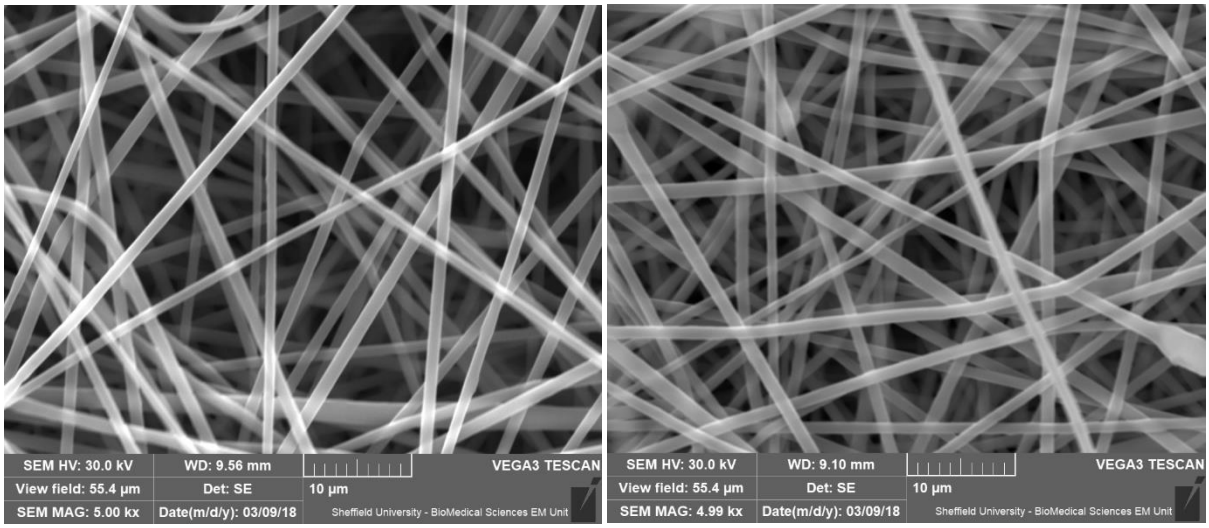

Figure 5.7: SEM images of the fibre density and size from changing the needle tip diameter.

A further two PET membranes, produced by varying the size of the needle tip, were not characterised either. These membranes were synthesised to mitigate an electrospinning problem occurring with the Taylor's cone expanding to too great a size, in which the increase in the size of the cone was causing stability issues during the spinning process. It was thought that this was related to mass flow in the needle leading to the polymer solution drying on the tip of the needle before it could be ejected as a jet. Changing the diameter of the needle (from 0.514mm to 0.838mm) was hypothesised as a potential solution, and the increase in the

needle diameter did help with the stability of the process, but it did not seem to significantly affect the material properties, as was observed by visual comparison by SEM (Figure 5.7). There was less than a 10% difference in the average fibre diameters produced as a result of the increase in needle diameter, and membrane thickness was also comparable due to the same collector distance and volume of polymer solution. The average fibre diameter values were found to be 1.018 ± 0.201 μm vs 1.043 ± 0.205 μm for the 0.838mm and 0.514mm needle tips, respectively. The final membrane which was not fully characterised was a PCL sample made during the investigation into varying the material parameters of the membranes by changing the electrospinning process parameters. The process parameter under investigation was the flow rate, and it was found that insufficient polymer was produced in the time available to recover a 45mm sample for testing. As such, it was omitted from the characterisation.

The key parameters that were retrieved during the characterisation process were the thickness of the membrane, the average fibre diameter, the density of the membrane, its porosity, the airflow resistivity value obtained by the '2LDensity' model, and the value of airflow resistivity multiplied by the membrane thickness. These parameters are arguably the most important parameters, both for describing a material and for explaining the absorption spectra. These parameters for each of the 26 membranes are summarised in Table 5.8. It is important to note that not all the values for parameters like airflow resistivity or porosity make physical sense. This is due to a range of difficulties associated with membrane characterisation and with the modelling process, for example difficulties in measuring membrane thickness – which would affect density and hence porosity calculations, and sensitivity of the model.

	Thickness h [µm]	Fibre diameter d_f [nm]	Membrane density ρ_m [kg/m^3]	Membrane porosity ϕ_m [-]	Median pore size $\bar{\sigma}_{s_m}$ [m]	Predicted airflow resistivity σ [Pa·s/m^2]	$\sigma \cdot h$ [-]
I	19.02	401 ± 211	155.37	0.89	1.07×10^{-5}	1.26×10^{6}	23.98
II	12.1	340 ± 128	303.99	0.78	2.49×10^{-5}	2.33×10^{5}	2.82
III	12.41	243 ± 111	395.51	0.71	9.87×10^{-6}	1.49×10^{6}	18.43
IV	220.16	1130 ± 234	35.87	0.97	1.21×10^{-5}	9.93×10^{5}	218.66
V	200.45	1111 ± 263	17.54	0.99	1.37×10^{-5}	7.74×10^{5}	155.19
10% PCL	176.21	1218 ± 219	179.34	0.85	2.41×10^{-5}	2.50×10^{5}	44.13
THF_A	12.15	1774 ± 979	1107.45	0.06	5.97×10^{-6}	4.06×10^{6}	49.37
THF_C	10.87	1334 ± 730	890.79	0.25	9.22×10^{-6}	1.70×10^{6}	18.50
THF_C (ii)	11.87	1052 ± 542	1165.35	0.01	6.28×10^{-6}	3.67×10^{6}	43.58
THF_F	12.56	512 ± 282	1446.75	-0.23	9.38×10^{-6}	1.65×10^{6}	20.67
CF_B	12.21	1606 ± 259	977.12	0.17	3.97×10^{-6}	9.19×10^{6}	112.25
CF_C	12.16	1398 ± 81	952.88	0.19	1.34×10^{-5}	8.10×10^{5}	9.85
CD1	5.77	2880 ± 2450	1503.01	-0.27	4.66×10^{-6}	6.81×10^{6}	39.30
CD2	7.84	3630 ± 1350	705.57	0.40	4.49×10^{-6}	7.18×10^{6}	56.30
CD3	5.41	2560 ± 1350	429.78	0.64	5.06×10^{-6}	5.66×10^{6}	30.64
FR2	11.33	2590 ± 1380	343.37	0.71	5.87×10^{-6}	4.21×10^{6}	47.67
V1	10.99	3190 ± 1600	438.97	0.63	6.08×10^{-6}	3.96×10^{6}	43.49

V2	12.75	2500 ± 147	405.56	0.66	7.46×10^{-6}	3.51×10^{6}	44.69
V3	15.33	5850 ± 2940	149.90	0.87	0.01	1.45	0.00
15kV PMMA	22.17	440 ± 140	360.18	0.68	5.05×10^{-6}	5.69×10^{6}	126.20
18kV PMMA	27.58	310 ± 80	193.78	0.83	4.74×10^{-6}	6.46×10^{6}	178.05
21kV PMMA	32.38	390 ± 110	157.68	0.86	4.51×10^{-6}	7.76×10^{6}	251.16
24kV PMMA	26.33	520 ± 140	211.34	0.81	4.84×10^{-6}	6.19×10^{6}	163.05
5gsm TPU	19.54	409 ± 366	959.82	0.17	1.24×10^{-5}	9.56×10^{5}	18.68
8gsm PVDF	19.21	395 ± 455	1356.09	-0.04	0.01	1.45	0.00
11gsm TPU	19.37	281 ± 313	1870.09	0.11	9.17×10^{-6}	1.74×10^{6}	33.77

Table 5.8: Material parameters for the 26 nanofibrous membranes fully characterised. Fibre diameter is presented as an average of 100 measurements per specimen, and the standard deviation.

5.3 Difficulties with modelling nanofibrous membranes

There were a number of difficulties encountered when attempting to model these nanofibrous membranes. Some difficulties were caused by the inherent properties of the membranes, such as their electrostatic charging and small thickness. The other difficulties were associated with attempting to adapt models for materials with much larger and longer pores. This section will discuss some of those difficulties, how they were attempted to be solved, and how they might better be solved in the future.

5.3.1 Problems associated with sample mounting

This problem was briefly discussed at the start of Chapter 5, where the two different methods of mounting the samples were illustrated (Figure 5.2 and 5.3, Chapter 5). Neither option, however, was perfect. By wrapping the sample around the melamine substrate, it was possible to reduce any circumferential airgap between the nanofibrous membrane and impedance tube wall. However, the folds of the membrane could result in the formation of small airgaps between the tube and the sample. Conversely, by placing the nanofibrous membrane on top of the substrate, the gaps between the sample and the tube were almost eliminated but it was possible to introduce circumferential airgaps between the nanofibrous membrane layer and the melamine layer.

Further airgap issues could be encountered as a result of the electrospinning processes. Due to timeframe limitations at the University of Sheffield, some of the polymer solutions were unable to be spun at sufficient durations for their electrospinning settings to yield sufficient membrane samples for complete coverage of the melamine substrate. These limitations were caused by restricted access to electrospinning equipment, in addition to numerous complications with the characterisation process as a result of equipment failure, reservations, or experimental duration (as with porosimetry, which can take 72 hours to run 3 samples).

In addition to airgap issues faced by mounting the membrane, there are further complications. When removing the sample from the aluminium foil backing and attempting to place it on the melamine the inherent static properties can result in partial delamination of the nanofibrous membrane. This then is suspected to be the primary cause of vibration between the substrate and the nanofibrous membranes. This vibration, as mentioned in Section 5.1.1 in Chapter 5, is attributed to cause an increase in the real part of the imaginary, which is otherwise unexpected and is not predicted by the '2L' or '2LDensity' models. This is despite changes in the 2LDensity model to account for the surface density of the membrane.

5.3.2 Problems associated with airgap

Whilst the airgap is not present for all membranes tested, there are several examples where an insufficient volume of membrane was synthesised, or difficulties in mounting the sample led to the presence of airgaps around the edge of the melamine susbrate. An extreme example of this air gap can be seen in Figure 5.8. In an effort to try and improve the model accuracy, the work by Pilon was adapted into the models (Pilon, 2002). This work takes into account of effect of a circumferential airgap on the material properties of the membrane plus melamine system.

Figure 5.8: An extreme example of the circumferential airgap issues arising from a shortage of synthesised membranes.

As a result of this airgap, these membrane and substrate samples could be considered a double porosity material, in which the pores of the membrane and the macroporous perforations/gaps make up the two porous networks. In this paper (Pilon, 2002) it is suggested that the total porosity in the material (ϕ_{total}) is defined by a ratio of the material pore size to the airgap pore size:

$$\phi_{total} = \frac{r_m^2}{r^2}$$

Equation 5.16

where

$$r_m = \sqrt{2rt - t^2}$$

Equation 5.17

where r is the radius of the impedance tube, and t is the size of the airgap in the impedance tube. Figure 5.9 illustrates r and t, as well as the type of double porosity network described in this section.

Pilon then demonstrated that the double porosity material will have a static visco-inertial permeability, Π_{dp}^{s}, which can be calculated from the permeability of the microporous network (or the membrane and melamine sample), Π^{s}, and the permeability of the macroporous network, Π_{m}^{s}, according to Equation 5.6:

$$\Pi_{dp}^{s} = (1 - \phi_{total})\Pi^{s} + \Pi_{m}^{s}$$

Equation 5.18

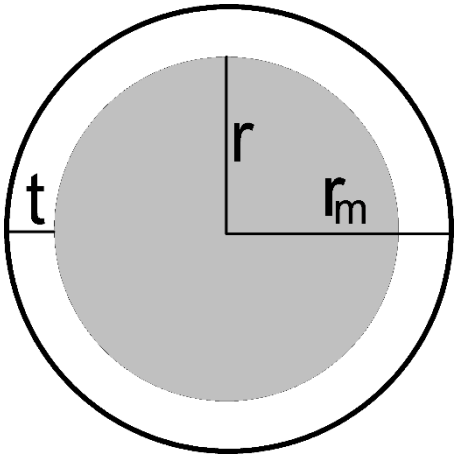

Figure 5.9: Diagram illustrating r, the radius of the sound impedance tube, r_m, the radius of the sample mounted in the tube, and t, the thickness of the airgap.

Considering that the measurements were made in a sound impedance tube, the terms Π^s and Π_m^s can be defined as follows:

$$\Pi^s = \frac{\mu}{\sigma}$$

Equation 5.19

$$\Pi_m^s = \frac{\phi_{total} r_m^2}{8}$$

Equation 5.20

where μ is the dynamic viscosity (used as 1.81x10^{-5} Pa·s in this case), and σ is the airflow resistivity of the material (membrane and melamine sample in this case).

The total airflow resistivity in the sample taking into consideration the airgaps, σ_{total}, can then be calculated using Equation 5.21, and from that the 'corrected' value of median pore size, $\overline{s_{total}}$ can then be estimated as seen in Equation 5.22:

$$\sigma_{total} = \frac{\mu}{\Pi_{dp}^{s}}$$

Equation 5.21

$$\overline{s_{total}} = \sqrt{\frac{8\sigma}{\sigma_{total} \cdot \phi_{total}}}$$

Equation 5.22

ϕ_{total} for this work was assumed to be equal to one, as a result of the very high airflow resistivity values of the membranes. Assuming that the predictions by Kozeny-Carman in Section 5.1 are reasonable – when they are more likely to be underestimated – would suggest airflow resistivity values in the magnitude of $1x10^7$ to $1x10^9$ Pa·s/m^2, which is very highly resistive. It was also noted during earlier works that changing the value of the porosity for the membrane and melamine system did not statistically significantly impact the inverted material parameters.

To look into the effects of the circumferential air gap in the materials tested during the scope of this PhD, the 15kV PMMA sample was chosen. The calculated values of the parameters covered by Equations 5.4 – 5.10 can be seen in Table 5.9. As is to be expected, the presence and increase in size of a circumferential air gap leads to a increase in the permeability of the membrane, a decrease in its airflow resistivity, and an increase in the effective median pore size of the membrane when considering its placement in a sound impedance tube. If we consider a tenfold increase in the size of the airgap (e.g. 10µm to 100µm) then airflow resistivity can be seen to decrease by a factor of 100. In fact, this relationship between airgap and airflow resistivity appears to be an inverse squared one, with a fivefold increase in airgap leading to a 25 times decrease in airflow resistivity, and a twentyfold increase in airgap leading to a 400 times decrease in airflow resistivity.

The value of $\overline{s_{total}}$ can then be substituted into the double layer model with membrane surface density (as covered in Section 5.2.4). This was done for each of the air gap sizes, and

then plot against frequencies, allowing for a visual comparison as to how the increase in airgap affects the predicted impedance values of the model (Figure 5.10). Increasing the size of the airgap results in a decrease in the value of the real part of the impedance, and significant (a factor of 6) changes in the value of the imaginary part of the impedance. The impact the airgap has seems to decrease as the airgap increases, for example, going from an airgap of 10 µm to 20 µm has a much greater impact on the impedance than going from 100 µm to 200 µm, or even 50 µm to 200 µm. This may account for some of the differences observed between measured and predicted values seen Figure 5.10 for example.

t [µm]	r_m [m]	ϕ_m [-]	$1-\phi_m$ [-]	Π_m^s [m^2]	Π_{dp}^s [m^2]	σ_{total} [Pa s m^2]	$\overline{s_{total}}$ [m]
0	0.00	0.00	1.000	0.00	3.69×10^{-13}	$4.91\times10^{+7}$	1.72×10^{-6}
10	6.71×10^{-4}	8.89×10^{-4}	0.999	5.00×10^{-11}	5.03×10^{-11}	$3.60\times10^{+5}$	2.01×10^{-5}
20	9.48×10^{-4}	1.78×10^{-3}	0.998	2.00×10^{-10}	2.00×10^{-10}	$9.05\times10^{+4}$	4.00×10^{-5}
50	1.50×10^{-3}	4.44×10^{-3}	0.996	1.24×10^{-9}	1.24×10^{-9}	$1.45\times10^{+4}$	9.98×10^{-5}
100	2.11×10^{-3}	8.87×10^{-3}	0.991	4.96×10^{-9}	4.96×10^{-9}	3652.14	1.99×10^{-4}
200	2.98×10^{-3}	0.0177	0.982	1.96×10^{-8}	1.96×10^{-8}	921.31	3.96×10^{-4}

Table 5.9: Calculated values for each of the parameters, leading to Π_{dp}^s, σ_{total}, and $\overline{s_{total}}$ for the 15kV PMMA sample.

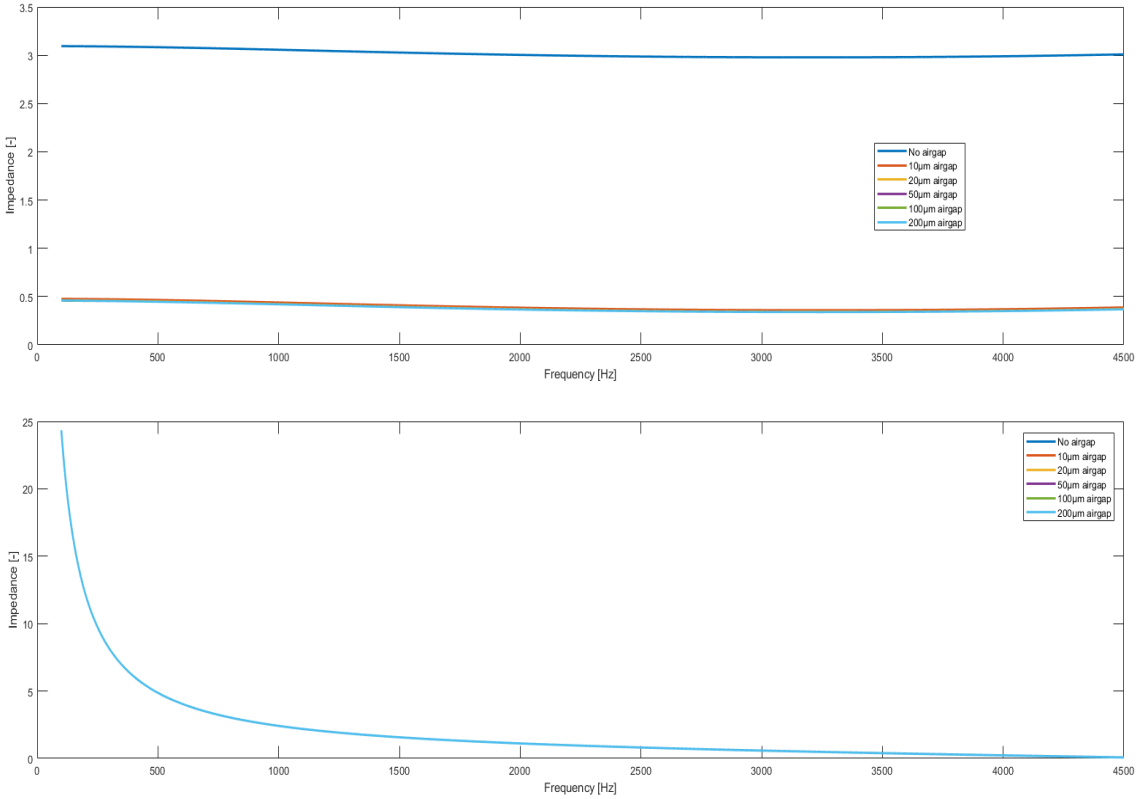

Figure 5.10: Results of using the airgap-corrected value for median pore size in the two layer model.

A circumferential airgap also impacts the low frequency absorption of the sample in the greatest manner, effectively halving the absorption coefficient beneath 1500Hz, and reducing it by 25-33% up to 2000Hz. Interesting, it also appears as is the size of the airgap is less impactful than its presence alone, with there being very little change between 20 µm and 200 µm sizes. This is likely down to the membrane influence, as it is so highly resistive that the introduction of any airgaps will lead to a noticeable decrease in that resistivity – it was noted earlier that the size of the airgap and decrease in resistivity are linked via an inverse squared law. Another possible reason for the decrease in sensitivity to airgaps as the size of the airgap

increases could be due to the material thickness. The above equations and calculations are assuming that the melamine sample is a perfect fit in the impedance tube and that there are no circumferential airgaps present in that layer. The membrane thickness in this instance is only 22 µm and so above a 20 µm airgap, the airgap is equivalent or greater to the size of the membrane layer.

5.3.3 Model sensitivity

As can be seen in Tables 5.3 - 5.5 there is some variability in the retrieved values of pore size and corresponding flow resistivity, even between specimens of the same sample. In addition, there are also much greater variations in predicted results between certain samples. An example of this is membrane sample V2 and membrane sample V3, in which plausible results for pore size and sigma are retrieved for sample V2, but a porosity value of 0.01 and an airflow resistivity value of 1.448 Pa·s/m^2 are retrieved for sample V3. This is believed to be caused by the model being too sensitive to and dependent on significant changes in the parts of the surface impedance between the experimental data of the substrate and the membrane. This can be illustrated in Figure 5.11, which shows the real part of the impedance for samples V2 and V3 (top and bottom, respectively). This figure shows a noticeable difference between the real parts of the substrate and the membrane in the acoustical data for sample V2. This difference is much less pronounced in the acoustical data measured with sample V3 which can be related to the effect of the circumferential air gap. In each of the membranes for which the non-acoustical could not be accurately inverted, the difference between the real parts of the substrate and membrane are similarly small, and as a result it is suspected that the model is not sensitive enough to such comparatively minor changes in the impedance.

It is possible that the observed minor changes to the impedance of the membrane versus the substrate is influenced by the circumferential airgap as outlined in Section 5.4.2, utilising the work by Pilon which highlighted that a circumferential airgap will decrease the real part of the impedance (Pilon, 2002).

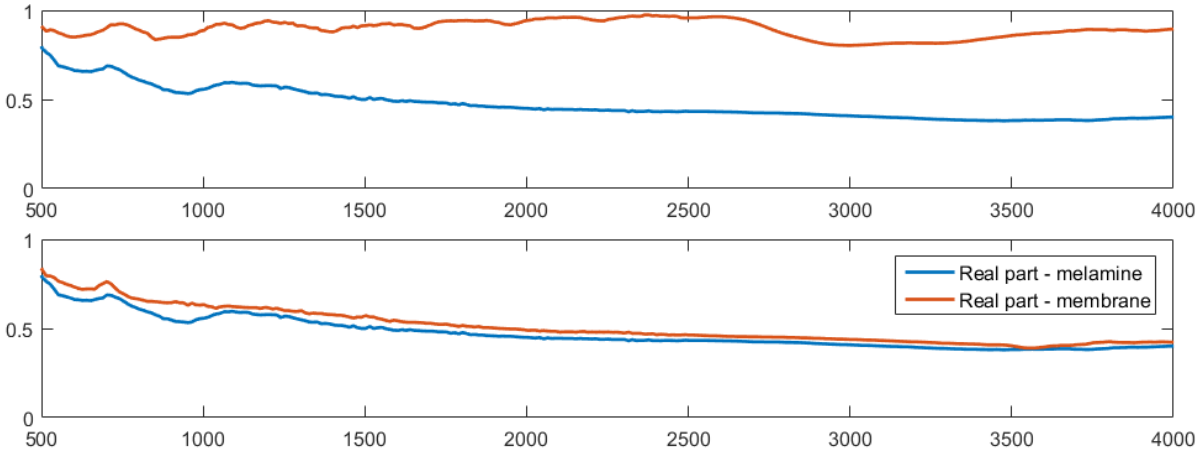

Figure 5.11: Comparison of the differences in real parts of the membrane and substrate for samples V2 (top) and V3 (bottom). The real part of membrane is represented by the combined real part of the melamine and membrane.

From Table 5.9, it is apparent that even small airgaps can have a great impact on the value of the retrieved pore size and airflow resistivity. If there was a 10 µm airgap on a membrane sample it is possible that the real part would still be significantly different enough that a value of pore size and airflow resistivity could be retrieved, but it would not be truly representative of the actual values within the material. It also follows that a much smaller airgap, for example 1 µm as either a circumferential airgap or a gap along part of the circumference, will also impact the retrieved values of pore size and airflow resistivity. Such small tolerances in the inversion process make it very challenging to invert truly accurate or representative values.

5.3.4 Knudsen Number considerations

When the pore size of a material becomes comparable to the mean molecular free path, l_{mean}, of a material – typically assigned a value of 60 nm for air in normal conditions, such as seen in this work – the no-slip conditions assumed at the pore surface are no longer valid and as a result, the slip effects must be considered. When modelling the acoustical

properties of such a material the slip effect on the velocity and thermal impacts must be considered, as it has been shown that these impacts provide 'significant' changes to attenuation coefficients and sound speed values. In this instance, the thermal impacts are describing the temperature spikes on the walls of the materials pores. A review of previous works on boundary slip and how it affects other parameters such as sound propagation in Umnova, *et al*, 2009.

The effect of the Knudsen number on flow resistivity can be described in the following four equations:

$$\sigma_{II}(K) = \frac{\sigma_{II}(K=0)}{1 + 4KF(\phi)}$$

Equation 5.23

where

$$\sigma_{II}(K=0) = \frac{8(1-\phi)\eta}{(-2\ln(1-\phi) - 2\phi - \phi^2)a^2}$$

Equation 5.24

$$F(\phi) = \frac{\phi^2}{-2\ln(1-\phi) - 2\phi - \phi^2}$$

Equation 5.25

These equations lead to an expression describing the adjusted airflow resitivity, $\sigma(K)$:

$$\sigma(K) = \frac{2(\sigma_{II}(K=0))}{1 + \frac{4K}{1K}F(\phi)}$$

Equation 5.26

where K is the Knudsen number $= l_{mean}/a$. For a perfect slip condition $K \to \infty$ and σ_{II} will equal zero.

To assess if no-slip conditions could be affecting the modelling results presented earlier in this chapter, the values of $K, \sigma_{II}(K=0), F(\phi)$, and $\sigma(K)$ were calculated. The values of K and $\sigma(K)$ are presented in Table 5.10, along with the parameters used in their calculation.

Mean molecular pathway, a	Porosity, ϕ	Knudsen number, K	Adjusted airflow resistivity, $\sigma(K)$
3.99×10^{-6}	0.83	0.0150	9.6543
3.99×10^{-6}	0.98	0.0150	0.2893

Table 5.10: Effect of considering no-slip conditions on the materials used in this work.

The values of ϕ and a are averaged from modelled and estimated values of the PMMA samples which are described in Table 5.1. The values of K and a seen here do fall within the 'Knudsen regime' (Lockerby, *et al*, 2004). Despite this, we believe it is unlikely that the observed results will influence the classically estimated values of flow resistivity and hence are not contributing to the issues presented with modelling in Section 5.1 of Chapter 5.

5.4 Acoustic characterisation of nanofibrous membranes

This section presents the acoustical data retrieved from two microphone impedance tube testing for the membranes, using the methods outlined at the start of Chapter 5. The greatest overall acoustic performances were seen with membrane samples IV and V, and the 18kV PMMA and 24kV PMMA membrane samples. The absorption spectra for these three materials can be seen in Figure 5.12.

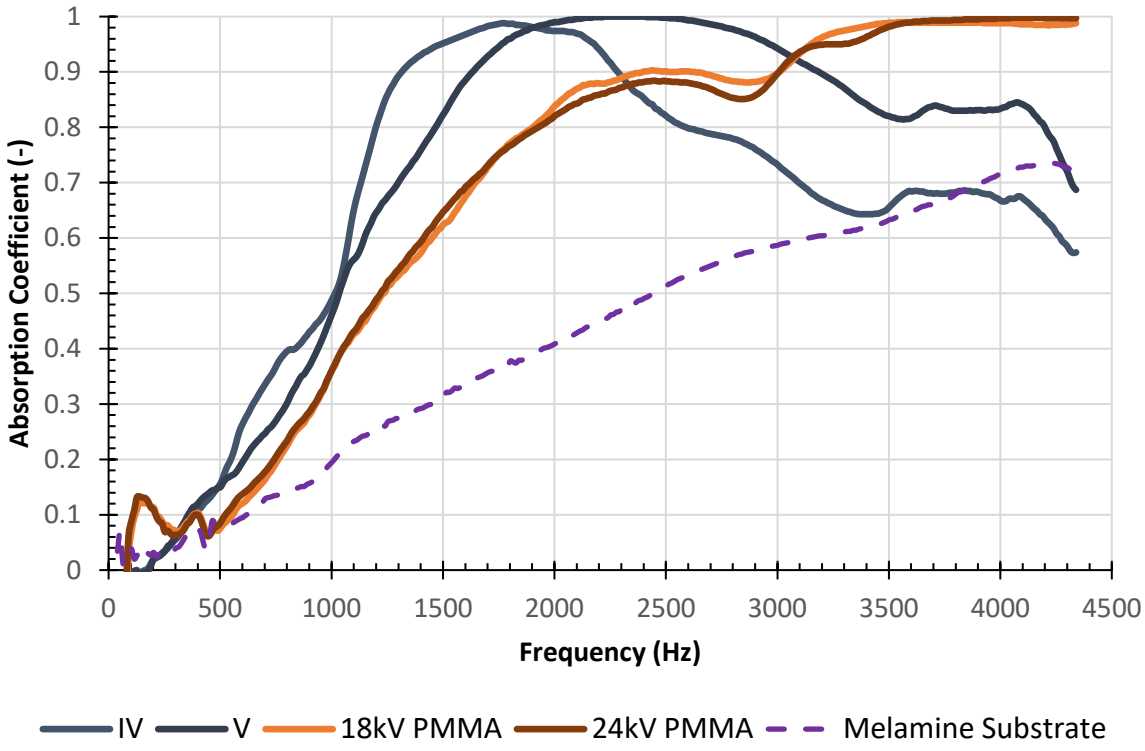

Figure 5.12: Absorption spectra for the top four performing membrane samples.

The first observation is that there are three very differently shaped spectra in this comparison, each of which has been governed by a combination of material parameters. For example, the

shift towards the low frequencies seen with membrane samples IV and V is as a result of their thickness (220µm and 200µm, respectively). In both these samples, there is then a rapid decrease in the value of absorption coefficient, whilst the 18kV and 24kV PMMA membrane samples are still increasing. This is caused by the difference in fibre diameters, with the average of membrane sample IV being 1130 nm versus the 310 nm average of the 18kV PMMA membrane sample. This section will attempt to explain the relation between the material parameters characterised in Table 5.8 and the absorption spectra obtained via two-microphone impedance tube testing.

In a similar approach, an investigation into how changing the electrospinning parameters covered in Section 3.2 impacts the acoustic performance will also be presented.

5.4.1 Relationship of acoustic performance to membrane properties

In Chapter 4, it was established that the key parameters in determining the acoustic performance of a fibrous nonwoven material are its fibre diameter, its density, and its thickness. This appears to also be partially true in the case of the nanofibrous membranes, though in addition to those, pore size and airflow resistivity (both of which are dependent on porosity, and so density) also appear to have a greater impact on the acoustic performance.

The acoustical data obtained from the investigation into varying the electrospinning and chemical parameters of PET revealed some interesting relations. Directly comparing Samples IV and V to I – III was challenging due to such a large difference in the thickness of the materials (200 µm vs 10 – 20 µm, respectively). Alternatively, comparing the properties of Samples I – III and IV – V separately made it apparent that fibre diameter had a significant impact on the acoustic performance. This was best illustrated by comparing the absorption of Samples II and III (Figure 5.14). In Table 5.8 it can be seen that these membrane samples have similar thicknesses, densities, and porosities, but the fibre diameter differs. The average fibre diameter in Sample II was 340 nm, whilst the average fibre diameter of Sample III was 240 nm (Figure 5.13). This difference in fibre diameter lead to a 10% difference in the acoustic absorption performance across a large part of the frequency range.

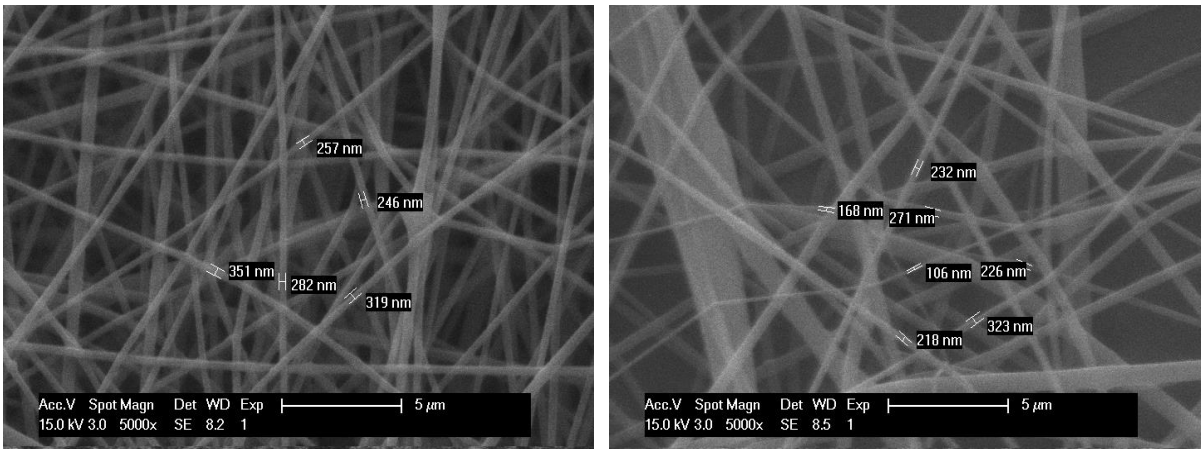

Figure 5.13: Comparison of fibre diameters in Samples II (left)and III (right).

The average fibre diameter present within the nanofibrous membrane also impacts the frequency range in which peak absorption occurs. Referring back to Figure 5.12, it is clear that the smaller fibre diameters present in the 18kV and 24kV PMMA samples increase the absorption coefficient at higher frequencies. There is a clear decrease in the acoustic absorption performance of membrane samples IV and V with their significantly larger fibre diameters. This effect can be explained by the increase in the real part of the surface impedance of the membrane/substrate system. In this way the real part, R, becomes comparable to the imaginary part, X, which is relatively large for the melamine layer only. The real part in the membrane/substrate system is controlled by the resistance of the nanofibrous membrane, which is the product of the membrane's flow resistivity and its thickness. The absorption coefficient of this kind of layer system reaches a maximum when $R \sim X$ (see eq. 4.5.6 on page 4.12 in Ingard, 1994). In order to maximise absorption, the correct combination of thickness and airflow resistivity is needed as they both impact on different parts of the frequency range. The value of R becomes more comparable to X as the layer thickness increases, whilst decreasing the fibre diameter will increase flow resistivity – also making R more comparable to X.

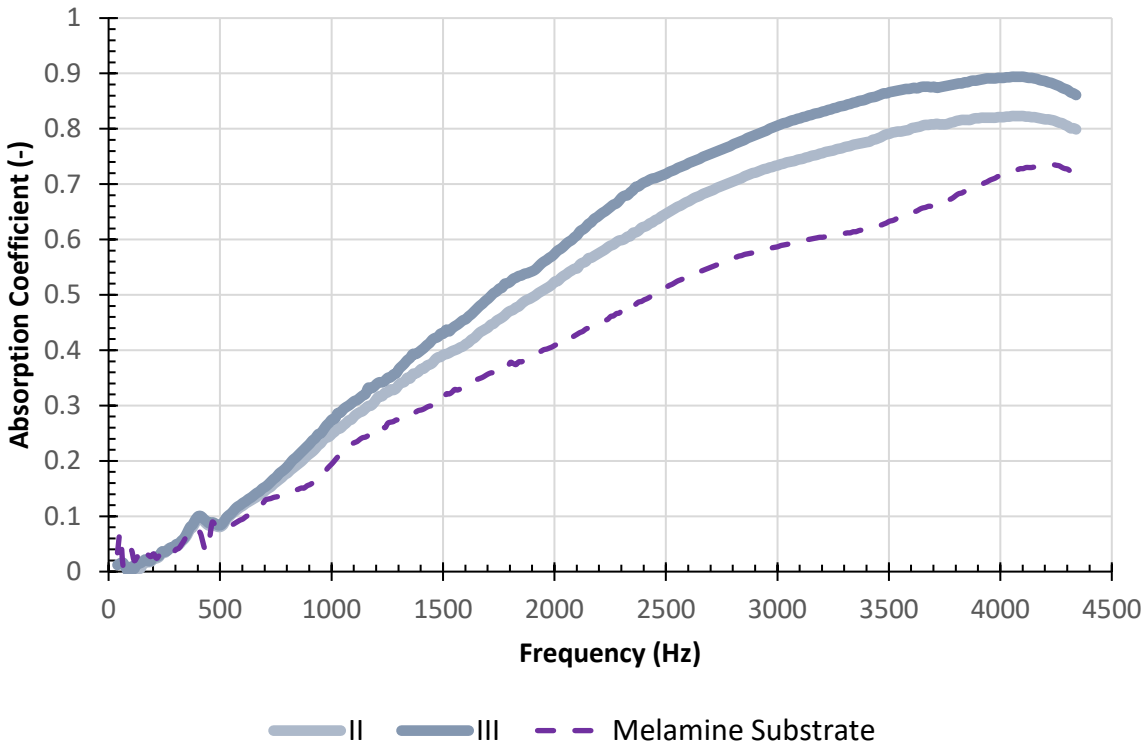

Figure 5.14: Absorption spectra for membrane samples II and III, highlighting the impact that changes to fibre diameter have.

One other important parameter was membrane thickness. An increase in the low frequency absorption attained with membrane samples IV, V, and 10% PCL is a result of the difference in their thickness (Figure 5.16). This increase in thickness appeared to predominately impact the lower frequency absorption, with some decrease in absorption performance observed at frequencies above 3500Hz. This echoes what is reported both by literature and our own experiments for the nonwoven media such as covered in Chapter 4 (Ingard, 1994; Coates, Kierzkowski, 2002). Interestingly, the increase in thickness between Samples I and II (19 µm vs 12 µm, respectively) resulted in approximately a 10% increase in sound absorption between 2000 – 4500 Hz, further reinforcing that lower frequency sound absorption properties in nanofibrous membranes is governed by thickness. Figure 5.15 presents SEM images highlighting the difference in thickness between Sample II and Samples V.

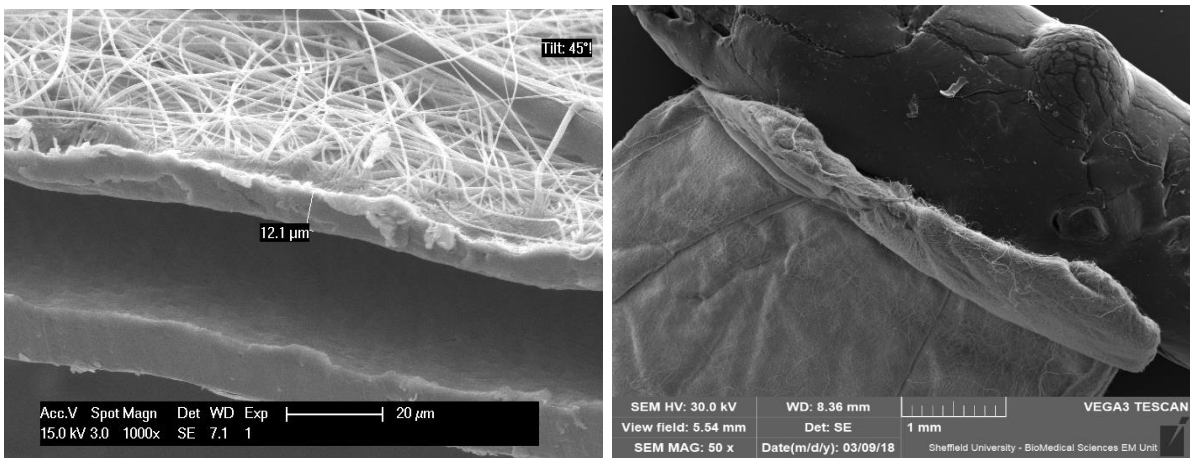

Figure 5.15: Visual comparison of thickness differences in Sample II (left) and V (right).

Unfortunately, neither I or my collaborators were able to synthesise a material with a thickness of around 200 µm and a fibre diameter in the range of 200 – 400 nm to see if the smaller fibre diameter remedied the reduction in the acoustic performance above 3500 Hz seen with these thicker membranes. Comparison of Samples IV and V with the 10% PCL Sample does however show that further increasing the fibre diameter to an average of around 1200 µm (versus 1100 µm for membrane samples IV and V) results in a decrease in the overall absorption across the whole frequency range. This could suggest that decreasing the fibre diameter whilst maintaining a 200 µm thickness may yield an even greater increase in the absorption across the full frequency range.

The results suggest that decreasing the average fibre diameter in a material will increase its fibre density and decrease the average pore size too. This proves true in the case of these nanofibrous membranes, where there is the general trend of decreasing pore size with decreasing fibre diameter. This is in agreement with literature reports for microfibrous porous media as covered in Chapter 4 (Koizumi, *et al*, 2002). As with a decrease in fibre diameter, this also appears to result in increased acoustic performance towards the higher frequencies. This is perhaps most evident while comparing the acoustic absorption of membrane samples CF_B and CF_C (Figure 5.17). In Table 5.8 they have similar values of fibre diameter, similar thickness, and similar densities but the difference in pore sizes is 108%.

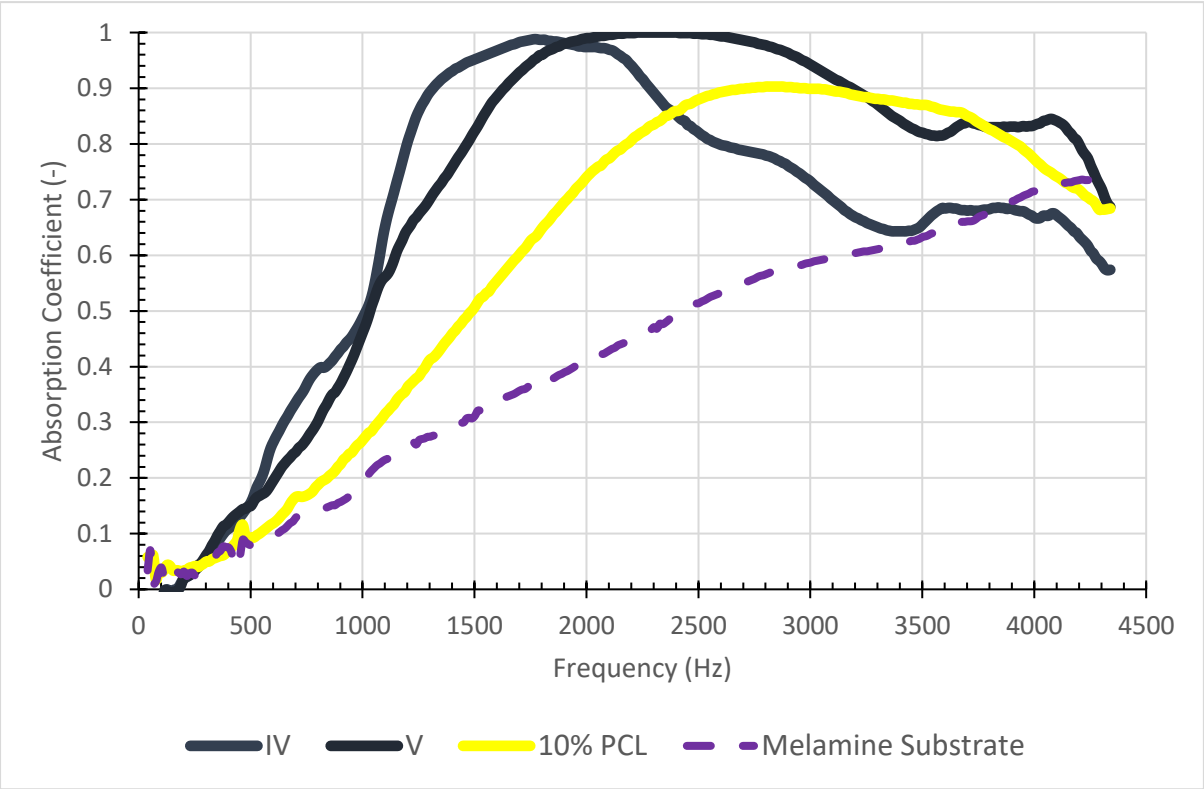

Figure 5.16: Absorption spectra for the three thickest membrane samples, highlighting impact of membrane thickness on low frequency absorption.

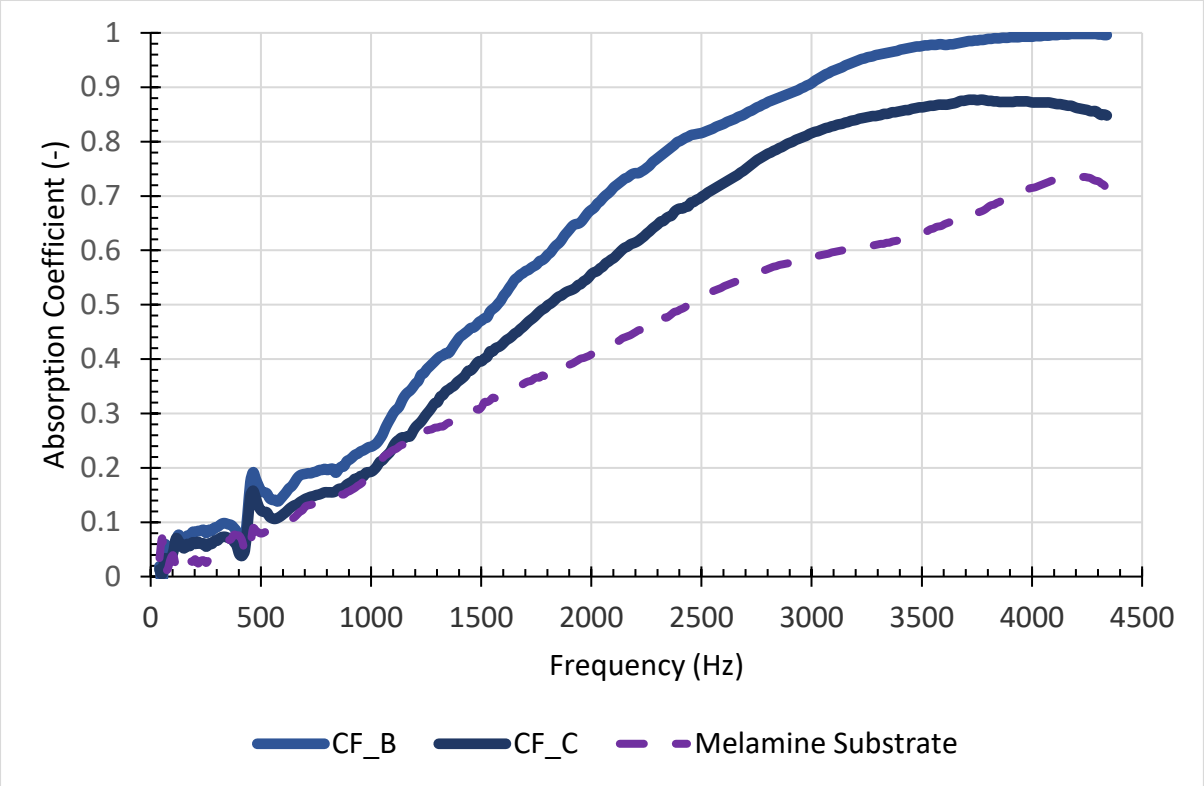

Figure 5.17: Absorption spectra for CF_B and _C, comparing the impact pore size has on acoustic performance.

The smaller pore size seen in Sample CF_B (Figure 5.18) results in an improved absorption curve, with higher values of absorption from as low as 500 Hz, up the maximum measured frequency of 4350 Hz. The reasoning behind this observation is that smaller pore sizes will increase the airflow resistivity of the membrane (also visible in Table 5.8, with the airflow resistivity of Sample CF_B being an order of magnitude greater than that of Sample CF_C). A more significant illustration of the impact that pore size can have on the absorption spectra can be seen by comparing the 15kV PMMA membrane sample with the 5gsm TPU membrane sample (Figure 5.19).

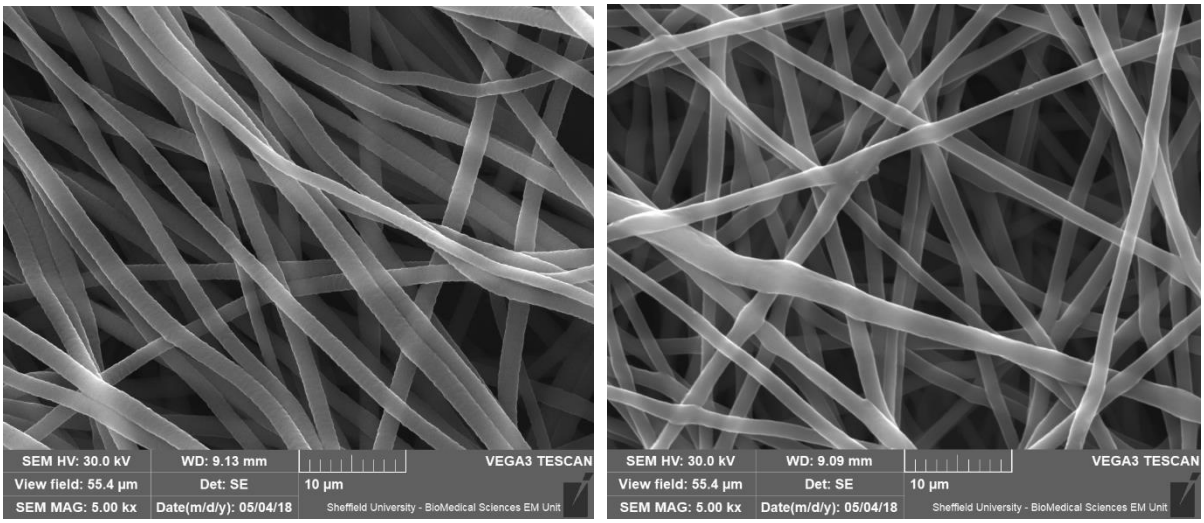

Figure 5.18: Comparison of pore sizes in Sample CF_B (left) and CF_C (right).

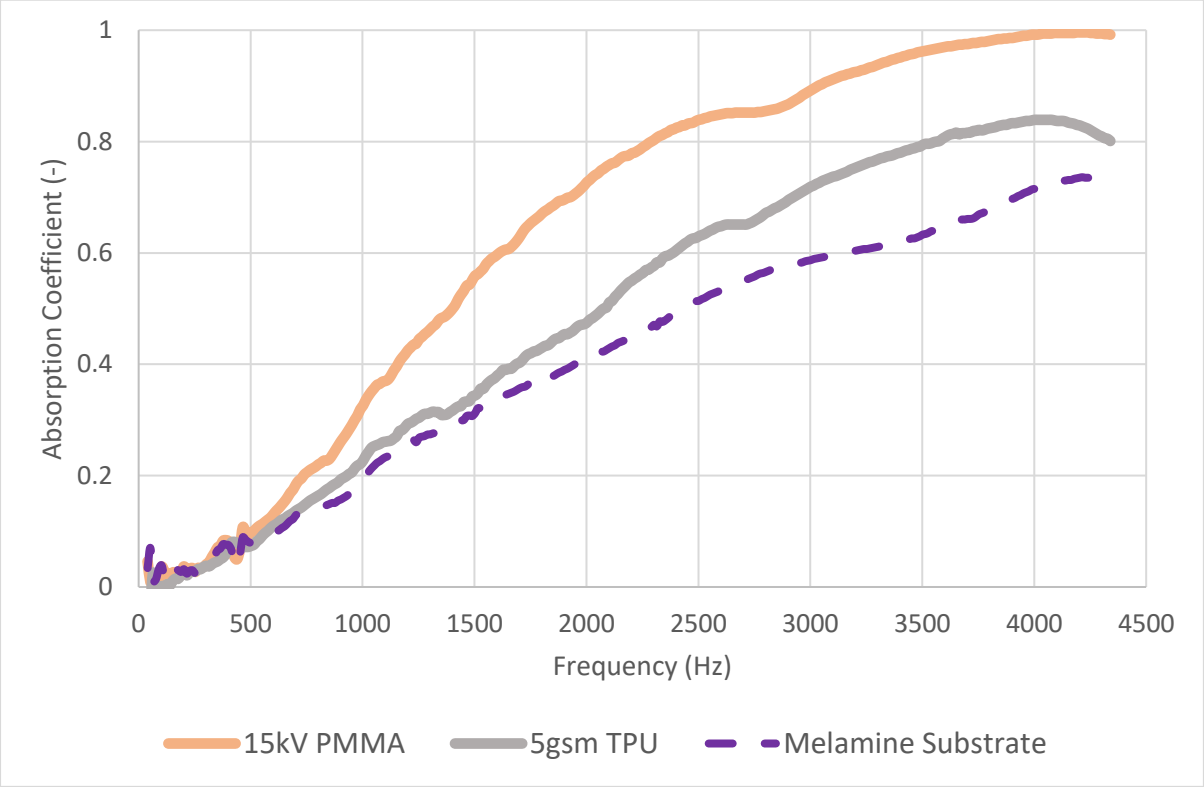

Figure 5.19: Comparison of 15kV PMMA and 5gsm TPU membrane samples, highlighting the importance of pore size on acoustic performance of the membranes.

By comparing the two in Table 5.8 it is clear that the only significant difference between the two membrane samples is the pore size and density (which appears to have no statistically significant effect on performance in nanofibrous membranes), with 5gsm TPU having a median pore size 84% larger than that of 15kV PMMA.

There is a correlation between greater acoustic performance and higher values of airflow resistivity, but it is challenging to state that empirically due to the difficulties faced with retrieving a value of flow resistivity. The summary of the results shown in Table 5.8 and Figure 5.12 suggests that there is a correlation between a higher value of the membrane's flow resistance, $\sigma \cdot h$, and a better acoustic performance. The results shown in Figure 5.12 illustrates that the best acoustical performance is attained with membranes that possess the highest values of $\sigma \cdot h$ (with the exception of Sample CD1, which is believed to be caused by the circumferential airgap impact as discussed in Section 5.3.2). To understand whether this increase in performance is governed solely by a very high airflow resistance, a non-porous material (cling film) of comparable thickness (40µm) was placed on top of the same melamine substrate and tested acoustically. The spectra from this test can be seen in Figure 5. 20, below. The density of this low-density poly(ethylene) based clingfilm, as stated by Dow Chemical is 900kg/m^3.

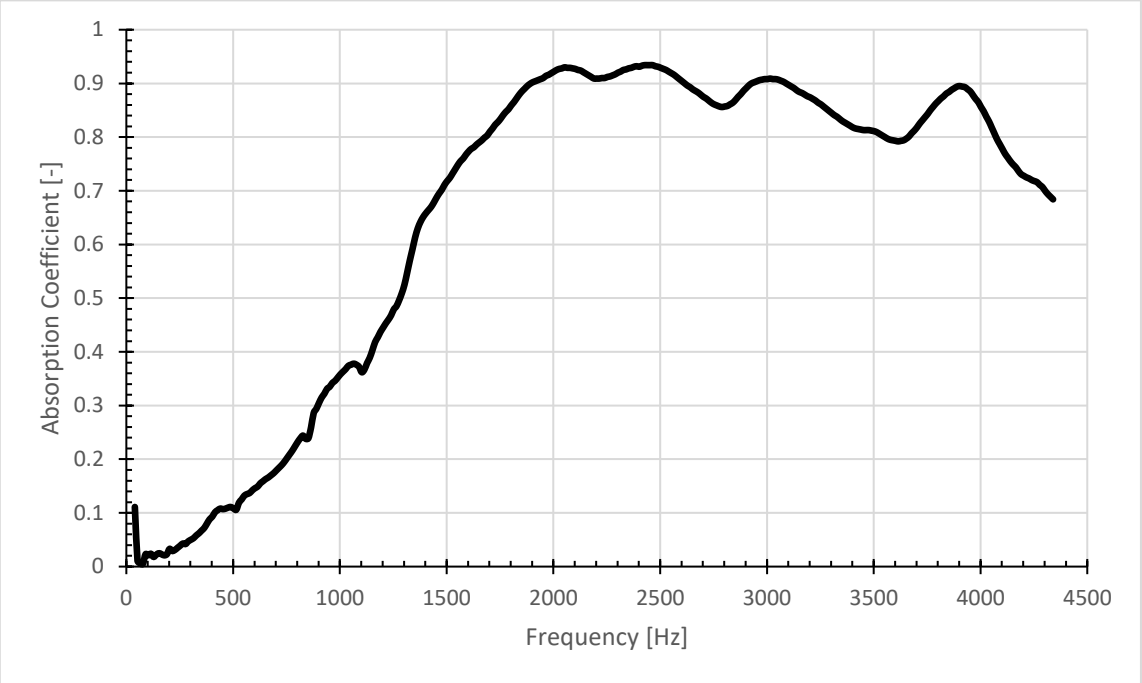

Figure 5.20: Absorption spectra for melamine substrate plus melamine substrate.

The impact on absorption is similar to that seen with the nanofibrous membranes. The cling film will be impervious to air and so will have an airflow resistivity much greater than the membranes tested in this section. Any effect on absorption as seen in this figure will only be caused by the mass effect of the membrane on the surface of the substrate. This is relatively easy to model and can be seen in Figure 5.21 below. The observed increase in the absolute part of the imaginary impedance is to be expected and matches the modelled observations. The effect in the real part of the impedance is trickier to model as it will be affected by the vibration of the cling film on the surface of the substrate, but the observed result still matches the modelled result to a reasonable degree. What this shows is that the effects seen with the nanofibrous membrane are not solely down to the mass effect of the membrane on the surface of the melamine, or down to the very high airflow resistivity present within the membrane samples. Other non-acoustical parameters also have a very apparent effect on the

shape of the absorption curve and at the frequency at which the absorption coefficient reaches a maximum.

A further comparison of the acoustic absorption coefficient of Samples I, II, IV and V also revealed that the density of these membranes did not appear to correlate significantly to the absorption. The density of 303.99 kg/m^3 for membrane sample II was almost twice that of Sample I, with a density of 155.37 kg/m^3, yet the latter membrane exhibited the greater performance as a result of its greater thickness. This could also be seen with Samples IV and V, with densities of 35.87 kg/m^3 and 17.54 kg/m^3, respectively. Sample V out-performed Sample IV at higher frequencies despite having a density one half of that of Sample IV. The one exception to this is membrane sample CD1, which yielded one of the best acoustic performances. Despite CD1 and CD3 having similar material properties such as thickness and fibre diameter, Sample CD1 has an 18% difference in flow resistivity and a density value 350 times greater (Figure 5.21) which contributed to a value of absorption coefficient approximately 41% larger (Figure 5.22). As we could not accurately model or measure the airflow resistivity it is difficult to assess the impact of density alone, but given the relative increases in value of each parameter, I believe that density does play an important role in the determination of absorption values in membranes.

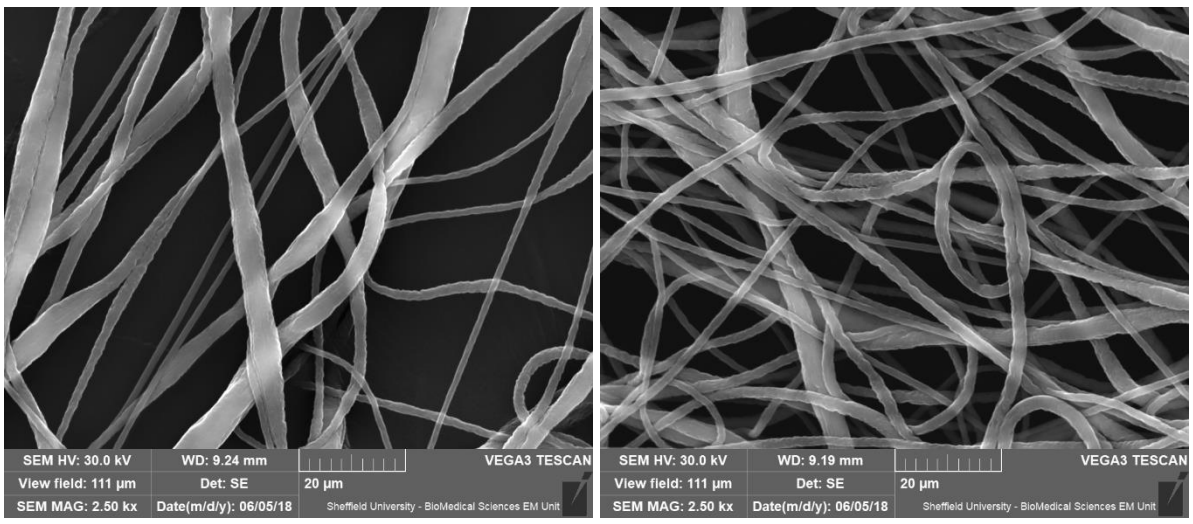

Figure 5.21: SEM images comparing density of Samples CD3 (left) and CD1 (right).

It could also be said that porosity did not correlate with the absorption. There was no clear advantage being seen for higher or lower values of porosity, though this is slightly harder to quantify due to the issues associated with measuring for porosity. Without a reliable and accurate method to measure fibre density in these membrane samples, the true value for fibre density in nonwoven materials had to be used in the estimation of porosity. As a result, there are some instances (see Table 5.8) where the porosity values made no sense or were significantly different to the expected from the SEM images. Without accurate values of porosity for all membranes is not possible to link porosity to the acoustic performance.

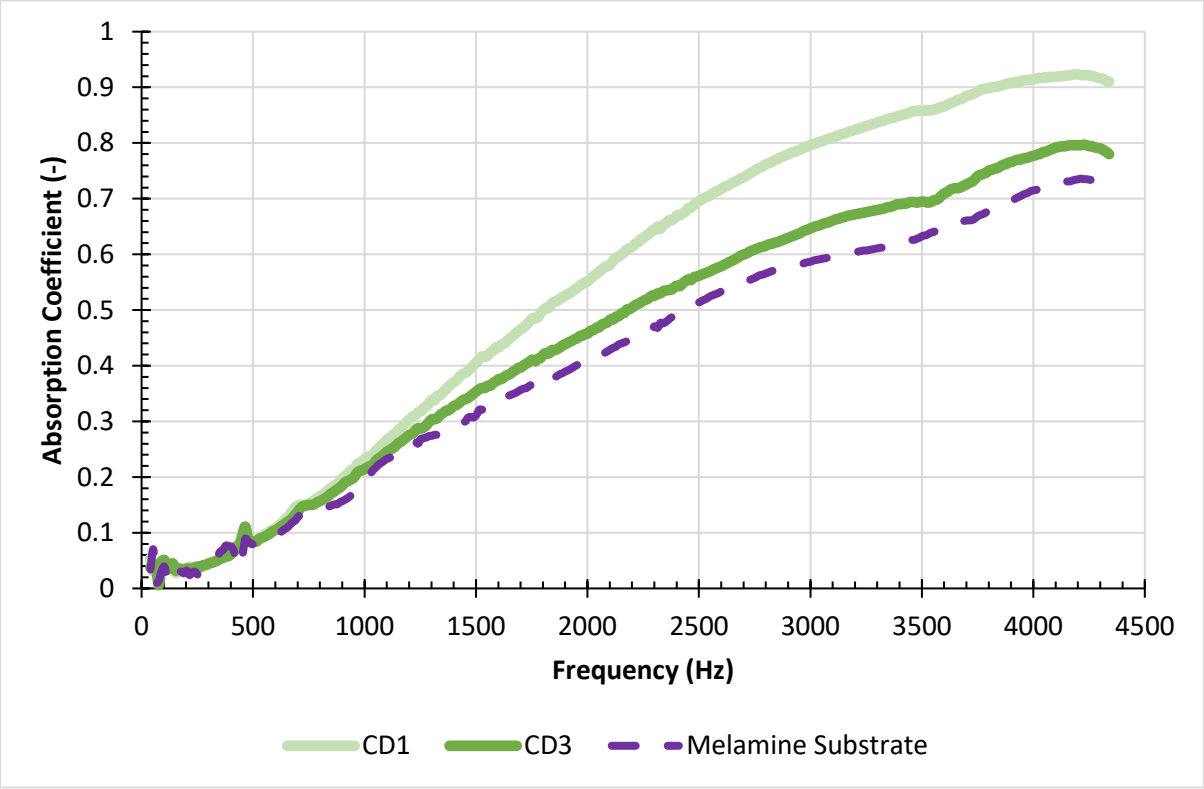

Figure 5.22: Absorption spectra for membrane samples CD1 and CD3, highlighting the single instance found where density had a significant impact on acoustic performance.

5.4.2 Impact of electrospinning parameters on acoustic performance

When electrospinning these materials, changing a number of parameters in the process will produce different fibres. The electrospinning process and the parameters which can be changed are covered in detail in Section 2.5.2 in Chapter 2. These include changes to the polymer solution, such as concentration or surface tension, as well as changes to the set-up of the electrospinning rig, such as voltage and collector distance. This section will attempt to relate changes in these areas to the acoustic performance of membranes made via this process and to understand how to tailor the process to a certain acoustic performance.

It is apparent that by increasing the voltage by just 4kV (Sample V1 to Sample V3, for example) the maximum value of absorption decreases by 17% (0.863 to 0.751, respectively). Literature by Deitzel concluded that increasing the voltage in the electrospinning process will increase the mass flow rate of fibre to the collector, which itself often leads to greater entanglement of fibres, fibre deformation and the formation of bead on string morphologies (Dietzel, *et al*, 2001). This bead on string morphology will have a greater average fibre diameter than a smooth regular fibre, and as seen earlier in this chapter a smaller fibre diameter results in increased acoustic performance. This was also visible during the SEM, where the average fibre diameter of Sample V1 was 3.19 ± 1.60 µm whilst Sample V3's average fibre diameter was 5.41 ± 2.03 µm. The increase in entanglement and presence of beads can be seen in Figure 5.23. As outlined in Section 5.4.1, fibre diameter is one of the dominating factors in controlling the absorption properties of a membrane, and smaller fibres generally result in a smaller pore size, high flow resistivity and greater acoustic absorption.

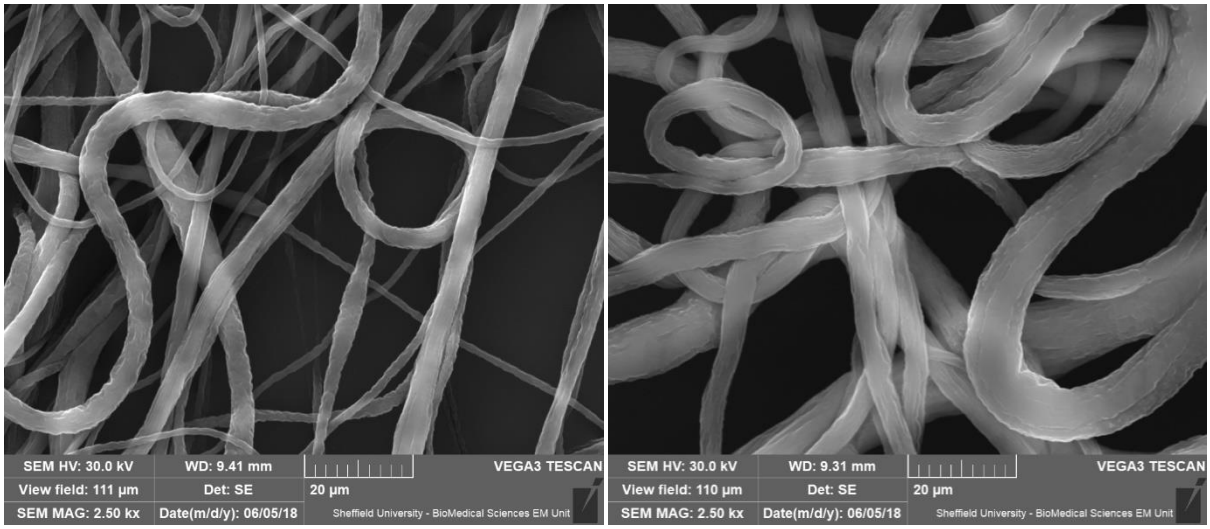

Figure 5.23: Comparison of Samples V1 (left) and V3 (right), where it can be seen that V3 has greater entanglement, much larger fibre diameters, and less regular fibre morphology.

Lower voltages can therefore provide improved acoustic performance by decreasing the average fibre diameter and improving the homogeneity of the fibres.

Changing the collector distance can again impact the formation of fibres and their morphology. It has been reported (Ghelich, *et al*, 2015) that too large a collector distance or too small a collector distance will result in a greater number of fused fibres, or an increase in fibre diameter. The former of which is caused by the polymer jet having insufficient whipping time, so the fibres are drying on the collector plate and fusing; the latter observation proposed to be caused by a reduction in the electrostatic field strength resulting in less stretching of the polymer jet (Lauricella, *et al*, 2017). Whilst this increase in fibre diameter was not seen in this PhD, possibly due to relatively small changes in collector distance (a maximum of 6cm), it was observed that increasing the collector distance from 16cm to 22cm (as seen in CD1 to CD3) led to a decrease in acoustic performance of 16%, which can be attributed to the increased diameter and increase in median pore size.

This decrease in absorption was most likely caused by an increase in the median pore size of CD3. An increase in the collector distance leads to the polymer jet drying before depositing the jet on the collector – meaning the polymer jet had less time to whip and thin. Comparing the SEM images of the two (Figure 5.25), it appears as if CD1 has slightly smaller fibre diameters which are less aligned than in CD3, contributing to an overall smaller pore size. This confirms that in CD3 the sample dried before reaching the collector, whipping less and forming a more aligned membrane.

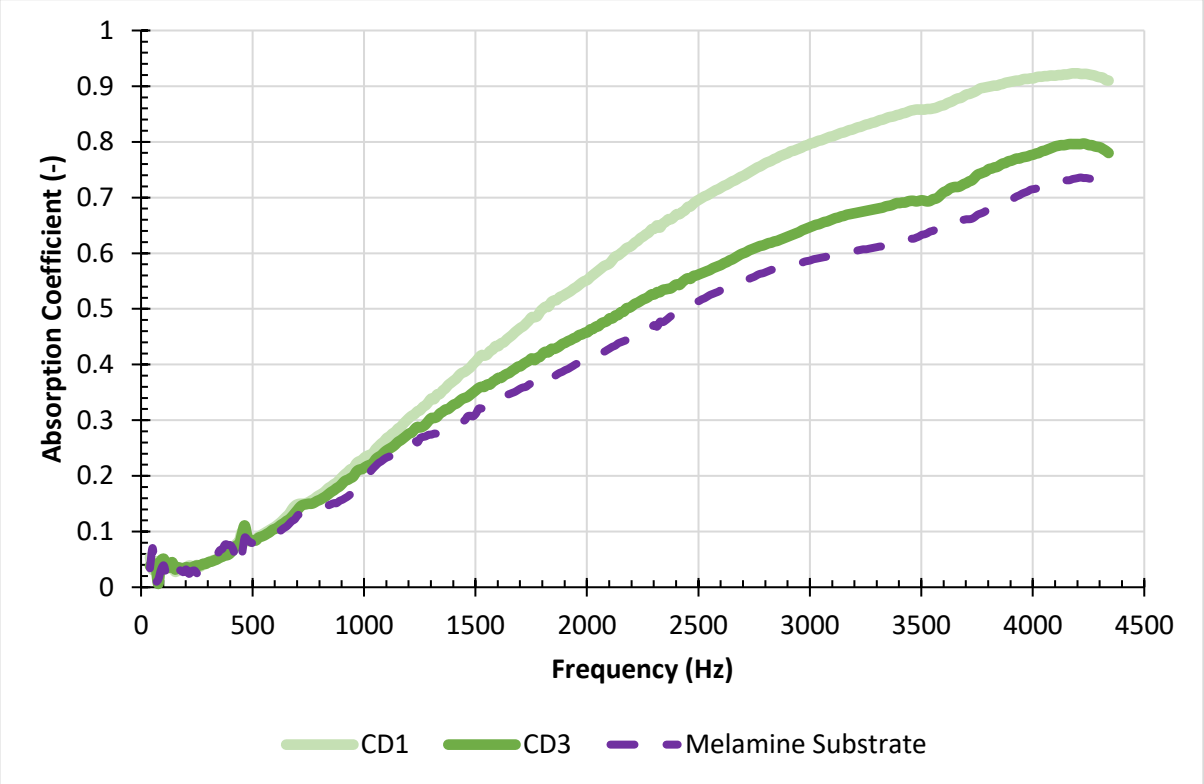

Figure 5.24: Comparison of absorption spectra in samples with increasing collector distance.

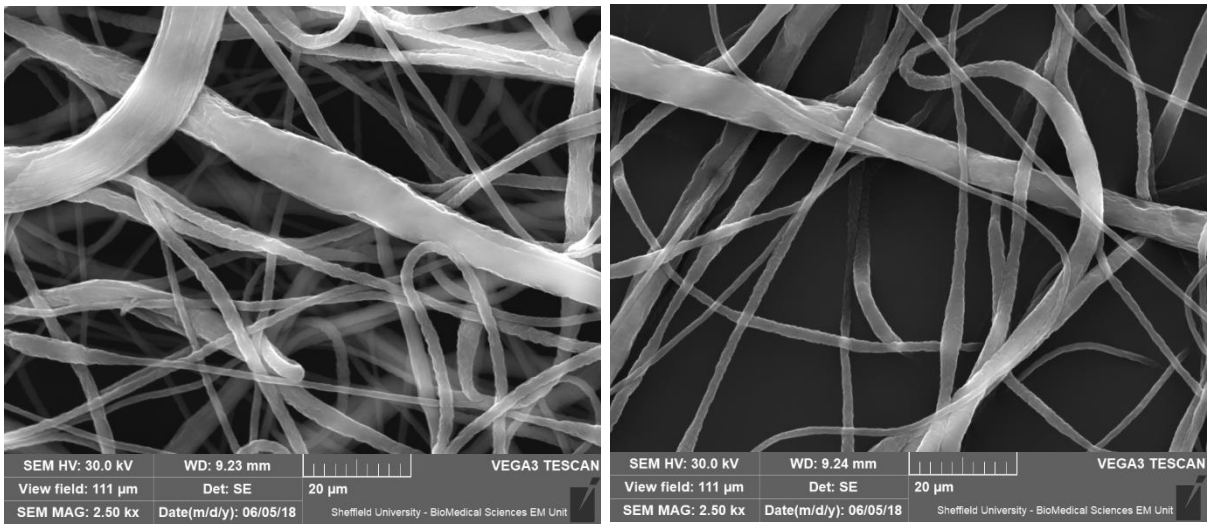

Figure 5.25: SEM images of Samples CD1 and CD3, showing difference in spatial arrangement of the fibres and fibre diameters.

Comparing the absorption spectra for Samples V1 and FR2 suggests that decreasing the flow rate has a small impact on the maximum acoustic absorption which decreases by just 2% (0.866 to 0.850, respectively). This change is small enough to be attributed to an experimental error, losses in the impedance tube or natural variation in the consistency of the electrospinning process. This change in flow rate predominately appears to impact the fibre diameter, but not in a great enough way to significantly affect the absorption properties of the membrane. As such, it could be stated that changing the flow rate does not impact the acoustical performance of nanofibrous membranes.

The experiment looking into the use of different needle diameters to reduce the problem of an overly large and unstable Taylor's cone (shown in Figure 5.26) revealed that changing the needle tip had a negligible effect on the acoustic performance. This could possibly be explained by the relative change in the material properties. The two membranes generated using a 0.514mm needle tip and 0.838mm needle tip did not have significant different material parameters. These membranes had similar fibre diameters. It could therefore be said that changing the needle tip to improve the stability or flow rate within the

electrospinning process will not affect the acoustic performance of the resulting nanofibrous membrane.

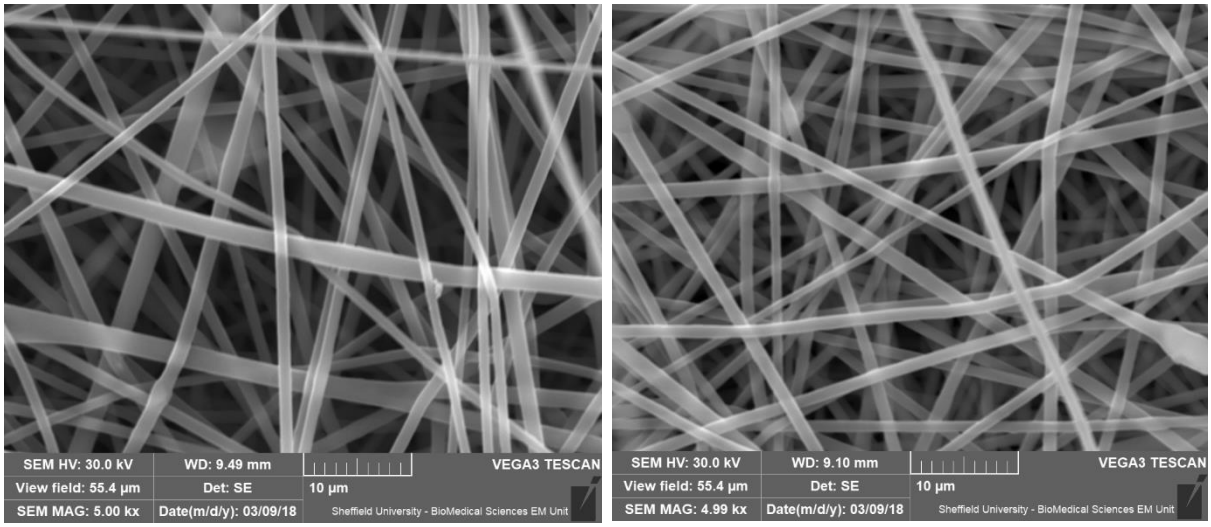

Figure 5.26: SEM images of the fibre diameters and membrane structures from the 0.514mm (left) and 0.838mm needle tips (right).

The concentration of the polymer in the solution was also found not to be a dominant factor in dictating the acoustic performance. This was the area of investigation in the first five PET-based syntheses, where the only variable was the concentration of the PET polymer solution. All other parameters in the process were controlled, and the volume spun for each solution of concentration was within 10% of each other, so in theory, thickness and density should have been similar. The acoustic absorption data shown in Figure 5.18 suggest that the material properties such as fibre density and pore size exert a relatively greater impact on the acoustics. Whilst the concentration of the polymer can be used to partially control the fibre diameter, it is not the most effective method of doing so and generally needs to be varied alongside other electrospinning parameters like the voltage.

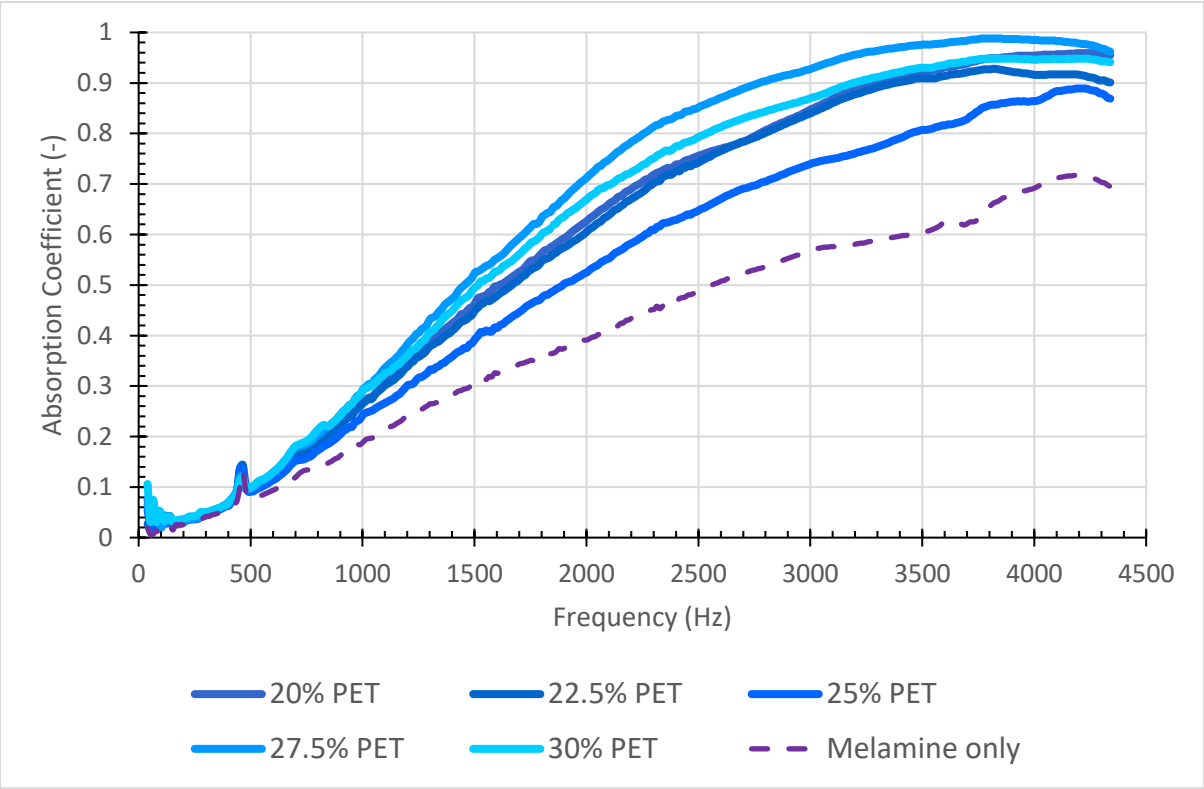

Figure 5.27: Absorption coefficient for 20-30% PET in TFA membranes on the top of a 16mm layer of melamine foam used as a substrate.

The set of membranes synthesised from a 12.5% concentration of PCL, with varying solvent systems were used to observe the effect solvent had on the synthesised membrane performance and material characteristics, in particular the fibre diameter and fibre morphology (i.e. ribbon, bead on string, fibrous, open-pore, closed-pore, etc). The acoustic absorption coefficient of these membranes can be seen in Figure 5.28. The exact ratios of each solvent used to create the solvent system are given in Tables 3.9 and 3.10 in Chapter 3. Each solution was spun for a total of 0.5 mL, with the maximal volume spun being 0.5402 mL and the average being 0.5182 mL. The other electrospinning parameters such as the voltage, collector distance, and flow rate were also kept constant to try and keep material density and membrane thickness roughly the same.

The maximum absorption was obtained with Sample CF_B reaching the maximum absorption of 0.998 at 4200 – 4250 Hz. The minimum effect was for Sample THF_C for which the maximum absorption was 0.891 at 4039 Hz. Sample THF_C also exhibited significantly lower performance than the other membranes through the mid-range frequencies, having at least 10% lower values of absorption from 2000 – 3500Hz. The performance of Samples THF_F and CF_C are nearly identical, as well as for Sample s THF_A and THF_C(ii) (see Figure 5.28).

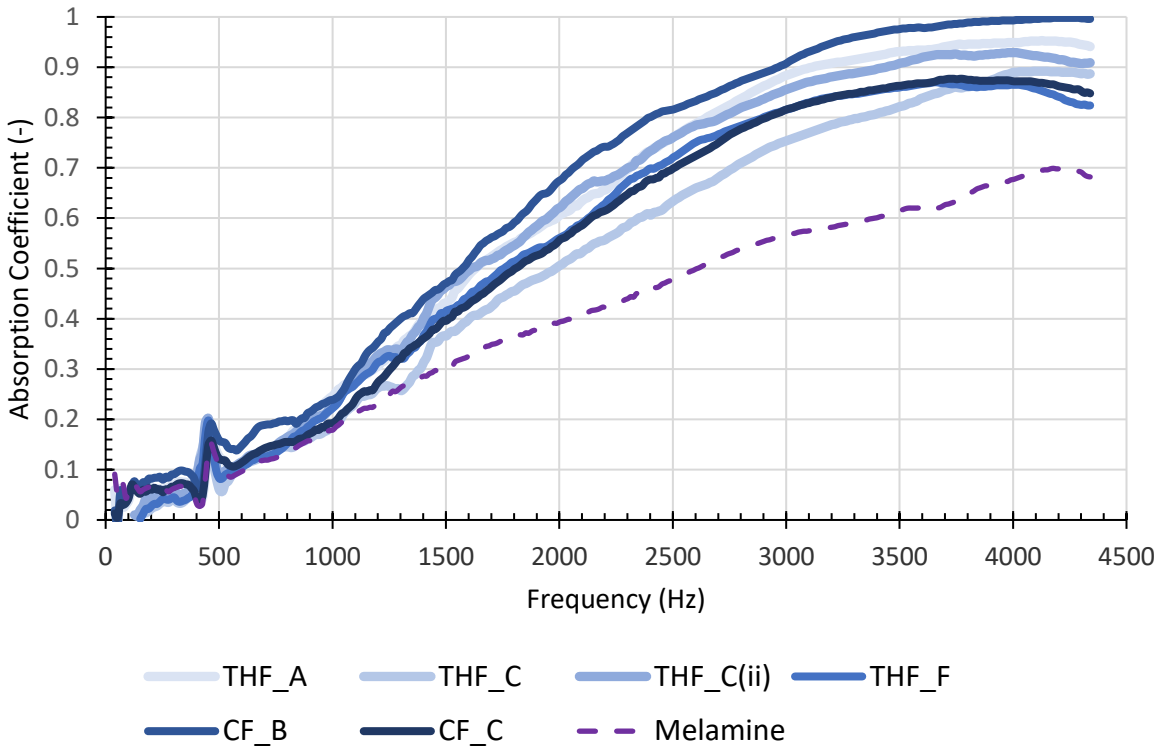

Figure 5.28: Absorption spectra for varied solvent systems.

The solvents and their ratios for this section of work can be found in Table 3.10 in Chapter 3. There is a correlation between improved absorption and membranes synthesised from THF based solutions. Whilst it is apparent from Table 5.6 in Chapter 5 that changing the solvent system had an impact on the fibre size, the best performing membranes from this section did not possess the smallest fibre diameters – in fact the two best performing membranes,

Sample CF_B and THF_A had the two largest diameters. The performance cannot be explained by thickness either, as all samples had thicknesses within 10% of each other. Density did vary significantly, as is to be expected when thickness remains relatively constant but the fibre diameter changes, and also does not offer a clear insight into the reasons for the observed performance differences.

It was observed, however, that the two best performing samples were electrospun from solutions using DMSO as a bad solvent. No membranes were synthesised using the same ratio of good to bad solvent as in the case of THF_A and CF_B, however. This means it cannot be empirically stated that either DMSO as a bad solvent or a 10% ratio of DMSO yields the best acoustically performing PCL fibres. Further work with a greater range of blend ratio and solvents would be needed to draw a conclusive verdict from this work.

5.5 Conclusion

This chapter was concerned with the properties of nanofibrous membranes made with different polymers. The presented results show that these materials are capable of improving the acoustic absorption coefficient of a relatively thin layer of porous substrate when added as a top layer by up to 100%. These membranes can be utilised for high-noise environments, e.g. to reduce the thickness of sound control solutions in automobiles, decreasing the overall weight, improving the quality of the interior space, and vehicle fuel efficiency. This type of acoustic material could also be applied to the aerospace industry where the size of engine nacelles could be reduced, thereby improving fuel efficiency. It has been demonstrated with several different membranes that it is possible to double the absorption coefficient across a range of frequencies. This range covers the frequencies at which noise occurs in automobiles and so offers a great improvement to the acoustics of automotive spaces. It has also been found experimentally that decreasing the fibre diameter of the nanofibres results in an improved acoustic performance – albeit typically at higher frequencies over 2500Hz.

It has been demonstrated within this chapter that there is a fundamental lack of understanding as to how sound wave behave in these types of fibrous nonwoven membrane-

like materials. This can be seen by the great difficulties associated with modelling their acoustic and non-acoustic properties using classical approaches for modelling nanofibrous media.

One main reason for the difficulty associated with modelling these membranes is that they are difficult to accurately characterise. The inability to properly define basic material parameters such as thickness, density, or porosity have a huge impact on the inaccuracies associated with modelling these membranes. The inherent variances encountered by the electrospinning process only serve to compound these inaccuracies. A random deposition of fibres on the collector mean that parameters such as density and thickness can vary even across a single sample. This means that it is entirely possible to get a value of thickness, and hence density, that is not representative of the membrane as a whole, or is entirely different to that of the sample tested acoustically. Further errors and inaccuracies can be encountered in the acoustic testing stage, where mounting the sample can lead to delamination, changing the effective thickness of the membrane, or to the presence of very small air gaps behind areas of the membrane. These effects are hard to measure and model. Further more, as illustrated in Figure 5.10, the introduction of even small circumferential airgaps can have significant impacts on the surface impedance value of the material layer making the process of modelling an even greater challenge.

New methods are needed to accurately and quickly measure these materials and to facilitate the development of better prediction models. With these in place it would be possible to understand and optimise the design of membranes for specific acoustic performances and costs. These membranes could then be used in a range of industries to combat areas of high noise with lightweight and thin solutions. If the measurement of non-acoustical parameters could be made more accurate a model could be developed from the absorption spectra of these materials, rather than attempting to fit the absorption spectra and data to previously formulated models.

Chapter 6: Conclusion and Future Work

The main aim of this PhD project was to explore the use of polymer fibres for acoustic absorption and insulation, specifically for use within the automotive industry. Two approaches were adopted. The first approach was maximising the acoustic performance of fibrous absorbers which are currently in practice, i.e. nonwoven fibrous media with fibre diameter well above 1 μm. This was achieved through a better understanding of how the material parameters impact the acoustics and hence how those parameters can be optimised to attain a greater acoustical absorption performance. The second approach was to produce a different type of acoustic solution to radically decrease weight and thickness of current materials whilst maintaining or increasing their acoustical performance. This solution was based on nanofibrous membranes that were used as a 'skin' attached to the top of conventional porous layer.

This thesis presented the methodologies for both the synthesis and characterisation of the nonwoven fibrous and nanofibrous materials in Chapter 3. In the case of nonwoven materials, the industrial partner John Cotton Group Ltd supplied a range of samples to either pre-existing specifications, which meet automotive industry requirements, or to specifications given as a result of optimisation work conducted during the PhD. The nanofibrous materials were synthesized in house via electrospinning and through collaboration with NXTNANO (OK, USA) and the University of Surrey (Surrey, UK). The variation of both electrospinning and solution parameters allowed for a degree of control over material properties like fibre diameter, thickness, and pore size. Through these methods it was possible to characterise the materials efficiently and accurately, whilst also enhancing the understanding of how each material property impacts the acoustic performance of the specimen.

Characterising the material parameters of the nonwoven samples, followed by acoustic testing and modelling of the nonwoven fibrous samples made up the first half of the work completed during this PhD. By comparing the material parameters of the nonwovens to their acoustic performance, it was established that fibre diameter was arguably the most influential

non-acoustic parameter that controls the absorption coefficient of nonwoven fibrous media and is able to be changed without increasing mass or thickness – which would be a negative consideration for industrial applications. The other two parameters which are important to determining the acoustic absorption coefficient are the density and thickness. It was conclusively shown that membranes with smaller fibre diameters were superior, as demonstrated by an early experiment which showed that halving the fibre diameter increased the absorption coefficient by 50%. This hypothesis was further confirmed when four samples were made up with progressively smaller fibre diameters in the same composition as for a current automotive insulation product, which conclusively showed that decreasing the average fibre diameter, regardless of whether it is a blend of diameters or a single diameter material, offered increased acoustic performance. This increase in performance was caused by decreasing the fibre diameter and increasing the number of interactions an impeding soundwave had with the fibre, and by the amount of drag exerted on the propagating sound wave. These phenomena significantly contribute to an increase in viscous and thermal losses in the fibrous layer and its ability to absorb sound waves.

This knowledge, and its proof in real world compositions, is valuable for industrial application as it is a relatively cheap and easy change to implement. These solutions do not require any additional processing or the introduction of a new line/range of equipment to perform. By also not leading to any significant increase in bulk density or weight it also does not impact any of the weight or efficiency constraints currently exhibited in the automotive industry. Whilst smaller fibres can be more expensive than larger diameters to produce, those presented in the scope of this work are not so much more expensive that it offsets the 50% increase in sound absorption.

There are a large number of models for sound propagation in porous media which predict rather different acoustical and related non-acoustical properties for different types of media. It is currently a challenge to know which model would yield the most accurate predictions for a given type of fibrous media. In a bid to clarify the suitability of some models to nonwoven fibrous media, two extensive studies were conducted to explore the accuracy of some of the

more commonly used prediction models. The first study (Section 4.3.1 in Chapter 4) was to look at established type of fibrous media, whilst the second study (Section 4.3.2 in Chapter 4) was expanded to include materials with varying types of polyesters – such as hollow fibres, which are becoming more popular in industrial applications. The conclusion of this first study was that for nonwoven fibrous material samples, the value of the flow resistivity inverted with either Padé approximation or Miki model is more accurate than that predicted using Bies-Hansen, Garai-Pompoli or Kozeny-Carman equations. In particular, the Miki model enables the inversion of flow resistivity of this type of fibrous media from measured surface impedance data with an accuracy of better than 15%. The Padé approximation model enables the inversion of flow resistivity with the accuracy of better than 42%. The latter error is likely related to the fact that the Miki model requires fewer parameters so that it can be more stable in the parameter inversion process. The pore structure of fibrous media with high porosity is relatively uniform so that the convergence of the Miki model for this type of media is better than that of the pore distribution model based on the Padé approximation. Furthermore, using a flow resistivity inversion based on the Miki or Padé approximation model is simpler as it can be run without the prior knowledge of any intrinsic material property other than the material's thickness, unlike other models such as the Kozeny-Carman equation, or much more complex models such as the Johnson-Champoux-Allard.

The second study was conducted on multicomponent fibrous nonwovens, and concluded that the results indicated that the adaption of the Kozeny-Carman model as proposed by Pelegrinis *et al* was the most suitable for the retrieval of the airflow resistivity value in multicomponent polyester media, with a prediction error of 8.43%. The Tarnow 'B' model, making use of drag force theory also exhibited relatively high accuracy, with a prediction error of 10.41%. It was also made clear that the choice of model is crucial to attaining reliable estimates of material parameters – especially the airflow resistivity of multi-component nonwoven materials.

However, the key takeaway from both studies was that new equations are required to relate the flow resistivity of blended fibrous media to the material density and fibre diameter distribution. It would be further beneficial if these equations or models are able to accurately

retrieve results without requiring the knowledge of a wide range of parameters. In many cases the characterisation methods used to obtain material parameters like pore size or porosity are either destructive or very slow, requiring expensive equipment. In this sense, inversion models applied to acoustical data would be preferable due to the short testing times and non-destructive nature.

It has been demonstrated within this chapter that there is a fundamental lack of understanding as to how sound wave behave in thin nanofibrous membranes. This can be seen by the great difficulties associated with modelling these membranes using classical modelling approaches for fibrous media. An attempt was made to account for the membrane vibration and to understand better the effect of circumferential gap. It was apparent that the imaginary part of the impedance exhibited much lower values than expected. There are also issues relating to the inaccuracy of material parameters which are inverted from the modelling process – which is quite likely caused by this lack of understanding of how sound waves propagate in thin membranes made of fibres whose diameter is close to molecular mean free path.

Whilst there have been a range of publications on the acoustical properties of nanofibrous membranes, there is still a relatively limited understanding of the reasons for the observed acoustical performance of these structures. It is possible that this lack of understanding is due to a range of complications relating to characterising these material's properties. Accurately measuring properties such as thickness of membranes can be challenging as the materials have such low tensile strength and rigidity that they rarely form a straight edge without rolling or curling over. Furthermore, due to the inherent nature of the synthesis methods for these materials they rarely possess a constant material thickness, instead it varies from location to location. The same is true for pore size, as it is also governed by the random nature of the synthesis processes and so is harder to control. Without an accurate understanding of these and other parameters it is possible to introduce substantial errors into any modelling or further characterisation. As an example, considering the relatively simplistic Kozeny-Carman equation for estimating flow resistivity it can easily be demonstrated that a 20% error in the

measurement of thickness (either due to curling or inhomogeneity) can quite readily be scaled up to a 63% error for the flow resistivity. This error increases exponentially with an increase in the initial error, and so it is critical that a method be developed that allows for the proper and accurate measurement of such parameters.

Before it is possible to develop any models or attempt to explain the observed behaviour of these properties it is essential that more specialised or more optimised approaches are developed. An easy example for this is the thickness of a material; as demonstrated in Section 3.3.2, accurately measuring the thickness via SEM is particularly challenging, mainly as a result of preparing the sample. During preparation it is necessary to cut the membrane and then mount it to the stub. In cutting the membrane it is possible to tear the edges, as well as delaminate them. Further delamination can occur when mounting the sample on the stub using the adhesive pads. Both of these issues can be minimalised by optimising the process. Instead of cutting the samples, embedding the membrane in a resin and then using a cryostat to ensure a clean-cut can result in a much more uniform edge with no tearing and minimal delamination as the membrane cannot be distorted whilst encased. An additional issue with measuring the thickness is that the best way of minimising the effects of rolling or curling of the membrane is to mount the membrane flush on the stub. This would then require tilting the stage in the SEM to measure the thickness, which introduces errors in the software being used to measure thickness. In order to avoid tilting the SEM it is possible to use products like Leit-C Plast which can be used to prop the sample up – but this can lead to some edge rolling. As such, there needs to be more robust methods in place to measure thickness, and this also applies to other material parameters like the porosity, pore size, and airflow resistivity.

With regards to future work, it would be interesting to continue exploring the impact that controlling the electrospinning process can have on fibres, and how they perform acoustically as a result. Within this work we have also learned that current modelling approaches for fibrous media may not obey the classical Newtonian flow laws through a stack of fibres. It is known that the physics do change when the diameter of the fibres become comparable to the mean molecular pathway, and some of the membranes presented within

this work are approaching that scale. Also, it is unclear if a fibrous structure with the thickness which is smaller or comparable to the viscous boundary layer can be modelled as a classic porous layer. In no-slip conditions it is surmised that the components closest to the wall are not subjected to frictional or thermal losses and so all components of the soundwave move at the same speed and in the same location. Recent attempts to apply this theory to some materials have been successful (Umnova, *et al*, 2009) but have not been observed to hold for the cases of nanofibrous and nanoporous materials tested. This lack of capability to model the materials synthesised during the second part of this PhD means that there is currently no way of tailoring the performance of these materials or even accurately predicting how they will perform.

The first focus of any future work would be to devise experimental methods to more precisely measure the acoustical properties of these systems. This will enable us to characterise more accurately the parameters relating to acoustical and related non-acoustical properties such as their fibre diameter, pore size, density and thickness. This in turn would lead to a greater understanding of how these materials behave acoustically and so enable more accurate modelling of the materials to be completed acoustic performance. In combination with this, there needs to be a focus on the synthesis of a range of membranes with very specific parameters, through a range of suitable methods.

The two main approaches for the generation of these membranes would be electrospinning and centrifugal jet spinning. Electrospinning has been covered extensively in this thesis already. Centrifugal jet spinning is a simpler process, wherein the polymer is either melted or dissolved, and then forced through a spinneret which is being spun at high rpm. Fibres are formed when the melted or dissolved polymer is forced out through the holes in the spinneret under centrifugation. It is capable of producing fibres of a similar diameter to electrospinning, whilst avoiding solvent waste or expense. It is also a much quicker process.

Better prediction models will be able to invert a range of key intrinsic material properties such as airflow resistivity, tortuosity, and porosity from the acoustical data. Being able to model these materials would allow for customisation in terms of their acoustical and material

properties of nanofibrous materials, potentially making them more viable options in industrial applications such as aerospace or automotive where considerations such as thickness and density are key.

In summary, there would be two objectives within any future work: (1) To synthesise a range of nanofibrous materials from a variety of approaches and with a range of polymers, and (2) utilise these materials for the development of a novel model which can be used to accurate predict the acoustical and material parameters of nanofibrous and nanoporous media.

References:

Akustik Forschung Dresden, http://www.akustikforschung.de/en/produkte/messgerate/stromungswiderstandsmessgerat-afd-300-acoustiflow/, last visited on 18/04/2017

Allard J.F., 1993, Propagation of Sound in Porous Media: Modelling Sound Absorbing Materials, 1st Ed, Elsevier, Amsterdam

Allard J.F., Depollier C., Guignouard P., *Free Field Surface Impedance Measurements Of Sound-Absorbing Materials With Surface Coatings*, Appl. Acoust., 1989, **26**(3): 199-207

Allard J.F., *New empirical equations for sound propagation in rigid frame fibrous materials*, J. Acoust. Soc. Am., 1992, **91**(6), 3346-3353

Allard J.F., 1993, *Propagation of Sound in Porous Media*, 1st Ed, Elsevier Applied Science, London

Allard J.F., Atalla N., 2009, *Propagation of Sound in Porous Media: Modelling Sound Absorbing Materials,* 2nd Ed, Wiley, New York

ASTM C830-00(2016), *Standard Test Methods for Apparent Porosity, Liquid Absorption, Apparent Specific Gravity, and Bulk Density of Refractory Shapes by Vacuum Pressure*, ASTM International, West Conshocken, PA, 2016

Attenborough K., *Acoustical characteristic of porous materials*, Phys. Rep., 1982, **82**(3), 179-227

Attenborough K., *Acoustical impedance models for outdoor ground surfaces*, J. Sound. Vib., 1985, **99**, 521-524

Bakker R.H., Pedersen E., van den Berg G.P., Stewart R.E., Lok W., Bouma J., *Impact of wind turbine sound on annoyance, self-reported sleep disturbance and psychological distress*, J. Sci. Tot. Env., 2012, **425**, 42-51

Barrett E.P., Joyner L.G., Halenda P.P., *The determination of Pore Volume and Area Distribution in Porous Substances. I. Computations from Nitrogen Isotherms*, J.Am. Chem. Soc., 1951, **73**, 373-380

Basu C., *Effective Tortuosity and Different Acoustic Waves in Porous Media*, Il Nuovo Cimento D., 1992, **14**(9), 947-953

Baxa D.E., 1982, *Noise Control in Internal Combustion Engines*, 1st Ed, John Wiley & Sons, New Year

Bies D.A., Hansen C.H., *Flow Resistance Information for Acoustical Design*, Appl. Acoust., 1980, **13**(5), 357-391

Biot M.A., *Theory of elastic wave propagation in a fluid saturated porous solid, Parts I and II*, J. Acoust. Soc. Am., 1956, **28**, 168–191

Bosworth L.A., Downes S., *Acetone,* a *Sustainable Solvent for Electrospinning Poly(e-Caprolactone Fibres: effect of Varying Parameters and Solution Concentrations on Fibre Diamter*, J. Polym. Environ., 2012, **20**, 879-886

Boyle R., *A defence of the doctrine touching the spring and weight of the air*, London, England, 1662

Browning E., 1969, *Toxicity of industrial metals*, 2nd Ed, Butterworths, London,

Buskirk Jr V., Middleton P., *Rieter Automotive: Lightweight Noise Protection*, Technical Textiles, 1999, **42**, 45

Cameron C.J., Wennhage P., Goransson P., Rhamqvist S., *Structural-acoustic Design of a Multi-functional Sandwich Panel in an Automotive Context*, J. of Sandw. Struct. and Mater., 2010, **12**, 684-708

Carman P.C., *Fluid Flow through Granular Beds*, Trans. Instn. Chem. Engrs., 1937, **15**, S32-47

Castagnède B., Aknine A., Brouard B., Tarnow V., *Effects of compression on the sound absorption of fibrous materials*, Appl. Acoust., 2000, **61**, 173-182

Chandra R., Rustgi R., *Biodegradable polymers*, Progr. Polym. Sci., 1998, **23**, 1273-1335

Chegolya A.S., Shevchenko V.V., Mikhailov G.D., *The formation of polyethylene terephthalate in the presence of dicarboxylic acids*, J. Polym. Sci.: Part A Polym. Chem., 1979, **17**, 889-904

Coa Q., Cai Y., Jing B., Liu P., *Structure and mechanical properties of thermoplastic polyurethane, based on hyperbranched polyesters*, J. Appl. Polym. Sci., 2006, **102**, 5266-5273

Coates M., Kierzkowski M., *Acoustic Textiles - Lighter, Thinner And More Absorbent*, Technical-Textiles-International, 2002

Conrad J., 2001, 'Engineering Acoustics and Noise Control', in Prentice-Hall N.J., Alton Everest F. (eds) *The Master Handbook of Acoustics*, 4th ed, McGraw-Hill, New York

Darcy H., *Détermination des lois d'écoulement de l'eau à travers le sable*, In appendix - Note D - of "Les fontaines publiques de la ville de Dijon", 1856, 590-591

Davies C.N., *The separation of airborne dust and particles*, Proc Inst Mech Eng B J Eng Manuf., 1953, **1**, 185-213

Deitzel J.M., Kleinmeyer J., Harris D., Beck Tan N.C., *The effect of processing variables on the morphology of electrospun nanofibers and textiles*, Polymer, 2001, **42**, 261-272

Delany M.E., Bazley E.N., *Acoustical properties of fibrous absorbent materials*, Appl. Acoust., 1970, **3**, 105-116

Ding W., Wei S., Zhu J., Chen X., Rutman D., Guo Z., *Manipulated Electrospun PVA Nanofibers with Inexpensive Salts*, Macromol. Eng., 2010, **295**, 958-965

Dockrell J.E., Shield B.M., *Acoustical barriers in classrooms: the impact of noise on performance in the classroom*, Brit. Educ. Res. J., 2006, **32**, 509-525

Dong H., Cao S.-G., Li Z.-Q., Han S.-P., You D.-L., Shen J.-C., *Study on the enzymatic polymerization mechanism of lactone and the strategy for improving the degree of polymerization*, J. Polym. Sci. Part A: Polym. Chem., 1999, **37**, 1265-1275

Doutres O., Atalla N., Dong K., *Effect of the microstructure closed pore content on the acoustic behaviour of polyurethane foams*, J. Appl. Phys., 2011, **110**, 64901

Egab L., Wang X., Fard M., *Acoustical characterisation of porous sound absorbing materials: A review*, Int. J. Veh. Noise. Vib., 2014, **10**(1), 129-149

Eur-Lex, Regulation (EC) No 661/2009 of the European Parliament and of the Council of 13 July 2009 concerning type-approval requirements for the general safety of motor vehicles, their trailers and systems, components and separate technical units intended therefor (Text with EEA relevance), 2009, available online at https://eur-lex.europa.eu/legal-content/EN/ALL/?uri=CELEX%3A32009R0661, last accessed 05/02/2019

Frenot A., Chronakis I.S., *Polymer nanofibers assembled by electrospinning*, Curr. Opin. Colloid Inerface Sci., 2003, **8**(1), 64-75

Freymann R.F., 2000, *Advanced Numerical and Experimental Methods in the Field of Vehicle Structural-acoustics*, 1st Ed, Hieronymus, Germany

Garai M., Pompoli F., *A simple empirical model of polyester fibre materials for acoustical applications*, J. Appl. Acoust., 2005, **66**, 1383-1398

Ghelich R., Rad M.K., Youzbashi A.A., *Study on Morphology and Size Distribution of Electrospun NiO-GDC Composite Nanofibers*, J. Eng. Fiber. Fabr., 2015, **10**(1), 12-19

Gross J.R., Hurley J.S, Boehmer B.E., Moose R.T, *Nonwoven material for acoustic insulation, and process for manufacture*, US Patent 7918313B B2

Gross R.A., Kalra B., *Biodegradable Polymers for the Environment*, Science, 2002, **297**(5582), 803-807

Gupta P., Elkins C., Long T.E., Wilkes G.L., *Electrospinning of linear homopolymers of poly(methyl methacrylate): exploring relations between fibre formation, viscosity, molecular weight and concentration in a good solvent*, Polym., 2005, **46**, 4799-4810

Hahladakis J.N, Costas A.V., Weber R., Iacovidou E., Purnell P., *An overview of chemical additives present in plastics: Migration, release, fate and environmental impact during their use, disposal and recycling*, J. Haz. Mat., 2018, **344**, 179–199

Happel J., *Viscous flow relative to arrays of cylinders*, J. Acoust. Soc. Am., 1947, **19**, 866-871

Harrison M., 2004, *Vehicle Refinement Controlling Noise and Vibration in Road Vehicles*, 1st Ed, Butterworth-Heinemann, Oxford

Hasimoto H., *On the periodic fundamental solutions of the stokes equations and their application to viscous flow past a cubic array of spheres*, J. Fluid. Mech., 1959, **5**, 317-328

Helmer A., 2002, *Application of Nonwoven and Fiber Structure in the Car and Their Acoustic Performance*, Melliand International, 2002, **8**, 60

Horoshenkov K.V., *A review of Acoustical Methods for Porous Material Characterisation*, Int. J. Acoust. Vib., 2017, **22**(1), 92-103

Horoshenkov K.V., Attenborough K., Chandler-Wilde S.N., *Pade approximants for the acoustical properties of rigid frame porous media with pore size distribution*, J. Acoust. Soc. Am., 1998, **104**, 1198-1209

Horoshenkov K.V., *Characterisation of Acoustic Porous Materials*, Proceedings of the Institute of Acoustics, 2006, **28**, 1

Horoshenkov K.V., Groby J-P., Dazel O., *Asymptotic limits of some models for sound propagation in porous media and the assignment of the pore characteristic lengths, J. Acoust. Soc. Am.*, 2016, **139**, 2436-2474

Horoshenkov K.V., Khan A., Bécot F.-X., Jaouen L., Sgard F., Renault A., Amirouche N., Pompoli F., Prodi N., Bonfiglio P., Pispola G., Asdrubali F., Hübelt J., Atalla N., Amédin C.K., Lauriks W., Boeckx L., *Reproducibility experiments on measuring acoustical properties of rigid-frame porous media (round-robin test)*, J. Acoust. Soc. Am., 2007, **122**(1), 345-353

Horoshenkov K.V., Swift M.J., *The Effect Of Consolidation On The Acoustic Properties of Loose Rubber Granulates*, Appl. Acoust., 2001, **62**(6), 665-690

Hsieh Y., Lin J., Ding B., Yu J., *Direct Fabrication of Highly Nanoporous Polystyrene Fibres via Electrospinning*, ACS Appl. Mat. Interfaces, 2010, **2**(2), 521-528

Huang H, Oizumi S., Kojima N., Sakai Y., *Avidin-biotin binding-based cell seeding and perfusionculture of liver-derived cells in a porous scaffold with a three-dimensional interconnected flow-channel network*, Biomater., 2007, **28**, 3815-3823

Huang Z.-M., Zhang Y.-Z., Kotaki M., Ramakrishna S., *A review on polymer nanofibers by electrospinning and their applications in nanocomposites*, Comp. Sci. Tech., 2003, **63**, 2223-2253

Hurrell A.I., Horoshenkov K.V., Pelegrinis M.T., *The accuracy of some models for the airflow resistivity of nonwoven materials*, Appl. Acoust., 2018, **130**, 230-237

Hutmacher D.W., Woodruff M.A., *The return of a forgotten polymer – Polycaprolactone in the 21st century*, Progr. Polym. Sci., 2010, **35**, 1217-1256

Ibrahim M.A., Melik R.W., *Physical Parameters Affecting Acoustic Absorption Characteristics of Fibrous Materials*, Proceedings of the mathematical and physical society of Egypt, 1978, **46**, 125-130

Ingard K.U., 1994, *Notes on Sound Absorption Technology*, Poughkeepsie, NY: Noise Control Foundation

ISO10534-2:1998, *Determination of Sound Absorption Coefficient and Impedance in Impedance Tubes, Part 2: Transfer-Function Method International Organization for Standardization*, Geneva, Switzerland, 1998

ISO9053:1991, *Acoustics – Determination of airflow resistance – Part 1: Static airflow method*, Geneva, Switzerland, 1991 (revised 2018)

Johnson D.L., Koplik J., Dashen R., *Theory of dynamic permeability and tortuosity in fluid-saturated porous media*, J. Fluid. Mech., 1987, **176**, 379-402

Kamatani H., Konagaya S., *Effect of phosphorous compounds on the activity of catalyst (Zn(II), Co(II), Mn(II)) in the polycondensation of bis(2-hydroxyethyl)terephthalate*, Kobunishi Ronbunshu, 1979, **36**, 293-298

Kamatani H., Konagaya S., Nakmura Y., *Effect of phosphoric acid on the polycondensation of bis(hydroxyethyl)terephthalate catalyzed by Sb(III) compounds*, Polymer J., 1980, **12**, 125-130

Kang C., Lee B.C., Ihm D.W., *Modelling of semibatch direct esterification reactor for poly(ethylene terephthalate) synthesis*, J. Appl. Polym. Sci., 1996, **60**, 2007-2015

Katsogiannis K.A.G., Vladisavljevic G.T, Georgiadou S., *Porous electrospun polycaprolactone (PCL) fibres by phase separation*, Euro. Pol. J., 2015, **69**, 284-295

Kesel C.D., Wauven C.V., David C, *Biodegradation of polycaprolactone and its blends with poly(vinylalcohol) by micro-organisms from a compost of house-hold refuse*, Polym. Degrad. Stab, 1997, **55**, 107-113

Kirchhoff G.R., 1876, *Vorlesungen uber mathmatische Physik*, 1st Ed, Teubner, Leipzig

Knapen E., Lanoye R., Vermeir G., Van Gemert D., *Sound Absorption By Polymer-Modified Porous Cement Mortars*, 6th International Conference on Materials Science and Restoration, MSR-VI Aedificatio Publishers, 2003, 347-358

Ko B.-T., Lin C.-C., *Synthesis, Characterization, and Catalysis of Mixed-Ligand Lithium Aggregates, Excellent Initiators for the Ring-Opening Polymerization of L-Lactide*, J. Am. Chem. Soc., 2001, **123**(33), 7973-7977

Kobayashi S., *Enzymatic Polymerization: A new method of polymer synthesis*, J. Polym. Sci. Part A: Polym. Chem, 2000, **37**(16), 3031-3056

Kobayashi S., Takeya K., Suda S., Uyama H., *Lipase-catalyzed rig-opening polymerization of medium-size lactones to polyesters*, Macromol. Chem. Phys., 1998, **199**, 1729-1736

Koizumi T., Tsujiuchi N., Adachi A., *The development of sound absorbing materials using natural bamboo fibers*, WIT Press, 2002, **59**, 157-166

Kozeny J., *Über kapillare Leitung des Wasser sim Boden; (Aufsteig, Versickerung und Anwendung auf die Bewässering)*, Hölder-Pichler-Tempsky, 1927

Kuwabara S., *The forces experienced by randomly distributed parallel circular cylinders or spheres in a viscous flow at small reynolds numbers*, J. Phys. Soc. Jpn., 1959, **14**, 527-532

Labet M., Thielemans W., *Synthesis of polycaprolactone: a review*, Chem. Soc. Rev., 2009, **38**, 3484-3504

Lafarge D., Lemarinier P., Allard J.-F., Tarnow V., *Dynamic compressibility of air in porous structures at audible frequencies*, J. Acoust. Soc. Am., 1997, **102**(4), 1995-2006

Lam C.X.F., Teoh S.H., Hutmacher D.W., *Comparison of the degradation of polycaprolactone and polycaprolactone-(β-tricalcium phosphate) scaffolds in alkaline medium*, Polym. Int., 2007, **56**, 718-728

Langmuir I., Report of smokes and filters, Part IV of a report for the office of scientific research and development, OSRD No. 865, Ser. No. 353, Filtration of aerosols and the development of filter materials, by Rodebush, W. H. *et al*, 4th September 1942

Lauricella M., Cipolletta F., Pontrelli G., Pisignano D., Succi S., *Effects of orthogonal rotating electric fields on electrospinning process*, Phys. Fluids, 2017, **29**(8), 082003

Leclaire P.,Umnova O., Horoshenkov K.V., *Porosity measurement by comparison of air volumes*, Rev. Sci. Instrum. 2003, **74**(3), 1366-1370

Lee K.H., Kim H.Y., Khis M.S., Ra Y.M., Lee D.R., *Characterization of nano-structured poly(epsilon-caprolactone) nonwoven mats via electrospinning*, Polymer, 2003, **44**, 1287-1294

Lee Y., Joo C., *Sound Absorption Properties of Recycled Polyester Fibrous Assembly Absorbers*, Autex Res. J., 2003, **3**(2), 78-84

Li-na J.I., *Study on Preparation Process and Properties of Polyethylene Terephthalate (PET)*, Appl. Mech. Mater., 2013, **312**, 406-410

Lind-Nordgren E., Göransson P., *Optimising open porous foam for acoustical and vibrational performance*, J. Sound Vib., 2010, **329**, 754-767

Linton Johnson D., Plona T.J., Scala C., Pasierb F., Kojima H., *Tortuosity and Acoustic Slow Waves*, Am. Phys. Soc., 1982, **49**(25), 1840-1844

Lockerby D.A., Reese J.M., Emerson D.R., Barker B.W., *Velocity boundary conditions at solid walls in rarefied gas calculations*, Phys. Rev. E, 2004, **70**, 017303

Lopes-da-Silva J.A., Rei M.F., Vlerinho B., *Solvent and Concentration Effects on the Properties of Electrospun Poly(ethylene terephthalate) Nanofiber Mats*¸ J. Polym. Sci. B.: Polym. Phys., 2008, **46**, 460-471

Lopes-da-Silva J.A., Veleirinho B., *Application of electrospun poly(ethylene terephthalate) nanofiber mat to apple juice clarification*, Proc. Biochem., 2009, **44**, 353-356

Luciani A., Coccoli V., Orsi S., Ambrosio L., Netti P.A., *PCL microspheres based functional scaffolds by bottom-up approach with predefined microstructural properties and release profiles*, Biomater., 2008, **29**, 4800-4807

MacDonald, W.A., *New advances in poly(ethylene terephthalate)polymerization and degradation*, Polym. Int., 2002, **51**, 923-930

Mahalingam S., Raimi-Abraham B.T., Craig D.Q.M., Edirisinghe M., *Solubility-spinnability map and model for the preparation of fibres of polyethylene (terephthalate) using gyration and pressure*, Chem. Eng. J., 2015, **280**, 344-353

Manning J., Panneton R., *Acoustical model for shoddy-based fiber sound absorbers*, Text. Res. J., 2013, **83**, 1356-1370

Materiacustica S.R.L., http://www.materiacustica.it/mat_Prodotti_3Mics.html, accessed on 20/09/2016

MatWorks, http://uk.mathworks.com/matlabcentral/fileexchange/8277-fminsearchbnd--fminsearchcon, last visited on 22/09/2016

Mazoochi T., Hamadanian M., Ahmadi M., Jabbari V., *Investigation of the morphological characteristics of nanofibrous membrane as electrospun in the different progressing parameters*, Inter. J. Indust. Chem., 2012, **3**(2), 1-8

Miki Y., *Acoustic properties of porous materials – Generalization of empirical models*, J. Acoust. Soc. Jap., 1990, **11**, 25-28

Miki Y., *Acoustical properties of porous materials – Modifications of Delany-Bazley models*, J. Acoust. Soc. Jpn., 1990, **11**(1), 19-24

Mohanty A.R, Fatima S., *An overview of automobile noise and vibration control*, Noise Notes, 2006, **13**(1), 43-56

Nair L.S., Laurencin C.T., *Biodegradable polymers as biomaterials*, Progr. Polym. Sci., 2007, **32**, 762-798

Narang P.P., *Material Parameter Selection in Polyester Fibre Insulation for Sound Transmission and Absorption*, Appl. Acoust., 1995, **45**, 335-358

Nelder J.A., Mead R., *A simplex method for function minimization*, Comput. J., 1965, **7**(4), 308-13

Oh S.-H., Kim H.-S., Park Y., *Active Control of Road Booming Noise in Automotive Interiors*, J. Acoust. Soc. Am., 2002, **111**, 180–188

Okada M., *Chemical syntheses of biodegradable polymers*, Progr. Polym. Sci., 2002, **27**, 87-133

Paul D.R, Barlow J.W., Keskkhula H., 1985, 'Polymer Blends' in Mann G. (ed) *Encyclopedia of Polymer Science and Engineering*, 2nd Ed, vol. 12, Wiley, New York, 118-256

Pelegrinis M., Horoshenkov K. V., Burnett A., *An application of Kozeny - Carman flow resistivity model to predict the acoustical properties of polyester fibre*, J. Appl. Acoust., 2016, **111**, 1-4

Pena J., Corrales T., Lzquierdo-Barba I., Doadrio A.L., Vallet-Regi M., *Long term degradation of poly(ε-caprolactone) films in biologically related fluids*, Polym. Deg. Stab., 2006, **91**, 1424-1432

Pilon D., Panneton R., *Effects of circumferential air gaps on the measurement of the absorption coefficient of poroelastic materials*, JASA, 2002, **112**, 2383

Platel R.H., Hodgson L.M., Williams C.K., *Biocompatible Initiators for Lactide Polymerization*, Polym. Rev., 2008, **48**, 11-63

Publications Office of the European Union, Regulation (EU) No 540/2014 of the European Parliament and of the Council of 16 April 2014 on the sound level of motor vehicles and of replacement silencing systems, and amending Directive 2007/46/EC and repealing Directive 70/157/EEC (Text with EEA relevance), 2014, available online at https://publications.europa.eu/en/publication-detail/-/publication/fe98a835-e656-11e3-8cd4-01aa75ed71a1/language-en, last accessed 05/02/2019

Nichols Jr R.H., *Flow-resistance characteristics of fibrous acoustical materials*, J. Acoust. Soc. Am., 1947, **19**(5), 866-871

Rafler G., Reinisch G., Bonatz E., *Kinetics, mass transport and thoughts about the mechanism of the formation of polyethylene terephthalate by metal ion catalysis*, Acta. Chim., 1974, **81**, 253-267

Rao M.D., *Recent Applications of Viscoelastic Damping for Noise Control in Automobiles and Commercial Airplanes*, JSV, 2003, **263**(3), 457-474.

Ravindranath K., Mashelkar R.A., *Polyethylene Terephthalate – I. Chemistry, Thermodynamics and Transport Properties*, Chem. Eng. Sci., 1986, **41**(9), 2197-2214

Rayleigh J.W.S., 1877, *Theory of Sound*, 1st Ed, MacMillan and Co, London

Reneker D.H., Chun I., *Nanometre diameter fibres of polymer, produced by electrospinning,* Nanotech., 1996, **7**(3), 216-223

Robb B., Lennox B., 2011, '*The electrospinning process, conditions and control*' in Bosworth L., Downes S. (ed) Electrospinning for Tissue Regeneration | Electrospinning for Tissue Regen., 1st Ed, Elsevier BV, United Kingdom, 51-66

Rocca M.C., Carr G., Lambert A.B., MacQuarrie, D.J., *Process for the oxidation of cyclohxanone to ε-caprolactone*, US Pat., 6531615 B2, 2003

Sagartzazu X., Hervella-Nieto L., Pagalday J.M., *Review in Sound Absorbing Materials*, Arch. Computat. Methods Eng., 2008, **15**, 311-342

Saha P., *Developing Vehicle Sound Packages*, JSV, 2011, Sound and Vibration, 10-13

Saha P., *Application of Noise Control Materials to Trucks and Buses*, SAE Technical Paper 2002-01-3063, 2002.

Scheidegger A.E., 1963, *The physics of flow through porous media,* Ed: Adrian E*,* 2nd Edition, University of Toronto Press, Toronto

Seddeq H.S, *Factors Influencing Acoustic Performance of Sound Absorptive Materials*, AJBAS, 2009, **3**(4), 4610-4617

Shah T.H, Bhatty J.I., Gamlen G.A., *Affects of the chemistry of poly(ethylene terephthalate): 5. Polymerization of bis-(2-hydroxyethl)terephthalate by various metallic catalysts*, Polymer, 1984, **25**, 1333-1336

Shenoy S.L., Douglas Bates W., Frisch H.L., Wenk G.E., *Role of chain entanglements on fibre formation during electrospinning of polymer solutions: good solvent, non-specific polymer-polymer interaction limit*, Polymer, 2005, **46**, 3372-3384

Shepherd D., McBride D., Welch D., Dirks K.N., Hill E.M*., Evaluating the impact of wind turbine noise on health-related quality of life*, Noise Health, 2011, **54**, 333-339

Singer J.E., Glass D.C., Cohen S., *Apartment Noise, Auditory Discrimination, and Reading Ability in Children*, J. Exp. Soc. Psychol., 1973, **9**, 407-422

Sinha V.R., Bansal K., Kaushik R., Kumria R., Trehan A., *Poly-ε-caprolactone microspheres and nanospheres*, Int. J. Pharm., 2004, **278**, 1-23

Sivalingham G., Madras G., *Modeling of Lipase Catalyzed Ring-Opening Polymerization of ε-Caprolactone*, Biomacromol., 2004, **5**(2), 603-609

Smallwood I.M., *Handbook of organic solvent properties*, 1996, 1st Edition, Arnold, Great Britain

Strain I.N., Wu Q., Pourrahimi A.M., Hedenqvist M.S., Olsson R.T., Andersson R., *Electrospinning of recycled PET to generate tough mesomorphic fibre membranes from smoke filtration*, J. Mat. Chem. A., 2015, **3**, 1632-1640

Subramanian S., Surampudi R., Thomson K., Vallurupalli S., *Optimization of Damping Treatments for Structure Borne Noise Reduction*, Sound and Vibration, 2004, **38**, 14–18

Sun H., Mei L., Song C., Cui X., Wang P., *The in vivo degradation, absorption and excretion of PCL-based implant*, Biomater., 2006, **27**(9), 1735-1740

Tan S.-H., Inai R., Kotaki M., Ramakrishna S., *Systematic parameter study for ultra-fine fiber fabrication via electrospinning process*, Polymer, 2005, **46**, 6128-6134

Tarnow V., *Airflow resistivity of models of fibrous acoustic materials*, J. Acoust. Soc. Am., 1996, **100**, 3706-3713

Taylor G., *Disintegration of Water Droplets in an Electric Field*, Proc. R. Soc. A, 1964, **280**, 383-397

Thier-Grebe R., Rabe M., *Polyester with titanium dioxide catalyst 'C-94'*, Property Acordis 2000:1-11

Tomita K., *Some considerations on the catalysis mechanism of metal compounds in the polycondensation process of bis(2-hydroxyethyl)terephthalate*, Kobunshi Ronbunshu, 1976b, **33**, 96-101

Tomita K., *Studies on the formation of polyethylene terephthalate: 6. Catalytic activity of metal compounds in polycondensation of bis(2-hydroxyethyl)terephthalate*, Polymer, 1976a, **17**, 221-224

Umnova O., Tsiklauri D., Venegas R., *Effect of boundary slip on the acoustical properties of microfibrous* materials, J. Acoust. Soc. Am., 2009, **126**(4), 1850-1861

Van Natta F.J., Hill J.W., Carruthers W.H., *Polymerization and ring formation, ε-caprolactone and its polymers*, J. Am. Chem. Soc., 1934, **56**, 455-459

Vehicle Certification Agency, Cars and Noise¸ available online at https://www.vehicle-certification-agency.gov.uk/fcb/cars-and-noise.asp, last accessed 05/02/2019

Voronina N.N., Horoshenkov K.V., *A new empirical model for the acoustic properties of loose granular media*, Appl. Acoust., 2003, **64**(4), 415-432

Wang L.-N., Wangg Y.-W., Liu W.-T., Xia X.-L., He S.-Q., Liu H., *Crystallization behaviour and mechanical properties of an electrospun ethanol-mediated poly(ethylene terephthalate) fibrous membrane*, J. Appl. Pol. Sci., 2015, **132**(32), 42341

Wentzel R.E., Saha P., *Emperically Predicting the Sound Transmission Loss of Double-Wall Sound Barrier Assemblies*, SAE Technical Paper **951268**, 1995.

Yang T., Mishra R., Horoshenkov K.V., Hurrell A., Saati F., Xiong X., *A study of some airflow resistivity models for multi-component polyester fiber assembly*, Applied Acoustics, 2018, **139**, 75-81

Ye L., Liu T., Liu Y., Nie F., *Synthesis and properties of polyester-based TPUs prepared by solution polymerization*, Macromol. Eng., 2008, **37**, 331-340

Yoda K., *Catalytic action of metal compounds in transesterification*, J. Chem. Soc. Japan, 1971, **74**, 1476-1482

Zander N.E., Gillan M., Sweetser D., *Recycled PET nanofibers for Water Filtration Applications*, Mater., 2016, **9**, 247-257

Zein I., Hutmacher D.W., Tan K.C., Teoh S.H., *Fused deposition modelling of novel scaffold architectures for tissue engineering applications*, Biomater., 2002, **3**, 1169-1185

Zhang C., Yuan X., Wu L., Han Y., Sheng J., *Study on morphology of electrospun poly(vinyl alcohol) mats*, Eur. Polym. J. **41**(3), 423-432

Zhong X., Kim K., Fang D., Ran S., Hsiao B.S., Chu B., *Structure and process relationship of electrospun bioadsorbable nanofibre membranes*, Polymer, 2002, **43**, 4403-4412